Multi-Scale Mathematical Modelling of Brain Networks in Alzheimer’s Disease

Submitted by Luke William Tait to the University of Exeter as a thesis for the
degree of Doctor of Philosophy in Mathematics
June 2019

I certify that all material in this thesis which is not my own work has been identified and that any material that has previously been submitted and approved for the award of a degree by this or any other University has been acknowledged.

Signature: ....

Abstract

Perturbations to brain network dynamics on a range of spatial and temporal scales are believed to underpin neurological disorders such as Alzheimer's disease (AD). This thesis combines quantitative data analysis with tools such as dynamical systems and graph theory to understand how the network dynamics of the brain are altered in AD and experimental models of related pathologies.

Firstly, we use a biophysical neuron model to elucidate ionic mechanisms underpinning alterations to the dynamics of principal neurons in the brain's spatial navigation systems in an animal model of tauopathy. To uncover how synaptic deficits result in alterations to brain dynamics, we subsequently study an animal model featuring local and long-range synaptic degeneration. Synchronous activity (functional connectivity; FC) between neurons within a region of the cortex is analysed using two-photon calcium imaging data. Long-range FC between regions of the brain is analysed using EEG data. Furthermore, a computational model is used to study relationships between networks on these different spatial scales.

The latter half of this thesis studies EEG to characterize alterations to macroscale brain dynamics in clinical AD. Spectral and FC measures are correlated with cognitive test scores to study the hypothesis that impaired integration of the brain's processing systems underpin cognitive impairment in AD. Whole brain computational modelling is used to gain insight into the role of spectral slowing on FC, and elucidate potential synaptic mechanisms of FC differences in AD. On a finer temporal scale, microstate analyses are used to identify changes to the rapid transitioning behaviour of the brain's resting state in AD.

Finally, the electrophysiological signatures of AD identified throughout the thesis are combined into a predictive model which can accurately separate people with AD and healthy controls based on their EEG, results which are validated on an independent patient cohort. Furthermore, we demonstrate in a small preliminary cohort that this model is a promising tool for predicting future conversion to AD in patients with mild cognitive impairment.

Acknowledgements

I would like to thank my supervisors Dr Marc Goodfellow and Dr Jon Brown for their support, guidance and encouragement. Marc has always been extremely supportive of my ideas and pushed me to grow as a researcher, and I am particularly grateful for his always being available and providing a friendly environment in which to learn and develop my skills. When I began my PhD, I had no academic background in biology, neuroscience, or Alzheimer's disease, so I'd particularly like to thank Jon for being a valuable source of knowledge in these fields and making this thesis possible. Finally, both Marc and Jon have always enthusiatically encouraged me to follow my passion of applied, interdisciplinary research, encouraging me to surround myself by a broad network of experimental and clinical collaborators, go to conferences, and giving me the opportunity to perform some experimental research. For this I am extremely grateful. Thank you both.

Whilst it would be impossible to acknowledge every academic who has supported me throughout the course of my PhD, there are a number of people who deserve a special mention. I'd like to thank Kyle Wedgwood for his great expertise and mentorship in the field of dynamical systems theory. I also thank Krasimira Tsaneva and Jamie Walker for our yearly assessments - your feedback and guidance have been invaluable. I thank Wessel Woldman for our many academic discussions, for his advice and support, and for always being a source of laughter. For many insightful discussions about modelling and analysis of EEG, I thank Marinho Lopes, Leandro Junges, Lauric Ferrat, and once again Wessel Woldman. I'd additionally like to acknowledge Prof John Terry and the Quantitative Biology and Medicine at Exeter group for the guidance, support, friendships, and opportunities being part of this team has offered.

For their support with the clinical and experimental aspects of my research and providing data for me to work with, I thank my collaborators George Stothart, Nina Kazanina, Elizabeth Coulthard, Francesco Tamagnini, Edoardo Barvas, and Prof Andrew Randall. I additionally thank the Alzheimer's Society for their support and opportunities for public engagement, and the members of the Alzheimer's Society Doctoral Training Centre for being excellent source of knowledge about dementia and Alzheimer's disease throughout my PhD.

Finally I thank my family and friends for their constant love, encouragement

and support. I couldn't have got to where I am without support from my parents and grandparents, and I can't express my gratitude enough for everything you do. Thanks to Charlee for his friendship and support, not just through my PhD, but for as long as I remember. Finally, thank you Katherine for believing in me, for your love and encouragement, and for keeping me sane through the process of writing this thesis. I couldn't have done it without you.

Contents

List of Figures

List of Tables

Author’s Declarations

I declare that the work in this thesis was carried out in accordance with the requirements of the University’s Regulations and Code of Practice for Research Degree Programmes and that it has not been submitted for any other academic award. Except where indicated by specific reference in the text, the work is the candidates own work. Work done in collaboration with, or with the assistance of, others, is indicated as such. Any views expressed in the dissertation are those of the author.

List of Abbreviations

Aβ	Amyloid-beta
AD	Alzheimer’s disease
AHP	After hyperpolarization
AP	Action potential
CHMP2B	Charged multivesicular body protein 2b
EC	Effective connectivity
EEG	Electroencephalography
eLORETA	Exact low resolution brain electromagnetic tomography
FC	Functional connectivity
FFT	Fast Fourier transform
fMRI	Functional magnetic resonance imaging
FTD	Frontotempotal dementia
HOA	Healthy older adult
iAAFT	Iterative amplitude adjusted Fourier transform
LFP	Local field potential
LZC	Lempel-Ziv complexity
MCI	Mild cognitive impairment
MD	Mean degree
mEC	Medial entorhinal cortex
mEC-SC	Medial entorhinal cortex stellate cell
MEG	Magnetoencephalography
MMSE	Mini-mental state examination
NFT	Neurofibrillary tangle
NMM	Neural mass model
ODE	Ordinary differential equation
PET	Positron emission tomography
PLF	Phase locking factor
PSC	Post-synaptic current
PSP	Post-synaptic potential
QIF	Quadratic integrate-and-fire
ROI	Region of interest
SC	Structural connectivity

SDE	Stochastic differential equation
SN	Saddle-node bifurcation
SNIC	Saddle-node on invariant circle bifurcation
SNP	Saddle-node of periodics bifurcation
SVM	Support vector machine
SW	Small-worldness
TG	Transgenic
WT	Wild-type

Chapter 1

Introduction

1.1 Introduction and overview of thesis

Theoretical physicist and popular science writer Michio Kaku wrote that:

> *"There are 100 billion stars in the Milky Way galaxy, roughly the same as the number of neurons in our brain. You may have to travel twenty-four trillion miles, to the first star outside our solar system, to find an object as complex as what is sitting on your shoulders."*
> – Kaku (2014)

What makes the human brain so complex? Containing 86 billion neurons (Azevedo et al., 2009) wired up to form a heirarchical network at multiple spatial scales (Sporns et al. (2005); Betzel and Bassett (2017); Figure 1.1), any network scientist would agree that the structural connectome of the brain is highly complex (Rubinov and Sporns, 2010). Adding to this complexity are the multi-scaled electrical dynamics on this network (Deco et al., 2008); from the spiking dynamics of single neurons (Izhikevich, 2007), to the emergence of oscillations in neuronal ensembles (Wallace et al., 2011) and the synchronization of brain regions at a whole-brain scale (Smith et al., 2009).

Neurological disorders such as Alzheimer's disease (section 1.2) can result in perturbations to brain dynamics and connectivity on all spatial scales (reviewed in section 1.3). By combining electrophysiological brain imaging data (Wickenden, 2014) with mathematical analysis techniques such as time series analysis (Kantz and Schreiber, 2004; Dauwels et al., 2011) and graph theory (Rubinov and Sporns, 2010), these perturbations to dynamics can be characterised quantitatively to gain insight into how brain function is altered in disease (reviewed in section 1.8). Furthermore, mathematical models of neuronal systems (section 1.5-1.7) are a powerful tool for gaining insight into the biological mechanisms underpinning alterations to brain dynamics in disease (de Haan et al., 2012a; Abuhassan et al., 2014; Dermitas et al., 2017), examining the interplay between

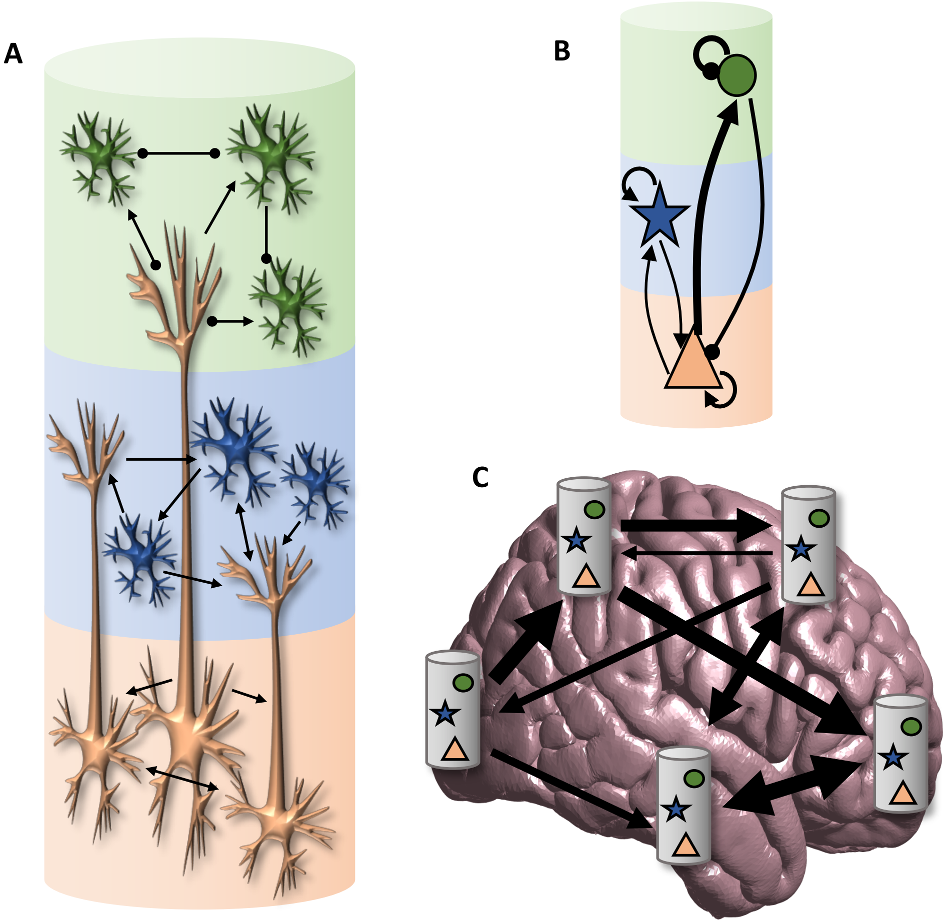

Figure 1.1: **Brain networks at multiple spatial scales** (A) At the microscale, neurons are wired up through synaptic connections. Groups of neurons with similar properties (represented by colours in the figure), are organized in layers. Connections can be excitatory (arrows) or inhibitory (circles). (B) At the meso-scale, we can consider populations of neurons with similar properties as a *neural mass*, and the connectivity between neural masses has weights dependent on the number and strength of connections between neurons within the population. (C) At the whole brain macro-scale, we can consider different regions of the brain as a neural mass. The macro-scale network is the density of connections between regions of the brain. Brain networks at all scales can additionally be functional, i.e. defined by synchronous activity instead of strength of synaptic connections.

dynamics and coupling at different spatial scales of the brain (Deco et al., 2014; Schmidt et al., 2014; Ness et al., 2018), and understanding the relationship between complex network structure and emergent dynamics (Barahona and Pecora, 2002; Lopes and Goltsev, 2019). Computational models have so much potential to unravel the complexity of brain dynamics that there are currently many large-scale research projects dedictated to building realistic brain models such as The Virtual Brain (Ritter et al., 2013), the Blue Brain Project (Markram, 2006), and the Human Brain Project (Markram et al., 2015).

In this thesis, we combine mathematical modelling and data analysis to understand alterations to the brain's electrical dynamics in Alzheimer's disease. In chapters 2-3, we study how neuronal dynamics are perturbed in two transgenic rodent models of dementia pathologies (Götz and Ittner, 2008; Roberson, 2012; Webster et al., 2014). Animal models allow for the use of invasive neuroimaging at high spatial resolution (Suter et al., 1999; Stosiek et al., 2003; Buzsáki, 2004), giving insight into cellular and synaptic mechanisms of altered neuronal dynamics due to specific dementia-related pathologies and genetic defects (Brown et al., 2011; Chong et al., 2011; Tamagnini et al., 2015; Busche et al., 2015a,b; Witton et al., 2016; Booth et al., 2016a). In chapter 2, we use biophysical models of a neuron to understand the ionic mechanisms underpinning altered dynamics of stellate neurons in the entorhinal cortex of an animal model of Alzheimer's pathology[1] (Booth et al., 2016a). In chapter 3, functional connectivity (co-activity, quantified by statistical similarities in dynamics) between networks of neurons on a local and whole-brain scale is then explore through computational analysis of functional brain imaging data recorded on distinct spatial scales in an animal model of frontotemporal dementia to understand synaptic deficits.

Despite the experimental practicality of using animal models to research electrophysiological dysfunction in dementia, there are also many limitations to consider. No animal models at present are able to fully capture the Alzheimer's disease pathologies and disease progression (Drummond and Wisniewski, 2017), and clinical trials have often demonstrated poor translationality in pharmacological intervention between rodents and humans (Drummond and Wisniewski, 2017; King, 2018), with a failure rate of clinical drug trials of 99.6% in the decade of 2002-2012 (Cummings et al., 2014). Whilst animal models are therefore useful tools to study how particular pathologies related to Alzheimer's disease will affect neural tissue, it is important to test whether electrophysiological alterations are translational between humans and animals.

Therefore chapters 4-6 apply computational modelling and data analysis to data recorded from people with Alzheimer's disease. This data is non-invasive, recording the electric potential on the scalp due to the electrical activity of the brain using a method called *electroencephalography* (EEG). Chapter 4 uses techniques from physics to estimate the brain activity based on the EEG data (Michel et al., 2004), and then combines time series analysis, graph theory, and whole-brain dynamic modelling to estimate alterations to the large scale network structure of the brain[2]. By combining these results with cognitive test scores, insight into the relationship between neuronal function and behaviour is uncovered. This work studies properties of the brain on a temporal scale of the order of tens of seconds, so in chapter 5 we study the how EEG *microstates* (Khanna et al., 2015), which are periods of stability on a temporal scale of tens to hundreds of

---

[1] This work was published in the *Journal of Theoretical Biology* as Tait et al. (2018)

[2] This work was published in *Clinical Neurophysiology* as Tait et al. (in press)

milliseconds, change in Alzheimer's disease.

In chapter 6 we combine the electrophysiological signatures of Alzheimer's disease identified in chapters 4-5 to build a statistical model predicting the likelihood of a person having the disorder. We show that using a small number of quantitative measures derived only from non-invasive electrophysiological data, the model can predict to 85% accuracy whether a person has Alzheimer's disease. These results are validated in an independent test set of clinical data. Finally, using the model we find we can also predict conversion to Alzheimer's disease within four years for 10 out of 11 peole with mild cognitive impairment, giving promising preliminary results suggesting that EEG is a potentially useful tool for aiding early diganosis of Alzheimer's disease.

The remainder of this chapter is laid out as follows. In the next section (section 1.2), we introduce Alzheimer's disease and dementia, and their characteristic pathologies. The following section (section 1.3) introduces concepts in neuroscience and electrophysiology and reviews literature on the field of Alzheimer's disease. Particularly, this section introduces some of the types of data that will be analysed and modelled throughout the thesis. Sections 1.4-1.7 focus on the quantitative methods and tools used throughout the thesis, giving a general background to dynamical systems modelling, modelling of neuronal systems at multiple spatial scales, and some of the models used in this thesis. Finally, we introduce analysis techniques used in the thesis to quantify neuronal dynamics (section 1.8).

1.2 Alzheimer's disease and dementia

Dementia is an umbrella term for a group of neurological disorders affecting 50 million people worldwide, a number which is expected to triple to 152 million by 2050 (Alzheimer's Disease International, 2018). Alzheimer's disease (AD) is the leading cause of dementia, causing between 50 and 70% of all dementias (Burns and Iliffe, 2009; World Health Organization, 2017). The other three primary diseases causing dementia are vascular dementia (approximately 25% of cases), Lewy body dementia (15%), and frontotemporal dementia ($<$5%) (Burns and Iliffe, 2009). These numbers account for the fact that some people exhibit mixed dementia (caused by more than one underlying disease), explaining the $>$100% sum of prevalences of aetiologies. Each of these dementia subtypes has different underlying pathologies and symptomatic progressions, but are all characterised by progressive cognitive decline (Agronin, 2014). This thesis focuses on AD and related pathologies.

Common symptoms of AD in the early stages include memory loss, difficulties with language, and disorientation to space and time. Cognition declines pro-

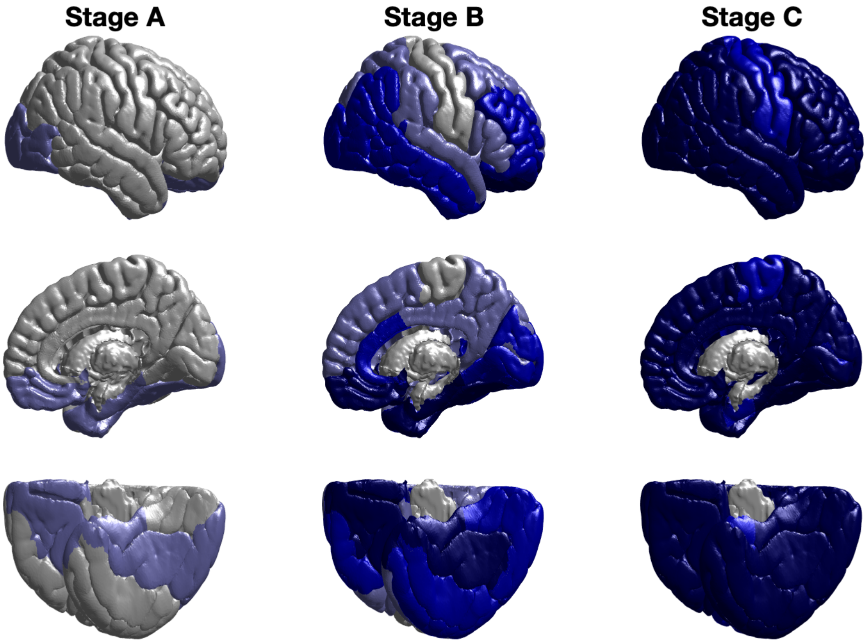

Figure 1.2: **Topographical staging of Aβ plaques.** Stages A-C of the Aβ plaque progression in AD as defined by Braak and Braak (1991), showing only cortical pathology. Grey regions have no plaques, and darker blues show progressively higher severity of the pathology. Stage A is preclinical, whilst B and C are progressive staging of clinical dementia (Braak and Braak, 1991). This figure is largely based upon Figure 4 of Braak and Braak (1991), mapped onto the ICBM152 MNI average brain (Mazziotta et al., 2001) with regions discretized according to the Desikan-Killiany atlas (Desikan et al., 2006).

gressively throughout later stages (Agronin, 2014). There is currently no cure for AD, and disease progression eventually leads to death in many cases; using the World Health Organization's guidelines (Becker et al., 2006), the UK Office for National Statistics (2018) has reported that for the years 2015-2017, dementia was the leading cause of death in the UK (with later statistics currently unavailable).

Braak and Braak (1991) described the neuropathological staging of AD, characterized by two primary pathologies. The first pathology characteristic of AD is extracellular amyloid-beta (Aβ) plaques or deposits. Aβ are peptides formed from cleavage of the amyloid precursor protein (APP) via the amyloidogenic pathway. The healthy function of APP is not well understood (Hiltunen et al., 2009). The topographical progression of Aβ plaques is shown in Figure 1.2. Whilst the severity of Aβ plaque deposits are reasonably uncorrelated with symptomatic severity, soluble Aβ pools preceeding plaque formation correlate with clinical state (Murphy and LeVine III, 2010), suggesting it may be earlier staged soluble forms of Aβ that are causative of cognitive symptoms of AD. This hypothesis has had validation in rodents, where it has been demonstrated that soluble - but not insoluble - Aβ caused synaptic impairments (Shankar et al., 2008). Impairments in cognitive domains such as spatial working memory and recognition memory have been observed in transgenic animal models with Aβ pathologies (Webster et al., 2014).

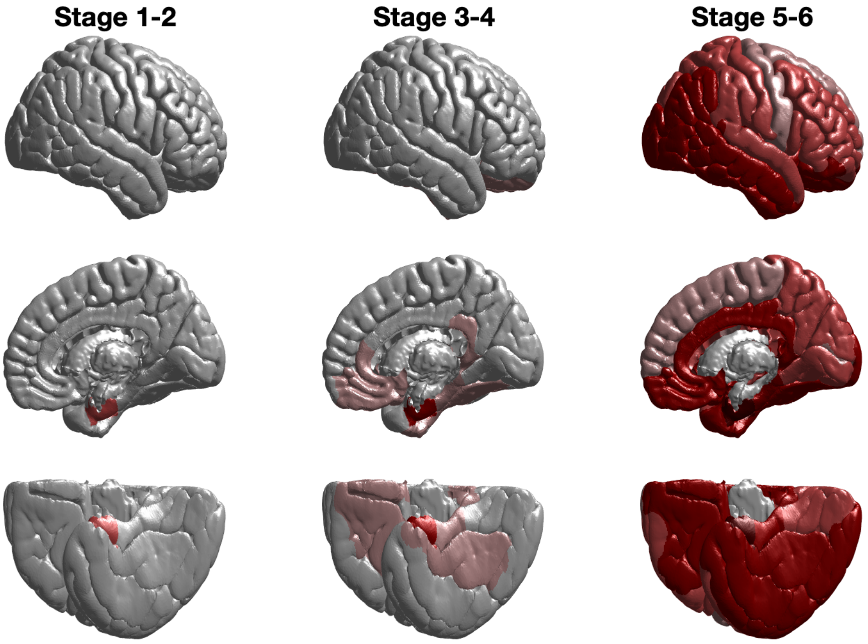

Figure 1.3: **Topographical staging of tau neurofibrillary tangles.** Stages of the tau tangle progression in AD as defined by Braak and Braak (1991), showing only cortical pathology. Grey regions have no tangles, and darker reds show progressively higher severity of the pathology. Stages I-II are preclinical, III-IV show incipient AD, and V-VI are end-stage AD (Braak and Braak, 1995). This figure is largely based upon Figure 1 of Braak and Braak (1991), mapped onto the ICBM152 MNI average brain (Mazziotta et al., 2001) with regions discretized according to the Desikan-Killiany atlas (Desikan et al., 2006).

The second primary pathology characteristic of AD is intracellular neurofibrillary tangles (NFTs) caused by hyperphosphorylated tau proteins. Tau is a protein coded by the microtubule associated protein tau (*MAPT*) gene, and plays a role in cytoskeleton stabilisation in neurons (Guo et al., 2017). Hyperphosphorylated tau and NFTs are associated with impaired axonal transport and synaptic dysfunction (Guo et al., 2017), and can be a pathology of not only AD, but also other neurodegenerative disorders such as frontotemporal dementia (Shiarli et al., 2006) and Parkinson's disease (Zhang et al., 2018).

The topographical progression of NFTs in AD is shown in Figure 1.3. Tau pathology in AD starts in the entorhinal regions of the brain, which acts as a bridge between the cortex and hippocampus (Canto et al., 2008) and plays a crucial role in the spatial memory and navigation systems (Moser et al., 2008). An early stage symptom of AD is impaired orientation to space (Lithfous et al., 2013; Allison et al., 2016), and animal models of tauopathy have demonstrated impaired spatial memory (Ramsden et al., 2005; Yue et al., 2011; Blackmore et al., 2017; Fu et al., 2017) and electrophysiological alterations to the neuronal map of space (Booth et al., 2016a; Fu et al., 2017). Chapter 2 focuses on the dynamics of neurons in the entorhinal cortex which play a crucial role in spatial memory (Tennant et al., 2018), and how they are altered in an animal model of

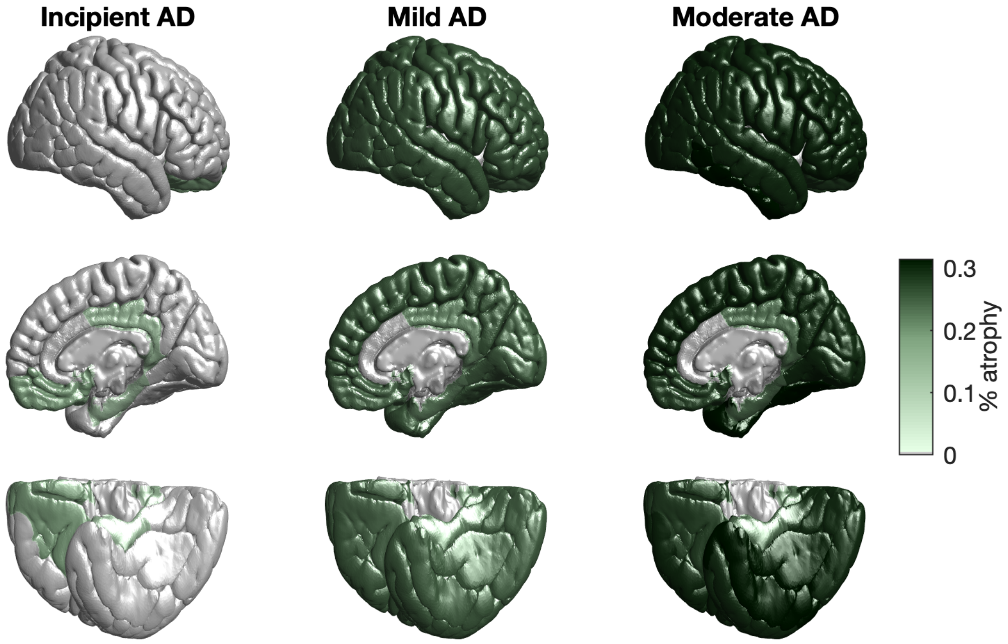

Figure 1.4: **Topographical staging of cortical atrophy**. Grey regions have no significant atrophy, whilst percentage reduction in grey matter volume is presented by the colour scale. This figure is largely based upon Table 2 of Frisoni et al. (2009), mapped onto the ICBM152 MNI average brain (Mazziotta et al., 2001) with regions discretized according to the Desikan-Killiany atlas (Desikan et al., 2006).

tauopathy.

Progressive neurodegeneration is known to occur in AD, resulting in grey matter atrophy including cortical thinning and reduced volume (Pini et al., 2016). There is evidence to suggest tau neurofibrillary tangles play a crucial role in cortical atrophy and neurodegeneration. Tau pathology is found in a broad range of neurological disorders featuring neurodegeneration including AD, frontotemporal dementia, amyotrophic lateral sclerosis (ALS), and Parkinson's disease (Spillantini and Goedert, 2013). In animal models of AD, those featuring tauopathy often exhibit severe cortical atrophy while models of amyloidopathy do not (Götz and Ittner, 2008; Jankowsky and Zheng, 2017). Furthermore, the topographical progression of cortical atrophy (Frisoni et al. (2009); shown in Figure 1.4) correlates with tau pathology (Pini et al., 2016). Particularly, at the incipient stages of AD the spatial distribution of atrophy closely resembles that of tau NFTs at Braak stages 3-4 (Figure 1.3), which correspond to incipient AD (Braak and Braak, 1995), and spreads throughout the rest of the cortex at later stages. Medial temporal structures, including the entorhinal cortex and hippocampus, are crucially some of the earliest regions to atrophy. Subcortical structures are also known to exhibit varying degrees of grey matter atrophy (Pini et al., 2016). Crucially, neurodegeneration also includes severe loss of synapses as well as neurons (Selkoe, 2002), which is believed to result in cognitive impairment in AD (Morrison and Baxter, 2012).

1.3 Electrophysiology and Alzheimer's disease

In this section, we will introduce some important concepts in neuroscience, particularly electrophysiology and neural dynamics, and briefly review how these properties of the brain change in Alzheimer's disease.

The *neuron* is the basic functional unit of the brain (Young et al., 2015). A neuron is a type of cell found throughout the nervous system which, through electrical dynamics, can recieve and transmit nerve impulses. The electrical dynamics of a neuron are regulated by transmembrane currents which are the result of flow of charged ions through channels in the membrane (Figure 1.5).

A crucial property of neurons is *excitability* (Izhikevich, 2007). At rest, charged ions are distributed across the neuronal membrane such that the neuron is negatively polarised, usually with a membrane potential in an approximate range of -40 to -90 mV, but which varies depending on the neuron (Tripathy et al., 2014). Small perturbations to a neuron at rest - for example input from a neighbouring neuron - will cause a small perturbation to the membrane potential of the neuron, which will then return to rest. However, when the input to the neuron is sufficiently depolarising, the membrane potential of the neuron reaches a *threshold* and the neuron rapidly depolarises. This is called an action potential (AP), or colloquially a spike, and causes the neuron to send electrical signals to its own neighbours. Hodgkin and Huxley (1952) quantitatively and experimentally described the generation of APs in terms of ions passing through the membrane of the squid giant axon by a process which is outlined in Figure 1.5. The spiking activity of a neuron is therefore often modelled as a binary point process (at any given time the neuron is spiking or not), and such spiking dynamics in single cells and populations of neurons is believed to be crucial for information encoding (Panzeri et al., 2015).

Experimental methods exist to record membrane dynamics of neurons - see Suter et al. (1999) for a review. Since these methods are highly invasive, usually requiring a slice of brain, research to understand how neuronal dynamics are altered in AD is predominantly performed in rodent models of AD pathology. Spatially heterogeneous alterations to cortical and hippocampal neuronal excitability have been reported in animal models of tauopathy (Rocher et al., 2010; Crimins et al., 2012; Menkes-Caspi et al., 2015; Booth et al., 2016a,b) and amyloidopathy (Brown et al., 2011; Tamagnini et al., 2015; Heggland et al., 2019). Particularly relevant to chapter 2 of this thesis are alterations to excitability of stellate cells in the medial entorhinal cortex (mEC-SCs) in a mouse model of tauopathy reported by Booth et al. (2016a). mEC-SCs play a crucial role in the spatial navigation systems of the brain (Tennant et al., 2018) which are disrupted in AD (Lithfous

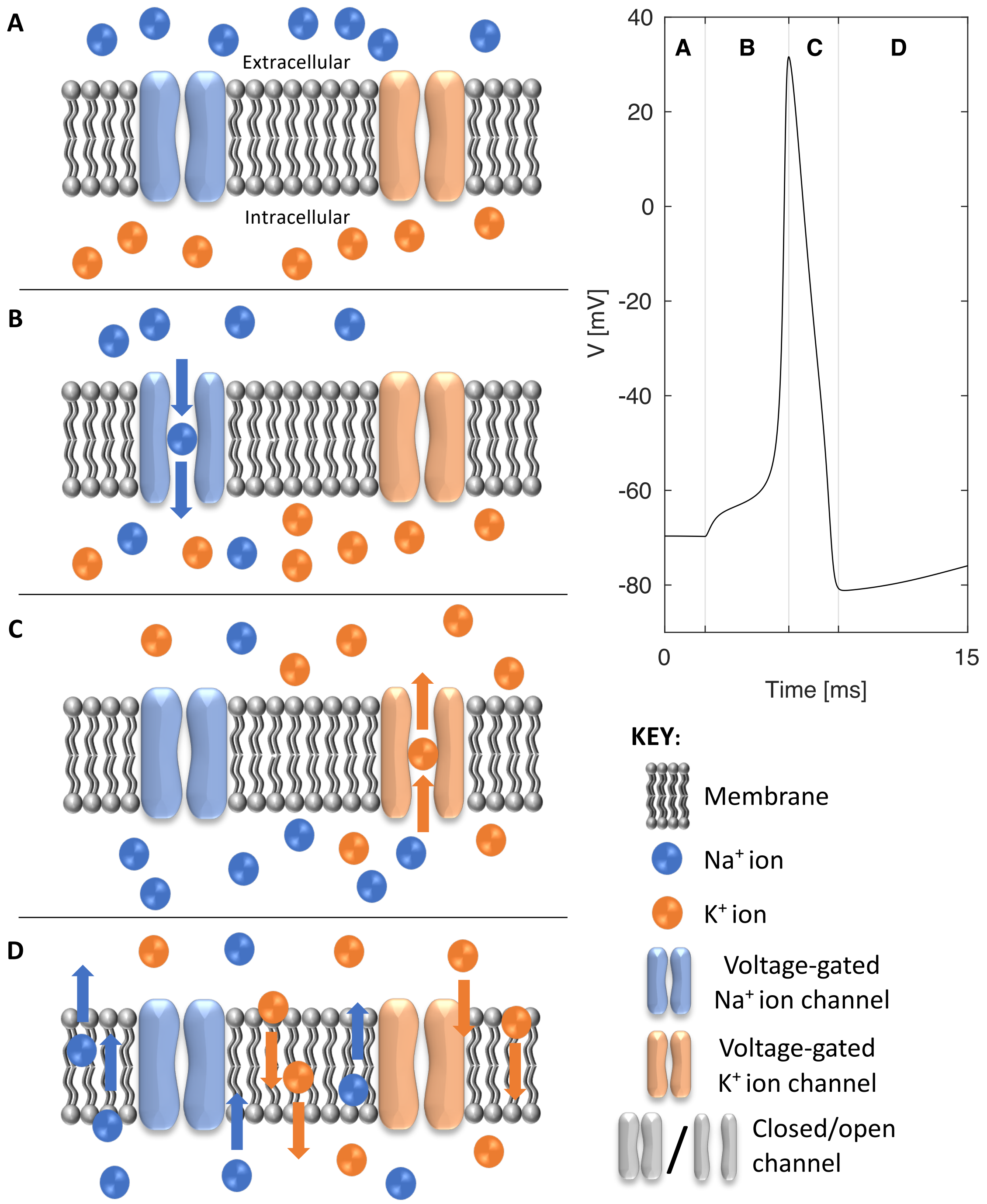

Figure 1.5: **Generation of an action potential in a neuron,** as described by Hodgkin and Huxley (1952) for the squid giant axon. (Left) The neuronal membrane, and the flow of charged ions. (Right) A plot of membrane potential against time. (A) At rest, charged Na^+ (extracellular) and K^+ (intracellular) ions are distributed across the membrane to cause depolarization of the membrane. (B) During action potential initiation, Na^+ channels in the membrane open and cause an influx of Na^+ ions into the cell, causing depolarisation. (C) When the cell is depolarised, Na^+ channels close and K^+ channels open, causing membrane repolarisation. (D) Following this, all ion channels inactivate and ions cross the membrane aided by sodium-potassium pumps (not shown in figure) to return to the initial equilibrium in A. This period is knows as the *refractory period*.

et al., 2013; Allison et al., 2016) and animal models of tauopathy (Fu et al., 2017). In an experimental tauopathy model, Booth et al. (2016a) reported alterations to ‘clustered’ AP patterns in which multiple APs are fired consecutively between long quiescent periods, which are studied using mathematical techniques in chapter 2.

When a neuron fires an AP, it sends an electrical signal to neighbouring neurons via synapses. The pre-synaptic neuron releases a neurotransmitter which binds to receptors in the post-synaptic neuron. The outcome of this can be inhibitory (causing the post-synaptic neuron to temporarily hyperpolarise and become less excitable) or excitatory (causing the post-synaptic neuron to temporarily depolarise and become more excitable) (Börgers and Kopell, 2005). Whether a signal is excitatory or inhibitory depends primarily on its neurochemical basis; excitatory signals are predominantly mediated by glutamate, whilst inhibitory signals are mediated by GABA. Neurons which predominantly release glutamate are therefore often referred to as excitatory cells, whilst those which predominantly release GABA are often referred to as inhibitory cells. Ensembles of excitatory and inhibitory neurons within a region of the cortex are synaptically connected in a laminar structure, in which layers are organized by neurons with similar morphological and electrophysiological properties (Mountcastle, 1997). This balance of excitation and inhibition may result in synchronous AP firing patterns of locally synaptically connected neurons (Whittington et al., 2000). Synchronous AP activity or post-synaptic potentials (PSPs) can be imaged in slices or *in vivo* using multi-electrode arrays (Buzsáki, 2004) or two-photon calcium imaging (Stosiek et al., 2003) and quantified using statistical measures of synchrony (Dombeck et al., 2009; Goncalves et al., 2013). In trangsenic models of amyloidopathy, spontaneous hyperactivity and increased coactivation between local cortical neurons has been observed (Busche and Konnerth, 2016), however in tauopathy and combined amyloid-tau models neurons have been found to be silenced (Busche et al., 2019). These results suggest different synaptic deficiencies in amyloid and tau models of AD pathology, dominated by tau pathology (Busche et al., 2019). In chapter 3, two-photon calcium imaging data is used to uncover alterations to local neuronal synchrony in a mouse model of frontotemporal dementia.

Synchronous activity in local networks of neurons can give rise to neuronal oscillations at multiple temporal scales (Buzsáki, 2006). The resulting post-synaptic currents (PSCs) onto the dendrites of pyramidal cells aligned vertically along the cortical column (represented by the pale orange neurons in Figure 1.1A) summates, and measurements of the local extracellular potential due to these transmembrane PSCs (Eccles, 1951; Olejniczak, 2006; Einevoll et al., 2013; Mazzoni et al., 2015) display oscillatory activity (Buzsáki, 2006). An example of this oscillatory activity arising from simulated spiking neurons is shown in Figure 1.6, using the model of hippocampal theta (4-12 Hz) and gamma (30-80 Hz) rhythms de-

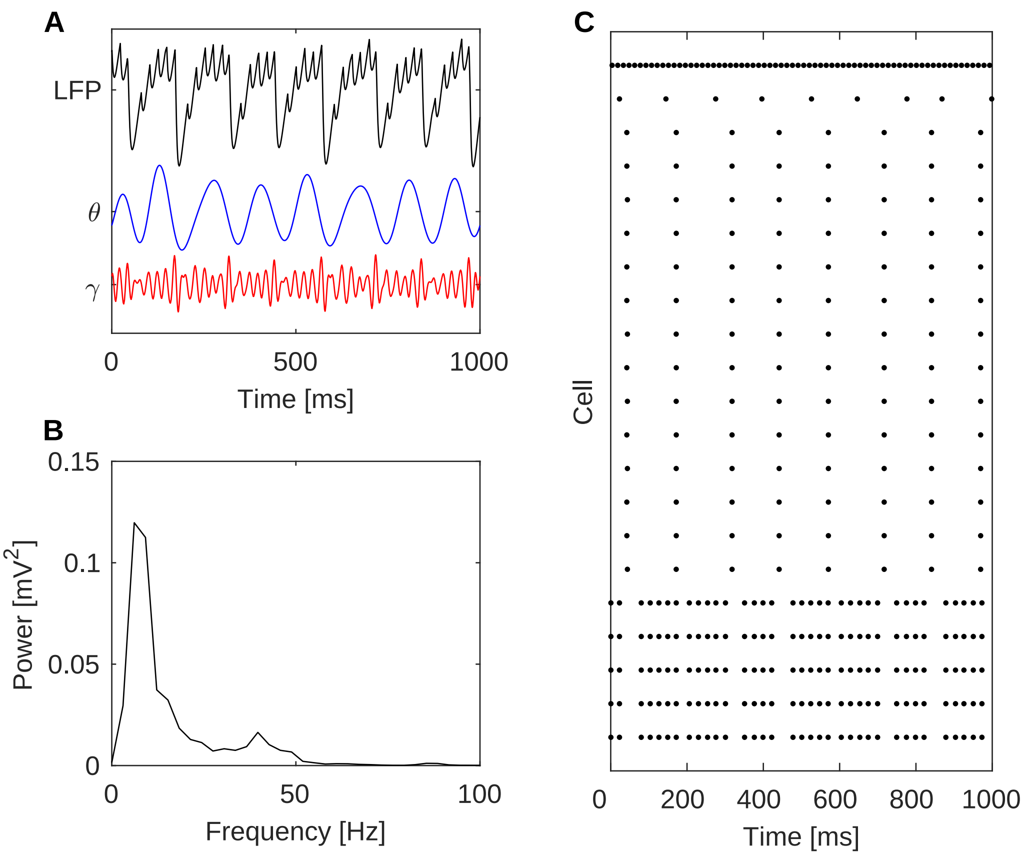

Figure 1.6: **Oscillations arise from networks of spiking neurons.** Simulations of spiking neurons generating theta (4-12 Hz) and gamma (30-80 Hz) rhythms seen in hippocampal LFPs in rodents *in vivo*. A description of the model used to generate this figure and examples of experimental data can be found in Wulff et al. (2009). (A) Simualted hippocampal LFP (black). The same LFP is shown filtered into the theta (blue) and gamma (red) bands. (B) The power spectrum of this LFP shows there are peaks at around 7 Hz and 40 Hz, demonstrating that organized oscillations have arisen from the spiking neurons. (C) Raster plot of the spiking neurons generating this oscillation. Black dots represent the instant a neuron has fired an AP.

scribed in (Wulff et al., 2009) (data showing these rhythms *in vivo* is also demonstrated in the cited paper).

These *local field potentials* (LFPs) may be recorded intracranially, for example in rodents (Booth et al., 2016a) or humans having undergone surgery for clinical purposes (e.g. for presurgical evaluation in epilepsy (Goodfellow et al., 2016)). Due to the invasive nature of these techniques, intracranial LFP studies have been predominantly performed in experimental rodent models of Alzheimer's disease. In the entorhinal-hippocampal circuit, rodent models of tauopathy have exhibited alterations to frequencies and power of organized neuronal oscillations related to memory consolidation during sleep (Witton et al., 2016), and spatial memory and learning (Booth et al., 2016a,b; Ciupek et al., 2015; Nakazono et al., 2018). Similar alterations have been observed in models of amyloidopathy

Modality	Invasive	Signal	Space	Spatial resolution	Temporal resolution
Patch clamp	Yes	Membrane potential of neuron	Source	Single ion channel to whole cell	Sub-millisecond
MEA	Yes	Extracellular PSCs	Sensor	Ensembles of neurons in parallel	Sub-millisecond
Two-photon Ca^{2+} imaging	Yes	Calcium dynamics	Source	Ensembles of neurons in parallel to cortical columns	Milliseconds to seconds
LFP	Yes	Extracellular PSCs	Source	Cortical column	Milliseconds
EEG	No	Electric field on scalp due to extracellular PSCs	Sensor	~10 mm	Milliseconds
MEG	No	Magnetic field due to electric field	Sensor	~5 mm	Milliseconds
PET	No	Metabolic activity	Source	~5 mm	Tens of seconds
fMRI	No	Blood oxygen level	Source	1-5 mm	Seconds

Table 1.1: **Review of electrophysiological imaging techniques.** Spatial and temporal resolutions are approximate, and are based on ranges given in Suter et al. (1999), Lütcke et al. (2013), and Boly et al. (2015). Measures marked as *source* space directly measure from their respective source, whilst measures marked *sensor* require some analysis to establish origins of signals.

(Goutagny et al., 2013; Zhang et al., 2016; Nakazono et al., 2018).

Whilst these invasive LFP recordings in rodents can give insight into potential mechanisms of Alzheimer's disease, for example those underpinning memory impairments and disorientation to space, there are limitations to using rodent models of disease (discussed in section 1.1). In order to study electrophysiological properties in human AD, non-invasive measurements must be used. There are a large number of non-invasive functional neuroimaging technologies available each with their own advantages and limitations. For brevity, a detailed review of these methods is not included here, and we divert the reader to reviews by Crosson et al. (2010) and Boly et al. (2015), as well as a summary of modalities in Table 1.1. Here, we will focus on resting-state electroencephalogram (EEG), which is the focus of chapters 4-6.

EEG is generated by the same transmembrane post-synaptic currents as the LFP (Olejniczak, 2006). Synchronous PSCs in cortical neural masses generate electric fields which conduct onto the scalp. By placing electrodes onto the scalp, neural oscillations can be recorded in a non-invasive manner. EEG has the advantage over other commonly used neuroimaging techniques such as fMRI or PET of recording signals directly generated by electrical neuronal activity, meaning dynamics are fast and allow for high temporal resolution (Boly et al., 2015). However, due to electric field spread, EEG has low spatial resolution (Boly et al., 2015) and additional techniques such as *source localization* must be used to estimate the anatomical origin of the electrical field (Michel et al., 2004). Furthermore

EEG is limited by predominantly recording cortical dynamics (Olejniczak, 2006), and cannot easily record deep structures. Depending on the hypotheses to be tested and analytical techniques to be used, as few as eight (Khanna et al., 2014) or as many as 256 (Hassan et al., 2014) electrodes may be placed on the scalp. EEG also has the advantage over fMRI, PET, or MEG of being relatively inexpensive (Crosson et al., 2010). Inexpense, combined with EEG's current implementation in healthcare systems for diagnosis of epilepsy (Smith, 2005), makes it a prime candidate for both research and clinical environments, such as aiding early diagnosis of AD (Poil et al., 2013).

In the EEG of people with AD, slowing of neuronal oscillations beyond the level typically seen in aging has consistently been reported for over thirty years (Duffy et al., 1984; Strik et al., 1997; Adler et al., 2003; Lindau et al., 2003; Dauwels et al., 2011; Hatz et al., 2015a; Liu et al., 2016; Wang et al., 2015; Engels et al., 2016; Ianof et al., 2017; Goossens et al., 2017). A number of computational studies have explored mechanisms of how oscillations in neural ensembles may change frequency. Alterations to membrane and synaptic time constants of neurons within the population can alter the frequency of emergent oscillations (David and Friston, 2003; Moran et al., 2007). Whilst slowing can additionally be a result of increasing both excitation and inhibition proportionally (Jansen and Rit, 1995), severe loss of synapses has been reported even at early stages of AD (Selkoe, 2002) so increased connectivity is unlikely except perhaps as a compensatory mechanism (Abuhassan et al., 2014). Disruption to the balance of excitation and inhibition has been described as a potential mechanism for slowing of neuronal oscillations, including degeneration in either inhibitory (Moran et al., 2007; Zavaglia et al., 2010) or excitatory synapses (Moran et al., 2007; de Haan et al., 2012a; Abuhassan et al., 2014). Alternatively, global or long range mechanisms are also possible. David and Friston (2003) suggested that increased propogation delays between cortical regions can slow the neuronal oscillations of both regions. Whilst David and Friston (2003) presented this in the context of increased tract lengths, demyelination of white matter in AD (Nasrabady et al., 2018) could also result in increased propogation delays. Degeneration of corticothalamic or thalamocortical synapses result in slowing of thalamic oscillations, but are not sufficient to explain slowing of cortical oscillations recorded by EEG, which instead require local corticocortical synaptic impairment (Abuhassan et al., 2014).

In addition to slowing of cortical oscillations, alterations to synchronization of neural oscillations across the brain have been reported in AD, reviewed by Babiloni et al. (2016). However, reports of altered synchronization vary; whilst many studies report reduced synchrony in people with AD (Adler et al., 2003; Pijnenburg et al., 2008; Wang et al., 2014, 2015; Hata et al., 2016), others have reported increases in synchrony (Koenig et al., 2005a; Cantero et al., 2009; Gallego-Jutgla et al., 2015). Potential reasons for these inconsistencies are discussed in more detail in chapter 4 (section 4.4.2). More consistent have been reports of less efficient topologies of whole brain synchronization networks in AD (Stam et al., 2007a; de Hann et al., 2009; Wang et al., 2014; Berlot et al., 2016; Afshari and Jalili, 2017; Vecchio et al., 2017; Sami et al., 2018). Evidence for impaired connectivity between regions of the brain in AD can also be extended to other functional neuroimaging modalities such as MEG (Stam et al., 2009), fMRI (Badhwar et al., 2017), and PET (Cope et al., 2018), structural imaging of white matter tracts (Rose et al., 2000; Mito et al., 2018), and neuropsychological studies (Delbeuck et al., 2003). A leading hypothesis for how cognitive impairment arises in AD is that alterations to the macro-scale functional connectome compromises the ability of distributed processing systems to integrate or exchange information (Delbeuck et al., 2003; Uhlhaas and Singer, 2006). This *disconnection hypothesis* is discussed in further detail in chapter 4.

1.4 Dynamical systems and qualitative modelling of the neuron

In the previous section, we introduced the concept of neuronal excitability and the action potential. In this section, we will describe how an area of mathematics called *dynamical systems theory* can be used to build a computational model of a neuron which qualitatively exhibits these properties (whilst more biophysically and quantitatively realistic models of the neuron are discussed in section 1.5). This chapter aims to give a brief introduction to key methods and tools from dynamical systems theory in the context of neuroscience (Izhikevich, 2007; Gerstner et al., 2014), with a focus predominantly on microscale neuronal dynamics. More detailed overviews of dynamical systems theory are given in textbooks such as Glendinning (1994), Kuznetsov (1998), Robinson (1998), and Hirsch et al. (2003). Furthermore, more in depth reviews of applications of dynamical systems theory to neuroscience are given by Izhikevich (2007) and Gerstner et al. (2014), whilst broader applications of dynamical systems theory in science and engineering are given by Strogatz (2014).

Dynamical systems theory is the study of the mathematical description of a temporally evolving system (a *dynamical system*). This can be anything from an object under the influence of gravity as described by Isaac Newton in 1687, to the dynamics of the membrane potential of a neuron or oscillations in the local field potential. There are two key mathematical formulations for a dynamical system; *continuous* dynamical systems are formulated by a system of differential equations, whilst *discrete* dynamical systems are formulated by iterative maps or difference equations (Strogatz, 2014). The primary tool used in this thesis is the former, although a specific application of maps as a tool for studying continuous dynamical systems will be briefly introduced in section 1.4.4

A continuous dynamical system of dimension m can be described by the first order differential equations

$$\dot{\mathbf{x}} \equiv \frac{d\mathbf{x}}{dt} = \mathbf{f}(\mathbf{x}), \tag{1.1}$$

where $\mathbf{x} \in \mathbb{R}^m$ and $\mathbf{f} : \mathbb{R}^m \to \mathbb{R}^m$. The *flow* of the system is defined as follows:

Definition 1. *The **flow** $\varphi(t, \mathbf{x})$ of a system of differential equations of the form Equation 1.1 is the set of solutions of these equations such that $\varphi(t, \mathbf{x}_0)$ is the solution at time t with initial condition (at $t = 0$) $\mathbf{x}_0 = \mathbf{x}(0)$ - Glendinning (1994).*

In lay terms, we define the flow as the solution to the dynamical system for a given initial condition. Typically when modelling electrophysiological dynamics of a neuron, the membrane potential V is a variable in the system of equations, so a one-dimensional neuronal model might be of the form $\dot{V} = f(V)$. However, this is not guaranteed; for example, phase models of the neuron do not explicitly model V (Ermentrout and Kopell, 1986). For this reason, throughout this section we will keep the discussion to general systems of equations as described in Equation 1.1 unless discussing a specific neuronal model.

1.4.1 Modelling the neuron during quiescence

To build a model neuron, we can consider a current clamp experiment such as the one shown in Figure 1.7[3]. In this section, we will study the neuron during quiescence, so let us consider only the values of input current I that are not sufficiently depolarizing to initiate action potentials (i.e. the current is below *rheobase*, I_ρ). For a particular current I, the membrane potential of the neuron V evolves towards a fixed value and then does not move away from this value. From a dynamical systems perspective, this fixed value would be described as an *invariant set*, formally defined as

Definition 2. *A set M is **invariant** if for all $\mathbf{x}_0 \in M$, $\varphi(t, \mathbf{x}_0) \in M$ for all t - Glendinning (1994).*

That is, a flow initially in an invariant set M remains in M for all time (Strogatz, 2014). In the case of the neuron at rest, the membrane potential reaches a fixed value and then does not chage, meaning this invariant set consists of a single

---

[3] The data presented in Figure 1.7 was collected by the author of this thesis from a neuron in layer 2/3 of the mouse entorhinal cortex.

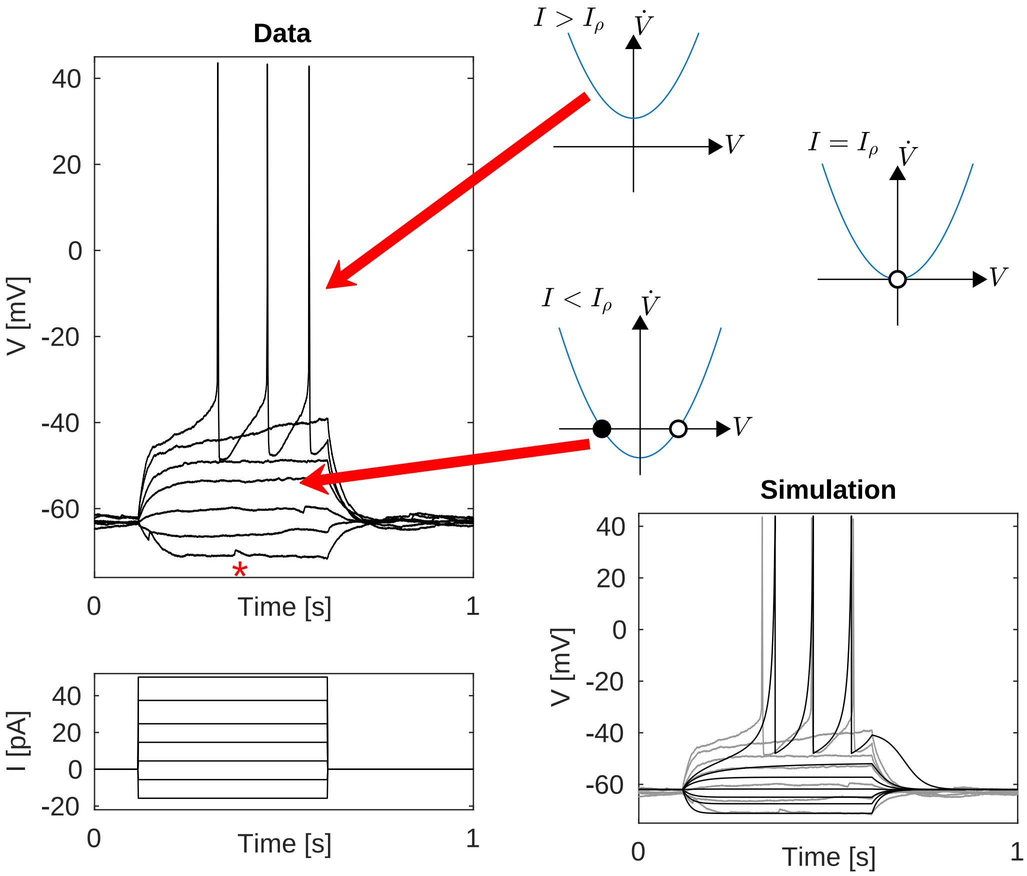

Figure 1.7: **Bifurcations in neural dynamics - from resting to spiking**. This figure shows an example of a current clamp experiment in a neuron. A step current (bottom left) is applied across the membrane of the neuron, and the membrane potential V of the neuron is recorded (top left). For currents I below some critical value I_ρ, called rheobase, V reaches a steady state. Above this critical value, the neuron fires action potentials. Therefore a key feature of mathematical models of neurons is that they may be described by $\dot{V} = f(V; I)$ and undergo a bifurcation at $I = I_\rho$. A simple example of this is the quadratic integrate-and-fire (QIF) neuron (see section 1.4.2 for a description of the QIF neuron and the integrate-and-fire reset condition), in which $f(V; I)$ is a quadratic function. The plots at the top right show that in such a system, there exists a stable and an unstable steady state for $I < I_\rho$, which collide to form a non-hyperbolic equilibrium at $I = I_\rho$, and are abolished for $I > I_\rho$. Therefore this model of a neuron transitions to spiking via a saddle node bifurcation (described further in section 1.4.1). By resetting V to some value V_{reset} when it reaches a value V_{peak}, regular spiking can be achieved for $I > I_\rho$. An example simulation of the data using a quadratic integrate-and-fire neuron is shown in the bottom right figure in black, overlaid on the data (grey) for comparison purposes.

point $\mathbf{x}^* \in \mathbb{R}^m$. This particular type of invariant set is known as a *steady state*, fixed point, or equilibrium of the system, which satisfies

$$\mathbf{f}(\mathbf{x}^*) = \mathbf{0}. \tag{1.2}$$

Therefore a neuron model $\dot{\mathbf{x}} = \mathbf{f}(\mathbf{x}; I)$ with parameter $I < I_\rho$ might be chosen such that there exists some $\mathbf{x}^*$ that satisfies $\mathbf{f}(\mathbf{x}^*; I) = \mathbf{0}$ to qualitatively describe the non-spiking dynamics of the membrane potential.

However, this condition alone is not sufficient to ensure that the behaviour of the steady state matches the behaviour of the quiescent neuron. Neurons regularly receive small perturbations away from the steady state due to stochastic ion channel gating and post-synaptic potentials (White et al., 2000). An example of the latter is marked by a red star in Figure 1.7. Note that following the perturbation, the membrane potential stays in the neighbourhood of the steady state and eventually returns to it. From a dynamical systems perspective, this means the steady state is *stable*. Whilst there exist various definitions of stability (Glendinning, 1994), the most useful definition in the context of this thesis is

Definition 3. *An invariant set M is* ***stable*** *if it satisfies both of the following conditions:*

i. Lyapunov stability: Flows in the neighbourhood of M remain in the neighbourhood of M,

ii. Asymptotic stability: There exists some neighbourhood $U \supset M$ where all flows initially in U tend to M as $t \to \infty$.

- Kuznetsov (1998); Strogatz (2014).

Stability of a steady state can be established by the following theorem:

Theorem 1. *Let $\mathbf{x}^*$ be a steady state of a dynamical system of the form Equation 1.1. Let $A \equiv J(\mathbf{f})|_{\mathbf{x}^*}$ be the Jacobian matrix of $\mathbf{f}(\mathbf{x})$ evaluated at $\mathbf{x}^*$. Then $\mathbf{x}^*$ is stable if all eigenvalues $\lambda_j \in \mathbb{C}$, $j = 1, 2, \ldots, m$ of A satisfy $\Re(\lambda_j) < 0$. - Kuznetsov (1998)*

This outcome is a result of the Hartman-Grobman theorem, which states that

Theorem 2. ***Hartman-Grobman Theorem****. Let $\mathbf{x}^*$ be a* hyperbolic *(all eigenvalues of $J(\mathbf{f})|_{\mathbf{x}^*}$ have non-zero real part) steady state of a non-linear dynamical system of the form Equation 1.1. Then the non-linear system is locally topologically equivalent near $\mathbf{x}^*$ (see Definition 4) to the linearized system $\dot{\xi} = J(\mathbf{f})|_{\mathbf{x}^*}\xi$. - Kuznetsov (1998)*

A more rigorous statement and proof of this theorem can be found in Robinson (1998). Topological equivalence is defined as

Definition 4. *A dynamical system is **topologically equivalent** to another dynamical system if there exists a homeomorphism $h : \mathbb{R}^m \to \mathbb{R}^m$ that maps orbits of the first system onto the second system. - (Kuznetsov, 1998)*

Local topological equivalence near a steady state restricts this to a small neighbourhood of the steady state.

Perturbations to a linear system of differential equations $\dot{\xi} = A\xi$ grow or decay proportional to $\exp \lambda_j t$ in the direction of the jth eigenvector of A (Strogatz, 2014), where λ_j is the jth eigenvalue of A, meaning that the linearization of a dynamical system about a steady state satisfies Definition 3 if $\Re(\lambda_j) < 0 \ \forall j$. Therefore the steady steady state of the original non-linear system is also stable, by the Hartman-Grobman theorem.

We have now described properties of a simple dynamical system describing a neuron in the non-firing regime when a small current $I < I_\rho$ is applied. When the input to the neuron is sufficiently depolarising ($I > I_\rho$; Figure 1.7), the neuron enters a spiking regime in which action potentials are fired and the membrane potential no longer tends to a fixed value. In dynamical systems theory terms, this means that at $I = I_\rho$ the steady state is either abolished or loses stability. This sudden qualitative change in dynamics of the system as a parameter is varied is known as a *bifurcation* (Strogatz, 2014), more formally defined as

Definition 5. *A **bifurcation** is the appearance of a topologically nonequivalent phase portrait under variation of parameters. - Kuznetsov (1998)*

When describing bifurcations, it is often useful to discuss the normal form of the bifurcation,

Definition 6. *The **normal form** of a bifurcation is locally topologically equivalent to any generic system which undergoes the same bifurcation in the neighbourhood of the bifurcation parameter - Kuznetsov (1998); Izhikevich (2007); Strogatz (2014).*

Figure 1.7 shows an example of a bifurcation in a one-dimensional system which satisfies the case in which the steady state is abolished as I is increased above I_ρ, replicating the loss of stable steady state in the membrane potential of the neuron. This bifurcation, called the **saddle-node (SN) bifurcation**, has the normal form

$$\dot{x} = x^2 + \mu \tag{1.3}$$

(Strogatz, 2014). For $\mu < 0$, there is a stable steady state at $x^*_- = -\sqrt{-\mu}$ and an unstable steady state at $x^*_+ = +\sqrt{-\mu}$. As $\mu \to 0$ from the negative side, these steady states move together and at $\mu = 0$ collide to form a single non-hyperbolic steady state. For $\mu > 0$, there are no real solutions so no steady states.

The saddle node bifurcation *qualitatively* captures the loss of quiescence in the neuronal membrane potential. To obtain a more *quantitatively* accurate representation of the membrane potential, a transformation of variables can be made such that the steady states match the values of the membrane potential and the bifurcation occurs at $\mu = I_\rho$, whilst remaining topologically equivalent to Equation 1.3 (Izhikevich, 2007; Gerstner et al., 2014).

1.4.2 Action potentials in one-dimensional models: Class 1 excitability and the SNIC bifurcation

The previous section described how a saddle node bifurcation can be used to mathematically model the resting state of the neuron and its sudden disappearance as the current injected into the neuron reaches and exceeds a critical value I_ρ. However, this bifurcation is unable to capture the spiking dynamics of the neuron when $I > I_\rho$, as for $\mu > 0$ in Equation 1.3 $x \to \infty$ as $t \to \infty$. In the neuron, which we will assume here fires tonic APs for $I > I_\rho$, the membrane potential repeats itself periodically in the spiking regime. From a dynamical systems perspective, this is a *periodic orbit*, defined as

Definition 7. *The trajectory* $\Gamma = \{\varphi(t, \mathbf{x}) | 0 \leq t < T\}$ *is called a* ***periodic orbit*** *of period* T *if* $\varphi(t + T, \mathbf{x}) = \varphi(t, \mathbf{x})$ *and* $\varphi(t + S, \mathbf{x}) \neq \varphi(t, \mathbf{x})$ *for* $0 < S < T$. *- Glendinning (1994); Hirsch et al. (2003)*

Periodic orbits cannot exist in one-dimensional systems defined on the line (Strogatz, 2014). However, one dimensional systems defined on a periodic phase space, known as an *invariant circle*, are able to exhibit periodic orbits. Examples of invariant circles can be formed by considering the variable x to be the phase of an oscillator, or by restricting the phase space to the interval $[x_r, x_p)$ and then forming a loop from this interval with a requirement if $x \geq x_p$, then $x \leftarrow x_r$. The latter is an integrate-and-fire reset condition (Izhikevich, 2007).

Consider a one-dimensional model of the neuronal membrane potential based on the normal form of the saddle node bifurcation (Equation 1.3), with an integrate-and-fire type reset condition. This model is known as the quadratic integrate-and-fire (QIF) model (Izhikevich, 2007; Gerstner et al., 2014). At $\mu = 0$ the system undergoes a **saddle node on an invariant circle (SNIC)** bifurcation. As with the SN bifurcation, as $\mu \to 0$ from the negative, a stable and unstable steady state collide and disappear. However, in the case of the SNIC bifurcation, the system has a periodic orbit on an invariant circle for $\mu > 0$. The QIF neuron can be made a quantitatively more realistic representation of the membrane potential through a transformation of variables (Izhikevich, 2007; Gerstner et al., 2014), and a simulation of a current clamp experiment using the QIF model is shown in Figure 1.7.

Alternatively, Equation 1.3 can be written as the normal form of the SNIC bifurcation through the transformation of variables $x = \tan(\theta/2)$, which is known as the Ermentrout-Kopell or theta model (Ermentrout and Kopell, 1986; Izhikevich, 2007; Gerstner et al., 2014). The theta model is particularly useful due to its low computational expense since, unlike the QIF model, no manual reset is required.

The SNIC bifurcation has a key role in neuroscience as the method by which class 1 excitable neurons, which can fire APs at an arbitrarily low frequency depending on the strength of the applied current, transition into the spiking regime (Hodgkin, 1948; Izhikevich, 2007). Conversely class 2 excitability, which corresponds to a minimum AP frequency that is relatively insensitive to changes in the strength of applied current (Hodgkin, 1948; Izhikevich, 2007), cannot be modelled by a SNIC bifurcation. Planar neuronal models exhibit a much broader range of dynamics including class 2 excitability (Izhikevich, 2007) so these are the focus of the following section.

1.4.3 Planar systems: complex eigenvalues allow for subthreshold oscillations and class 2 excitability

The one-dimensional QIF/theta neuron models are limited in their range of dynamics; for a given current injection I they either fire APs tonically or are at rest. Extensions to planar (two-dimensional) models are able to greatly broaden the range of neuronal dynamics (Izhikevich, 2007). Particularly, the addition of a second variable allows *complex* eigenvalues of the Jacobian matrix, which are related to phenomena not possible in one-dimensional phase space such as subthreshold oscillations/resonance and class 2 excitability (Izhikevich, 2001, 2007).

Let us begin by defining a *focus* as a steady state which has a pair of complex conjugate Jacobian eigenvalues,

Definition 8. *Let $\mathbf{x}^*$ be a steady state of an $m > 1$ dimensional dynamical system in the form Equation 1.1, and let $A \equiv J(\mathbf{f})|_{\mathbf{x}^*}$ be the Jacobian matrix of $\mathbf{f}(\mathbf{x})$ evaluated at $\mathbf{x}^*$. Then $\mathbf{x}^*$ is a **focus steady state** if there exists a pair of complex conjugate eigenvalues $\lambda_\pm \in \mathbb{C}$ of A.*

We can characterize the effect of the complex conjugate eigenvalues following Glendinning (1994). In a planar system, the Jacobian matrix evaluated at a focus can be written as

$$A \equiv J(\mathbf{f})|_{\mathbf{x}^*} = \begin{bmatrix} a & -\omega \\ \omega & a \end{bmatrix}, \tag{1.4}$$

where $a = \Re(\lambda_\pm)$ and $\omega = \Im(\lambda_\pm)$. The linearization of the system $\dot{\xi} = A\xi$ can therefore be rewritten in polar coordinates as the uncoupled system

$$\begin{aligned} \dot{r} &= ar \\ \dot{\theta} &= \omega. \end{aligned} \tag{1.5}$$

Hence trajectories are a logarithmic spiral with frequency ω into ($a < 0$; stable focus) or away from ($a > 0$; stable focus) the origin (Glendinning, 1994). It is clear that since $a = \Re(\lambda_{\pm})$ characterizes the stability of the focus, Theorem 1 holds for complex eigenvalues. By the Hartman-Grobman theorem, these results hold for a non-linear system in the neighbourhood of the focus. Furthermore these results can be generalized to two-dimensional manifolds of higher order systems (Glendinning, 1994). Stable focuses can be used to model subthreshold resonance and stochastically driven subthreshold oscillations (Izhikevich, 2001, 2007), which have been observed in biological neurons (Alonso and Klink, 1993; White et al., 1998; Izhikevich, 2001; Dorval and White, 2005). Including resonance in planar neuron models can be crucial for explaining organization of network dynamics related to cognitive processes (Hasslemo and Shay, 2014).

Planar models with complex eigenvalues can also give rise to class 2 excitability via a Andronov-Hopf or **Hopf bifurcation** (Izhikevich, 2007). The normal form of the Hopf bifurcation is

$$\begin{aligned} \dot{x}_1 &= (a + \beta(x_1^2 + x_2^2))x_1 - \omega x_2 \\ \dot{x}_2 &= (a + \beta(x_1^2 + x_2^2))x_2 + \omega x_1, \end{aligned} \tag{1.6}$$

where $\beta = \pm 1$ defines whether the Hopf bifurcation is *supercritical* ($\beta = -1$) or *subcritical* ($\beta = +1$) (Kuznetsov, 1998). For the entire (a,ω,β) parameter space, there is a single steady state at the origin. The Jacobian of the system is equivalent to Equation 1.4, meaning that for $a < 0$ ($a > 0$ resp.) the steady state is a stable (unstable resp.) focus. Written in polar coordinates, Equation 1.6 is

$$\begin{aligned} \dot{r} &= r(a + \beta r^2) \\ \dot{\theta} &= \omega. \end{aligned} \tag{1.7}$$

From these equations, it becomes clear that in the case of the supercritical Hopf bifurcation ($\beta = -1$), there is a stable limit cycle with radius $\sqrt{a}$ for $a > 0$ corresponding to a stable steady state in the equation for r. Conversely in the case of the subcritical Hopf bifurcation ($\beta = +1$) there is an unstable limit cycle with radius $\sqrt{-a}$ for $a < 0$. Bifurcation diagrams for the Hopf bifurcations are shown in Figure 1.8.

In both cases, close to the bifurcation the limit cycle has frequency ω. Therefore neuron models that transition from quiescence to spiking via a supercritical

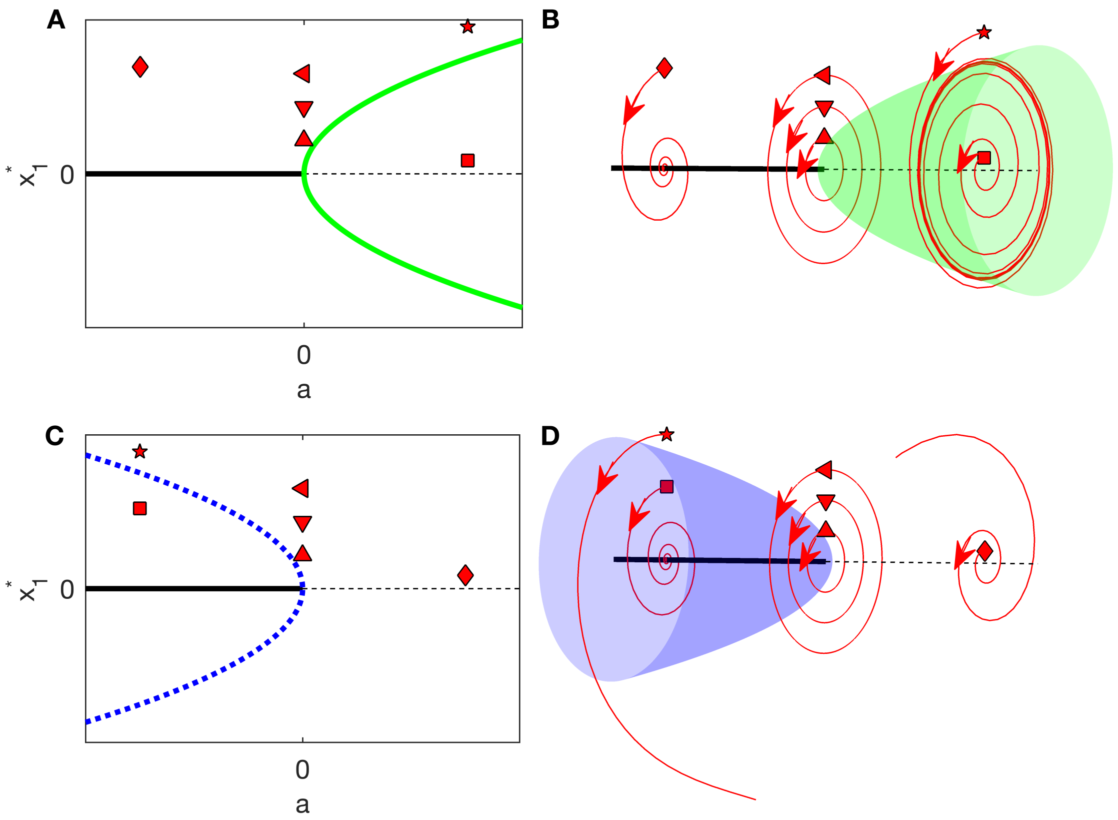

Figure 1.8: **Hopf bifurcations**. In all plots, solid/dashed black lines are stable/unstable steady states, green/blue lines or surfaces are stable/unstable limit cycles, and red lines are trajectories of the system starting with a given initial condition. (A) The bifurcation diagram for a supercritical Hopf bifurcation in the (a, x_1) plane. Shapes correspond to initial conditions of trajectories shown in B. (B) The bifurcation diagram for a supercritical Hopf bifurcation in the (a, x_1, x_2) space and example trajectories of the system. (C-D) As for A-B, but for the subcritical Hopf bifurcation.

Hopf bifurcation exhibit class 2 excitability (Izhikevich, 2007). A well known example of a planar neuron model exhibiting class 2 excitability by this mechanism is the FitzHugh-Nagumo model (FitzHugh, 1961; Nagumo et al., 1962; Gerstner et al., 2014). Furthermore, the supercritical Hopf bifurcation has been suggested as a mechanism by which sustained subthreshold oscillations in a neuron are generated (White et al., 1995). Additionally, whilst the focus of this section is in single-cell dynamics, the supercritical Hopf bifurcation plays a crucial role in generating macro-scale neuronal oscillations and is the basis of the macro-scale models presented in this thesis; this macro-scale modelling is discussed further in section 1.6.

1.4.4 Calculating periodic orbits with Poincaré return maps

A crucial feature of the supercritical/subcritical Hopf bifurcation discussed in the previous section is the generation of a stable/unstable periodic orbit. Whilst the existence and stability of a periodic orbit in the normal form of the Hopf bifurcation could be conveniently calculated through the use of polar coordinates, in general this is not tractable, particularly for high dimensional dynamical systems such as the biophysically realistic neuron model presented in chapter 2. Therefore in this thesis, numerical solutions are used to find periodic orbits using the concept of a *Poincaré return map*.

The Poincaré return map converts a continuous dynamical system to a discrete dynamical system. Let us define the Poincaré section as follows:

Definition 9. *Let Γ be a periodic orbit of an m-dimensional dynamical system of the form Equation 1.1. A* ***Poincaré section*** *S is an $m-1$ dimensional smooth hypersurface which intersects Γ at a point $\bar{\mathbf{x}} \in \Gamma$ transverse to the flow, i.e. no trajectories starting at S flow parallel to S. - Kuznetsov (1998); Strogatz (2014).*

The simplest choice of S is often a hyperplane orthogonal to Γ at $\mathbf{x}_0$ (Kuznetsov, 1998). For modelling a spiking neuron, the choice of Poincaré section might be defined around a particular value of V through which the neuron passes during the course of the action potential (Channell et al., 2007).

A Poincaré return map can then be defined:

Definition 10. *Let S be a Poincaré section as described in Definition 9. A trajectory starting at $\mathbf{x} \in S$ sufficiently close to $\bar{\mathbf{x}}$ at time t will return to point $\mathbf{y} \in S$ at time $t+\tau$. The map $P : S \to S$, $\mathbf{x} \mapsto \mathbf{y} = P(\mathbf{x}) := \varphi(t+\tau, \mathbf{x})$, is called the* ***Poincaré return map****. - Kuznetsov (1998); Strogatz (2014)*

It is clear from this definition that a periodic orbit Γ of the flow is equivalent to a fixed point $\bar{\mathbf{x}}$ of the map, which satisfies

$$P(\bar{\mathbf{x}}) = \bar{\mathbf{x}}. \tag{1.8}$$

An example of a Poincaré section and Poincaré return map is shown in Figure 1.9.

It is often useful to use index notation to denote iterations of a map, such that $\mathbf{x}[k+1] = P(\mathbf{x}[k])$ and $\mathbf{x}[k+N] = P^N(\mathbf{x}[k])$. Fixed points of the map can be computed numerically by calculating consecutive iterations of the map and testing for convergence (Burden and Faires, 2010), or through use of a numerical boundary value problem solver (Shampine and Kierzenka, 2001). An example iterative scheme is shown in Figure 1.9B.

Since a periodic orbit of the flow (or fixed point on the map) is an invariant set, the definition of stability is given in Definition 3. Much like with steady states of the

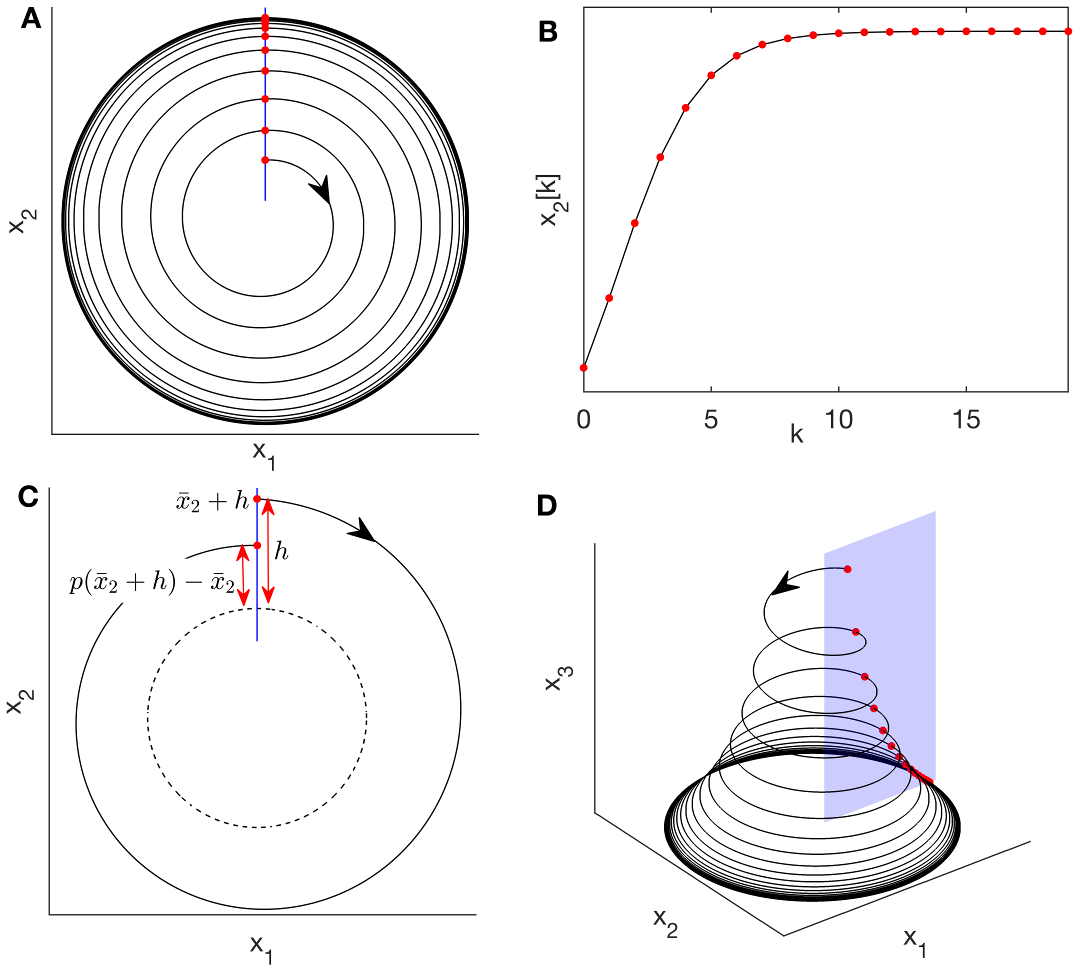

Figure 1.9: **Poincaré return maps and linearization**. (A) An example flow for the system of equations Equation 1.6 with $(a, \beta) = (1, -1)$ is shown in black. An example Poincaré section for this system is shown in blue. Red dots represent returns to the Poincaré section, i.e. iterations of the Poincaré return map. (B) The value of x_2 at each iteration of the map. Note that as the 2-dimensional flow in A converges to the stable limit cycle, the 1-dimensional map converges to a steady state. (C) Linearization of the steady state of the map can be performed by perturbing the system and calculating the return map. The dotted black line is the stable limit cycle of the system and the solid black line is the flow of a system perturbed from the steady state $\bar{x}_2$ on the Poincaré section by h. Note h should be small, and is greatly scaled up in the figure for illustrative purposes. The linear derivative about the steady state is $(p(\bar{x}_2 + h) - \bar{x}_2)/h$. If this derivative has magnitude greater than 1 then the system is unstable, and less than 1 the system is stable. This can be generalized to higher dimensional systems by perturbing in each dimension and building a Jacobian matrix. All eigenvalues of the Jacobian must have a magnitude less than 1 for stability. (D) Visualisation of an example 3D flow, with corresponding 2D Poincaré section.

flow, stability of a fixed point on the map can be assessed through linearization of the map about the fixed point. First, let us define the *multipliers* of a system.

Definition 11. *Let $\bar{\mathbf{x}}$ be a fixed point of a discrete dynamical system $\mathbf{x} \mapsto p(\mathbf{x})$, where $\mathbf{x} \in \mathbb{R}^m$ and p is a smooth map. Let $A \equiv J(p)|_{\bar{\mathbf{x}}}$ be the Jacobian of p evaluated at $\bar{\mathbf{x}}$. The* ***multipliers*** *of the system at $\bar{\mathbf{x}}$ are the eigenvalues $\mu_j \in \mathbb{C}$, $j = 1, 2, \dots, m$ of A.*

The stability of the fixed point can be characterized by the following theorem.

Theorem 3. *A fixed point $\bar{\mathbf{x}}$ of a discrete dynamical system is stable if all multipliers μ of the system at $\bar{\mathbf{x}}$ satisfy $|\mu| < 1$ - Kuznetsov (1998)*

Since a Poincaré return map is often not explicitly defined, numerical methods must be used to compute the $J(P)|_{\bar{\mathbf{x}}}$. In this thesis, $A \equiv J(P)|_{\bar{\mathbf{x}}}$ was calculating using the Fréchet derivates of the map about $\bar{\mathbf{x}}$ (Levedev and Vorovich, 2002) as follows:

$$A_{i,j} = \frac{P(\bar{\mathbf{x}} + h\mathbf{e}_j)_i - \bar{\mathbf{x}}_i}{h}, \tag{1.9}$$

In short, a small perturbation with magnitude h was applied to the fixed point in the direction of the unit vector $\mathbf{e}_j$ and the map calculated. The distance of the return point in the ith direction from the fixed point, normalized by h, is the (i, j)th entry to the Jacobian (Levedev and Vorovich, 2002). Figure 1.9C shows an example calculation of Fréchet derivatives for a two-dimensional flow/one-dimensional Poincaré return map.

The methods described here can be applied to identify and characterize stability of periodic orbits of a continuous dynamical system such as spiking regimes in neuron models. Bursting can also be characterized, since periodic bursts of n APs are equivalent to a fixed point on the map $Q(\mathbf{x}) = P^n(\mathbf{x})$, which will be discussed in more detail in section 1.4.5. Furthermore, whilst chaotic dynamics are not described in detail here for brevity (see e.g. Robinson (1998), Hirsch et al. (2003), Sprott (2003), or Strogatz (2014) for a review of chaos), chaotic spiking can also be characterized from the Poincaré return map by calculating the maximum Lyapunov exponent on the map (Sprott, 2003). Use of such methods plays a crucial role in understanding neuronal dynamics and their alteration in an animal model of AD in chapter 2.

1.4.5 Bistability and fast-slow bursting

In nature, many neurons exhibit values of input current for which *both* spiking and resting coexist. In these parameter regimes, from a dynamical systems perspective the neuron is *bistable*.

Definition 12. *A dynamical system is called **monostable** if it has a single stable invariant set. A dynamical system is **bistable** (or **multistable**) if two (or more) stable invariant sets coexist. - (Izhikevich, 2007)*

Bistability can play a crucial role in neuronal bursting, where a number of APs are fired in rapid succession followed by a quiescent period. In general, a bursting neuron can be considered an example of a *fast-slow* dynamical system, where the AP dynamics occur on a fast time scale and the transition between spiking and quiescent periods occurs on a slow time scale (Izhikevich, 2007). A fast-slow system can be defined as follows:

Definition 13. *A dynamical system of the form Equation 1.1 is a **fast-slow system** if it can be rewritten as*

$$\begin{aligned}\dot{\mathbf{y}} &= \mathbf{g}(\mathbf{y}, \mathbf{u}) \\ \dot{\mathbf{u}} &= \mu \mathbf{h}(\mathbf{y}, \mathbf{u}),\end{aligned} \tag{1.10}$$

where

i. $\mu \ll 1$

*ii. The **fast subsystem** is described by* $\mathbf{y} \in \mathbb{R}^{m_f}$ *and* $\mathbf{g} : \mathbb{R}^{m_f} \to \mathbb{R}^{m_f}$

iii. The slow dynamics are described by $\mathbf{u} \in \mathbb{R}^{m_s}$ *and* $\mathbf{h} : \mathbb{R}^{m_s} \to \mathbb{R}^{m_s}$ *such that* $m_f + m_s = m$

- (Izhikevich, 2007).

For brevity here we shall discuss only the case of a single slow variable ($m_s = 1$) which constitute the majority of fast-slow bursters (Izhikevich, 2000). To make this explicit, we will henceforth write the slow equation in the scalar form $\dot{u} = \mu h(\mathbf{x}, u)$. For $m_s = 1$, all bursters are bistable (Izhikevich, 2000) (described in more detail below). However, it is worth noting that for $m_s > 1$, monostable bursters can exist (Izhikevich, 2000).

Typically the fast subsystem of a bursting neuron will have a dynamic structure such that for $u < u_{c,1}$ there is a stable steady state or low amplitude periodic orbit (sustained subthreshold oscillations), for $u > u_{c,2}$ there is only the stable high amplitude periodic orbit (spiking), and for $u_{c,1} < u < u_{c,2}$ there is bistability (Figure 1.10A). The slow evolution of u drives the fast subsystem through a hysteresis loop, periodically switching between the steady state/low amplitude periodic orbit and high amplitude periodic orbit branches as each branch loses stability (Izhikevich (2000); Figure 1.10A). Izhikevich (2000) (Table 3) defined a classification of such bursters based on the bifurcations which occur at $u = u_{c,1}$ and $u = u_{c,2}$. For brevity, we will focus here on the case where the subthreshold dynamics are described by a steady state.

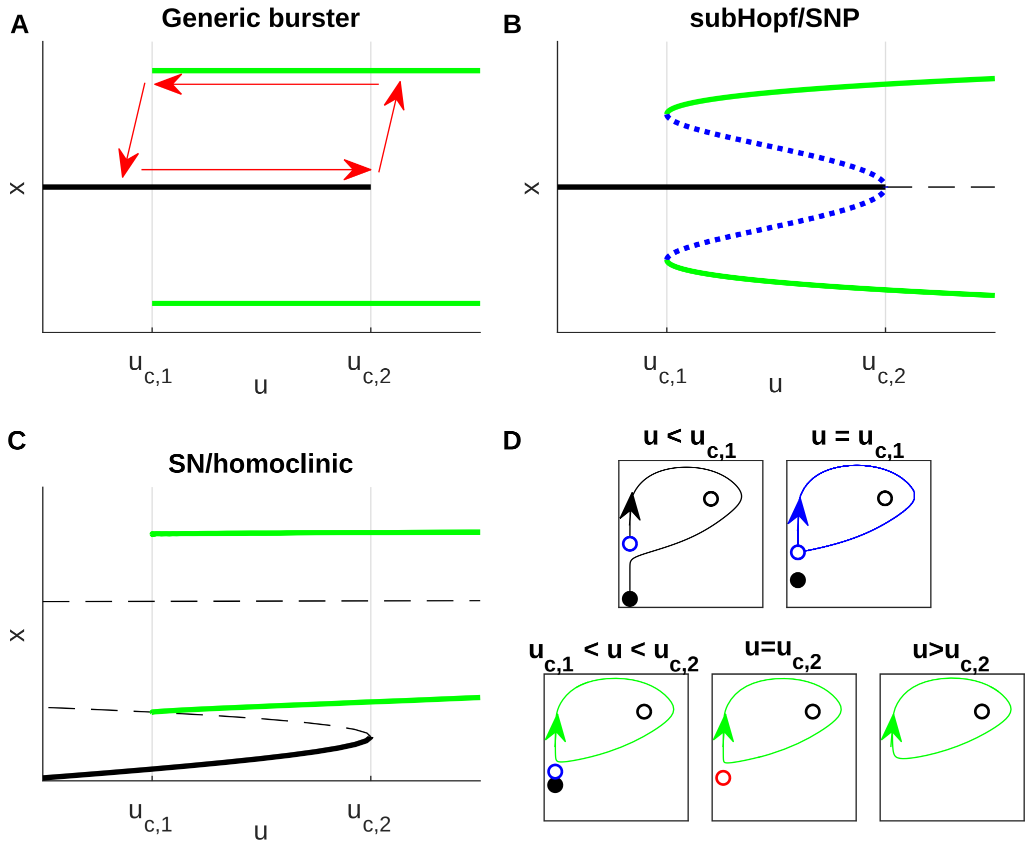

Figure 1.10: **Bistability in fast-slow bursters and the homoclinic bifurcation**. In figures A-C, solid/dashed black lines are stable/unstable steady states. Solid green/dotted blue lines are the maxima and minima of a periodic orbit. (A) A generic bifurcation diagram for a bistable fast-slow burster with one slow variable. Typically there is a stable steady state for the slow variable $u < u_{c,1}$, a stable periodic orbit for $u > u_{c,2}$, and bistability for $u_{c,1} < u < u_{c,2}$. As the variable u evolves slowly, the system moves through a hysteresis loop (shown in red). (B-C) Bifurcation diagrams for the supHopf/SNP and SN/homoclinic bursters found commonly in neuronal dynamics. (D) Phase portraits for the SN/homoclinic burster. Green lines are periodic orbits. Blue lines are homoclinic orbits. Black lines are example trajectories. Filled circles are stable steady states. Black/blue/red unfilled circles are unstable/saddle/non-hyperbolic steady states. The bottom row shows the SN bifurcation which occurs at $u_{c,2}$ as u is decreased, with no qualitative change to the periodic orbit. In the bistable regime, trajectories moving from the unstable manifold of the saddle either tend towards the periodic orbit or the stable steady state. As u is decreased to $u_{c,1}$ (top right), the periodic orbit collides with the unstable manifold of the saddle to form a homoclinic orbit. Trajectories from the unstable manifold of the saddle either move along this orbit or move to the stable steady state. Finally as u is decreased further (top left) the periodic orbit is broken and all trajectories along the unstable manifold of the saddle move to the stable steady state.

The bifurcations at $u = u_{c,2}$ are bifurcations of steady states such as SN, SNIC, and sub-/super- critical Hopf bifurcations (Izhikevich (2000) Table 3). Conversely, the bifurcations at $u = u_{c,1}$ are bifurcations of stable periodic orbits. Whilst the SNIC and supercritical Hopf bifurcations also fall into this category, we shall further introduce two new bifurcations of periodic orbits which are commonly found in neurons exhibiting bistable behaviour.

The first bifurcation of periodic orbits we shall introduce is called the **saddle node of periodics (SNP)** bifurcation. Much like the saddle node bifurcation for steady states, the SNP bifurcation is characterized by a stable and an unstable periodic orbit colliding and disappearing (Kuznetsov, 1998; Izhikevich, 2007; Strogatz, 2014). The SNP is therefore analogous to the SN bifurcation for fixed points on a Poincaré return map. The Hodgkin-Huxley model, which is the first biophysically realistic quantitative description of the membrane potential (see section 1.5), has bistable regimes of the subHopf/SNP class due to the SNP bifurcation at $u_{c,1}$ and a subcritical Hopf bifurcation at $u_{c,2}$ (called subHopf/fold cycle in the classification by Izhikevich (2000)). Bistability of the subHopf/SNP type has also been identified as a mechanism underpinning the generation of sustained subthreshold oscillations in a neuron (Rotstein et al., 2006), and used to model transitions into pathological hypersychrony of macro-scale neuronal network oscillations (Petkov et al., 2014). A bifurcation diagram of the subHopf/SNP burster is shown in Figure 1.10B.

The second bifurcation of periodic orbits is called the **homoclinic bifurcation**. All of the previously discussed bifurcations have been *local bifurcations*, meaning they can be detected from studying linearizations of a system in the neighbourhood of a steady state (or fixed point on a Poincaré return map) and are locally topologically equivalent to a normal form in the neighbourhood of the bifurcation. The homoclinic bifurcation cannot be treated this way, and is an example of a *global bifurcation* (Kuznetsov, 1998). Here we only include a qualitative description of the homoclinic bifurcation, but a more mathematically rigorous description can be found in Glendinning (1994) and Kuznetsov (1998).

On one side of the homoclinic bifurcation, there exists a stable periodic orbit and a saddle steady state. At the bifurcation, the periodic orbit and steady state collide to form a *homoclinic orbit*:

Definition 14. *Let* Γ *be a an orbit of a dynamical system of the form Equation 1.1, starting at the point* $\mathbf{x}_0$. Γ *is a* ***homoclinic orbit*** *if* $\varphi(t, \mathbf{x}_0) \to \mathbf{x}^*$ *as* $t \to \pm\infty$*, where* $\mathbf{x}^*$ *is a steady state of the system.*

On the other side of the bifurcation the periodic orbit has been annihilated. The key feature of the homoclinic bifurcation is the behaviour of the unstable manifold of the saddle. An example of the homoclinic bifurcation is shown graphically in Figure 1.10C-D. At the bifurcation, the unstable manifold joins with the stable manifold to form the homoclinic orbit, but either side of the bifurcation the manifold splits one way or another. Whilst bursters with a homoclinic bifurcation at $u_{c,1}$ can exhibit any of the four bifurcations of steady states at $u_{c,2}$, bistability of the SN/homoclinic type (called fold/homoclinic in Izhikevich (2000)) is found in the Hindmarsh-Rose and reduced Morris-Lecar models (Izhikevich, 2000). A bifurcation diagram and phase space of SN/homoclinic bistability are shown in Figure 1.10C-D.

1.4.6 Spike adding through flip bifurcations and the flip cascade

Often in models of bursting neurons there are sudden changes in the number of spikes per burst as a parameter is smoothly varied. An important mechanism by which this can occur is the flip bifurcation (Channell et al., 2007; Barrio and Shilnikov, 2011; Tsaneva-Atanasova et al., 2010). The flip bifurcation is a local bifurcation of periodic orbits, meaning it can be studied locally on fixed points of the Poincaré return map corresponding to periodic orbits of the flow. The normal form of the flip bifurcation is the map

$$x \mapsto P(x) = -(1+\alpha)x + x^3, \tag{1.11}$$

for $|\alpha| \ll 1$ (Kuznetsov, 1998). There is a fixed point at $\bar{x} = 0$ which is stable for $\alpha < 0$ and unstable for $\alpha > 0$, hence it is clear a bifurcation occurs at $\alpha = 0$. To fully understand the dynamics of the flip bifurcation, we can also study the second iterate $x \mapsto P^2(x) \equiv P(P(x))$, which naturally has the same fixed point at the origin with the same stability as $P(x)$. However, for $\alpha > 0$, $P^2(x)$ additionally has fixed points at $x \approx \pm\sqrt{\alpha}$ (Kuznetsov, 1998). The points are stable and correspond to a *period two* cycle of the map $x \mapsto P(x)$. For this reason, the flip bifurcation is often also called the period doubling or spike adding bifurcation. The bifurcation diagram for $P^2(x)$ is shown in Figure 1.11A.

An interesting phenomenon is the flip *cascade* (Kuznetsov, 1998), which is an additional route to changing the numbers of spikes in a burst of neurons through chaos (Channell et al., 2007; Tsaneva-Atanasova et al., 2010), and plays a key role in spike-adding in chapter 2. In a flip cascade, a series of flip bifurcations occur, changing the period of the orbit on the map until the dynamics become chaotic. An example of this is shown for the logistic map $x \mapsto p(x) = \alpha x(1-x)$ (Strogatz, 2014) in Figure 1.11B. Crucially, there are intermittent periods of regular, non-chaotic orbits on the map, with a period that differs from the period of the previous non-chaotic orbit (Strogatz, 2014). Therefore a flip cascade through chaos can act as a path between orbits of the map with different periods.

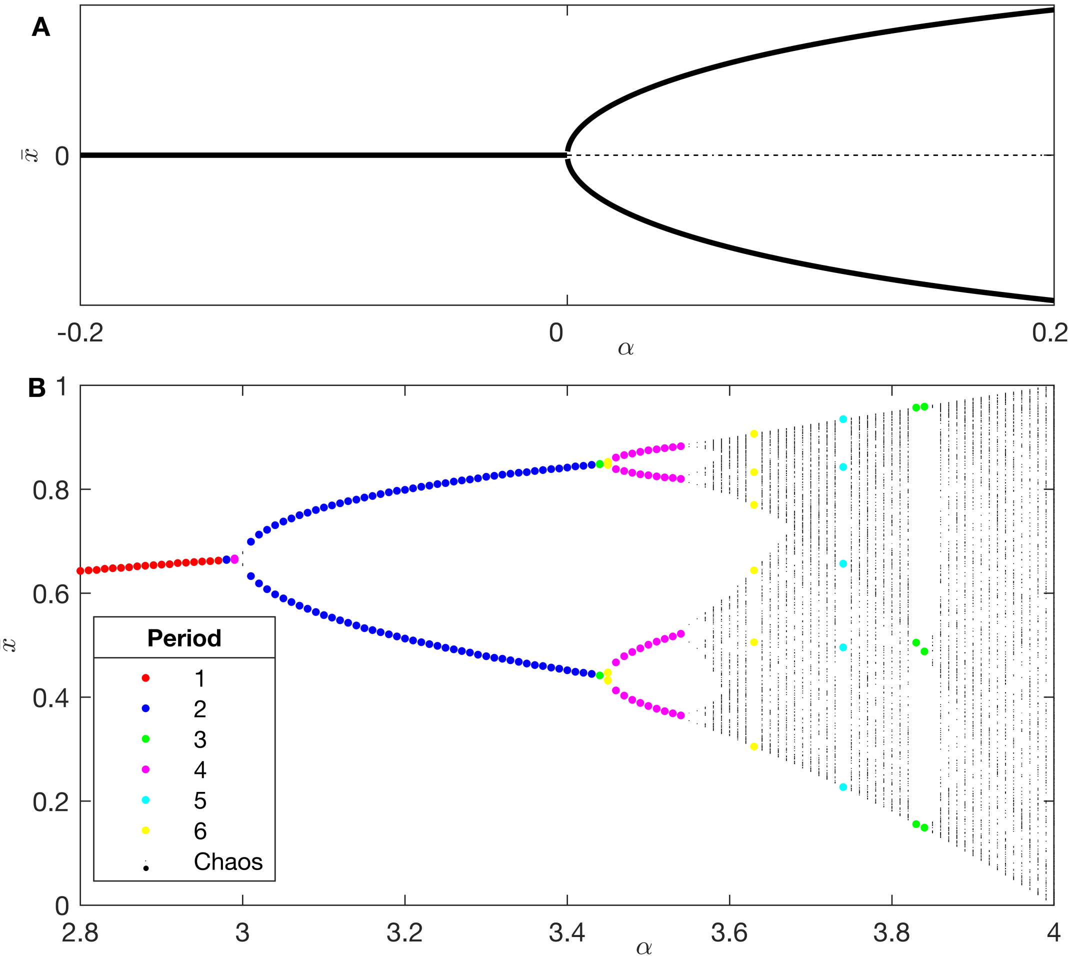

Figure 1.11: **Flip bifurcations**. (A) Bifurcation diagram for the flip bifurcation. Solid/dashed black lines are stable/unstable fixed points on the *second* iterate of the map ($P^2(x)$). Since the flip bifurcation holds in the limit of small $|\alpha|$ (Kuznetsov, 1998), shown here is the case for $|\alpha| \leq 0.2$ and neglecting $O(x^5)$ terms (Kuznetsov, 1998). (B) Orbit diagram demonstrating a flip cascade into chaos and intermittent regions of non-chaotic orbits, demonstrating how a flip cascade can be a path through chaos to a change of period of an orbit. For demonstration purposes, the orbit diagram shown here is for the logistic map.

1.5 Biophysical modelling of the neuron

Section 1.4 introduced qualitative descriptions of neuronal excitability from a dynamical systems perspective, and introduced some low dimensional models of the neuron based upon this bifurcation behaviour. This type of model is known as a *phenomenological model*, meaning it is grounded in replicating dynamic phenomena without a detailed biophysical description. Such models are highly useful for simulating large populations of synaptically connected neurons in parallel to study network dynamics (Izhikevich, 2003; Börgers and Kopell, 2005). However, phenomenological models are of limited use for understanding ionic mechanisms of neuronal dynamics - for example how changes to the flow of charged ions across the membrane alter the dynamics of neurons in disease. For this purpose,

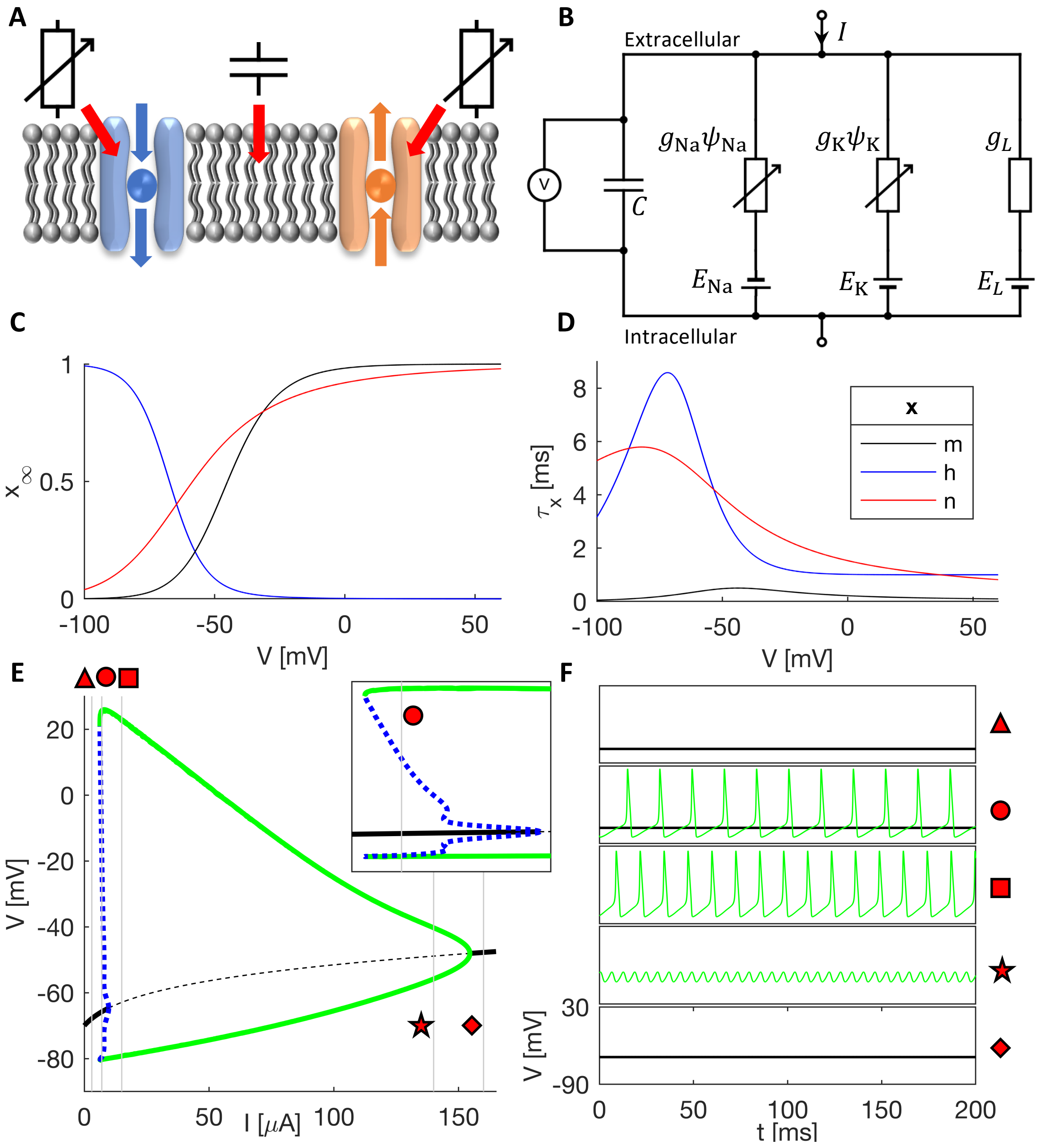

Figure 1.12: **Quantitative description of action potential generation in the Hodgkin-Huxley model**. (A) The cell membrane acts as a resistor-capacitor circuit, with the membrane acting as a capacitor and the voltage gated ion channels acting as variable resistors allowing for the flow of current. (B) The full circuit diagram of the membrane as described by Hodgkin and Huxley (1952). (C) Equilibrium functions for the Hodgkin-Huxley gating variables m (Na$^+$ activation), h (Na$^+$ inactivation), and n (K$^+$ activation). (D) Time constants for the gating variables. (E-F) Bifurcation diagram and simulations for the Hodgkin-Huxley model. In E, Solid/dashed black lines are stable/unstable steady states, solid green/dotted blue lines are stable/unstable periodic orbits. For low input current I, the neuron is at rest (triangle). As I is increased, stable and unstable limit cycles appear through a SNP bifurcation, and a region of bistability exists (enhanced in the inlay), i.e. both resting and spiking regimes coexist (circle). As I is increased further, the steady state becomes unstable via a subcritical Hopf, i.e. the neuron can only spike (square). As I is increase beyond physiological ranges, the limit cycle tends towards low amplitude oscillations (star), which eventually disappear via supercritical Hopf bifurcation (diamond).

more detailed *biophysical* models of the neuron must be used.

Hodgkin and Huxley (1952) famously studied the squid giant axon to build a biophysical quantitative description of the membrane potential of the neuron. The membrane of the neuron was described as an electrical circuit (shown in Figure 1.12A-B), describing the insulating membrane as a capacitor and ion channels as variable resistors allowing the flow of current. This resistor-capacitor circuit is described by the equation

$$C\dot{V} = I - I_{\text{ion}}, \tag{1.12}$$

where I is the applied current across the membrane, I_{ion} is the ionic current, C is the capacitance of the membrane and V is the membrane potential. The ionic currents are described by

$$I_X = g_X \psi_X (V - E_X), \tag{1.13}$$

where X is an element in the set of ionic currents (e.g. $X \in \{\text{Na}^+, \text{K}^+\}$ for the Hodgkin-Huxley model described below and in Figure 1.5), g_X is the maximal conductance of the current X, ψ_X is the fraction of channels in the conducting state, and E_X is the equilibrium potential of the current.

A simple example of a model in this form is the leaky integrate-and-fire neuron (Deco et al., 2008), where I_{ion} is an Ohmic 'leak' current, i.e. $I_{\text{ion}} = I_L = g_L(V - E_L)$. This one-dimensional model can be used to study how properties such as the membrane resistance ($R = 1/g_L$), membrane capacitance (C), and membrane time constant ($\tau = RC$) influence the subthreshold dynamics of neurons in a computationally inexpensive manner. Whilst this model does not simulate an action potential, an AP threshold may be assigned in an integrate-and-fire fashion (section 1.4.2). A crucial advantage of this model is that the frequency-current relationship can be analysed analytically (Deco et al., 2008). Additional biophysical currents of the form Equation 1.13 can be added to the leaky integrate-and-fire model to analyse their roles in modulating the dynamics of a neuron where a detailed knowledge of the mechanisms of action potential generation is not required e.g. the role of the hyperpolarisation activated I_h current on the generation of subthreshold oscillations (Rotstein et al., 2006) and spatial firing patterns (Bonilla-Quintana et al., 2017).

Hodgkin and Huxley (1952) used this electrical circuit description to model the mechanisms of AP generation. To do so, the activation of sodium and potassium currents were quantified using a voltage clamp technique. Their results are described qualitatively in Figure 1.5. Firstly, voltage gated ion channels for the different types of ions were described in terms of gating functions. Namely, Na$^+$ ion channels were modelled by three activation gates (m) and one inactivation gate (h), such that

$$\psi_{\text{Na}} = m^3 h. \tag{1.14}$$

K$^+$ ion channels were modelled by four activation gates, so

$$\psi_{\text{K}} = n^4. \tag{1.15}$$

Here, ψ_X are described in Equation 1.13. Assuming that the proportion of gates which are opening or closing is voltage dependent, each of these gating variables can be modelled as

$$\dot{x} = \alpha_x(V)(1-x) - \beta_x(V)x, \tag{1.16}$$

where $\alpha_x(V)$ and $\beta_x(V)$ are rate constants and $x \in \{m, h, n\}$. By writing

$$x_\infty(V) = \frac{\alpha_x(V)}{\alpha_x(V) + \beta_x(V)} \tag{1.17}$$

$$\tau_x(V) = \frac{1}{\alpha_x(V) + \beta_x(V)}, \tag{1.18}$$

equation 1.16 can be rewritten as

$$\dot{x} = \frac{x_\infty(V) - x}{\tau_x(V)}. \tag{1.19}$$

This equation can be interpreted as follows: $x_\infty(V)$ is the voltage dependent steady state value of x, and $\tau_x(V)$ is the voltage dependent time constant for x.

By holding the neuron at a given membrane potential and recording the conductance of Na$^+$ and K$^+$ currents, equations for these rates of changes of gating variables could be calculated. Plots of x_∞ and τ_x for each of the gating variables described by Hodgkin and Huxley (1952) are shown in Figure 1.12C-D. Under this biophysical formulation of the neuron model, action potentials can be generated which closely match those seen in the data (Hodgkin and Huxley, 1952). This type of ODE formulation makes an analysis of the mechanisms of AP generation possible using dynamical systems theory. Figure 1.12E shows an example bifurcation diagram for the Hodgkin-Huxley model, demonstrating the bifurcations by which spiking arises as the input current is changed. Simulations of examples of dynamics in the Hodgkin-Huxley model are shown in Figure 1.12F. Biophysically realistic models are often more high dimensional and computationally expensive than their phenomenological counterparts, but can be used to study the roles of different ionic currents in modulating neuronal dynamics. In chapter 2, we use a 12-dimensional model in the Hodgkin-Huxley formulation to study the mechanisms underpinning altered temporal firing patterns in an animal model of tauopathy.

The models outlined above are all deterministic. In reality, there are two primary biological sources of noise in neurons, synaptic noise and channel noise (White et al., 2000). Synaptic noise due to incoming spikes from neighbouring neurons can be modelled as a point Poisson process run through a synaptic response kernel acting on the membrane potential of the neuron (Fernandez and White, 2008). Channel noise arises due to spontaneous fluctuations in the opening and closing of ion channels in the neuron and can be modelled in a biophysically realistic manner using continuous time Markov chain approaches (White et al., 2000) in which the rate constants $\alpha_x(V)$ and $\beta_x(V)$ of Equation 1.16 are described by a Markov model instead of an ODE. This is computationally expensive, so to reduce computational expense phenomenological SDE approximations of channel noise ranging from white noise currents on the membrane potential to detailed coloured noise on the ion channels may be used (Goldwyn and Shea-Brown, 2011).

1.6 Modelling a neural mass

In section 1.3, we introduced the concept of emergent neuronal oscillations in large connected ensembles of neurons. There are two main approaches to modelling such a system. The first approach is to simulate a large number of neurons in parallel using the types of single cell model presented in section 1.5 (Izhikevich, 2003; Börgers and Kopell, 2005; Wulff et al., 2009; Solanka et al., 2015). An example of such a simulation is shown in Figure 1.6. Advantages to this approach include the ability to explore how single cell dynamics or network topologies can influence network dynamics (Börgers and Kopell, 2005; Pastoll et al., 2013), but a crucial disadvantage of this approach is that the system typically ends up extremely high dimensional as typically each neuron requires at least one equation to describe membrane dynamics (section 1.5) and at least one equation to describe synaptic dynamics. This high dimensionality results in great computational expense and a system that is intractable for quantitative analysis such as bifurcation analyses.

An alternative approach is to develop a lower dimensional system which replicates the dynamics of neural populations without directly modelling each neuron in the population, referred to here as a *neural mass model* (NMM). To do so, Wilson and Cowan (1972) modelled the firing rate of a neural mass consisting of an excitatory and inhibitory population of neurons. Each population is modelled by a single firing rate variable bounded between zero (no neurons in the population firing) and one (all neurons in the population firing). The Wilson-Cowan model works on the assumption that with no external input the firing rate of the populations decay to zero, and that input to the populations is transformed to a firing rate via a sigmoid function. As input to the inhibitory or excitatory population is varied, oscillations emerge in the model via a Hopf bifurcation, making the model an appropriate low dimensional model of cortical neuronal oscillations (Hlinka and Coombes, 2012).

Jansen and Rit developed a more biologically plausable model of a neural mass (Jansen et al., 1993; Jansen and Rit, 1995). Jansen-Rit type NMMs contain two blocks. The density of incoming pulses of APs to a post-synaptic population (e.g. the firing of a neighbouring pre-synaptic population) is transformed into an average membrane potential for the post-synaptic population by convolution with a synaptic response kernel. This population's mean membrane potential is then transformed to a firing rate using a sigmoid function, which can then be used as an input to neighbouring populations. To calculate these transformations, each block of PSPs is represented by a second-order ODE (Jansen and Rit, 1995). Jansen and Rit originally described three populations in their model, namely pyramidal cells, inhibitory interneurons, and stellate/excitatory interneurons. Many extensions have since been made to the Jansen-Rit model. Fast gamma rhythms have been accounted for in models by including recurrent inhibition among the inhibitory population (Moran et al., 2007), or through the addition of a neurophysiologically realistic fast inhibitory subpopulation (Wendling et al., 2002). This inhibitory feedback in the Wendling model is thought to be important in the generation of pathological dynamics in epilepsy (Wendling et al., 2002; Ferrat et al., 2018). Ursino et al. (2010) extended the Wendling model further to include recurrent inhibition on the fast inhibitory population, allowing for the generation of gamma oscillations in an isolated network of inhibitory neurons in line with data. Further extensions have included as many as fourteen populations (Sotero, 2016).

A second approach to developing biophysically derived models of a neural mass is to start with a high dimensional model of many neurons synaptically connected and use mean field theory to develop a low dimensional reduction of the mean firing rate of such a population. The method for building such a mean field neural mass model for a population of leaky integrate-and-fire neurons is reviewed by Deco et al. (2008). A widely used mean field model based on leaky integrate-and-fire neurons is that of Wong and Wang (2006) and its reduction made by Deco et al. (2013). More recently, mean field models have been developed from heterogeneous networks of quadratic integrate-and-fire and the related theta neuron models (Luke et al., 2013; Montbrió et al., 2015; Coombes and Byrne, 2019), and used to model interneuron network gamma (ING) (Devalle et al., 2017) and both strong and weak pyramidal-interneuron network gamma (PING) rhythms (Keeley et al., 2019). These models allow for tracking of the degree of synchrony *within* the population (Devalle et al., 2017; Coombes and Byrne, 2019), which Coombes and Byrne (2019) suggested makes them a prime candidate for the next generation of neural mass models. Mean field models have additionally been derived from higher dimensional neuron models exhibiting more broad repertoirs of firing behaviour such as the Izhikevich neuron (Visser and Van Gils, 2014).

Alternatively, neural oscillations can be modelled from a purely phenomenological point of view, with no basis in the biophysics of neural systems. For example, the Kuramoto model describes the phase dynamics of an oscillator in a one-dimensional equation, but has been demonstrated to be useful for studying pathological synchronization of neural oscillators in epilepsy (Schmidt et al., 2014) and understanding the dynamics of travelling waves on a cortical sheet (Breakspear et al., 2010). In this thesis, we use a phenomenological model of the neural mass given by the equations

$$\begin{aligned}\dot{v} &= (a - v^2 - u^2)v - \omega u + \sigma\eta(t)\\ \dot{u} &= (a - v^2 - u^2)u + \omega v,\end{aligned} \tag{1.20}$$

where $\langle\eta\rangle = 0$ and $\langle\eta(t),\eta(s)\rangle = 0$. In the deterministic case $\sigma = 0$, this model is the normal form of the supercritical Hopf bifurcation (Equation 1.6). Therefore the stochastic system is characterized by noisy perturbations on the limit cycle if $a > 0$, whilst for $a < 0$ the the origin corresponds to a focus, resulting in noisy output with a preferential frequency at ω. If a is negative with a magnitude close to zero, the system essentially exhibits noise induced oscillations as the steady state is only weakly attractive. As the magnitude of $a < 0$ increases, the steady state becomes more strongly attractive and the resonance phenomena is damped, resulting in the output appearing more noisy. A similar model has been used by Deco and colleagues (Deco et al., 2017a,b; Dermitas et al., 2017) to model neural oscillations.

A key motivation for the use of this model is that many more biophysically derived neural mass models undergo a supercritical Hopf bifurcation as local connectivity is increased; for low connectivity the populations do not synchronize and the system tends to steady state, but as connectivity between (or within) excitatory and inhibitory populations is increased a bifurcation will occur and the system will oscillate. Examples of the Hopf bifurcation as local coupling is increased in the Wilson-Cowan model (Wilson and Cowan, 1972), Jansen-Rit model (Jansen and Rit, 1995), and quadratic integrate-and-fire mean field model of hippocampal gamma (Keeley et al., 2019) are shown in Figure 1.13 alongside the bifurcation diagram for the Hopf model. Therefore the parameter a can be viewed as a proxy for the degree of local coupling in the model (Dermitas et al., 2017). This is important for chapter 3, where macro-scale LFP data is integrated with local two-photon calcium imaging data of neuronal circuits to study the interplay between local coupling and global synchrony. A second motivation for use of the Hopf model is that the frequency of oscillations is determined explicitly by a single parameter. This

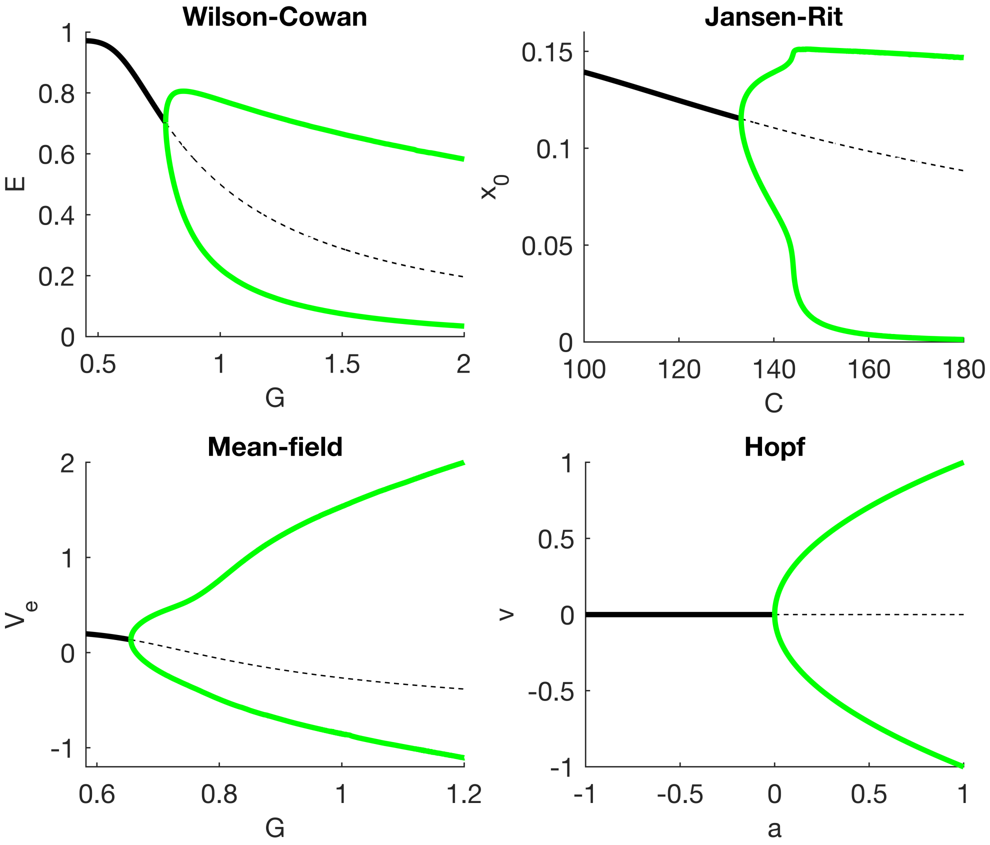

Figure 1.13: **Hopf bifurcations in neural mass models**. Bifurcation diagrams for the Wilson-Cowan (Hlinka and Coombes, 2012), Jansen-Rit (Jansen and Rit, 1995), and mean-field model of hippocampal gamma (Keeley et al., 2019) as coupling between populations is varied. For the Wilson-Cowan and mean-field models, all parameters that couple populations are multiplied by a scaling constant G. For the Jansen-Rit model, the parameter C is as described in Jansen and Rit (1995). All other parameters are the same as those described in their respective citations. Each model undergoes a supercritical Hopf bifurcation as the local coupling is increased and the populations begin to synchronize and oscillate. These results motivate the use of a phenomenological model based on the normal form of the Hopf bifurcation (bottom right) described in Equation 1.20, and justify the interpretation of parameter a as a measure of local coupling between populations.

was useful in chapter 4 for exploring how heterogeneous oscillatory slowing in AD might affect synchrony between neural oscillators without the requirement of biophysical interpretations of the local mechanisms underpinning the slowing (e.g. altered local coupling (Jansen and Rit, 1995) or membrane/synaptic time constants (David and Friston, 2003)).

1.7 Whole brain modelling

In this section, we discuss how spatially extended networks of neural mass models (section 1.6) can be used to model whole brain dynamics such as those recorded by multi-electrode EEG. In whole brain models, anatomically or functionally defined regions of the brain are represented by a neural mass model, and these neural masses are coupled via a connectome to study brain-wide synchronization (Finger et al., 2016; de Haan et al., 2017; Dermitas et al., 2017; Zimmerman et al., 2018). A simplified representation of such a whole brain model is shown in Figure 1.1C. The connectome can be derived from structural imaging data (Finger et al., 2016; Zimmerman et al., 2018) (structural connectivity; SC) or estimated based on functional data using parameter optimization techniques (Friston et al., 2003; Freestone et al., 2014; Shan et al., 2017) (effective connectivity; EC). Multimodal approaches may involve estimating EC from functional data but using structural connectomes to form prior estimations or to constrain the effective connectivity (Dermitas et al., 2017).

In this thesis, a whole brain model of the human brain is presented in chapter 4 and the mouse brain in chapter 3. Both models place the phenomenological model of a supercritical Hopf bifurcation described in Equation 1.20 onto each brain region. The equations for region i are therefore described by

$$\begin{aligned}\dot{v}_i &= (a - v_i^2 - u_i^2)v_i - \omega_i u_i + G\sum_{j\neq i} K_{ij}(v_j - v_i) + \sigma\eta_i(t)\\ \dot{u}_i &= (a - v_i^2 - u_i^2)u_i + \omega_i v_i,\end{aligned} \tag{1.21}$$

where G is a global coupling constant and matrix K is the connectome, where element K_{ij} is the influence of node j on node i. K is a weighted matrix, and can be either symmetric (undirected connections) or asymmetric (directed connections). All other parameters and variables are as described in Equation 1.20. Note the parameter a does not have an index i in these equations; in this thesis we assume the same value of a for each node, and introduce heterogeneity through the intrinsic frequencies ω_i. This is justified for the specific hypotheses being tested within their relevant chapters, but essentially reduces the already large parameter space of the model.

Coupling between neural masses can additionally be performed on intermediate spatial scales. Jansen and Rit (1995) studied the generation of evoked potentials in two cortical columns, each represented by a neural mass model, located within the visual cortex. Schmidt et al. (2014) coupled oscillators within regions of the brain to generate a multi-scaled whole brain model to describe how both local and global coupling can influence pathological brain dynamics. Extending the neural mass from a point source to a spatially extended field results in *neural* *field models* (Deco et al., 2008) which can be simulated on a grid over the cortex (Spiegler and Jirsa, 2013; Sanz-Leon et al., 2015) and used to study dynamics such as travelling waves and bumps on the cortical surface (Coombes, 2005). Whilst these extensions of whole brain neural mass models on intermediate spatial scales may increase biophysical realism and result in a broader repertoire of dynamics, this comes at the cost of greatly increased computational expense and a larger parameter space making the model less tractable for numerical analysis. Some of this local coupling may furthermore be captured phenomenologically within the description of the point neural mass dynamics, for example in parameter a of the Hopf model used in this thesis, as described in section 1.6.

1.8 Quantifying neural dynamics

This section introduces methods used to quantify neural dynamics used in this thesis. The primary focus of this section is methods used to quantify dynamics of the EEG used in chapters 3-6 but some methods are more broadly applicable; for example, functional connectivity and graph theoretical analyses (sections 1.8.2-1.8.3) are applied to two-photon calcium imaging data in chapter 3. Conversely, some methods such as microstate analysis (section 1.8.4) are strictly defined as properties of the EEG.

1.8.1 Power spectrum

A simple univariate measure of the EEG is the power spectrum, which aims to characterize the contribution of different frequencies of neuronal oscillations to the EEG. An EEG time series can be expressed as a sum of sine waves, each wave characterized by an amplitude, frequency, and phase (Nunez and Srinivasan, 2006) by performing a Fourier transform on the EEG time series, for example using the fast Fourier transform (FFT) algorithm (Frigo and Johnson, 1998). The resulting power (amplitude squared)-frequency relationship is known as the power spectrum of the EEG (Buzsáki, 2006; Nunez and Srinivasan, 2006), and is a representation of the EEG in the frequency domain. Power spectra computed directly from the FFT of the signal are often noisy due to finite and stochastic data, so methods such as Welch's method (Welch, 1967), multi-tapered Fourier transforms (Percival and Walden, 1993), and Fourier analysis of estimated autoregressive model parameters (Akin and Kemal Kiymik, 2000) can be used to reduce the noise on the spectrum. The power spectrum of EEG is known to change in different cognitive states, which has lead to the classification of a small number of frequency bands commonly studied in the EEG (Buzsáki, 2006; Nunez and Srinivasan, 2006), for example by studying total or relative power within a given band.

Power spectral analyses have been crucial in EEG research in AD for studying the characteristic slowing of oscillations in people with AD, reviewed in section 1.3.

1.8.2 Functional connectivity

Functional connectivity between two time series (e.g. signals recorded by two EEG electrodes) quantifies statistical similarities between those time series. Most measures of FC are examples of *bivariate* measures, which take a pair of time series x and y and quantifies coactivity of this pair of time series. Using bivariate measures for each pair of time series in a multivariate EEG, a *functional network* can be constructed where the nodes of the network correspond to a time series (e.g. an EEG electrode) and edge (i, j) corresponds to the strength of the functional connectivity between nodes i and j. Alternatively, some measures are multivariate (accounting for all signals simultaneously) or global (giving information on synchrony in the whole network without information on edges) (Dauwels et al., 2010). For brevity, a small number of relevant bivariant measures will be discussed here, but excellent reviews of functional connectivity measures are given by David et al. (2004) and Dauwels et al. (2010).

A simple measure of functional connectivity between time series x and y is the correlation coefficient,

$$r_{x,y} = \frac{1}{N} \sum_{k=1}^{N} \frac{(x(k) - \bar{x})}{\sigma_x} \frac{(y(k) - \bar{y})}{\sigma_y}, \tag{1.22}$$

where N is the number of time points, $\bar{x}$ denotes the mean of x, and σ_x denotes the standard deviation of x (and similar for y). Correlation is a *linear* measure quantifying the degree to which fluctuations of the signals about the mean are linearly related.

When working in *sensor space* (i.e. the analysed time series are those directly recorded by an EEG electrode), volume conduction must be considered. The activity of a point on the brain will conduct to multiple electrodes on the scalp, and this mixing is assumed to be linear and approximately instantaneous (Nunez and Srinivasan, 2006). Therefore volume conduction can result in spurious correlations in sensor space due to common sources. Source space reconstruction (Michel et al., 2004) can be used to account for the effects of volume conduction, but since the inverse problem is highly ill-posed these methods are often regularized and hence spurious instantaneous linear correlations may instead arise due to source leakage effects (Pascual-Marqui et al., 2011). Instead, approaches are often taken to study time lagged measures of functional connectivity.

One such measure is the maximum of the cross-correlation function (the correlation between x and y, shifted by lag τ, as a function of τ) rejecting peaks at zero lag (Schmidt et al., 2014). Taking the Fourier transform of the cross-correlation function results in the *coherence* between signals, which can be viewed as a frequency domain measure of linear correlation (Nunez and Srinivasan, 2006). Whilst it is not possible to explicitly remove zero lag correlations when using coherence, Nolte et al. (2004) showed that the imaginary part of coherence tends to zero as the phase difference tends to zero and hence cannot give rise to spurious connections due to linear mixing. However, the imaginary part of coherence will also underestimate functional connectivity for small but non-zero phase lags, so Pascual-Marqui et al. (2011) presented a lagged coherence measure normalized by the real part of coherence which reduces this underestimation of FC for small lags (Pascual-Marqui et al., 2011).

Coherence as a measure of synchrony mixes phase and amplitude effects (Lachaux et al., 1999). To test for phase binding without amplitude effects at a given frequency within a narrow frequency band, Lachaux et al. (1999) presented the *phase locking factor* (PLF),

$$c_{xy} = \frac{1}{T}\left|\sum_{k=1}^{T} e^{i\Delta\phi_{xy}(k)}\right|, \tag{1.23}$$

where T is the number of sampling points and $\Delta\phi_{xy}(k)$ is the difference between the instantaneous phases of signals x and y at sampling point k (e.g. calculated by the Hilbert transform). As with the cross-correlation function, zero lag connections can be manually removed. Alternatively, measures such as the phase lag index (PLI) (Stam et al., 2007b) which averages over the sign of the phase difference at each time point are small if the lag fluctuates around zero, making them insensitive to zero lag connections. However, it should be noted that PLI does not quantify the degree of phase locking in the same manner as PLF; instead, PLI quantifies consistency in which time series is leading/lagged. The weighted PLI is a measuring which combines PLI and imaginary coherence to reduce sample-size bias, reduce sensitivity to uncorrelated noise, and increased power to detect phase synchronization (Vinck et al., 2011).

Following calculation of a functional network, it is important to test whether edges in the network are significant or an effect of finite window size in the data. A method to do so is to generate surrogate data which preserves the univariate properties of the data (e.g. amplitude distribution, power spectrum), but eliminate multivariate dependencies (Schreiber and Schmitz, 1996; Sun et al., 2012; Lancaster et al., 2018). By calculating a large number of surrogate data sets and computing the functional connectivity between these surrogates, a null distribution of edges can be generated to compare the empirical edges against and test for significance (Rummel et al., 2011; Sun et al., 2012; Schmidt et al., 2014). In this thesis, namely chapters 3 and chapter 4, the iterative amplitude adjusted

Fourier transform (IAAFT) method (Schreiber and Schmitz, 1996) is used to generate surrogates for testing significance of edges in a functional network (Rummel et al., 2011; Schmidt et al., 2014). IAAFT surrogates preserve the distribution of amplitudes and the power spectrum of the data, whilst removing any phase relations in the multivariate data (Schreiber and Schmitz, 1996).

Additionally, model based measures can give directed information, known as *effective connectivity*. Multivariate autoregressive (MVAR) models assume that the dynamics of a node are a stochastic process modulated by a linear mixture of its own history and the history of all other nodes in the networks, meaning it is an example of a multivariate measure. There exist a large number of ways to construct directed functional connectivity matrices from the coefficients of an MVAR model in both the frequency and time domain, reviewed by Dauwels et al. (2010). Models based in biophysics can also be used to estimate effective connectivity; for example, *dynamic causal modelling* involves placing neural mass models at each node and using Bayesian methods to infer the effective connectivity between regions (Friston et al., 2003). Dynamic causal modelling is not the only such technique, a range of parameter optimization methods are available to estimate the effective connectivity of a model based on functional data (Freestone et al., 2014; Shan et al., 2017; Dermitas et al., 2017).

Different functional (or effective) connectivity measures can give very different results for the same data (David et al., 2004; Dauwels et al., 2010; Jalili, 2016; Hassan et al., 2017), so it is important an appropriate measure be chosen for the data. Many other factors can also affect the resulting functional network structure, including epoch length (Fraschini et al., 2016), network size (Joudaki et al., 2012), and choice of whether to binarize the network (e.g. by thresholding the network) or keeping weighted edges (Jalili, 2016).

1.8.3 Graph theory

Once a functional network has been calculated using the methods from the previous section, the field of graph theory can be used to quantify properties of these networks. A detailed review of graph theoretical measures of macro-scale brain networks is given by Rubinov and Sporns (2010). Consider a weighted, undirected functional network or *graph* $G = (V, E, W)$, where V is a set of N nodes, E is a set of edges, and W is the set of weights for the edges. We shall represent this graph by the weighted adjacency matrix C, where element c_{ij} is the FC value (correlation, coherence, PLF, etc) between nodes i and j.

The *degree* of node i is the sum of weighted connections of the node (Rubinov and Sporns, 2010), given by

$$d(i) = \sum_{j \neq i} c_{ij}, \tag{1.24}$$

and is a measure of how synchronized node i is to the rest of the network. Degree is an example of a local measure, with a value for each node. The *mean degree* of the network is then given by

$$\mathrm{MD} = \frac{1}{N}\sum_{i=1}^{N} d(i), \tag{1.25}$$

and is a global measure (one value for the whole network) of how synchronous the network is on average. The mean degree gives no information on the topological structure of the network, so a number of other graph theoretical measures can be used to further quantify topology. There exist a large number of local and global measures of topology of a network (Rubinov and Sporns, 2010), so here we restrict our discussion to those used in this thesis and related measures.

Two vital subsets of measures quantify *integration* and *segregation*. A node that is highly integrated is likely to be closely connected to all nodes in the network, such that the node has a short *average path length*

$$L_i = \frac{1}{(N-1)}\sum_{j=1}^{N} \delta_{ij}, \tag{1.26}$$

where δ_{ij} is the path length between nodes i and j, and is calculated using the Dijkstra algorithm (Dijkstra, 1959). The *closeness centrality* of node i is L_i^{-1}. A related measure is the *efficiency* of a node i,

$$E_i = \frac{1}{(N-1)}\sum_{j=1}^{N} \frac{1}{\delta_{ij}}, \tag{1.27}$$

which is a measure of how efficiently information is transferred between node i and all other nodes in the network on average (Latora and Marchiori, 2001). A node with short average path length (high closeness centrality) and high efficiency are said to be integrated with the rest of the network. A globally integrated network is then a network with short *characteristic path length* (Rubinov and Sporns, 2010)

$$L = \frac{1}{N}\sum_{i=1}^{N} L_i \tag{1.28}$$

and high *global efficiency* (Latora and Marchiori, 2001)

$$E = \frac{1}{N}\sum_{i=1}^{N} E_i. \tag{1.29}$$

Segregation of a network refers to the formation of groups or clusters of highly connected nodes. The *clustering coefficient* (Watts and Strogatz, 1998) of a node

i is given by

$$C_i = \frac{\sum_{j \neq i} \sum_{k \neq i,j} (c_{ij} c_{ik} c_{jk})^{1/3}}{\kappa_i (\kappa_i - 1)}, \tag{1.30}$$

where κ_i is the number of connections made by node i (the binary degree of i). The clustering coefficient can be interpreted as the probability that given two nodes j and k are neighbours of node i, nodes j and k are neighbours of each other (weighted by strengths of edges) (Watts and Strogatz, 1998; Rubinov and Sporns, 2010). A second measure related to segregation of a network is the *local efficiency* (Latora and Marchiori, 2001), which is defined for node i ($E_{\ell,i}$) as the global efficiency of a sub-network consisting of only the neighbours of i. Therefore a network has groups and clusters of nodes with efficient information transfer within these clusters (i.e. is segregated) if it has high *mean local efficiency* (Latora and Marchiori, 2001)

$$E_\ell = \frac{1}{N} \sum_{i=1}^{N} E_{\ell,i} \tag{1.31}$$

and high global clustering coefficient (Watts and Strogatz, 1998; Rubinov and Sporns, 2010)

$$C = \frac{1}{N} \sum_{i=1}^{N} C_i. \tag{1.32}$$

Integration and segregation of a network are not mutually exclusive. A *small-world* network (Watts and Strogatz, 1998) is both integrated and segregated, with high global clustering coefficient and low characteristic path length (Humphries and Gurney, 2008), or, equivalently, high local and global efficiency (Latora and Marchiori, 2001). Humphries and Gurney (2008) introduced a measure of *small-worldness*,

$$\text{SW} = \frac{(C/C_0)}{(L/L_0)}, \tag{1.33}$$

where C and L are defined as in Equations 1.32 and 1.28 respectively, and C_0/L_0 are the global clustering coefficient/characteristic path length of a random network with the same edge distribution and mean degree as the empirical network. Functional and structural brain networks are believed to have a small-world structure (Bullmore and Sporns, 2009; Stam, 2014; Bassett and Bullmore, 2017), where the high segregation gives rise to the ability for specialized processing in strongly connected segregated brain regions and integration allowing for the brain to combine this specialized information (Rubinov and Sporns, 2010).

1.8.4 EEG microstates

Accurate estimation of the functional connectivity and graph theoretical measures discussed above require epochs of EEG data on the order of seconds in length (Gudmundsson et al., 2007; Fraschini et al., 2016), and assumes stationarity of the brain dynamics over this epoch. In reality, it is believed the resting state of the brain is composed of a number of 'resting state networks' each corresponding to different cognitive domains (Lehmann et al., 1998; Britz et al., 2010; Michel and Koenig, 2018), and that these networks remain stable for a tens to hundreds of milliseconds (allowing for changes in polarity) before rapidly transitioning to another network (Koenig et al., 1999; Khanna et al., 2015; Michel and Koenig, 2018). EEG *microstate* analysis is a method used to study this switching behaviour of the resting state (Khanna et al., 2015; Michel and Koenig, 2018) by studying the instantaneous topographic maps of the EEG.

The first microstate analyses used a method of adaptive segmentation in which the maxima and minima of consecutive EEG topographic maps were compared; a microstate was defined as the epoch for which the local maxima and minima stayed within a given window (Lehmann et al., 1987). Wackermann et al. (1993) followed this procedure and then performed a post-hoc clustering of the centroid locations of each microstate to find that almost all segments belonged to 2-6 (mean 3.7) microstate classes. This information that brain microstates formed a small number of classes lead to the development of k-means clustering methods (Koenig et al., 1999), which not only account for the maxima and minima of the field but the entire spatial topography. Furthermore, these methods allow for definition of regularly occuring maps. A large number of studies using different numbers of electrodes, participants, and filter settings have identified the same four canonical maps in the resting state EEG (see Figure 3 of Michel and Koenig (2018) for a review). These four classes have been labelled A, B, C, and D in the literature, and have been correlated with resting state networks related to various cognitive domains (Britz et al., 2010). These maps have also been validated using other clustering methods such as topographic atomize and agglomerate hierarchical clustering (TAAHC) (Khanna et al., 2014).

Microstates are known to change in healthy development and aging (Koenig et al., 2002) and neurological disorders including dementias (Ihl et al., 1993; Dierks et al., 1997; Strik et al., 1997; Stevens and Kircher, 1998; Nishida et al., 2013), schizophrenia (Koenig et al., 1999; Lehmann et al., 2005; Nishida et al., 2013), and depression (Strik et al., 1995; Atluri et al., 2018). The majority of microstate studies in AD were performed prior to the development of k-means type methods (Ihl et al., 1993; Dierks et al., 1997; Strik et al., 1997; Stevens and Kircher, 1998), meaning alterations to specific classes have not been well characterised. Furthermore the differences between temporal scales of microstates and spectral/functional network measures make EEG microstates a prime candidate for additional information as an electrophysiological biomarker. Therefore understanding changes to EEG microstates in AD and using these alterations as a biomarker is the focus of chapter 5.

Chapter 2

Modelling single cell dynamics in tauopathy

This chapter is based on the work published the Journal of Theoretical Biology as Tait et al. (2018) in collaboration with Dr Marc Goodfellow (supervision, methodological design), Dr Jon Brown (supervision, conceptualization), Dr Kyle Wedgwood (conceptualization, methodological design), and Prof Krasimira Tsaneva-Atanasova (supervision, conceptualization). The author's contribution to this chapter includes development and formal analysis of the model, visualization of the results, and writing of the chapter.

2.1 Introduction

The entorhinal cortex occupies a key role in the cortical-hippocampal circuit, acting as a gateway between the neocortex and hippocampus (Canto et al., 2008) and playing a pivotal role in working memory processing and spatial navigation (McNaughton et al., 2006; Moser et al., 2008). Many different functional cell types involved in the coding of spatial representation are found in the entorhinal cortex, including grid cells, border cells, head direction cells and speed cells (Hafting et al., 2005; Solstad et al., 2008; Giocomo et al., 2014; Kropff et al., 2015). Spatial information from these cells is transferred from layer II of the entorhinal cortex to place cells in the hippocampus, which in turn feed back into the entorhinal cortex (O'Keefe et al., 1998; Deng et al., 2010; Barak et al., 3015).

The principle neurons in layer II of the medial entorhinal cortex are reported to be predominantly (60-70%) stellate cells (mEC-SCs) (Alonso and Klink, 1993; Booth et al., 2016a). Analysis of recordings of mEC-SCs in brain slices demonstrates a number of key identifying electrophysiological properties, including a large membrane potential sag mediated by a hyperpolarisation activated cation current (I_{h}), subthreshold oscillations in the theta (4-12 Hz) range and clustered action potential firing (Alonso and Klink, 1993). Dorsoventral gradients in these electrophysiological properties (Giocomo et al., 2007; Garden et al., 2008; Giocomo and Hasselmo, 2008, 2009; Dodson et al., 2011; Booth et al., 2016a) reflect similar dorsoventral gradients in grid cell spacing (Hafting et al., 2005), implying a key role in spatial memory.

The disruption of memory systems is one of the hallmarks of dementia (McGowan et al., 2006). The most common cause of dementia, Alzheimer's disease, has been shown to affect the entorhinal cortex early in disease progression (Braak and Braak (1991); Figure 1.3). Experimental models of tau pathology have suggested a relationship between neurofibrillary tangles and spatial memory deficits (Fu et al., 2017) that may be underpinned by alterations in the intrinsic cellular dynamics described above (Booth et al., 2016a; Fu et al., 2017). It is therefore crucial if we wish to develop treatments and therapies to build our understanding of the mechanisms underlying mEC-SC dynamics so that we can further elucidate the cellular and network bases of spatial memory, and ultimately the causes and consequences of Alzheimer's disease.

There are many potential dynamical frameworks within which to mathematically model clustered firing of neurons or the generation of subthreshold oscillations (sections 1.4-1.5). Phenomenological models have used extrinsic rhythmic inputs to drive integrate-and-fire type neurons across bifurcations (Pastoll et al., 2013; Solanka et al., 2015), thus producing temporal periods of quiescence interspersed with bursts of action potentials, that may be reminiscent of clustered firing. Low dimensional neuronal models such as the Izhikevic neuron (which is a non-linear integrate-and-fire type neuron) have been used to model mEC-SC firing patterns (Izhikevich, 2007; Shay et al., 2016) but are also constructed from a phenomenological dynamical systems perspective and do not offer mechanistic insight at the single neuron level. For example, they do not allow understanding of the relationship between properties of membrane channels and the aforementioned dynamic firing patterns.

In order to develop a mechanistic, biophysical understanding, Fransén et al. (2004) developed a detailed, compartmental model of an mEC-SC, based on the Hodgkin-Huxley formulation (section 1.5). In addition to standard Hodgkin-Huxley ion channels, hyperpolarisation-activated, cation non-selective channels (I_h) were incorporated along with calcium-gated potassium channels including a potassium-mediated after-hyperpolarisation (AHP) current. It was demonstrated that this combination of channels was sufficient to describe limit cycle subthreshold oscillations in the theta (4-12 Hz) range and clustered action potential firing. A simulation study of the noise driven system demonstrated a dependence of clustered firing on the AHP conductance and the time scale of the slow I_h component (Fransén et al., 2004). To investigate the role that stochastic effects could play in generating stellate cell dynamics, Dudman and Nolan (2009) formulated a high dimensional, Markov chain model of stochastic ion channel gating and demonstrated that this model could reproduce the aforementioned dynamics due to intrinsic ion channel noise. Clustered action potential firing was generated by a transient increase in probability of action potential firing during recovery from the AHP. This required the I_{h} current, since simulations and experimental investigation of an I_{h} knockout resulted in loss of clustering.

These models have provided insight into the potential biophysical mechanisms underpinning the clustered action potential firing and subthreshold oscillations of mEC-SC. However, the dynamic mechanisms underpinning clustered action potential firing were not elucidated, which precludes a thorough understanding of the ways in which changes in parameters affect dynamics. Such understanding would help to build a more complete picture of the reasons why different firing patterns can emerge, for example due to diseases such as Alzheimer's disease. Furthermore, previous models have been cumbersome, either due to their dependence on calcium gated-channels or stochastic simulations. A simpler model would allow us to extend more readily into neuronal networks in the future in order to better understand the spatial structures underpinning memory processing in health and disease.

In order to advance such a framework, in this chapter, the model of Dudman and Nolan (2009) is converted to the deterministic Hodgkin-Huxley formulation. This results in an ordinary differential equation (ODE) model that retains the key components of I_{h} and I_{AHP}. As a single compartment model with only voltage-gated ion channels, this model is simpler than the multi-compartment model of Fransén et al. (2004) which includes both voltage- and calcium-gated ion channels. Upon introducing extrinsic noise to the membrane potential in a stochastic differential equation (SDE) framework, numerical simulations are used to demonstrate that this model is capable of generating clustered action potential firing as well as subthreshold membrane potential fluctuations with peak power in the theta band, in line with experimental results. Numerical bifurcation analyses demonstrate that clustered firing in the model arises due to a flip bifurcation (Channell et al. (2007); Barrio and Shilnikov (2011); section 1.4.6). Clustered action potential firing can, in turn, be understood in terms of a fast-slow system (section 1.4.5), in which the activation of the persistent sodium (NaP) and inactivation of the slow A-type potassium (Kas) channels act as slow variables, driving the fast sub-system through a hysteresis loop via subcritical Hopf and homoclinic bifurcations. Thus, in terms of the underlying dynamics, this model can be classified as a subcritical Hopf/homoclinic burster (Izhikevich, 2000). This model allows for clustered action potential firing to be controlled, making it a suitable model to study the role of dorsoventral gradients in clustering. It is thereby proposed that alterations to AHP or I_{h} conductances could mediate the quantitative changes in clustering observed experimentally. In experimental models of dementia (rTg4510), loss of clustered firing is found to correlate with significant changes to AHP amplitude (Booth et al. (2016a); Figure 2.1) but no change in I_h mediated sag (Booth et al., 2016a). Hence our results suggest a possible path through parameter space that account for the differences in patterned firing in rTg4510.

2.2 Materials and methods

2.2.1 Mathematical model

The stochastically gated Markov Chain model of layer II medial entorhinal cortex stellate cells (mEC-SCs) presented by Dudman and Nolan (2009) was converted to a system of stochastic differential equations (SDEs) in the Hodgkin-Huxley formulation (Hodgkin and Huxley (1952); section 1.5). For a given ion channel, Markov Chain models calculate the voltage dependent probability of a closed gate opening, $\alpha(V)$, and an open gate closing, $\beta(V)$ in order to estimate the fraction of gates open at a given time. Under the assumption that the number of ion channels is sufficiently high, we can make a density approximation; i.e. the fraction of gates open is equal to the probability of gates being open, and hence we can write the equations for the gating variables in the form of Equation 1.16. The presence of noisy fluctuations in the dynamics due to the intrinsic stochastic channel gating are not modelled explicitly, but approximated through the addition of extrinsic additive noise on the membrane potential.

The membrane potential is given by

$$C\frac{dV}{dt} = I_\text{app} - I_\text{NaT} - I_\text{NaP} - I_\text{Kdr} - I_\text{Kaf} - I_\text{Kas} - I_\text{h} - I_\text{AHP} - I_\text{L} + \sigma\eta(t) \tag{2.1}$$

where the term $\sigma\eta(t)$ is the extrinsic noise term, where σ is the noise variance and $\langle\eta(t)\rangle = 0$ and $\langle\eta(t), \eta(t')\rangle = \delta(t - t')$. Each ionic current is written in the form of Equation 1.13. The fraction of open gates for each channel is given by

$$\begin{aligned} \psi_\text{NaT} &= m_\text{NaT}^3 h_\text{NaT}, & \psi_\text{NaP} &= m_\text{NaP} h_\text{NaP} \\ \psi_\text{Kdr} &= n_\text{Kdr}^4, & \psi_\text{Kaf} &= m_\text{Kaf} h_\text{Kaf} \\ \psi_\text{Kas} &= m_\text{Kas} h_\text{Kas}, & \psi_\text{h} &= n_\text{h} \\ \psi_\text{AHP} &= n_\text{AHP}^3, & \psi_\text{L} &= 1, \end{aligned} \tag{2.2}$$

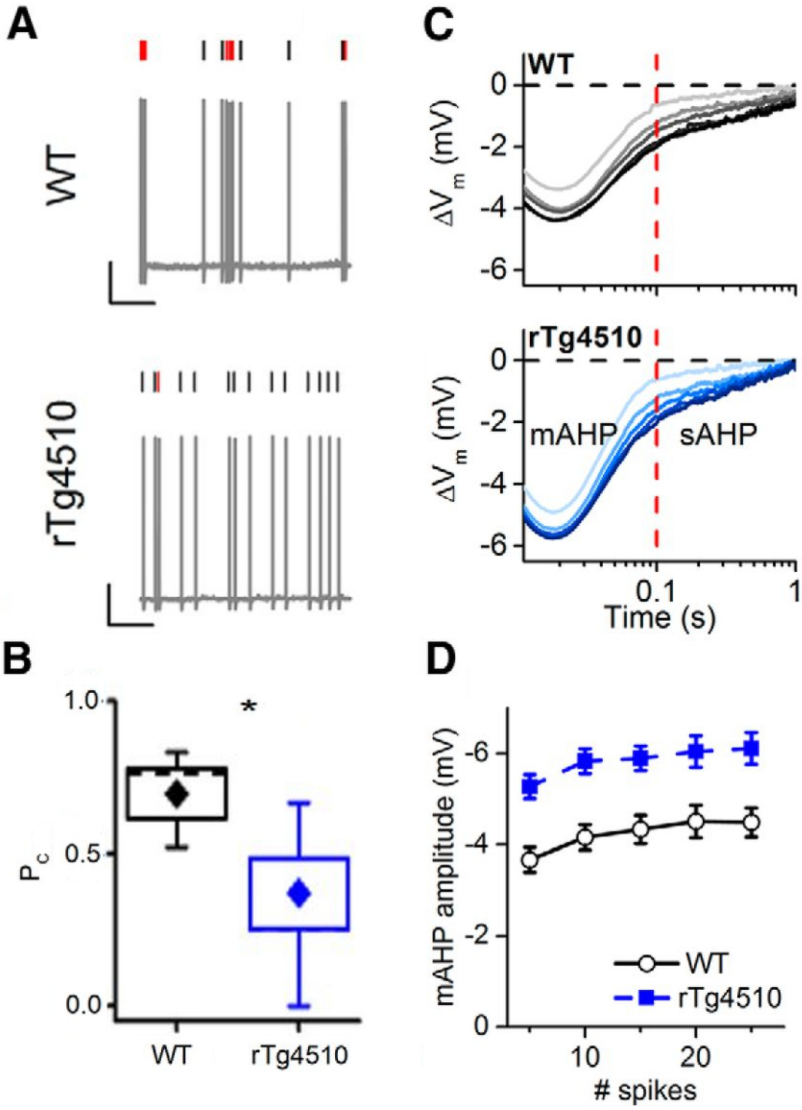

Figure 2.1: P_C **and AHP amplitude are altered in dorsal mEC-SCs**. Figure reproduced and modified from (Booth et al., 2016a) under the CC-BY 4.0 licence. (A) Example recordings of WT and rTg4510 dorsal mEC-SCs and raster plots, with clustered spikes appearing red in the raster plot. Calibration: 20 mV, 2 s. (B) Boxplots of P_C (see Figure 2.2) in WT and rTg4510 dorsal mEC-SCs demonstrate that rTg4510 cells were significantly less likely to fire APs in clusters. (C) Average AHP waveforms in dorsal mEC-SCs elicited by a train of 5, 10, 15, 20, and 25 (light through to dark colours respectively) depolarising current injections. Note that the AHP studied in this chapter is the medium AHP (mAHP), whilst this figure additionally shows the slow AHP (sAHP). (D) mAHP amplitude in dorsal mEC-SCs was significantly increased in rTg4510 animals for 5-25 depolarising current injections (all values tested).

with gating functions

$$
\begin{aligned}
\alpha_{m_{\text{NaT}}} &= \frac{0.38(V+33)}{1-e^{\frac{V+33}{9}}}, & \beta_{m_{\text{NaT}}} &= \frac{-2.3(V+58)}{1-e^{\frac{V+58}{12}}} \\
\alpha_{h_{\text{NaT}}} &= \frac{-0.03(V+48)}{1-e^{\frac{V+48}{12}}}, & \beta_{h_{\text{NaT}}} &= \frac{0.05(V+21)}{1-e^{\frac{V+21}{9}}} \\
\alpha_{m_{\text{NaP}}} &= \frac{1.6*10^{-4}(0.38(V+64.409))}{1-e^{-0.38023(V+64.409)}}, & \beta_{h_{\text{NaP}}} &= \frac{1.2*10^{-4}(-0.216(V+17.014))}{1-e^{0.21598(V+17.014)}} \\
\alpha_{h_{\text{NaP}}} &= \frac{1.5}{1+e^{\frac{-42.1-V}{3}}}, & \beta_{m_{\text{NaP}}} &= \frac{1}{1+e^{\frac{42.1-V}{3}}} \\
\alpha_{n_{\text{Kdr}}} &= \frac{0.02(V+38)}{1-e^{\frac{V+38}{10}}}, & \beta_{n_{\text{Kdr}}} &= \frac{-0.018(V+47)}{1-e^{\frac{V+47}{35}}} \\
\alpha_{m_{\text{Kaf}}} &= \frac{0.01(V+18.3)}{1-e^{-0.067(V+18.3)}}, & \beta_{m_{\text{Kaf}}} &= \frac{-0.01(V+18.3)}{1-e^{0.067(V+18.3)}} \\
\alpha_{h_{\text{Kaf}}} &= \frac{-0.01(V+58)}{1-e^{0.122(V+58)}}, & \beta_{h_{\text{Kaf}}} &= \frac{0.01(V+58)}{1-e^{-0.122(V+58)}} \\
\alpha_{m_{\text{Kas}}} &= \frac{0.001(V+18.3)}{1-e^{-0.067(V+18.3)}}, & \beta_{m_{\text{Kas}}} &= \frac{-0.001(V+18.3)}{1-e^{0.067(V+18.3)}} \\
\alpha_{h_{\text{Kas}}} &= \frac{-6.7*10^{-5}(V+58)}{1-e^{0.122(V+58)}}, & \beta_{h_{\text{Kas}}} &= \frac{-6.7*10^{-5}(V+58)}{1-e^{-0.122(V+58)}} \\
\alpha_{n_{\text{h}}} &= \frac{18.3*10^{-3}}{1+e^{\frac{V+114.2}{20.33}}}, & \beta_{n_{\text{h}}} &= \frac{3.3*10^{-2}}{1+e^{\frac{V+51.5}{10.94}}} \\
\alpha_{n_{\text{AHP}}} &= 1.5e^{\frac{-(t-t_{\text{spike}})}{25}}, & \beta_{n_{\text{AHP}}} &= 1.6
\end{aligned}
\tag{2.3}
$$

All equations are adapted from Dudman and Nolan (2009).

The transient sodium (NaT) and potassium delay rectifier (Kdr) are those of the classic Hodgkin-Huxley model and mediate action potential initiation and recovery respectively. Also included in the model are a persistent sodium (NaP) current, fast and slow potassium A-type currents (Kaf and Kas respectively), an Ohmic leak (L), and an inward hyperpolarisation activated (h) current.

Furthermore, a phenomenological spike-dependent outward after hyperpolarisation (AHP) current is included in the model. This current is modelled with $\alpha(V) = 1.5\exp(-(t - t_{\text{spike}})/\tau)$ and $\beta = 1.6$. Here, t_{spike} is the time of the last spike (defined as membrane potential rising through 0mV) and $\tau = 60$ such that the AHP lasts approximately 100ms (Booth et al., 2016a).

Noise variance was selected as follows. Having fixed all parameters but those being studied (g_{h} and g_{AHP}), these remaining two free parameters of the deterministic system were chosen such that the inter-spike interval of the model reflected experimental results (Booth et al., 2016a) ($g_{\text{h}} = 2.8$, $g_{\text{AHP}} = 0.425$). The system was simulated for a range of noise values to identify plausible values with realistic clustering dynamics as quantified by P_C (Nolan et al., 2007) (see Figure 2.2 and 2.3, and description below). This yielded a value of $\sigma = 0.197\mu A \cdot$ cm^{-2}, or equivalently $\sigma/C = 0.135$ mV·ms^{-1}. This value was used in all stochastic simulations

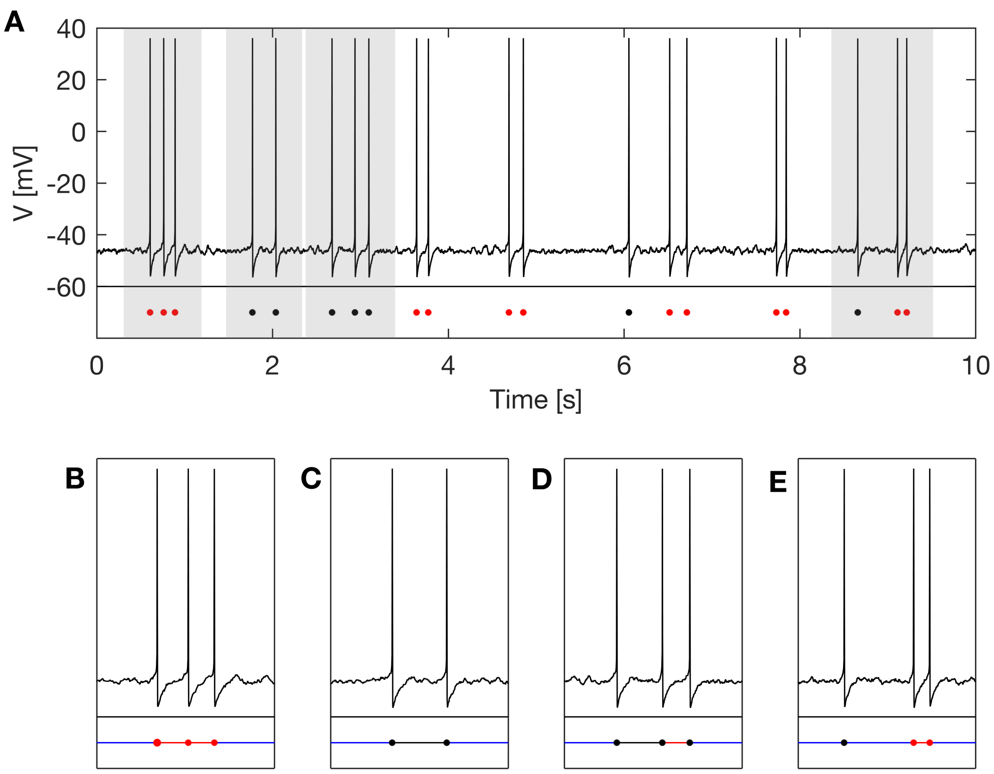

Figure 2.2: **Calculation of P_C.** (A) Example 10s simulation with raster plot of spikes (below), defined as the point at which $V = 0$ and $dV/dt > 0$. Spikes marked in red are classified as clustered spikes, whilst spikes marked in black are not clustered. Clusters are defined as two or more spikes with an ISI of < 250ms and preceeded and followed by quiescent periods of > 300ms. P_C is calculated as the ratio of clustered spikes to total number of spikes; in this example $P_C = 13/20 = 0.65$. (B-E) Shaded grey regions in A. In the raster plots below the traces, red dots are clustered spikes and black dots are non-clustered spikes. Blue lines represent epochs of > 300ms, black lines are epochs of < 300ms but > 250ms, and red lines are epochs of < 250ms. (B) Three clustered spikes. (C) Non-clustered spikes due to an ISI of > 250ms (black line in raster plot) excluding them from being classed as a cluster. (D) Non-clustered spikes since the ISI of the first and second spike is > 250ms and < 300ms. The second and third spike cannot constitute a cluster of two spikes since they are not preceeded by a period of > 300ms. (E) One sporadic spike and a cluster of two spikes. The first spike is classified as sporadic, but because the 2nd and 3rd spikes are now both preceeded and followed by a quiescent period of > 300ms, they constitute a cluster of two spikes. All time series shown here are simulations; for comparison purposes, examples of real data showing clustered AP firing are shown in Figure 2.1A.

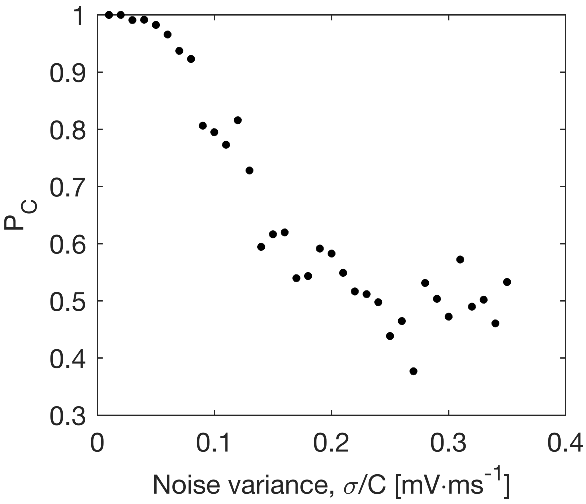

Figure 2.3: **Effect of noise variance on P_C.** Variance of noise σ/C in mV·ms^{-1} against P_C for the $(g_\text{h}, g_\text{AHP}) = (2.8, 0.425)$ regime. P_C in the experimental data for the WT animals was found to be 0.69, so noise variance was chosen to be 0.135 mV·ms^{-1}.

unless stated otherwise.

Simulations use the stochastic Heun method with a time step of 0.01ms. Parameters are those given in Table 2.1 unless stated otherwise. For spectral analyses, the multitapered power spectrum was calculated using the CHRONUX toolbox (`http://chronux.org/`, Mitra and Bokil (2008)) with 9 tapers and time-bandwidth product of 5.

Parameter	Value	Parameter	Value
C	1.46 μF·cm^{-2}	g_NaT	24 mS·cm^{-2}
I_app	0.3 μA·cm^{-2}	g_NaP	0.075 mS·cm^{-2}
E_Na	55 mV	g_Kdr	11 mS·cm^{-2}
E_K	-85 mV	g_Kaf	0.1 mS·cm^{-2}
E_h	-30 mV	g_Kas	0.5 mS·cm^{-2}
E_L	-88.5 mV	g_L	0.15 mS·cm^{-2}

Table 2.1: Parameters used in the stellate cell model

A cluster of action potentials is defined as two or more spikes with an inter-spike interval of < 250ms, preceeded and followed by a quiescent period of > 300ms. Clustering is quantified by P_C, which is the ratio of spikes defined to be within a cluster to total number of spikes (Nolan et al., 2007). Calculation of P_C is demonstrated in Figure 2.2.

2.2.2 Bifurcation analysis

In order to understand the underlying dynamics, the ordinary differential equation (ODE) formalism is given by the above system with $\sigma = 0$ in Equation 2.1. This ODE formalism allows for a bifurcation analysis of the system. To conduct the bifurcation analysis, a number of methods were used. Equilibria were found using either XPPAUT (Ermentrout, 2002) or Matlab's fsolve functions in a reduced system with no AHP current. This reduction is made since the AHP current is spike dependent and decays to zero in the absence of spikes.

Periodic orbits in the full model with AHP could not be analysed in XPPAUT due to the non-smooth nature of the AHP current. Instead, the Poincaré return map on the Poincaré section at $V = 0$ (at which non-smoothness due to the AHP current arises) was identified using Matlab. For tonic spiking, high precision numerical solutions were found using a boundary value solver in Matlab. Due to the high dimensionality and complexity of the model, for doublets and other multiplets this could not be implemented. Instead solutions were found using Matlab's ode45 (with tolerances set to 10^{-12}) with high precision event detection, and the return map identified using Picard iterations; i.e. for each crossing of the Poincaré section, the Euclidian distance to all past crossing of the Poincaré section was calculated and a periodic orbit identified as this distance being less than 10^{-12}. The Jacobian of the map was constructed by calculating Fréchet derivatives, and eigenvalues of the Jacobian used to assess stability and identify bifurcations in the map. Lyapunov exponents of the Poincaré return map were calculated to identify chaotic regimes (Sprott, 2003), where a negative maximum Lyapunov exponent (MLE_{map}) represents a steady state on the map (corresponding to a stable limit cycle in the flow) and a positive MLE_{map} represents a chaotic regime.

2.3 Results

2.3.1 Identifying parameter regimes of clustered firing

A number of experimental and modelling studies implicate the after hyperpolarisation (AHP) and hyperpolarisation activated current (I_{h}) in playing a role in clustered action potential firing (Booth et al., 2016a; Nolan et al., 2007; Dudman and Nolan, 2009; Fransén et al., 2004). Motivated by these studies, the effect of the AHP and h-current conductances (g_{AHP} and g_{h} respectively) on clustering was studied in our model.

To do so, we simulated 10 model neurons for 20s over a range of values of g_{AHP} and g_{h}. P_C, which quantifies the proportion of clustered firing (see section 2.2 and Figure 2.2), was calculated for each parameter set. A summary of our results depicted as a heatmap of P_C values and illustrated via exemplar membrane potential traces is shown in Figure 2.4A-B. For low values of g_{h}, the model cells only fire sporadic action potentials due to noise occasionally bringing the membrane potential above threshold (dark blue regions in Figure 2.4A). For very low g_{AHP}, as g_{h} is increased the system moves into a regime of tonic firing (yellow region in

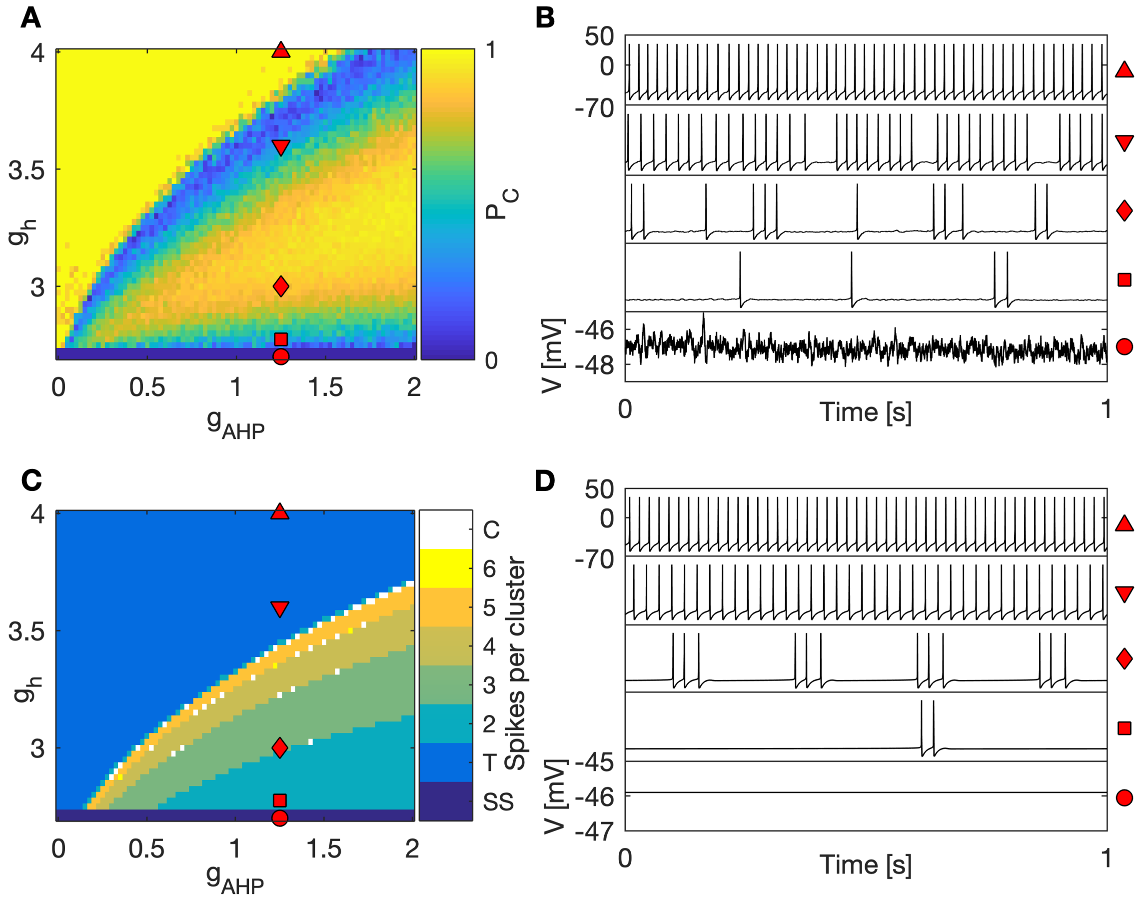

Figure 2.4: **Clustered parameter regimes in two parameter space.** (A) Heatmap of P_C over a range of values of g_{AHP} and g_{h}. Points marked by red shapes correspond to the time series in B. (B) Time series demonstrating exemplar simulated cells for the regimes marked in A. The red shapes to the right of the time series correspond to the location in parameter space in A. (C) Heatmap of spikes per cluster in the underlying deterministic system. In the colourbar, ‘SS’ refers to a steady state, ‘T’ refers to tonic firing, and ‘C’ refers to chaotic/irregular firing and integers indicate number of spikes per cluster. (D) Time series demonstrating the deterministic dynamics underlying the stochastic traces in B. The red shapes to the right of the time series correspond to the location in parameter space in C.

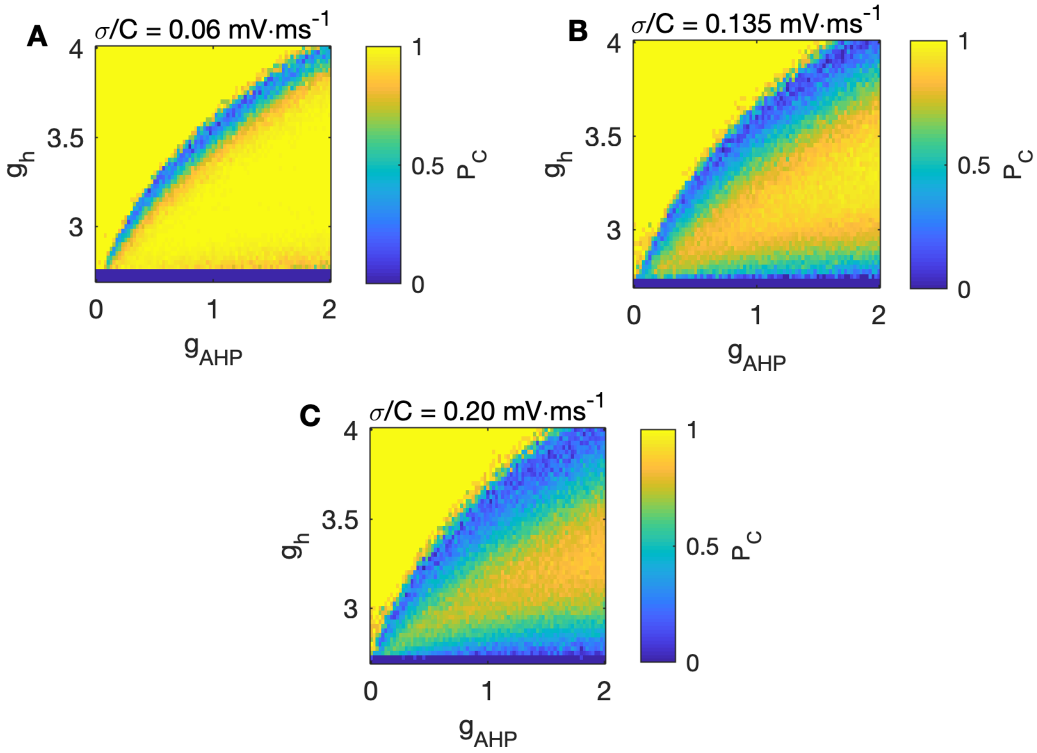

Figure 2.5: **Effect of noise variance on P_C heatmaps**. Two parameter sweeps showing P_C for g_{AHP} vs g_{h}, for different noise values. Whilst the tonic and steady state regimes (in the underlying deterministic system) are largely unaffected by changing noise, in a clustering regime noise has the affect of adding more sporadic spikes and hence scaling PC . The general pattern of PC values in the sweep remains the same.

Figure 2.4A). For intermediate values of g_{AHP}, as g_{h} is increased clustered parameter regimes occur (orange regions in Figure 2.4A) . For values of g_{AHP} sufficiently high for clustering to occur, as g_{h} is increased the system moves from very low P_C towards a peak at $P_C \approx 0.8$, and then back down to lower P_C (Figure 2.4A). Therefore, spontaneous activity in the model arises due to a combination of noise and the applied current. Time courses associated with these values can be seen in Figure 2.4B. For these simulations, noise variance was set to $\sigma/C = 0.135$ mV·ms^{-1} (see section 2.2). Figure 2.5 demonstrates that these results are robust to different values of noise, with noise values scaling P_C in the clustered regimes. The effect of noise on P_C for a single parameter regime is shown in Figure 2.3.

In order to understand these dynamics, the deterministic system was also simulated over the same range of parameters. A heatmap representing the number of spikes per cluster and exemplar membrane potential traces are plotted in Figure 2.4C-D. To directly compare the dynamics of the determinstic system to the stochastic system, in Figure 2.6 we present the heatmap of the deterministic system juxtaposed with heatmaps for the stochastic system at three different levels

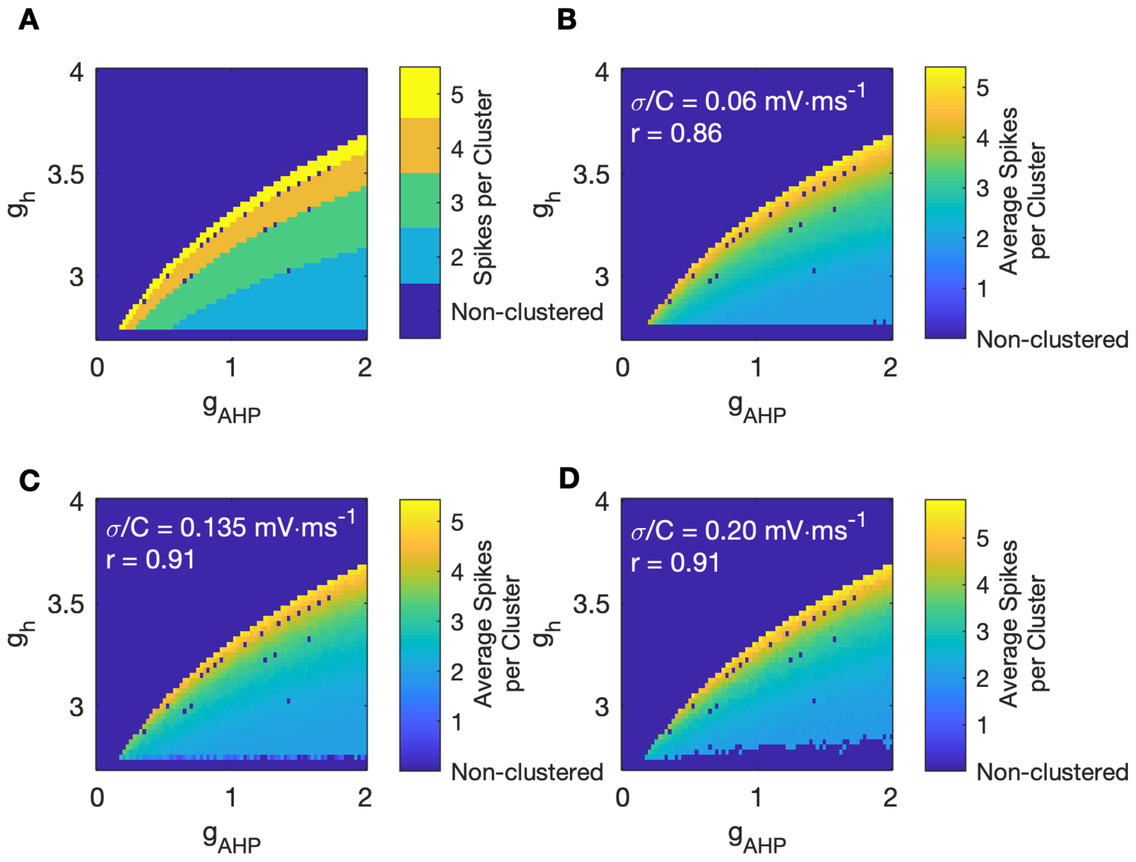

Figure 2.6: **Spikes per cluster in the stochastic system is correlated with spikes per cluster in the deterministic system**. (A) For comparison with B-D, spikes per cluster in the clustering regimes of the deterministic model (previously shown in Figure 2.4C) are shown. Dark blue regions represent either tonic firing, steady state, or chaotic regimes and are not included in the analysis. (B-D) Mean number of spikes per cluster in the stochastic system with three different levels of noise. Only clustered spikes were included (sporadic spikes ignored) in calculation. Text shows the noise level and correlation of number of spikes per cluster over the parameter sweep between each system and the deterministic system.

of noise variance. It can be seen in Figure 2.6 that the heatmaps for the determinstic and stochastic system appear qualitatively similar in terms of the number of spikes per cluster (similar positioning of coloured regions in the heatmaps). In order to quantify this similarity we calculated the Pearson's correlation between the number of spikes per cluster in the simulations of the determinstic system with the average number of spikes per cluster in the stochastic system. These values, which are indicated in the left hand corner of panels B-D of Figure 2.6, were above 0.86, suggesting that an understanding of the deterministic clustering dynamics can be informative for understanding the clustering dynamics of the stochastic system.

A two-parameter bifurcation analysis was performed over g_{h} and g_{AHP} (Figure 2.7). For low values of g_{h}, the deterministic system is in a stable steady state.

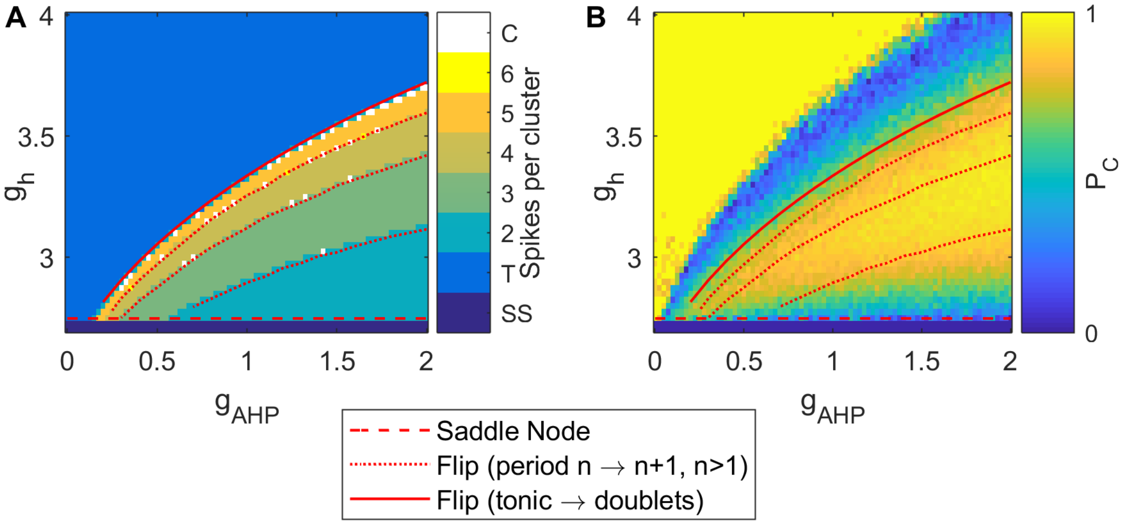

Figure 2.7: **Bifurcations in two parameter space.** (A) The heatmaps from Figure 2.4C is overlayed with lines indicating locations of bifurcations in the determinsitic system as g_{AHP} and g_{h} are varied. The dashed red line represents the location of a saddle node bifurcation. Dotted red lines show flip bifurcations that move the system from a period n to a period $n+1$ orbit, for $n>1$. The solid red line shows a flip bifurcation that moves the system from tonic firing to period 2 firing, before transitioning into a period adding cascade. (B) The same bifurcations are overlayed on the P_C heatmap of Figure 2.4A to enable a visualisation of the behaviour of the stochastic system relative to the bifurcations in the deterministic system.

This corresponds to the region of subthreshold sporadic excitability that generates occasional spiking in the stochastic system. As g_{h} is increased, a homoclinic bifurcation occurs at $g_{\mathrm{h}}^{\mathrm{HC}}=2.5477$, resulting in bistability between the steady state and a periodic orbit (not shown in Figure 2.7). This periodic orbit may be either period 1 (corresponding to tonic action potentials) or period >1 (corresponsing to clustering in the stochastic system) depending on g_{AHP}. As g_{h} is increased further to $g_{\mathrm{h}}^{\mathrm{SN}}=2.7484$, the stable steady state collides with an unstable steady state in a saddle node bifurcation, resulting in periodic solutions corresponding to action potential firing being the only stable solutions. The location of the saddle node and homoclinic bifurcations are independent of g_{AHP}. The saddle node bifurcation $g_{\mathrm{h}}^{\mathrm{SN}}$ is indicated by a dashed red line in two parameter space in Figure 2.7.

For $g_{\mathrm{h}}>g_{\mathrm{h}}^{\mathrm{SN}}$, only a stable periodic orbit exists, generated by the homoclinic bifurcation at $g_{\mathrm{h}}^{\mathrm{HC}}$. Orbits with a range of number of spikes per period can be found beyond this bifurcation. Period 1 orbits correspond to tonic action potentials, whilst period >1 orbits correspond to firing in multiplets, i.e. bursting. By comparing Figure 2.7A and B, one can observe that the regimes of period >1 in the deterministic system correspond to clustered action potential firing in the stochastic system. The transitions between orbits of different periods (eg. from period 2 doublets to period 3 triplets) occur via flip bifurcations (Channell et al. (2007); Barrio and Shilnikov (2011); section 1.4.6), drawn in Figure 2.7 by dot-

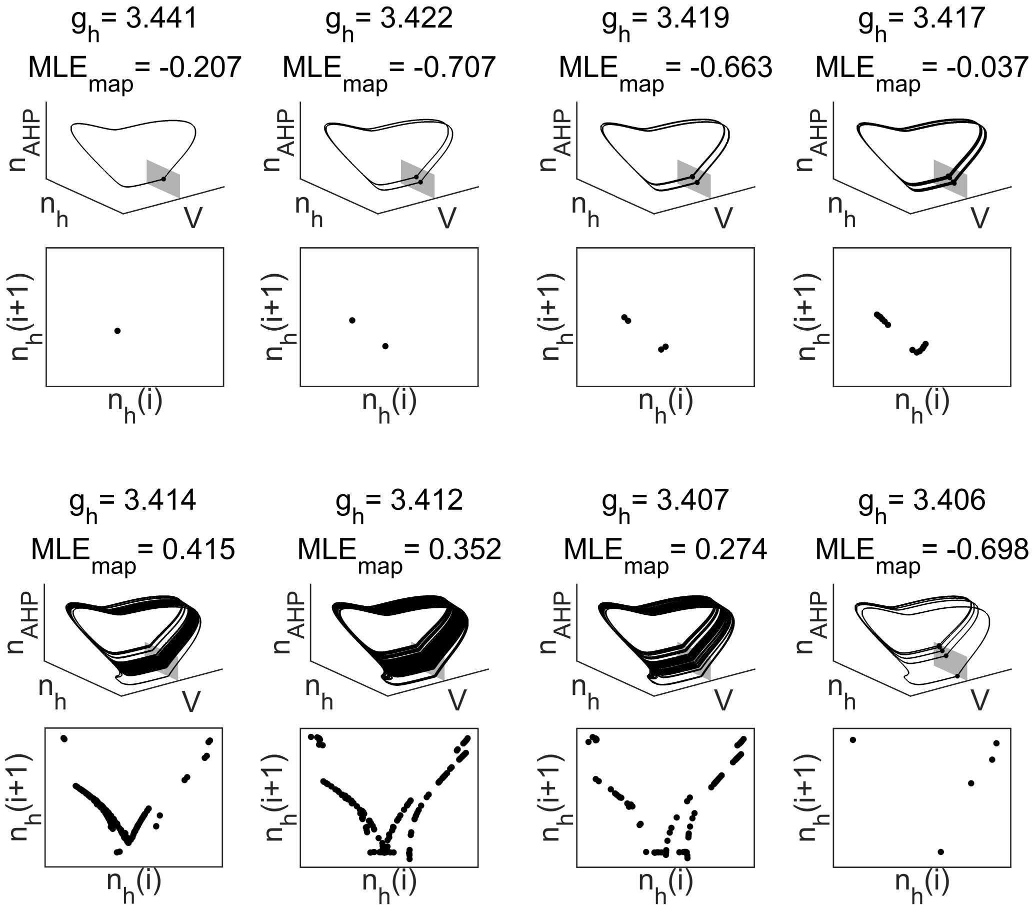

Figure 2.8: **Transition from tonic firing to period 5 bursting.** Each column represents a different parameter value as g_{h} is decreased. For all simulations, $g_{\text{AHP}} = 1.2$ and all other parameters are those in Table 2.1. Numbers shown at the top of each column are value of g_{h} and maximum Lyapunov exponent on the map (MLE$_{\text{map}}$). MLE$_{\text{map}}$ > 0 indicates chaos. For each parameter value, the top row demonstrates the flow in the $(V, n_{\text{h}}, n_{\text{AHP}})$ subspace about the Poincaré section $V = 0$ (shaded in grey) and the bottom row is the Poincaré return map for n_{h}. For the chaotic regimes, the system was simulated for 30 seconds to reach the attractor and then a further 30 seconds of simulations are shown. From a tonic regime, as g_{h} is decreased the system undergoes a flip cascade into chaos before transitioning into a period 5 (bursting) orbit.

ted red lines. The transition between period 1 oribits (tonic spiking) and orbits with period > 1 (bursting) is indicated by a solid red line in Figure 2.7. Seen in terms of decreasing values of g_{h}, the bifurcation underlying this transition is a flip bifurcation of the period 1 orbit into period 2 regime. As g_{h} is decreased further, the system undergoes a flip or spike adding cascade into chaotic dynamics, before a stable period 5 orbit is established. Poincaré return maps and Lyapunov exponents demonstrating an example of this transition are shown in Figure 2.8.

Moving beyond this bifurcation to high values of g_{h} and low values of g_{AHP} yields $P_C \approx 1$ in the stochastic system. This observation could be explained by a highly stable periodic orbit and therefore diminished effects of noise. However, in this case a high value of clustering arises due to the way P_C is calculated, essen-

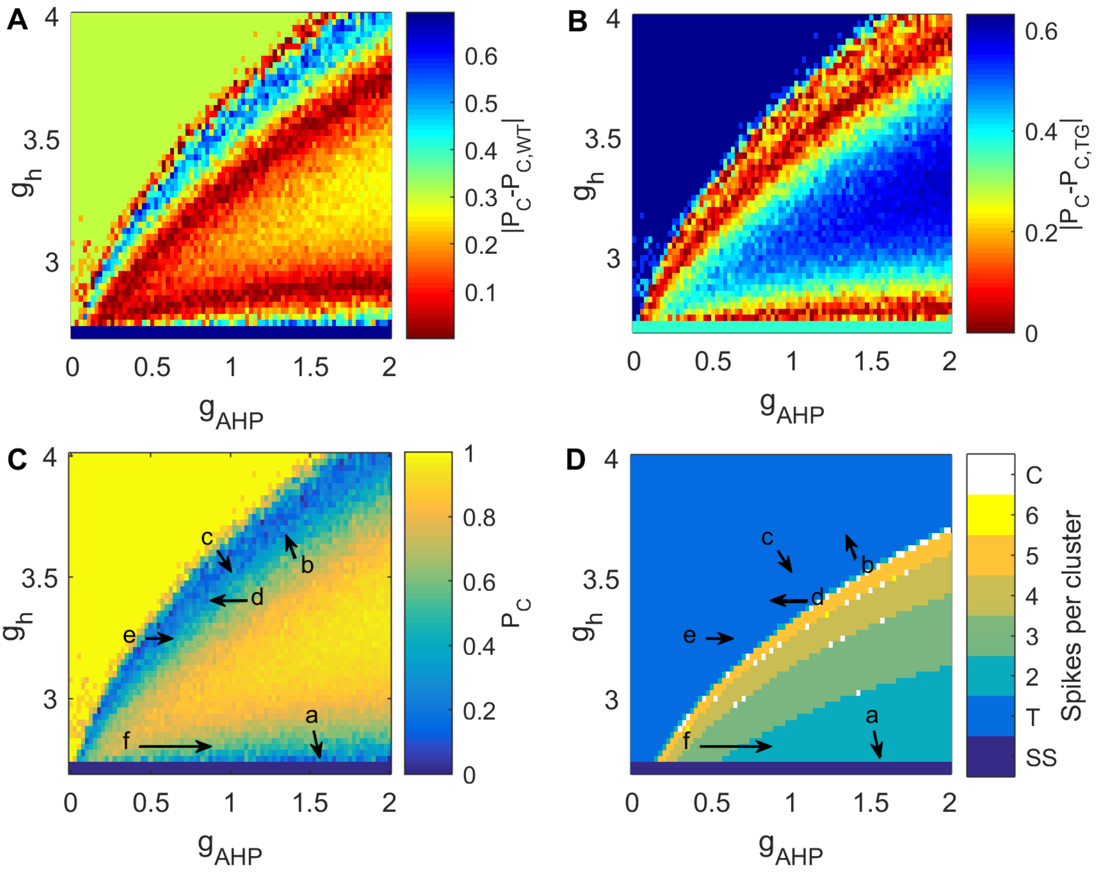

Figure 2.9: **Paths through parameter space that can result in reduced clustering observed in the rTg4510 model of dementia** (A) Heatmap of $|P_C - P_{C,WT}|$, where $P_{C,WT} = 0.69$ is the mean value of clustering seen in dorsal mEC-SCs in wild type animals (Booth et al., 2016a). Red indicates regions in which P_C of the model is close to $P_{C,WT}$, whereas blue indicates regions where the model is farthest from $P_{C,WT}$. (B) Heatmap of $|P_C - P_{C,TG}|$, where $P_{C,TG} = 0.37$ is the mean value of clustering seen in dorsal mEC-SCs in rTg4510 transgenic (i.e. dementia) animals (Booth et al., 2016a). (C) The heatmap of Figure 2.4A is overlayed with arrows indicating potential paths through the $(g_{\text{AHP}}, g_{\text{h}})$ parameter space that could lead to the changes in P_C obsvered in the rTg4510 experimental model. (D) The heatmap of Figure 2.4C is overlayed with arrows indicating potential paths through the $(g_{\text{AHP}}, g_{\text{h}})$ parameter space that could lead to the changes in P_C obsvered in the rTg4510 experimental model.

tially tonic firing with an ISI < 250ms is classified as a single cluster (Figure 2.2). As the flip bifurcation is approached from above and left, the orbit becomes less stable allowing noisy perturbations to cause deviations away from individual action potentials. This induces quiescent intervals that become large enough to fall in the range $[250, 300]$ms, thus causing the P_C value to drop substantially in magnitude, giving rise to the light blue upper region of low P_C in Figure 2.4A.

Experimental observations have shown dorsal P_C to be approximately 0.69 in healthy animals and approximately 0.37 in rTg4510 transgenic animals (Booth et al. (2016a); Figure 2.1B). We used these values to define possible paths through parameter space that may account for differences observed in rTg4510 (Figure 2.9). Given that experimental recordings found no differences in I_{h} but found differences in AHP amplitude (Booth et al. (2016a); Figure 2.1C-D), paths E and F in Figure 2.9C-D are the most likely changes in parameter space occuring in rTg4510. The dynamics of path F recreate firing patterns seen in data most realistically, since firing frequency in parameter sets in path E is much higher than in data (Booth et al., 2016a). This could be explained by the fact that in path E, clustering arises due to noise cancelling action potentials in a tonic firing regime, as opposed to underlying dynamics causing clustered firing. Path F suggests that the underlying noise-free system is undergoing a flip bifurcation from period 3 bursts to period 2 bursts, resulting in the reduced clustering seen in rTg4510.

2.3.2 Fast-slow analysis of deterministic clustering

The analysis above suggests that clustered firing patterns may arise due to noise perturbations to a periodic bursting regime. In order to further understand these dynamics, a fast-slow analysis was performed on the deterministic system within this regime. We chose parameters to be $g_{\text{AHP}} = 0.425$ and $g_{\text{h}} = 2.8$, which results in periodic bursts of three action potentials. We first examined simulations, which revealed two variables operating with a slow time scale, namely m_{NaP} and h_{Kas} (Figure 2.10A). Keeping the two slow variables fixed, the remaining (fast) subsystem was subjected to a numerical bifurcation analysis, which revealed two bifurcations of importance for describing the bursting dynamics (see Figure 2.10B). For low values of m_{NaP}, there exists a stable steady state which loses stability via a subcritical Hopf bifurcation (denoted SCH1) as m_{NaP} is increased (marked by a dashed red line in Figure 2.10B). For high values of m_{NaP} there exists a stable periodic orbit of period 1, which disappears via a homoclinic bifurcation (denoted HC1 and marked by a dotted red line in Figure 2.10B) as m_{NaP} is decreased. Between these two bifurcations there is a region of bistability between the steady state and the periodic orbit. These bifurcations in m_{NaP} are drawn over a range of values of h_{Kas} in Figure 2.10B. A full bifurcation diagram and example bistable region for m_{NaP} for $h_{\text{Kas}} = 0.19$ is shown in Figure 2.11.

Plotting the periodic solution of the full subsystem in the two variables (m_{NaP} and h_{Kas}, Figure 2.10B) is sufficient to describe the bursting dynamics. The trajectory follows a hysteresis loop through the fast subsystem. Beginning in the quiescent period between bursts, the two slow variables will be at a position in phase space such that the fast subsystem is on the steady state branch. The periodic solution's trajectory then moves along the steady state branch until SCH1 is reached, at which point the fast subsystem moves to the periodic orbit branch. This initiates the burst, with action potentials firing while slow variables move along the periodic orbit branch towards HC1. Once HC1 is reached, the burst

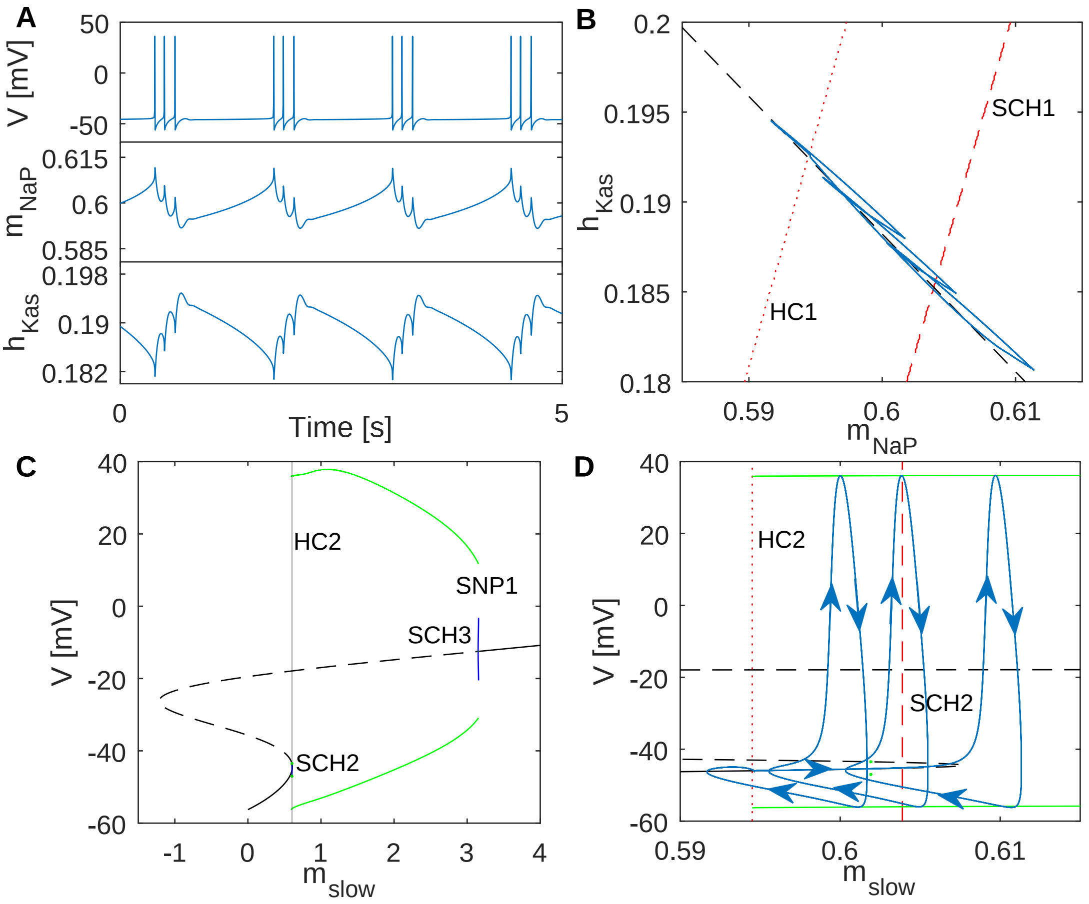

Figure 2.10: **Fast-slow analysis of deterministic bursting** (A) Membrane potential (top) and slow variables (m_{NaP}, middle and h_{Kas}, bottom) through four cycles of bursting in the deterministic system. (B) Bifurcations in the fast subsystem overlayed on the model trajectory in the $(m_{\text{NaP}}, h_{\text{Kas}})$ plane. The red dashed line indicates a subcritical Hopf bifurcation (SCH1), whereas the dotted red line indicates a homoclinic bifurcation (HC1). The black dashed line shows the linear model that combines h_{Kas} and m_{NaP} into a single slow variable, m_{slow}. (C) Bifurcation analysis of the fast subsystem of the model using m_{slow} as a bifurcation parameter. A stable equilibrium (solid black line) is shown to lose stability (dashed black line) via a subcritical Hopf bifurcation (SCH2). The stable periodic orbit (solid green line) disappears in a homoclinic bifurcation (HC2). A region of bistability exists (shaded region, zoomed in panel D). See text for a description of the remaning bifurcations. (D) A close up of the bifurcations occuring in the region of bistability shown in grey in panel C. The blue line indicates a trajectory of the full system through a single period of bursting, with arrows indicating the direction of time. Dashed and dotted red lines correspond to the bifurcations of the fast subsytem introduced in panel B.

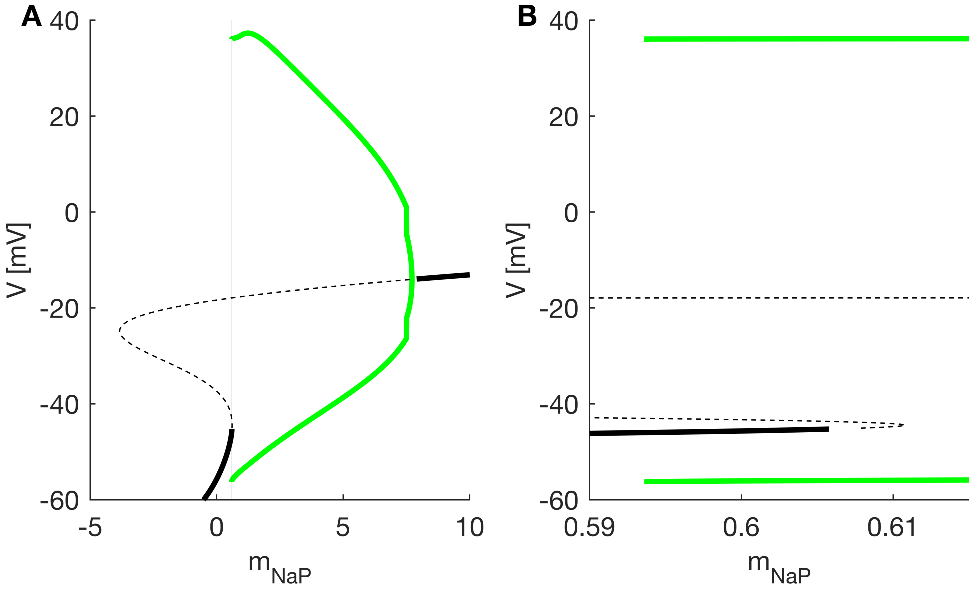

Figure 2.11: **Bifurcation diagram for m_{NaP} for a single value of h_{Kas}** (A) Full bifurcation diagram of the fast subsystem whilst $h_{\text{Kas}} = 0.19$. (B) Zoom in on the bistable region of A (shaded in grey) to demonstrate HC1 homoclinic and SCH1 subcritical Hopf bifurcations.

ends as the fast subsystem returns to the steady state branch.

Figure 2.10B suggests that the slow system can be reduced to a single slow variable m_{slow} with the approximation $m_{\text{NaP}} = m_{\text{slow}}$ and $h_{\text{Kas}} = -0.7657m_{\text{slow}} + 0.6477$. This linear approximation of the two slow variables is shown in Figure 2.10B. The full bifurcation diagram for the fast subsystem as m_{slow} is varied is shown in Figure 2.10C. As before, the stable steady state is lost via subcritical Hopf bifurcation (SCH2), and the stable periodic orbit is lost via homoclinic bifurcation (HC2). Figure 2.10C shows the remaining bifurcations. The unstable periodic orbit generated by SCH2 is lost via a homoclinic (HC3). The unstable steady state following SCH2 becomes stable via another subcritical Hopf (SCH3). The unstable periodic orbit generated by SCH3 collides with the stable periodic orbit generated in HC2 and both periodic orbits disappear via a saddle node of periodics (SNP1). As in the case of the two dimensional slow subsystem, there is bistability between the stable equilibrium and the stable periodic orbit (Figure 2.10D) resulting in traditional fast-slow hysteresis loop bursting. The trajectory of a single burst is shown in Figure 2.10D.

2.3.3 Subthreshold dynamics

In order to validate the model, we tested whether it reproduced experimental results that were not used in the development of the model; i.e. when choosing parameter regimes that allow for mEC-SC-like clustering dynamics. Subthreshold oscillations in the theta (4-12 Hz) range are another key electrophysiological

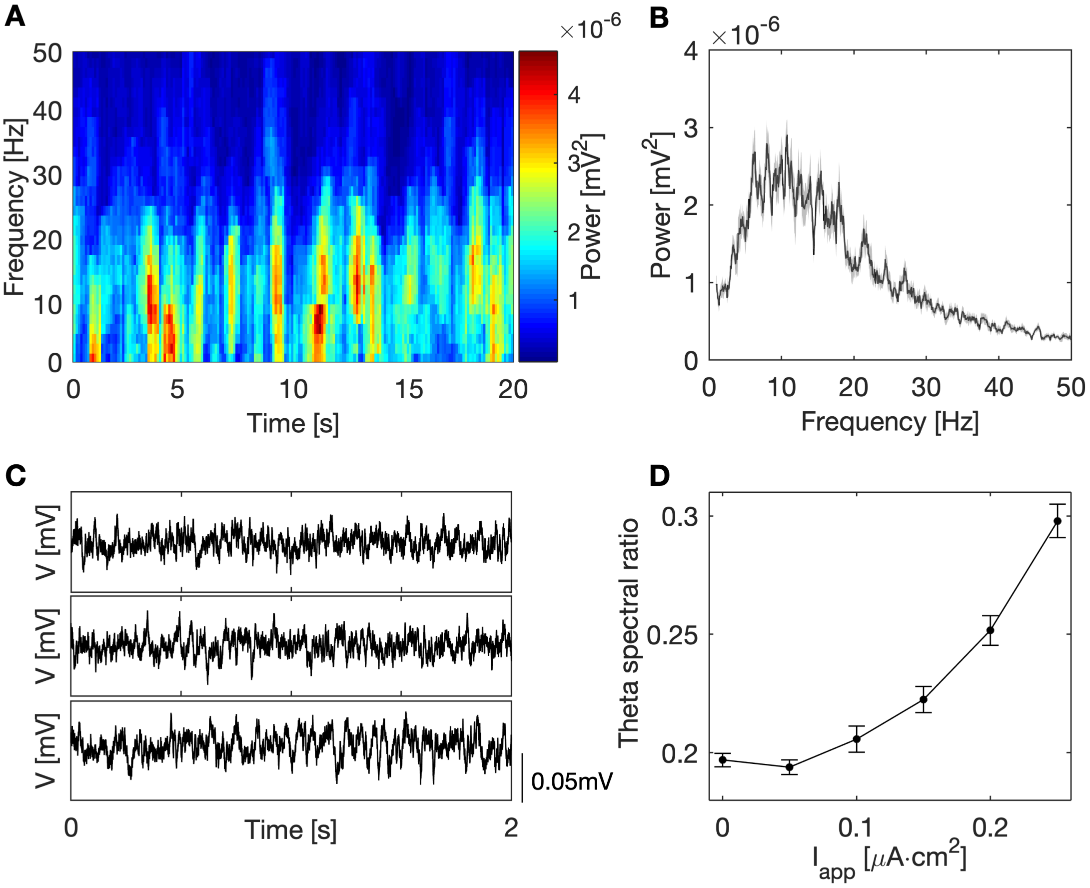

Figure 2.12: **Analysis of subthreshold dynamics** (A) Spectrogram of exemplar 20 second subthreshold simulations. (B) Power spectrum of 20s simulations (averaged over 10 cells). The shaded region shows standard error. (C) Exemplar simulations with $I_{\text{app}} = 0.05\mu$A·cm^{-2} (top), 0.15μA·cm^{-2} (middle), and 0.25μA·cm^{-2} (bottom). Vertical and horizontal scales are consistent for all values of I_{app}. (D) Theta spectral ratio, defined as the ratio of total theta power to total broadband (1-300 Hz) power, plotted as a function of I_{app}.

feature of mEC-SCs, so in this section we explore whether theta band subthreshold activity appears in the model.

The bottom trace of Figure 2.4B demonstrates the noise driven response of the model in its subthreshold regime. mEC-SCs have been shown to generate subthreshold membrane potential fluctuations with dominant frequencies in the theta band (Alonso and Klink, 1993). We therefore quantified the power spectrum of dynamics generated by our noise driven system. The stochastic system, with parameters chosen as in section 2.3.2, I_{app} set below action potential threshold (0.25μA·cm^{-2}), and white noise added to the membrane potential, was simulated for 20 seconds with low noise variance ($\sigma/C = 0.005$ mV·ms^{-1}). Figure 2.12A shows an example spectrogram, demonstrating high power between 0-20 Hz with a peak in the theta (4-12 Hz) range. The mean power spectrum over an ensemble of simulations (Figure 2.12B) shows peak power to be in the theta band, with peak frequency found to be at 10.40 ± 1.09 Hz (mean ± standard error). Whilst low

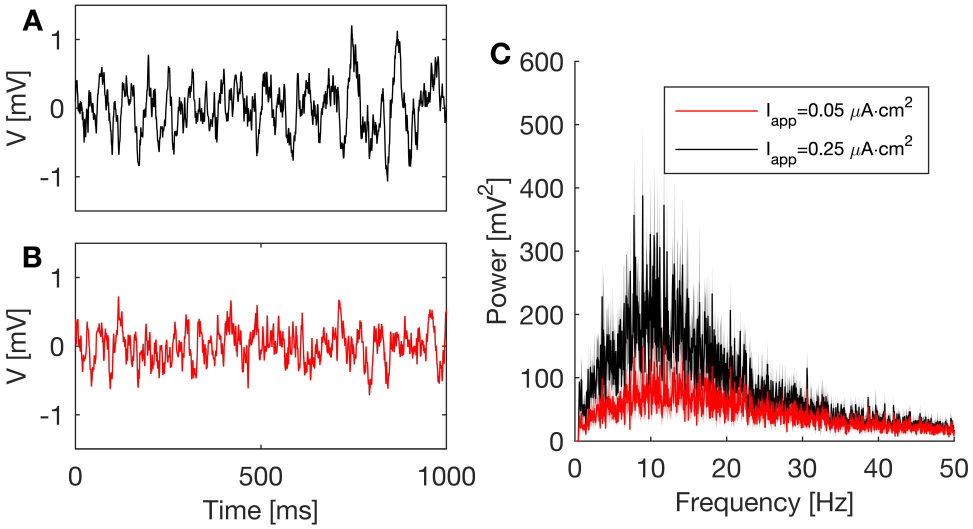

Figure 2.13: **Subthreshold theta fluctuations in a system with noise variance $\sigma/C = 0.135$mV·ms^{-1}** (A) Example membrane potential trace for system close to threshold ($I_{\text{app}} = 0.25\mu$A·cm^{-2}). (B) Example membrane potential trace for system far from threshold ($I_{\text{app}} = 0.05\mu$A·cm^{-2}). (C) Power spectrum for each value of I_{app}, averaged over 10 cells for 20 seconds. Close to threshold, the theta peak is greater, as seen in experiments.

noise variance was used in these simulations in order to elucidate mechanisms, Figure 2.13 shows simulations using the same amount of noise as in previous sections ($\sigma/C = 0.135$ mV·ms^{-1}) to demonstrate that theta range fluctuations still arise in the system with more realistic noise levels.

To further understand the origin of this subthreshold preferential theta power, we analysed the deterministic system. Figure 2.14 shows a bifurcation diagram in I_{app}. The deterministic system undergoes a saddle node bifurcation at $I_{\text{app}}^{\text{SN}} = 0.2738\mu$A·cm^{-2}; for $I_{\text{app}} < I_{\text{app}}^{\text{SN}}$ a stable steady state exists. A supercritical Hopf bifurcation occurs at $I_{\text{app}}^{\text{Hopf}} = 42.10\mu$A·cm^{-2}, generating a stable periodic orbit that is lost via a homoclinic bifurcation at $I_{\text{app}}^{\text{HC}} = 0.2401\mu$A·cm^{-2} demonstrating bistability between spiking and steady state in the range $I_{\text{app}}^{\text{HC}} < I_{\text{app}} < I_{\text{app}}^{\text{SN}}$. No other Hopf bifurcations occur in I_{app}, hence the deterministic system does not exhibit stable subthreshold oscillations within this parameter regime. We note that noise perturbations can drive the membrane potential above threshold even for $I_{\text{app}} < I_{\text{app}}^{\text{SN}}$ (see Figure 2.15 for anlaysis of spike onset in relation to injected current and differing noise variance). This justifies our choice of $I_{\text{app}} = 0.25\mu$A·cm^{-2} as this is sufficiently below threshold that no action potentials are observed.

In the absence of noise, the system is in a steady state and therefore no deterministic theta band oscillations arise. A potential mechanism by which white noise on a steady state can result in power spectral peaks is if the steady state is a focus. The resonant frequency of a focus can be calculated as the imaginary part

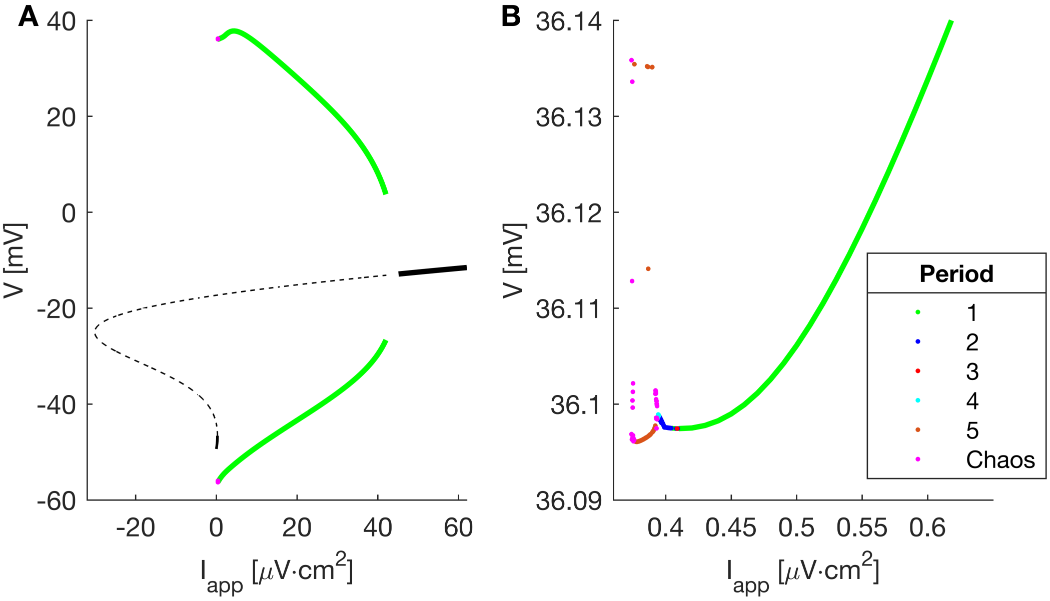

Figure 2.14: **Bifurcations in I_{app}** for values of g_{h} and g_{AHP} used in sections 2.3.2-2.3.3. (A) Full bifurcation diagram for I_{app}. (B) Flip bifurcations cause periodic bursting regimes to occur.

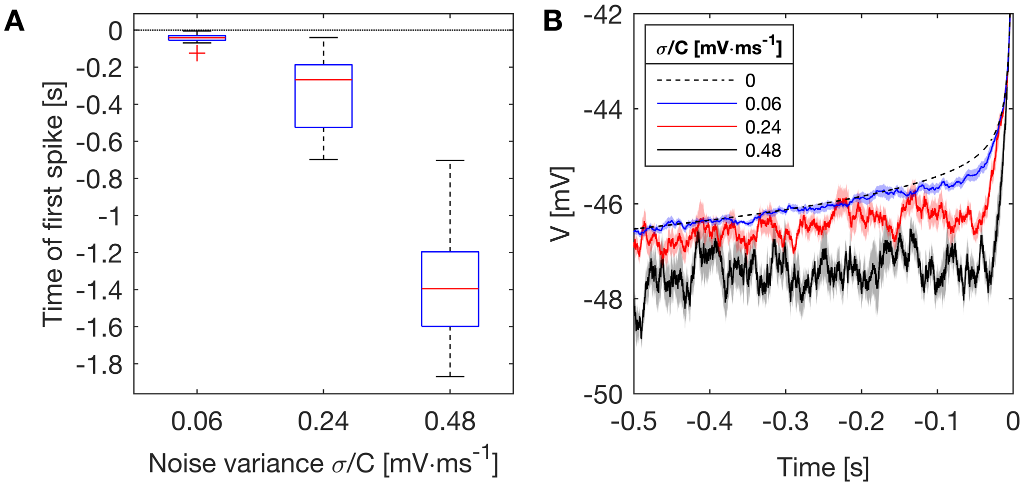

Figure 2.15: **Response of model stellate cell to current ramp** (A) Time of first spike of stochastic neurons (boxplot) during current ramp relative to time of first spike in the deterministic neuron (black dotted line, time = 0). Stochastic neurons fire earlier than the deterministic model in the current ramp experiment due to noise pushing the membrane potential above threshold. The larger the noise, the earlier the neuron fires due to excitability. (B) Each trace represents the mean of 10 simulations with a given noise level. Shaded regions represent standard error over the 10 simulations. Aligning time of first spike (time = 0), the stochastic system tends to exhibit a lower mean mebrane potential prior to the spike, particularly with large noise. This is because the first spike is, on average, earlier in the current ramp (see A), so input current is lower.

of the complex conjugate eigenvalues of the Jacobian normalised by a value of 2π. A pair of complex conjugate eigenvalues demonstrated that the steady state is a focus with a resonant frequency of 6.32 Hz. The effect of changing applied current was also tested (Figure 2.12C-D). In experimental recordings, theta power is seen to increase as I_{app} approaches threshold for action potential generation (Alonso and Klink, 1993). Figure 2.12C shows time series traces for a range of values of I_{app}, demonstrating theta power increasing as I_{app} is increased. Theta band spectral ratio was calculated as the ratio of total power in the theta band to total power in the 1-300 Hz broad band, shown in Figure 2.12D. This figure demonstrates the clear emergence of peak theta power as I_{app} is increased and threshold is approached. A Kruskal-Wallis test confirms a significant effect of applied current on spectral ratio ($\chi^2 = 44.97$, $p = 1.47 \times 10^{-8}$).

2.4 Discussion

In this chapter we analysed a conductance based model of a layer II medial entorhinal cortex stellate cell (mEC-SC), demonstrating that it is capable of generating clustered action potential firing with a range of quantitative P_C values that are observed in experiments. We demonstrated that these dynamics arise due to a subcritical Hopf/homoclinic bursting mechanism (section 1.4.5), which causes multiple period limit cycles that when perturbed by extrinsic noise display action potential clustering. We further demonstrated that the same model can generate experimentally observed subthreshold membrane potential fluctuations with power spectral peak in the theta band.

2.4.1 Derivation of the model, approximation of noise, and relationship to the Markov chain model

Dudman and Nolan (2009) presented a biophysically realistic Markov chain (MC) gated model of enthorhinal cortex stellate cells. MC models account for random fluctuations in the opening and closing of ion channels intrinsic to neurons (White et al., 2000; Goldwyn et al., 2011) by assigning them a voltage dependent probability of opening or closing. However, dynamic analysis of Markov chain models is challenging. Furthermore, Markov chain models are computationally expensive. For these reasons, in this paper, the MC gated model was converted to the deterministic Hodgkin-Huxley formulation for ion channel gates (Equation 1.16; Hodgkin and Huxley (1952)) under the assumption that the number of ion channels is sufficiently high that a density approximation can be justified, resulting in a system of ordinary differential equations (ODEs). Channel noise in the neuron was not explicitly modelled, but approximated by extrinsic, Gaussian noise on the membrane potential. We demonstrated that this was sufficient to produce clustered action potential dynamics and theta range subthreshold fluctuations in line with experiments (Alonso and Klink, 1993).

2.4.2 Action potential clustering

Clustered action potential firing, in which two or more action potentials are fired in succession before a long quiescent period, is a feature of *in vitro* recordings of layer II medial entorhinal cortex stellate cells. Action potential clustering is hypothesised to depend on the AHP and I_{h} currents based on computational studies and correlated gradients in dynamics associated with these currents (Booth et al., 2016a; Giocomo and Hasselmo, 2008; Nolan et al., 2007; Fransén et al., 2004; Pastoll et al., 2012; Yoshida et al., 2013; Garden et al., 2008; Giocomo and Hasselmo, 2009). Motivated by this, the dependence of these two parameters on clustering was tested in the model. A two parameter bifurcation analysis (Figure 2.4A) demonstrated that regions of quiescence, tonic firing, and clustered firing coexist. Furthermore, a range of values of P_C were found, allowing for control over the amount of clustering in the model.

Analysis of the deterministic model allowed for understanding of the mechanisms behind clustering (Figure 2.4C). Regions corresponding to tonic firing in the stochastic model correspond to regions of tonic firing in the deterministic model. As the regions of clustering are approached from the regions of tonic firing, a period doubling cascade occurs until stable multiplets (‘bursts’ of action potentials) are reached. Flip bifurcations (Channell et al. (2007); Barrio and Shilnikov (2011); section 1.4.6) occur, changing the number of spikes per burst. Eventually, firing is lost althogether via a homoclinic bifurcation as g_{h} is decreased. It is worth noting that a region of bistability exists before the homoclinic is reached in which the stable periodic orbit coexists with a stable steady state. In this region of bistability, it was found that simulations of the stochastic system starting on or near the periodic orbit are soon driven by noise towards the stable steady state, and hence sustained action potential firing in this region of the stochastic system is rare. Similar results occur for changes in I_{app} if g_{h} is held constant in certain parameter regimes (Figure 2.14), reflecting results in data that increasing applied current will increase number of spikes per cluster before moving the system into tonic firing (Alonso and Klink, 1993). This suggests that the different dynamics due to alterations in g_{h} may arise because of a change in resting membrane potential as g_{h} is varied. No such change in resting membrane potential is observed as g_{AHP} is altered. Analysis of a bursting regime demonstrated that bursting arises due to a fast-slow mechanism in which two slow variables drive the fast subsystem through a hysteresis loop. In terms of bifurcations in the fast sub-system, the bursting mechanism in this model can be classified as subcritical Hopf/homoclinic type (Izhikevich, 2000).

The generation of clustered action potential firing by deterministic, periodic bursting perturbed by extrinsic noise differs from past interpretations of clustering. In the Markov chain formalism of the model, Dudman and Nolan (2009) suggested clustering was the result of a transient increase in probability of firing during recovery from the AHP due to the stochastic mechanisms, and they demonstrated that clustering was not possible in the deterministic version of the model. In our study, we systematically explored the consequences of changing g_{h} and g_{AHP}, and found different dynamic regimes in the deterministic system, including steady state and tonic firing regimes that do not correspond to clustered firing in the stochastic model. It is possible that further exploration of the dynamics of the model of Dudman and Nolan (2009) would reveal similar bursting regimes to those reported herein. Although experimental verification of these interpretations is difficult, there are some agreements in mechanisms between these two models, however. The effect of changing g_{AHP} in the MC model has not been studied, but within a clustered parameter regime the affect of reducing g_{h} in the SDE model largely agrees with the results of reducing g_{h} in the MC model - a reduced value of P_C. The interpretation of increased probability of firing during recovery from AHP also emphasises the importance of the AHP current in clustering in the MC model.

A number of other parameters are likely to play a role in clustering. AHP halfwidth and I_{h} time constants may be important, as dorsoventral gradients in these properties also correspond to gradients in clustering (Giocomo et al., 2007; Giocomo and Hasselmo, 2008, 2009; Boehlen et al., 2010; Pastoll et al., 2012; Booth et al., 2016a), but these have not been studied here. Figures 2.3 and 2.5 demonstrate that the variance of noise chosen will also dictate the amount of clustering; increasing noise variance increases the likelihood of sporadic spiking or action potential cancellation, thus affecting the patterned firing.

2.4.3 Subthreshold theta resonance

Stellate cells in Layer II of the medial Entorhinal Cortex are known to exhibit subthreshold oscillations in the theta (4-12 Hz) range that increase in power as action potential threshold is approached (Alonso and Klink, 1993). Whilst no alterations to subthreshold oscillations were identified in the rTg4510 rodent model of tauopathy (Booth et al., 2016a), we studied subthreshold dynamics in the model to serve as validation that realistic mEC-SC like dynamics were captured.

It is believed that mEC-SC subthreshold oscillations are noise driven (White et al., 1998). In our deterministic (noise free) model, subthreshold oscillations do not exist, since we operated in a steady-state regime. However, the steady state is a focus with resonant frequency of 6.32 Hz, suggesting that with the addition of noise, a spectrum with preferential power in the theta band may arise. We found that a small amount of white noise on the membrane potential is sufficient to give rise to subthreshold dynamics with multiple peaks within the theta range and peak power at around 10 Hz. The difference in peak frequency found in simulations compared to the prediction from the linearisation of the focus may be due to noise in the simulated spectrum as well as noise induced frequency shifts (Bonnin and Corinto, 2013). Furthermore it was shown that the relative power in the theta band is significantly larger close to threshold than far below threshold.

To model the dynamics of subthreshold activity of stellate cells, two classes of model have previously been proposed. The first class of model utilises noisy perturbations to deterministic limit cycle dynamics. In this case, the output of the deterministic model would be regular, periodic oscillations and the related stochastic model would exhibit strongly periodic dynamics contaminated by noise. Previous models of subthreshold oscillations in stellate cells that fall into this class include those of Fransén et al. (2004); White et al. (1995); Dickson et al. (2000); and Rotstein et al. (2006). In the second class of model, such as the one presented in this study and the Izhikevich model (Izhikevich, 2007), theta band fluctuations arise due to noisy perturbations on a focus steady state, which results in a resonant response. In contrast to the aforementioned class of limit cycle models, fluctuations exist only in the presence of noise. Furthermore, in the noisy focus class of model, the dynamics appear less obviously periodic than in limit cycle models, resembling a stochastic process with peak power in the theta range. Experimental and modelling studies have suggested that removing channel noise results in loss of subthreshold oscillations (Dudman and Nolan, 2009; White et al., 1998; Dorval and White, 2005) and that stellate cell subthreshold dynamics are more reflective of a stochastic process with theta peak than a periodic process with additive noise (Dodson et al., 2011). These results are consistent with the noisy focus class of model, which the model we present belongs to. However, we note that the mechanisms of the two classes of model are closely related, since in theory, one expects to find a focus steady state close to a Hopf bifurcation into a limit cycle (White et al., 1995) with resonant frequency close to that of the limit cycle.

For biological insight into the currents involved in the generation of subthreshold limit cycles or resonance, reduced models, which remove currents that are predominantly active during action potential initiation or recovery, can be of interest. $I_{\mathrm{h}} + I_{\mathrm{NaP}} + I_{\mathrm{L}}$ models have been shown to generate theta band limit cycle oscillations (Fransén et al., 2004; Dickson et al., 2000; Rotstein et al., 2006). As discussed above, the alternative mechanisms of noise-perturbed focus and limit cycle dynamics are related, so it is of interest to test whether making similar reductions in our model maintains the theta band resonance. Setting all currents but I_{h} and I_{NaP} to their steady state value, we found that the corresponding steady state becomes a node and hence theta band resonance is lost. A detailed study of the mechanisms underlying the noise response of our model is an avenue for future work.

2.4.4 Implications for dementia

The entorhinal cortex is one of the first areas to be affected in dementias featuring a tau pathology such as Alzheimer's disease (Braak and Braak, 1991). In the rTg4510 mouse model of tauopathy, dorsoventral gradients in action potential clustering in layer II entorhinal cortex stellate cells were abolished (Booth et al., 2016a). A motivating application for a mathematical model of mEC-SCs in which action potential clustering can be controlled is to understand the mechanisms behind the dysfunction in clustered firing in animal models of dementia. Future work will involve exploring this relationship in more detail, but some key points can be stated from the work presented here. In the wild type animals, dorsal mEC-SCs fired highly clustered action potentials. This clustering was greatly reduced in the rTg4510 animals. Whilst I_{h} mediated sag amplitude was unaffected (suggesting no changes in g_{h}), an increase in amplitude of the AHP was seen in rTg4510 dorsal cells. The AHP amplitude, which scales with AHP conductance, has been demonstrated to be mechanistically related to P_C in this model and previous studies (Fransén et al., 2004; Fernandez and White, 2008). A possible mechanism for the reduced P_C in rTg4510 is an increase in g_{AHP}, resulting in the system undergoing a flip bifurcation resulting in fewer spikes per cluster. An example of this is the path through parameter space marked F in Figure 2.9, which results in realistic mEC-SC like clustering dynamics, with a change in parameters that reflects those seen in rTg4510. Future work will involve fitting parameters to the data to explore this in more detail.

Network activity was also seen to be disrupted in rTg4510 (Booth et al., 2016a). Dorsoventral gradients in phase-amplitude coupling (PAC) between theta and gamma rhythms in the local field potential was found to be disrupted in rTg4510 animals. Similar to clustering patterns, dorsoventral gradients in PAC were disrupted. Networks of modelled stellate cells, spatially extended along the dorsoventral axis, may be used to explore whether disruption in patterned action potential activity alone is sufficient to replicate deficiencies in PAC, or whether network properties such as dorsoventral gradients in inhibitory projections also come into play (Beed et al., 2013). Past computational studies of theta-gamma PAC have involved use of simple models that do not intrinsically fire in clusters such as the exponential integrate-and-fire (Solanka et al., 2015) or Hodgkin-Huxley (Wulff et al., 2009) models. Dorsoventral gradients in clustering intrinsic to cells cannot be studied using these models, and hence are not suitable to test whether intrinsic clustering is related to theta-gamma coupling. The model presented here is more suited to this type of study, as clustering can be controlled via biophysically realistic mechanisms.

2.4.5 Conclusions

In this chapter, we have presented a stochastic differential equation (SDE) model of Layer II medial entorhinal cortex stellate cells based on the Markov Chain formalism of the model presented by Dudman and Nolan (2009), but driven by extrinsic white noise to the membrane potential. We demonstrated that this model captures the key dynamics of mEC-SCs seen in electrophysiological recordings including subthreshold oscillations in the theta range and clustered action potential firing (Alonso and Klink, 1993). To understand the mechanisms underpinning clustered action potential firing, a numerical bifurcation analysis was performed on the underlying system of ordinary differential equations. Clustering was shown to arise due to flip bifurcations in the AHP and h-current conductance parameters, and is driven by two slow variables (m_{NaP} and h_{Kas}) driving the remaining fast subsystem through a subHopf/homoclinic type hysteresis loop. Furthermore, exploration of parameter space demonstrates that control of the AHP and h-current conductances allows for control of P_C, which quantifies the amount of action potential clustering exhibited by the model. The model provides an important tool for further understanding alterations to mEC spatiotemporal dynamics that arise in dementias featuring a tau pathology (Booth et al., 2016a).

Chapter 3

Multi-scale analysis of brain networks in an animal model of dementia

The work presented in this chapter was performed in collaboration with Dr Jon T Brown (EEG data acquisition, supervision, methodological design (data)), Dr Jon Witton and Prof Andrew Randall (two-photon calcium imaging data acquisition, methodological design (data)), and Dr Marc Goodfellow (supervision). Some of the work presented here was published as an abstract in the International Journal of Psychophysiology (Stothart et al., 2016). The author's contribution to this chapter includes preprocessing and formal analysis of the data, development of the method for network analysis of two-photon calcium data, development and analysis of the model, formulation of hypotheses and methodological design (modelling), interpretation of results, visualization of the data, and writing of the chapter.

3.1 Introduction

In the previous chapter, dynamics of single cells within a cortical slice were studied in an animal model of dementia. However, the cerebral cortex of the mouse contains 22 million neurons (Erö et al., 2018), which is scaled up to 16 billion cortical neurons in the human brain (Azevedo et al., 2009). These neurons are synaptically connected to form a complex multi-scaled network (section 1.1; section 1.3; Figure 1.1). Synaptic connectivity between neurons is known to be crucial for cognitive processing (Morrison and Baxter, 2012), allowing for the functional integration of brain regions, forming spatially distributed networks related to cognitive functioning (Britz et al., 2010; Reineberg et al., 2018). The disconnection hypothesis (section 1.3; chapter 4; Delbeuck et al. (2003)) proposes that the symptoms of dementia arise due to functional and structural disconnection between brain regions such that different processing systems of the brain can no longer integrate. It is therefore of crucial importance for the development of treatments and therapies for dementia to study neuronal network dynamics as well as single cell dynamics.

In humans, there is much evidence for the disconnection hypothesis on the macro-scale, including structural (Rose et al., 2000; Mito et al., 2018) and functional (Stam et al., 2009; Babiloni et al., 2016; Badhwar et al., 2017; Cope et al., 2018) neuroimaging. This is discussed in greater detail in chapter 4. Local synaptic loss has also been observed in people with dementia and animal models of dementia related pathologies (Davies et al., 1987; Selkoe, 2002). Computational modelling has suggested that alterations to the degree of local coupling can to some extent explain the breakdown of macro-scale functional networks (Dermitas et al., 2017), so to fully understand the mechanisms by which integration between systems of the brain is impaired in AD it is crucial to study networks at multiple spatial scales.

The low spatial resolution of most non-invasive functional neuroimaging techniques (reviewed in Table 1.1), means animal models of dementia are crucial if local networks of neurons are to be directly imaged. In this chapter, we study a transgenic mouse model expressing a mutant form of the *CHMP2B* gene (Ghazi-Noori et al., 2012), which encodes the charged multivesicular body protein 2b (CHMP2B). CHMP2B is a protein that plays a crucial role in regulating synaptic function in the brain (Chassefeyre et al., 2015). As a core subunit of the ensosomal sorting complex required for transport-III (ESCRT-III) (Ghazi-Noori et al., 2012), the primary role of CHMP2B is in transport of proteins to lysosomes during the process of autophagy (Rusten and Stenmark, 2009; Ghazi-Noori et al., 2012). CHMP2B proteins form clusters around the dendrites of neurons in the brain (Chassefeyre et al., 2015), and are believed to regulate many aspects of synaptic function including synaptic morphology, density, plasticity and electrophysiology (Chassefeyre et al., 2015).

Mutations to the *CHMP2B* gene have been identified in patients living with neurodegenerative disorders such as frontotemporal dementia (FTD) (Skibinski et al., 2005; Isaacs et al., 2011; Cruts et al., 2012), ALS (Cox et al., 2010), and Alzheimer's disease (Hooli et al., 2014). One particular mutation found in people with FTD occurs due to mis-splicing in the sixth splicing site, resulting in intron 5 (+201 bp) being retained (Skibinski et al., 2005). Mouse models expressing mutant human *CHMP2B*$^{\text{intron5}}$ have shown progressive local and long-range synaptic degeneration (Ghazi-Noori et al., 2012; Gascon et al., 2014) which are believed to contribute to behavioural and motor deficits reminiscent of those seen in FTD or ALS (Gascon et al., 2014; Vernay et al., 2016; Clayton et al., 2017). Therefore the *CHMP2B*$^{\text{intron5}}$ model is suitable to study functional connectivity on the local and whole-brain scales in the context of cognitive impairment in dementia due to synaptic deficiencies.

In this chapter, we study functional connectivity between neurons in the brain of *CHMP2B*$^{\text{intron5}}$ animals on both the local and whole brain scales *in vivo*. To test whether there exist impairments to synaptic communication between neurons within a local neighbourhood, we quantify synchronous neuronal activation in spontaneous two-photon calcium imaging data (Stosiek et al., 2003) recorded from the whisker barrel cortex during sedation[1] to construct a local scale functional network. To additionally test for impairments in long range communication between regions of the brain, synchronous neuronal oscillations in cortical intracranial skull-screw electroencephalogram (EEG)[2] are quantified. Finally, to try to understand whether there exists an interplay between functional networks on different spatial scales, we use a computational model of the mouse brain based on the Allen Mouse Brain Atlas (Lein et al., 2007) using a tractography derived connectome (Wook Oh et al., 2014) to control global coupling and which contains a local coupling parameter (sections 1.6-1.7).

3.2 Materials and methods

3.2.1 Experimental methods

All experiments and work described in section 3.2.1 were performed externally by collaborators[1,2]. Procedures were performed in accordance with the Animals (Scientific Procedures) Act 1986 and EU directive 2010/63/EU, and were subject to internal ethical reviews. Transgenic animals were bred at the University College London Institute of Neurology. EEG experiments were performed at the University of Exeter Medical School. Two-photon calcium imaging experiments were performed at the University of Bristol School of Physiology and Pharmacology. Experimental procedures are outlined below.

Two-photon calcium imaging

Surgery was performed on 4 male transgenic *CHMP2B*$^{\text{intron5}}$ and 4 male WT littermates aged 12-13 months. A virus containing the DNA for the genetically encoded flourescent calcium indicator GCaMP6s (Chen et al., 2013) was injected into layer 2/3 of the right whisker barrel cortex, and a glass cranial window implanted (Holtmaat et al., 2009). Following a four week post-surgical recovery,

---

[1] Data acquisition performed by Dr Jon Witton at the University of Bristol School of Physiology, Pharmacology, and Neuroscience

[2] Data acquisition performed by Dr Jon Brown at the University of Exeter Medical School

widefield imaging was used to locate the whisker barrel cortex based on flourescence in response to whisker stimulation, and the identified region tagged for two-photon imaging. A total of 11 WT and 9 *CHMP2B*$^{\text{intron5}}$ cortices were identified and imaged.

Immediately following the identification of a barrel cortex, two-photon calcium imaging proceeded. Spontaneous GCaMP6s signals were recorded for 520s sampled at 8 Hz. Regions of interest (ROIs) were identified similar to previous methods (Smith and Hausser, 2010), and a flourescent time series calculated by averaging the time series of all pixels in the ROI, and was corrected for neuropil flourescence (Chen et al., 2013). The relative neuronal flourescence time series $\Delta F/F$ was calculated (Dombeck et al., 2009).

Transients were identified using a template matching algorithm (Clements and Bekkers, 1997), in which the template was fit from the average of approximately 300 visually identified transients. Inactive neurons (time series not containing a transient) were removed.

EEG experiment

Eight microscrews were surgically implanted into the skulls of 6 male transgenic *CHMP2B*$^{\text{intron5}}$ mice and 4 male WT littermates aged 11-12 months. Microscrews were placed bilaterally above the primary motor cortex (M1; stereotaxic coordinates ML $\pm$ 1.3, AP +1.5 mm), primary somatosensory cortex (S1; ML $\pm$ 2.2, AP -0.9 mm), primary visual cortex (V1; ML $\pm$ 2.2, AP -3.2 mm), and cerebellum (ML $\pm$ 1.9, AP -6.0 mm). Following a one week, postsurgical recovery, EEG recordings were taken via the Neuralynx digital recording system, referenced to the channel in the right cerebellum, lowpass filtered at 400 Hz and sampled at a rate of 1 kHz. Two LEDs were recorded (sampled at 25 Hz) to track motion of the animals.

Animals were subject to a 12 hour light, 12 hour dark cycle. During light periods, animals were placed in their home cage with lid removed and allowed to move freely. EEG was recorded for up to 60 minutes. Three 20s artifact free epochs per subject were chosen in which the mouse was stationary and assumed to be sleeping.

3.2.2 Two-photon calcium imaging analysis

Previous studies have used zero-lag correlation on the raw $\Delta F/F$ traces to construct functional networks from two photon calcium imaging data (Dombeck et al., 2009; Goncalves et al., 2013). However, correlation between raw $\Delta F/F$ traces is affected by a number of factors unrelated to synchrony between the firing times of the neurons. These factors include low signal-to-noise ratio (Lütcke et al., 2013), periods in which neither neuron is firing which are neither indicative of synchrony or asynchrony between sparely firing neurons, and different cells within an animal potentially having slightly different calcium rise and decay times. Spike train synchrony methods avoid these issues but assume there is no information given within the spike itself (Kreuz et al., 2007), and hence these are unsuitable since the amplitude of transients is modulated by bursts of action potentials (Chen et al., 2013).

To avoid these issues, the method outlined in Figure 3.1 was used to construct functional networks. Data was mathematically reconstructed into a suitable format for correlation analysis. A template matching algorithm (Clements and Bekkers, 1997) was used to extract spike trains of transient onsets from the data[3] (Figure 3.1A). Each calcium event, intiated at time t_0, was modelled as an exponential rise and decay (Clements and Bekkers, 1997; Lütcke et al., 2013),

$$\Delta F/F = AH(t-t_0)(1-e^{-(t-t_0)/\tau_r})e^{-(t-t_0)/\tau_d} \tag{3.1}$$

where A is the transient amplitude, $H(t)$ is the Heaviside function, and τ_r and τ_d are rise and decay time constants. Then the reconstructed trace is

$$\Delta F/F = \sum_{i=1}^{N} A_i H(t-t_i)(1-e^{-(t-t_i)/\tau_r})e^{-(t-t_i)/\tau_d}, \tag{3.2}$$

where N is the number of spikes in the extracted spike train, A_i is the amplitude of the ith transient (calculated as the best fit for the model at each transient), and t_i is the onset time of the ith transient. Figure 3.1B shows that the reconstructed traces mostly perform well, however the primary limitation to reconstruction is the spike time extraction algorithm as some transients were missed (e.g. cell 3 in Figure 3.1B).

To calculate correlation between a pair of reconstructed traces, we first removed periods of inactivity from the traces (Figure 3.1C-D). Windows of activity were defined as regions in which one or both cells were 'spiking'; that is, from the onset of a transient until the trace had decayed to 1% of its amplitude. Periods of inactivity were defined as all time points that do not fall within a window of activity for one or both cells. Finally, we set the traces to unit variance. Correlation between the resulting traces x_i and x_j was calculated as

$$c_{ij} = \frac{x_i \cdot x_j}{\sqrt{x_i \cdot x_i}\sqrt{x_j \cdot x_j}}. \tag{3.3}$$

Connections were tested for significance through the generation of 99 multivariate shift surrogate data sets. Surrogate functional networks were constructed

---

[3] Spike time extraction performed by Dr Jon Witton

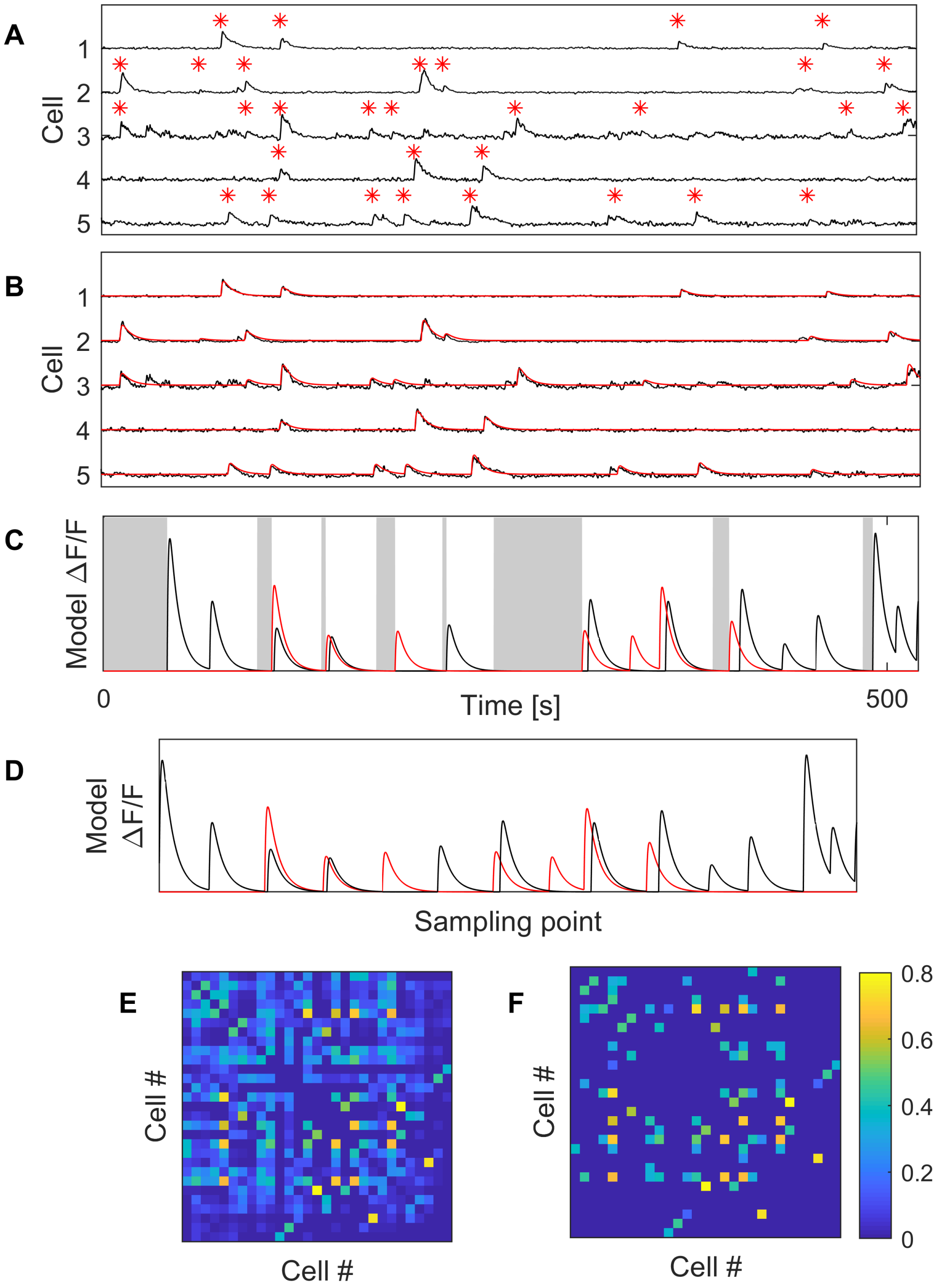

Figure 3.1: **Method of calculating synchrony between calcium transients.** (A) Spike times were extracted from the data using a template matching algorithm. (B) A mathematical model was used to reconstruct the data, removing noise and effects of irregularly shaped transients. (C-D) When calculating pairwise correlation between two time series, periods of inactivity in both cells were removed. (C) shows the reconstructed traces before removal, where areas shaded in grey are those classes as periods of inactivity in both cells, and (D) shows the traces following removal of periods of inactivity. (E) Networks were constructed by calculating the normalized vector product (correlation without demeaning) between reconstructed traces. (F) The network was then tested against shift surrogates, and non-significant edges were removed.

and edges in the empirical networks tested to 5% significance against those in surrogate networks. Edges with stronger indirect connections were additionally set to zero, using the Dijkstra algorithm to identify shortest path lengths between nodes (Dijkstra, 1959). Example functional networks constructed using this method are shown in Figure 3.1E-F.

3.2.3 EEG preprocessing and analysis

EEG preprocessing was performed using the Fieldtrip toolbox for EEG/MEG-analysis, developed at the Donders Institute for Brain, Cognition, and Behaviour (Oostenveld et al. (2011); `http://www.ru.nl/neuroimaging/fieldtrip`). Cortical channels over the left and right M1, S1, and V1 cortices were used in the analysis. To ensure the referencing procedure did not introduce connectivity bias towards the hemisphere in which the reference electrode was placed, EEG was re-referenced to both cerebellar channels. Data was bandpass filtered from 1-45 Hz, demeaned, and detrended.

Power spectral analysis was additionally performed using the Fieldtrip toolbox. Spectra were extracted using a multi-tapered Fourier transform, with tapers constructed from discrete prolate spheroidal sequences (Percival and Walden, 1993) with ±0.5 Hz smoothing, but results were consistent for other smoothing boxes. For each animal, spectra were averaged over the three 20 second epochs. Total power within a band was calculated as the integral of the spectra within that band.

Functional connectivity analysis was performed with custom written Matlab scripts. The phase locking factor (PLF) (Lachaux et al., 1999) was calculated between pairs of channels. To test edges for significance, 99 iterative amplitude adjusted Fourier transform (iAAFT) surrogate time series were constructed from the EEG using a maximum of 10 iterations (Schreiber and Schmitz, 1996) and PLF networks constructed from these surrogate time series. Edges of the empirical network were tested to 5% significance against the edges of the surrogate networks. Zero phase lag connections were set to zero to account for spurious correlations due to common sources. Edges with stronger indirect connections were additionally set to zero, using the Dijkstra algorithm to identify shortest path lengths between nodes (Dijkstra, 1959). For each animal, functional networks were averaged over the three 20 second epochs.

3.2.4 Computational model of the mouse brain

To test hypotheses relating macro-scale neuronal dynamics to local connectivity, we used a phenomenological model of neuronal oscillations based on the normal form of the Hopf bifurcation (described in detail in section 1.6), which has previously been used to model slow wave sleep oscillations in humans (Deco et al.,

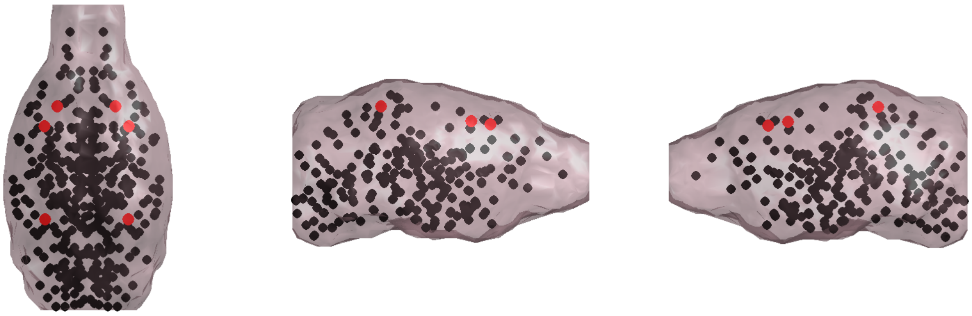

Figure 3.2: **Regions of interest used in simulations of mouse whole brain dynamics.** Each dot corresponds to the centroid of a region of interest used in the simulations of mouse whole brain dynamics. Black dots only have indirect influence on the EEG through connectivity, whilst dynamics at the red dots are taken as EEG electrodes.

2017b) and test changes in both local (Dermitas et al., 2017) and global dynamics (Dermitas et al., 2017; Tait et al., in press) in Alzheimer's disease patients.

Connectivity between regions of the brain is given by GK_{ij}, where G is a global coupling constant and K_{ij} gives the weight of connections between regions i and j. Whilst only a small number of regions of the brain were recorded by the EEG, it is likely that a broader range of brain regions play a role in the generation of organized neuronal oscillations during sleep/sedation (Neske, 2016). For this reason, we perform large scale simulations of the whole mouse brain, consisting of 213 regions per hemisphere defined by the Allen Mouse Brain Atlas (Lein et al., 2007) using an open access connectome derived from tractography data (Wook Oh et al., 2014) for the coupling matrix K_{ij}.

Intrinsic oscillator frequencies were uniformly distributed within the 1-4 Hz delta band, which is the dominant rhythm during sleep in mice (Lee et al., 2004) and was the dominant frequency in our data. To explore the effects of local and global coupling, parameters a and G were varied respectively. Simulated EEG was taken as the simulation output of the nodes most closely corresponding anatomically to the regions in which EEG electrodes were implanted, referenced to the output of the cerebellar nodes anatomically corresponding to the empirical reference electrodes. Figure 3.2 shows the centroids of each simulated region as defined according to the Allen Mouse Brain Atlas (Lein et al., 2007), with red dots showing the regions taken as EEG.

3.2.5 Statistical analysis

Due to the small sample sizes in this study, non-parametric tests were used unless otherwise stated. All values are reported as mean $\pm$ standard error on the mean (SEM). Pairwise comparisons were performed using the Mann-Whitney U test. When correction for multiple hypotheses is reported in the results, correction was performed using Bonferroni corrections. The choice of Bonferroni correction was motivated by the small number of hypotheses being tested (usually 6 corresponding to 6 electrodes); for numbers of hypothesis of the order 10, Bonferroni correction has similar statistical power as false discovery rate measures and has lower likelihood of false positives (Krzywinski and Altman, 2014).

3.3 Results

3.3.1 Two-photon calcium imaging analysis

To explore whether the local integration of neurons in the brain was impaired in *CHMP2B*$^{\text{intron5}}$, spontaneous neuronal activity in the whisker barrel cortex of WT and *CHMP2B*$^{\text{intron5}}$ transgenic mice was recorded using two-photon calcium imaging. There were significantly fewer cells in the *CHMP2B*$^{\text{intron5}}$ animals than the WT animals ($p = 0.0044$, WT 67.0 ± 4.2, TG 45.2 ± 4.5), and whilst there was additonally significantly fewer active cells in the *CHMP2B*$^{\text{intron5}}$ animals ($p = 0.0155$, WT 41.0 ± 3.2, range $20 - 61$; TG 25.6 ± 4.4, range $11 - 51$), there was no change in the fraction of cells which were active ($p = 0.3744$, WT $62.0 \pm 4.4\%$, TG $54.1 \pm 5.3\%$).

To quantify alterations in neuronal activity in *CHMP2B*$^{\text{intron5}}$, only the active cells were included in the analysis. In these cells, there were no differences in frequency of calcium events ($p = 0.9717$, WT 0.55 ± 0.04 events per minute, TG 0.55 ± 0.07 events per minute). Functional networks were calculated using the method outlined in section 3.2.2 (Figure 3.3A-B). Synchrony of calcium dynamics between neurons was increased in *CHMP2B*$^{\text{intron5}}$ animals, quantified by mean degree normalized by the number of active cells ($p = 0.0302$, WT 0.046 ± 0.005, TG 0.074 ± 0.012, Figure 3.3C).

To test whether topological reorganization of the network, for example through synaptic plasticity, might be related to this increased mean degree in *CHMP2B*$^{\text{intron5}}$ animals, we binarized the functional network by setting all non-zero edges equal to one and calculated the synchronizability as the Laplacian eigenratio λ_2/λ_N of this adjacency matrix (Pecora and Carroll, 1998; Tahaei et al., 2012). Synchronizability significantly increased in *CHMP2B*$^{\text{intron5}}$ animals ($p = 0.0209$, WT 0.023 ± 0.004, TG 0.120 ± 0.063, Figure 3.3D).

3.3.2 EEG analysis

We next tested whether there existed alterations to long range integration between regions of the brain by analysing cortical skull screw EEG. Power spectra were calculated for each electrode, shown in Figure 3.4. All electrodes demon-

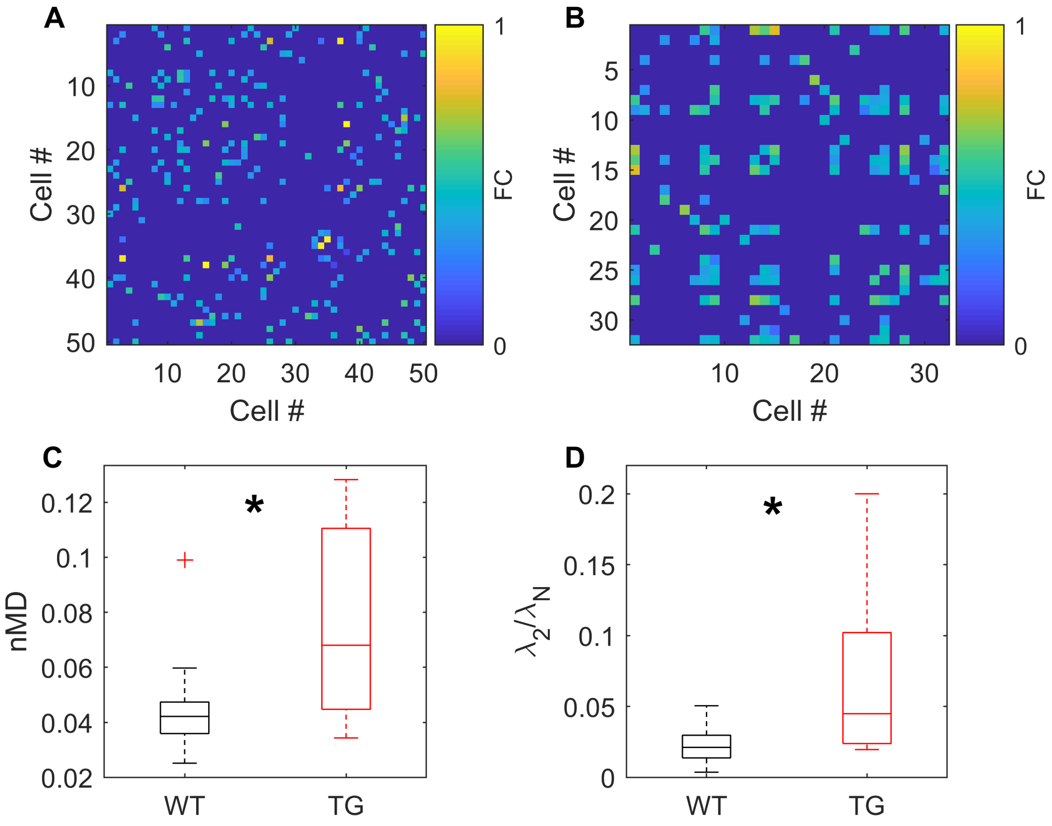

Figure 3.3: **Analysis of two photon calcium imaging data.** (A-B) Example representitative WT (A) and *CHMP2B*$^{\text{intron5}}$ (B) functional networks. Networks with similar number of cells, mean degree, and synchronizability to their respective group means are shown. (C) Mean degree, normalized by the number of cells in the network, was significantly increased in *CHMP2B*$^{\text{intron5}}$ TG animals. (D) Synchronizability, quantified by the Laplacian eigenratio λ_2/λ_N of the binarized adjacency matrix, significantly increased in *CHMP2B*$^{\text{intron5}}$ animals. Stars denote significance ($p < 0.05$).

strated dominant rhythms in the 1-4 Hz delta band, which is known to be the dominant neuronal rhythm during sleep. Visual inspection demonstrates that frontal electrodes, namely those above the primary motor (M1) and somatosensory (S1) cortices, demonstrated a reduced power in these slow rhythms, whilst no significant differences were observed in electrodes above the visual cortex (V1). Spatial distributions of delta power are shown in Figure 3.5A, demonstrating reductions in power predominantly in the frontal cortex. To test whether this reduced frontal lobe delta power was significant, spectra for the M1 and S1 electrodes in both hemispheres were averaged, and total delta power was calculated from this average spectrum. Total delta power was found to significantly reduce in the TG animals ($p = 0.0381$, WT 37.5 ± 3.2 μV^2, TG 22.5 ± 2.6 μV^2). The spectrum for each electrode was subsequently tested, identifying significant reductions ($p < 0.05$) in total delta power for the M1$_\text{L}$, M1$_\text{R}$, and S1$_\text{R}$ electrodes (where subscript L/R

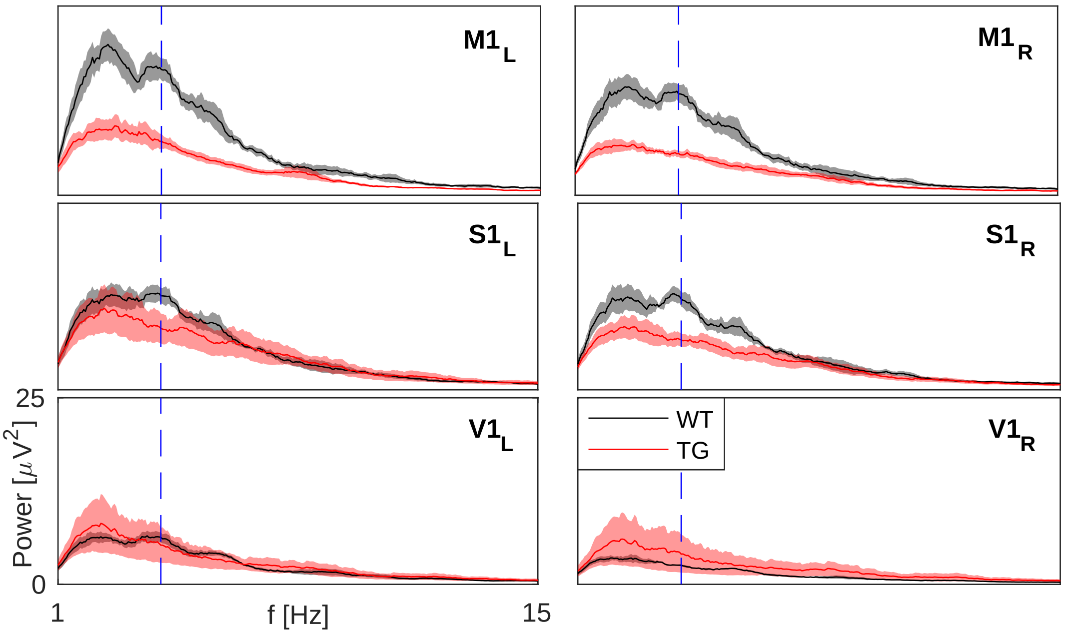

Figure 3.4: **Power spectral analysis of *CHMP2B*$^{\text{intron5}}$ EEG data.** Channelwise power spectrum between 1-15 Hz. Figure titles show the location of the electrode, with subscripts L/R for left/right hemispheres respectively. The vertical dotted blue line shows 4 Hz, so power to the left of this line demonstrates the delta band. Black show wild-type (WT) spectra, whilst red show *CHMP2B*$^{\text{intron5}}$ transgenic spectra (TG). Shaded regions are standard error of the mean.

denotes left/right hemisphere). Following Bonferroni post-correction for multiple hypotheses, only M1$_R$ remained significant (corrected p-value 0.038).

To test whether functional connectivity between regions was altered in this dominant delta band, EEG was bandpass filtered into the 1-4 Hz band and phase locking factor (PLF) was used to construct functional networks, shown for each animal in Figure 3.6. The functional network structure was stereotypical for the four WT animals, with high phase locking between frontal regions and less well connected visual regions, particularly V1$_R$. In *CHMP2B*$^{\text{intron5}}$ transgenic animals, however, there was no stereotypical structure and frontal connectivity appeared to be greatly reduced. To test this hypothesis, the mean degree of the functional networks were calculated and found to significantly decrease ($p = 0.0381$, WT 2.94 ± 0.15, TG 2.52 ± 0.12).

As with power, both frontal M1 channels demonstrated reduced degree (Figure 3.5B; Left M1: $p = 0.0095$, WT 2.90 ± 0.15, TG 2.01 ± 0.26; Right M1: $p = 0.0190$, WT 3.38 ± 0.13, TG 2.83 ± 0.24). Furthermore, all remaining left hemisphere channels were found to reduce in degree (Left S1: $p = 0.0095$, WT 3.29 ± 0.09, TG 2.85 ± 0.11; Left V1: $p = 0.0095$, WT 3.08 ± 0.10, TG 2.53 ± 0.14). Whilst none of these values were significant following Bonferroni correction, this is likely a result of low sample size and the low statistical power of Bonferroni correction since trends were common over all left hemisphere and frontal channels.

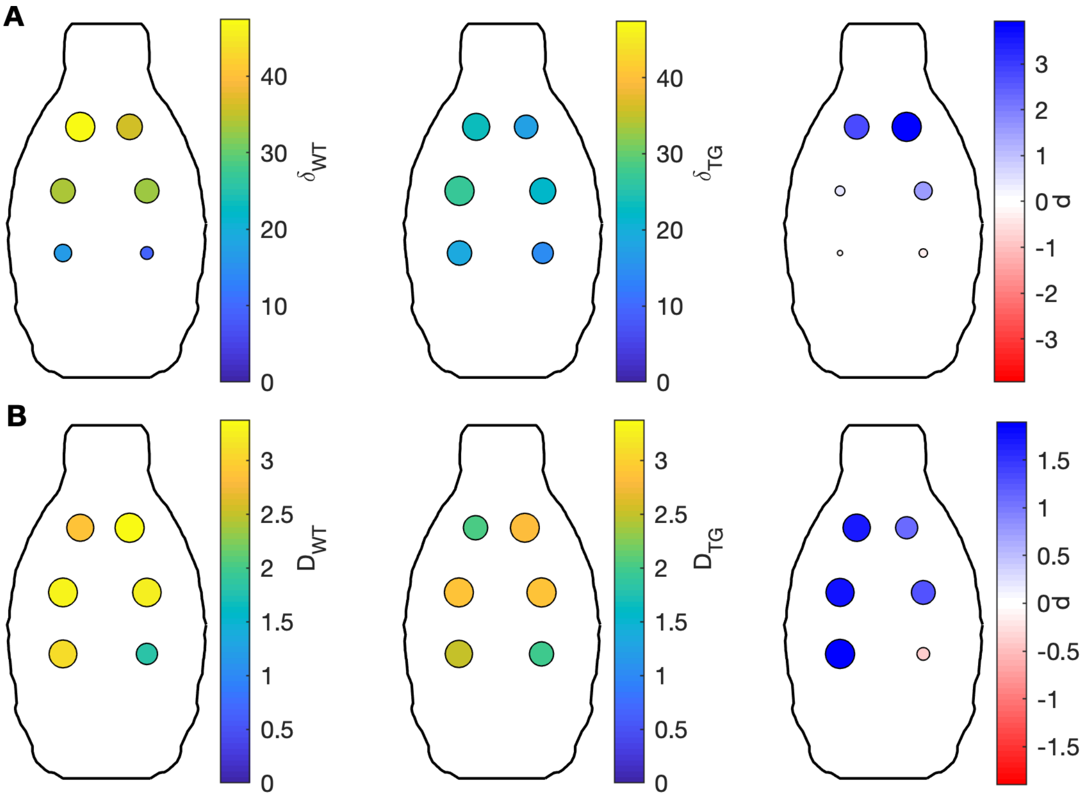

Figure 3.5: **Spatial distributions of power and functional network degree in the *CHMP2B*$^{\text{intron5}}$ data.** Shown in circles are the locations of the EEG electrodes. For all plots, colour denotes true value shown in the colour bars, whilst size of the circle shows absolute value as a fraction of the maximum in the subfigure. (A) Left - delta power, averaged over WT animals. Middle - delta power, averaged over TG animals. Right - Cohen's d showing effect sizes of differences in delta power between WT and TG animals. (B) As for A, but with degree of the functional network.

3.3.3 Computational modelling

To test whether there is a relationship between the degree of local coupling and long range coupling, a computational model of the mouse brain was used, in which a tractography derived connectome (Wook Oh et al., 2014) was used to couple regions of the brain which were simulated by a stochastic oscillator (section 3.2.4). As described in section 1.6, the parameter a was used as a proxy for local connectivity and the parameter G was used as a proxy for the degree of global coupling in the model.

Figure 3.7A-B shows the results of a two parameter sweep of G and a. For $a > 0$, the decrease in MD of the macro-scale functional networks in *CHMP2B*$^{\text{intron5}}$ (moving from regions of white to regions of red in Figure 3.7A-B) can be fully explained by an increase in parameter a. An example of such an alteration is demonstrated by path P1 in Figure 3.7B, where the start point of P1 represents realistic WT MD and the end point represents realistic *CHMP2B*$^{\text{intron5}}$ MD. However, for all $a > 0$ the simulated time series have a delta band signal-to-noise

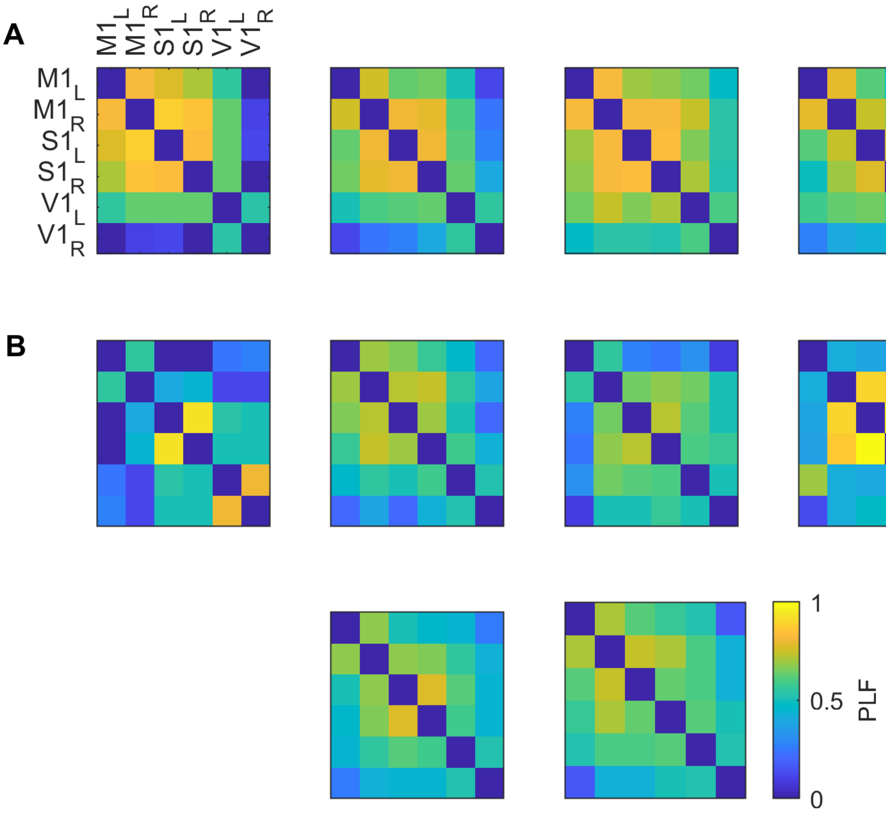

Figure 3.6: **Functional networks derived from the *CHMP2B*$^{\text{intron5}}$ EEG data** PLF networks for each animal from which EEG was recorded. (A) Wild-type animals demonstrated a stereotypical network structure, in which there was high frontal (M1 and S1) connectivity. (B) This stereotypical structure was lost in the *CHMP2B*$^{\text{intron5}}$transgenic animals.

ratio (δSNR; quantified as the ratio of variance of the delta band filtered signal to the variance of the broadband signal) approximately equal to one (Figure 3.7C). In the empirical data, the EEG has a δSNR of 0.41 ± 0.02 (averaged over both WT and TG data), with no significant differences between WT and TG ($p = 0.48$, Mann-Whitney U test). Therefore the parameter regime underpinning path P1 results in unrealistic dynamics, as can be seen by comparing example empirical time series (Figure 3.7D) to simulated time series (Figure 3.7E).

An alternative possible path through parameter space explaining the reduced MD in *CHMP2B*$^{\text{intron5}}$ coinciding with increased local coupling is given by path P2 in Figure 3.7B. The start point of P2 represents realistic WT MD with realistic δSNR. At the point in parameter space, increasing a results in an increase in MD, meaning that the increase in local coupling in *CHMP2B*$^{\text{intron5}}$ does not explain the reduced MD seen in the data. However, it is known that in *CHMP2B*$^{\text{intron5}}$ animals, there are severe white matter impairments (Ghazi-Noori et al., 2012), which would correspond to a drop in G. Therefore path P2 shows a path involving a drop in

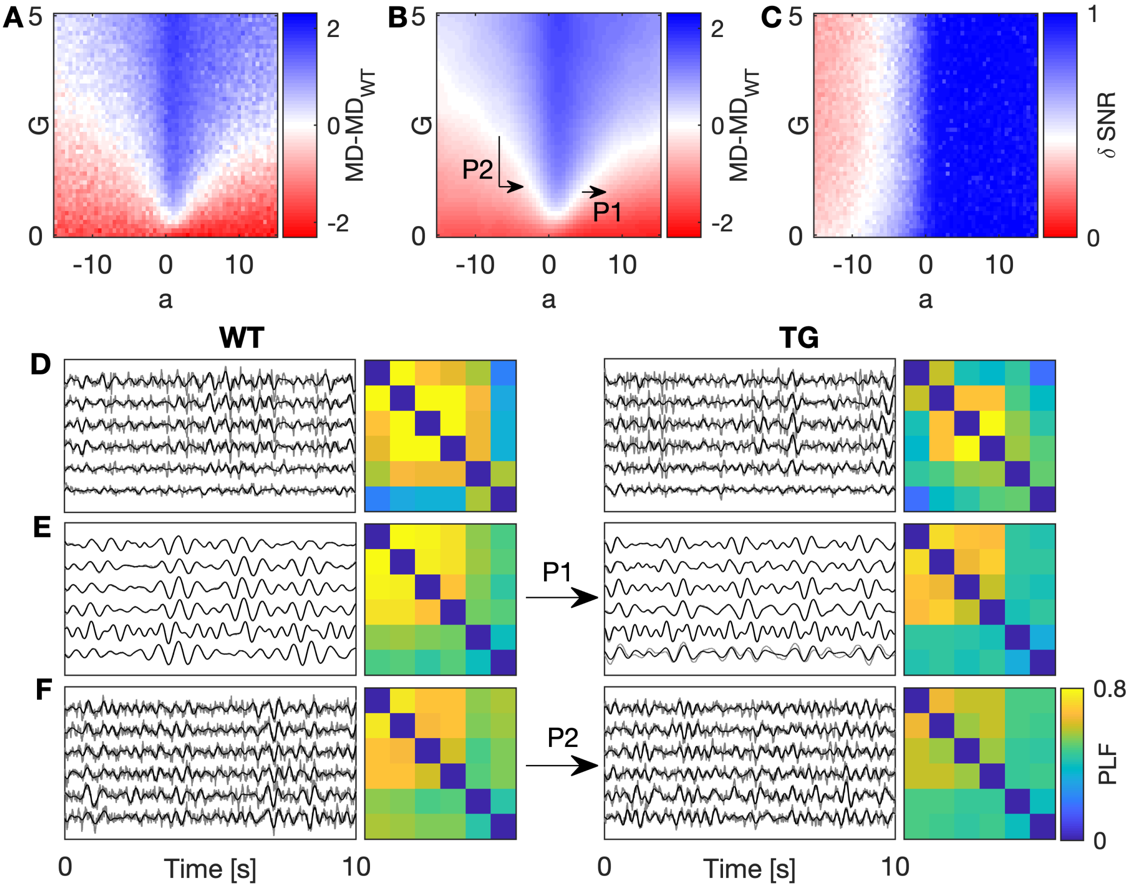

Figure 3.7: **Simulations of the mouse brain and EEG experiment.** (A) Effects of varying global coupling G and local coupling a in the model on the mean degree of the functional networks in the simulated EEG. Regions of white in the model are where the mean degree of the simulated functional network (MD) is approximately equal to the mean degree of the empirical average WT functional connectivity (MD_{WT}). (B) The figure in A, smoothed with a Gaussian filter to reduce the effects of noise. P1 and P2 are potential paths through parameter space explaining alterations to MD in *CHMP2B*$^{\text{intron5}}$(see text), which should feature an increase in a (due to increased local coupling) and possibly a decrease in G (due to known white matter deficits in *CHMP2B*$^{\text{intron5}}$), and should move from white to pale red. (C) Delta band SNR, quantified as the ratio of variance of the filtered (delta band) signal to variance of the broadband signal. SNRs close to those of the data are shown in white. (D) Representative empirical EEG data and the average empirical functional networks. In grey is the original signal, whilst black shows the 1-4 Hz filtered signal. (E) Simulated EEG data and resulting simulated functional connectivity for path P1 in B. (F) Simulated EEG data and functional connectivity for path P2 in B. In D-F, time series and functional networks are shown with the same order of electrodes as in Figure 3.6.

G and an increase in a, resulting in realistic *CHMP2B*$^{\text{intron5}}$ MD, with δSNR in a realistic parameter regime. Examples of the simulated time series and functional networks for P2 are shown in Figure 3.7F.

3.4 Discussion

This chapter studied perturbations to multi-scale functional networks in a transgenic animal model expressing a mutant form of the *CHMP2B* gene (Skibinski et al., 2005; Lindquist et al., 2008; Ghazi-Noori et al., 2012) which exhibits local and long range synaptic impairments (Ghazi-Noori et al., 2012; Gascon et al., 2014) and behavioural deficits reminiscient of those seen in dementias (Gascon et al., 2014; Vernay et al., 2016; Clayton et al., 2017). To study functional connectivity between neurons within a region of the brain (local FC), we analysed data from experiments imaging calcium dynamics of networks of neurons in layer II of the whisker barrel cortex under sedation and light anaesthesia. Functional networks demonstrated significantly higher synchrony and a topology with greater synchronizability in the transgenic *CHMP2B*$^{\text{intron5}}$ (TG) animals than the non-transgenic wild-type (WT) animals. A potential explanation for these functional network differences at the cellular scale may be alterations to the structure of the excitatory network, since the non-mutant form of the *CHMP2B* gene is involved in the maintence of excitatory synapses, and regulation of post-synaptic excitatory dendritic morphology, number of synapses, and plasticity of excitatory PSC amplitudes via LTP (Chassefeyre et al., 2015). Furthermore, in a transgenic model expressing *CHMP2B*$^{\text{intron5}}$, excitatory (but not inhibitory) post-synaptic density was found to increase (Gascon et al., 2014). Particularly, topological reorganization of the structural network through synaptic plasticity may explain both the alterations to both mean degree and topology of the functional network.

To study whole brain functional connectivity, we analysed data from skull-screw EEG recorded from six locations on the cortex during sleep. The dominant activity observed in the EEG was in the delta (1-4 Hz) band, consistent with past studies of EEG during sleep in mice (Lee et al., 2004). Reduced power of delta oscillations was observed in the frontal channels in the TG animals. This reduction in power is potentially a result of neuronal loss, as spatial distribution of these changes is consistent with reduced cortical volume due to neuronal loss in the *CHMP2B*$^{\text{intron5}}$ model (Clayton et al., 2017).

To avoid amplitude effects due to heterogeneous loss of spectral power when calculating functional connectivity between regions of the brain, phase locking factor was used to quantify synchrony of delta oscillations (Lachaux et al., 1999). Functional connectivity in this long range network was found to reduce, particularly in frontal and left hemispherical channels. Severe pathologies related to axonal degeneration have previously been reported in the corpus callosum and other white matter tracts in the *CHMP2B*$^{\text{intron5}}$ model, which is a likely mechanism underpinning this impairment to long range functional connectivity.

Computational modelling was used to gain insight into potential interplay between local and long-range functional connectivity. Using a model of coupled oscillators (section 1.7) and a realistic tractography derived connectome (Wook Oh et al., 2014), whole brain simulations of mouse delta activity were performed in which global coupling and local coupling were varied. The model exhibited parameter regimes in which an increase in local coupling was sufficient to explain the decrease in mean degree of the whole brain functional networks, but these regimes gave rise to hypersynchronous delta oscillations which did not reflect the data. In regimes for which the simulated dynamics more closely matched those of the data, increases/decreases in local or global connectivity were found to increase/decrease the mean degree of the functional network, which is consistent with both theoretical and computational results from analyses of multi-scaled coupled oscillator networks (Schmidt et al., 2014). A possible interpretation of these results is that increases in local coupling may be a compensatory mechanism for impairments to long-range coupling (or vice versa) to restore global integration of regions of the brain through functional connectivity. An example path through parameter space was shown, demonstrating that a severe loss of global coupling, for example through white matter impairments (Ghazi-Noori et al., 2012), will result in a severely reduced MD which can be compensated for through an increase in local coupling. Enhancements of local neuronal circuits through alterations to neurotransmitters and synaptic plasticity as a compensatory mechanism for network dysfunction in neurodegenerative disorders has in the past been suggested (Palop et al., 2006; Abuhassan et al., 2014). The increased synchronizability of the topology of the local networks studied in this chapter suggest that increases in local connectivity may arise due to topological reorganization of synapses into a more efficient structure.

A limitation of the model used here was homogeneity - the local coupling parameter was homogeneous across all nodes of the network, and impairments to white matter were simulated via a global coupling parameter which altered all edges homogeneously. This is a potential explanation of why the topology of the functional network was not significantly altered in our macro-scale simulations of the *CHMP2B*$^{\text{intron5}}$ dynamics compared to the simulations of WT dynamics. Whilst the empirical WT functional networks showed a stereotypical pattern across all animals, the *CHMP2B*$^{\text{intron5}}$ animals did not, suggesting that not only are the synaptic impairments spatially heterogeneous, these alterations are not homogeneous across animals. More detailed exploration of the parameter space must be performed to fully model this heterogeneity in alterations to the functional network. However, the simulations presented here are sufficient to uncover links between average synchrony in the local and global functional networks, and how these change in a rodent model of neurodegeneration.

Whilst no electrophysiological studies have been performed on human patients living with dementia due to mutations in *CHMP2B*, impaired functional connectivity between regions of the brain has been reported in human disorders with related phenotypes such as frontotemporal dementia (Pijnenburg et al., 2008) and Alzheimer's disease (Delbeuck et al., 2003) . Additionally, our results are similar to those of Busche et al. (2015a,b), where long range functional disconnection and increased local functional connectivity was identified in a model of amyloidopathy, one of the primary pathologies in Alzheimer's disease. These results broadly suggest a common mechanism among differing dementia aetiologies, and that whilst the *CHMP2B*$^{\text{intron5}}$ genotype differs from those of other dementias there are mechanistic similarities which potentially explains the behavioural similarities of progressive cognitive impairment.

Through studying the electrophysiological properties of integration between neurons on both the local and whole brain scales in an animal model expressing *CHMP2B* mutations (Ghazi-Noori et al., 2012), we have gained insight into mechanisms that may underpin neurodegenerative disorders such as frontotemporal dementia (Skibinski et al., 2005), amyotrophic lateral sclerosis (Cox et al., 2010), and Alzheimer's disease (Hooli et al., 2014). We hypothesise that white matter degeneration in *CHMP2B*$^{\text{intron5}}$ transgenic animals (Ghazi-Noori et al., 2012) results in functional disconnection between regions of the brain. Increases in functional connectivity in local networks of neurons, potentially through topological reorganization of synapses, may be a compensatory mechanism to enhance whole brain integration in the presence of axonal degeneration. This hypothesis was supported by computational modelling of the mouse brain. Experimental testing of these hypotheses is an avenue for future study.

Chapter 4

Network substrates of cognitive impairment in Alzheimer's disease

This chapter is based on the work published in Clinical Neurophysiology as Tait et al. (in press) in collaboration with Dr George Stothart (data acquisition, conceptualization), Dr Nina Kazanina (data acquisition, conceptualization), Dr Elizabeth Coulthard (clinical interpretation), Dr Jon T Brown (supervision), and Dr Marc Goodfellow (supervision, conceptualization, methodological design). The author's contribution to this chapter includes preprocessing and analysis of the data, development and analysis of the model, formulation of hypotheses and methodological design (modelling/analysis), interpretation of the results, visualization of the data, and writing of the chapter.

4.1 Introduction

In the previous chapter we studied a rodent model of neurodegeneration which exhibits long range synaptic impairments and behavioural alterations reminiscent of those seen in diseases causing dementia. Whilst the study used a rodent model of a very rare mutation causing frontotemporal dementia, it demonstrated that long range synaptic impairment can compromise the ability of distributed neuronal networks in the brain to synchronize (functional connectivity). This mechanism potentially underpins the behavioural alterations seen in these animals, due to the inability of different processing systems in the brain to integrate. In humans, a prevailing hypothesis is that cognitive impairment in AD is due to similar mechanisms of disrupted structural and functional connectivity; known as the *disconnection hypothesis* (Delbeuck et al., 2003).

Evidence for the disconnection hypothesis in human studies of AD comes from a wide range of behavioural, functional, structural, and effective connectivity studies. Structural imaging methods such as diffusion weighted imaging (DWI) and diffusion tensor imaging (DTI) have been used to identify reduced white matter integrity in AD (Rose et al., 2000; Mito et al., 2018), suggestive of long range synaptic disconnection. Although structural connectivity provides a substrate for functional integration, it does not allow for study of dynamic integration of nodes in brain networks (Honey et al., 2009), and therefore cannot fully explain emergent spatiotemporal brain dynamics (Tsang et al., 2017). In order to quantify co-activity between regions of the brain, functional networks can be elucidated from time series data (section 1.8.2). Disconnection in AD has been identified in functional networks derived from imaging modalities such as EEG (Babiloni et al., 2016), MEG (Stam et al., 2009), functional MRI (Badhwar et al., 2017), and PET (Cope et al., 2018). An advantage of using EEG/MEG is that it is primarily generated by post-synaptic potentials (Olejniczak, 2006) and is therefore more directly linked to neuronal activity than other functional imaging modalities such as functional MRI which tracks haemodynamic response to neuronal activity and thus operates on a much slower time scale (Crosson et al., 2010). Because of this high temporal resolution, EEG is able to shed light on disruptions to local dynamics such as slowing of neuronal oscillations in AD (Brueggen et al., 2017).

To bridge the gap between synchronized neuronal activity and synaptic connectivity, effective connectivity studies combine computational models with both structural and functional imaging to elucidate how changes in both intrinsic dynamics and structural connectivity alter functional networks. In AD, effective connectivity studies have been used to relate structural and functional disconnection (Dermitas et al., 2017; de Haan et al., 2012b), further supporting the disconnection hypothesis of AD. However, it is unclear whether observations of functional disconnection could be explained by alterations to local dynamics, such as observed in people with AD (Brueggen et al., 2017).

Intuitively, disconnection would lead to an impaired ability of brain regions to exchange information (Uhlhaas and Singer, 2006). However, the exact links between specific disruptions to connectivity and resulting cognitive deficits of AD have not been well characterised. Cognitive function can be quantified in dementia clinics via the mini-mental state examination (MMSE) (Folstein et al., 1975). The MMSE includes tests of cognitive abilities such as spatial and temporal orientation, attention, memory, language, recall, and motor skills, giving scores for ability in each area. A number of studies have correlated structural and functional disconnection with cognitive test scores in people with AD, typically focusing on global network properties and the total MMSE score (Wu et al., 2011; Stam et al., 2007a; Lo et al., 2010; de Hann et al., 2009). However, MMSE is a broad cognitive screen probing memory, language and visuospatial function, each of which are thought to depend on distinct neuroanatomical circuitry. A quantitative link between specific network deficits and individual cognitive domains might yield more precise information about the mechanisms of cognitive decline in AD, and therefore potentially inform treatment.

In this chapter, we study functional connectivity derived from the EEG of people with AD and healthy controls, and examine the relationship between network topology and cognitive ability. We hypothesise that in AD, specific alterations to functional networks will correlate with impairments in particular cognitive domains due to disruption of integration between brain areas related to these domains, in line with the disconnection hypothesis of AD. To test this hypothesis, local and global properties of the functional networks are quantified and correlated with MMSE subscores. To provide validation that changes to functional networks are a result of alterations to the structural connectome and not distributed heterogeneity in the intrinsic node dynamics, we use a computational model which reflects realistic changes in the frequency spectrum observed in the data. Our results give crucial insight into the role of functional and effective disconnection in deterioration of ability in specific cognitive domains in AD. Since subjects in the study were free from medication, our results provide valuable diagnostic biomarkers of AD that are not attributable to effects of medication.

4.2 Materials and methods

4.2.1 EEG acquisition

All data acquisition and work described in section 4.2.1 was performed externally by collaborators[1]. All appropriate approvals for the procedures were obtained from the National Research Ethics Service Committee South West Bristol (Ref. 09/H0106/90). Participants provided written informed consent before participating and were free to withdraw at any time. People with AD were recruited from memory clinics in the South West of England on a consecutive incident patient basis. The diagnosis of AD was determined by clinical staff using neurological, neuroimaging, physical and biochemical examination together with the results of family interview, neuropsychological and daily living skills assessment according to DSM-IV (American Psychiatric Association, 2000) and NINCDS-ADRDA guidelines (McKhann et al., 1984). All patients were free from any medication known to affect cognition, e.g. cholinergic medications prescribed to treat dementia symptoms, anti-psychotics, anti-depressents, benzodiazepines, Warfarin, etc. The HOA control group was recruited from the memory clinics' volunteer research panels and were in normal general health and had no evidence of a dementing or other neuropsychological disorders, according to NINCDS-ADRDA guidelines (McKhann et al., 1984). Exclusion criteria for all groups included poor

---

[1] Data was acquired by Dr George Stothart (University of Bath Department of Psychology) and Dr Nina Kazanina (University of Bristol School of Psychological Science)

general health or a history of transient ischemic attack or stroke, significant head injury and any other significant psychological disorder or neurological disease. Data on subjects is given in Tables 4.1 and 4.2. Resting-state, eyes open EEG (64 channel) was recorded from all subjects prior to the beginning of a battery of cognitive tasks. This period, and the subsequent battery of tasks, were consistent across the two groups. All recordings had an onset time in the period between approximately 10am and 4pm, with no significant differences in time of day between groups (range of time of recording onset, reported as hours:minutes after midnight: HOA 09:48-16:08, AD 10:05-15:53; $p = 0.1434$, two sample Kolmogorov-Smirnov test). A single 20 s epoch of EEG, sampled at 1 kHz, was extracted per subject.

4.2.2 EEG preprocessing

Independent component analysis was used to remove visual and cardiac artifacts. There were no significant differences in the number of artifacts removed between HOA and AD (HOA: 3.69 ± 0.46, range 0-10; AD: 4.09 ± 0.42, range 1-8; $p = 0.4747$, Mann-Whitney U-test). Line noise at 50 Hz was removed and replaced by linear interpolation of the power spectrum. Data was bandpass filtered at 1-200 Hz, demeaned, slow non-physiological trends up to third order polynomials removed, and re-referenced to average. These preprocessing steps were performed using the Fieldtrip toolbox for EEG/MEG-analysis, developed at the Donders Institute for Brain, Cognition and Behaviour (Oostenveld et al. (2011); `http://www.ru.nl/neuroimaging/fieldtrip`).

4.2.3 Source reconstruction

Source reconstruction was performed using the Fieldtrip toolbox (Oostenveld et al. (2011); `http://www.ru.nl/neuroimaging/fieldtrip`). A template 3 layer boundary element method volume conduction model (Oostenveld et al., 2003) was used in conjunction with a template cortical source model consisting of 5124 point sources on a canonical cortical surface taken from Statistical Parameter Mapping 8 (SPM8; `https://www.fil.ion.ucl.ac.uk/spm/software/spm8/`) and implemented in Fieldtrip. Use of template models has previously been demonstrated to perform well compared to individual models derived from MRI (Fuchs et al., 2002). Dipoles were oriented normal to the surface of the cortical sheet (Hassan et al., 2014). Figure 4.1 shows the template model.

Exact low resolution brain electromagnetic tomography (eLORETA) was used to solve the inverse problem and reconstruct source activity at each of the 5124 source points (Pascual-Marqui, 2007, 2009). eLORETA is a linear, regularized, weighted minimum norm inverse solution with theoretically exact, zero error lo-

	HOA	AD
Age (± SEM; years)	76 (± 7)	79 (± 9)
MMSE (± SEM)	29 (± 1)	23 (± 3)
n	26	21
Male	14	8
Female	12	13

Table 4.1: Age, gender, and cognitive data for HOA and AD cohorts

	HOA	AD	p
Orientation to time	4.83 (± 0.41)	3.19 (± 1.42)	0.0074
Orientation to place	5.00 (± 0.00)	4.13 (± 0.72)	0.0084
Immediate recall	3.00 (± 0.00)	2.94 (± 0.25)	0.6098
Serial 7s	4.83 (± 0.41)	3.75 (± 1.61)	0.1346
World backwards	5.00 (± 0.00)	4.81 (± 0.40)	0.2923
Registration recall	2.67 (± 0.52)	0.44 (± 0.81)	0.0003
Language	7.83 (± 0.41)	6.44 (± 1.09)	0.0081
Pentagons	1.00 (± 0.00)	0.81 (± 0.40)	0.2923

Table 4.2: Mini-mental state exam sub-scores for HOA and AD cohorts. Values reported are mean ± SEM. Additionally, we report (uncorrected) p-values for each subscore.

Band name	Frequency range [Hz]	Relative Power p-value AD vs. HOA
δ	1-4	0.6849
θ	4-8	0.0187*
α	8-13	0.8052
β	13-30	0.4446
γ	30-45	0.5310

Table 4.3: Frequency bands used in the analysis. For each band, a Mann Whitney U test was performed on relative power within that band, testing AD vs HOA (see section 4.3.1).

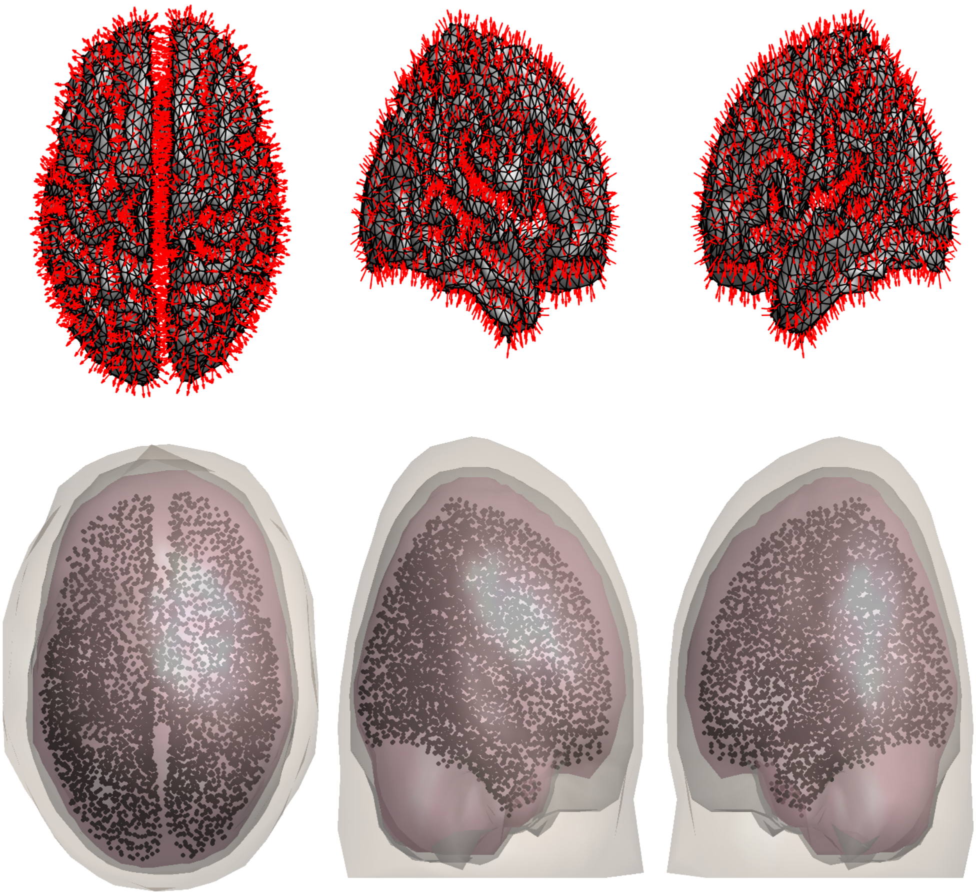

Figure 4.1: **Template head model used for source reconstruction**. (Top) Template cortical surface is shown in grey. Black dots represent source points distributed along the surface. Red arrows show dipole orientation, normal to the surface. (Bottom) Template boundary element method volume conduction model. Black dots are the same as those shown in the top row of figures, representing source points. Pink (inner layer) is conductive brain tissue. Dark grey (middle layer) is skull tissue, and light grey (outer layer) is scalp tissue.

calization even in the presence of structured biological or measurement noise (Pascual-Marqui, 2007), is suited to the study of whole brain phase synchronization (Pascual-Marqui et al., 2011; Finger et al., 2016), and the LORETA family of solutions have been validated against numerous imaging modalities (Dierks et al., 2000; Vitacco et al., 2002; Mulert et al., 2004; Pizzagalli et al., 2004; Zumsteg et al., 2005, 2006; Olbrich et al., 2009) and simulations (Pascual-Marqui et al., 2011; Finger et al., 2016).

4.2.4 Power spectral analysis

All power spectra were extracted by computing the Fourier transform of the data. The five frequency bands of interest are given in Table 4.3 (Buzsáki, 2006), whilst the broadband was defined as 1-45 Hz as this encompasses the range of these bands. Total power in a band $[f_1, f_2]$ was computed as $\sum_{f\in[f_1,f_2]} P(f)\Delta f$, where

ROI	N (right)	N (left)
Frontal Lobe		
Superior frontal gyrus	174	168
Medial frontal gyrus	188	158
Inferior frontal gyrus	76	77
Orbital gyrus	171	160
Precentral gyrus	168	133
Paracentral gyrus	37	40
Temporal Lobe		
Superior temporal gyrus	142	85
Middle temporal gyrus	71	91
Inferior temporal gyrus	90	87
Fusiform gyrus	108	102
Parahippocampal gyrus	96	91
Posterior superior temporal sulcus	40	34
Parietal Lobe		
Superior parietal lobule	107	100
Inferior parietal lobule	285	301
Precuneus	116	126
Postcentral gyrus	152	131
Occipital Lobe		
Medioventral occipital cortex	125	168
Lateral occipital cortex	132	196
Others		
Insular gyrus	86	89
Cingulate gyrus	199	224

Table 4.4: ROIs for parcellation of source data. N is the number of source points from the 5124 original cortical sources within the ROI, and the label left/right represents hemisphere.

$P(f)$ is the power at frequency f and Δf is the frequency resolution of the data. The *relative power* spectrum (Wang et al., 2015) is defined as the power spectrum normalized by total broadband power and acts as a probability distribution over frequencies, i.e. the relative power at a given frequency is the contribution of that frequency to the overall power.

In order to calculate the peak frequency of a spectrum $P(f)$ in a band $f \in [f_1, f_2]$, the spectrum was smoothed with a moving average filter of order 1 Hz (20 frequency points in this data). Peaks of the spectrum with widths at half prominence greater than 0.5 Hz were then extracted. These steps reduced the likelihood that peaks were due to noise in the spectrum. The peak frequency was then the extracted peak with maximum amplitude within the band of interest (Klimesch, 1999).

4.2.5 Functional connectivity analysis

To build functional networks, source reconstructed data was parcellated into 40 regions of interest (ROIs) based on the Brainnetome atlas (Fan et al. (2016); `http://atlas.brainnetome.org/`). A list of ROIs is given in Table 4.4. The Brainnetome atlas contains 48 regions of the brain; however, source points were restricted to the cortical surface and hence the 8 subcortical nuclei (amygdala, hippocampus, basal ganglia, and thalamus in the left and right hemispheres) were omitted.

Parcellation was performed by taking the first principal component of all source points within a given ROI in order to construct a single time series for that ROI (Hassan and Wendling, 2018). For eLORETA solutions, which constrain spatial smoothness and are low resolution, the activity of local voxels is highly correlated. The time course of the first principal component of all voxels in the ROI is a single time series whose value at each time point is minimally different to the activity of all voxels, i.e. it maximises the spatial variance explained. Functional networks were constructed by calculating the phase locking factor (PLF) (Lachaux et al. (1999); Equation 1.23) between pairs of ROI time series. PLF was calculated using custom written routines using MATLAB R2017b (`www.mathworks.com`).

To test edges against the null hypothesis that functional connections are due only to power spectral composition and distribution, each edge was tested to 5% significance vs 99 iterative amplitude adjusted Fourier transform surrogates (Schreiber and Schmitz, 1996). Due to the low resolution nature of eLORETA and therefore the potential for source leakage, PLF values with zero phase lag connection were set to zero (section 1.8.2). Furthermore, spurious indirect functional connections may arise due to strong indirect connections. For example, if node A strongly influences both node B and node C, we might observe a functional connection between nodes B and C due to common drive. Therefore, edges between pairs of nodes for which there existed a shorter indirect path were set to zero (Schmidt et al., 2014). The shortest path between nodes was calculated using the Dijkstra algorithm (Dijkstra, 1959), where the symmetric, direct distance between nodes i and j is given by $1/c_{ij}$.

Graph theoretical measures outlined in section 1.8.3 were used to quantify statistical properties of the functional network structure.

4.2.6 Computational model

To model whole brain networks, we used the phenomenological Hopf model based on that of (Dermitas et al., 2017) described in sections 1.6 and 1.7. The dynamics of each of the 40 ROIs described in Table 4.4 was described by Equation 1.20. Here, we set $\sigma = 0.02$ and $a = -0.05$ for all nodes in line with Dermitas et al. (2017), as these values were found to give the best fit to empirical functional connectivity matrices.

We optimized the effective connectivity matrix K such that the simulated functional connectivity recreated target empirical functional connectivity using a simple procedure based on that of Dermitas et al. (2017). Our target empirical functional connectivity matrix was the median of all HOA functional connectivity matrices. The optimization was performed by setting the natural frequency for each node, i, (ω_i) to the corresponding median peak frequency for each ROI in HOA subjects. The effective connectivity was initialized with $K_{ij} = 1$ if there exists some anatomical connection between ROIs i and j and $K_{ij} = 0$ otherwise, based on template structural imaging data from the Brainnetome atlas (Fan et al. (2016); `http://atlas.brainnetome.org/`). An iterative algorithm was used to optimize the weights on this matrix, where the effective connectivity at iteration n is given by

$$K_{ij}[n] = K_{ij}[n-1] + 0.2(c_{ij}^{\text{emp}} - c_{ij}^{\text{sim}}[n-1]), \tag{4.1}$$

where c_{ij}^{emp} is the target empirical functional connectivity, whilst $c_{ij}^{\text{sim}}[n]$ is the simulated functional connectivity at iteration n.

To choose an optimum matrix K, an error function was defined as Error$[n] = 1 - r(c^{\text{sim}}[n], c^{\text{emp}})$, where $r(A, B)$ is the correlation of the edges of functional connectivity matrices A and B. Due to the stochastic nature of the Hopf simulations resulting in noise on the error, instead of choosing the iteration with minimum error as optimum (Dermitas et al., 2017), we apply a moving average filter of order 25 iterations to the error function and select the minimum of this. Effective connectivity is chosen as the mean effective connectivity of the 25 iterations averaged over at the minimum.

During all subject specific simulations, the effective connectivity matrix remained at this value unless otherwise stated. Natural frequencies of the oscillators were the individual subject's peak power spectral frequencies. In simulations for which global connectivity G was optimized, Matlab's fzero function (`https://www.mathworks.com/help/matlab/ref/fzero.html`) was used with the difference between the empirical and simulated mean degrees as the error function.

4.2.7 Statistical analysis

All p-values reported here were computed using the Mann-Whitney U-test, which is non-parametric and therefore makes no assumptions about the distribution of the data. Families of tests were corrected for multiple hypotheses using the Bonferroni correction - specifically, p-values were multiplied by the number of hypotheses being corrected for. Significant results were those with Bonferroni adjusted

p-values less than 0.05. Effect sizes for the Mann-Whitney U-test are given by the rank biserial correlation (Cureton, 1956; Wendt, 1972), which is equivalent to the Mann-Whitney U statistic normalized between zero and one, given by

$$\bar{U} = 1 - \frac{2U}{n_1 n_2}, \tag{4.2}$$

where $\bar{U}$ is the rank biserial correlation, U is the U-statistic, and n_i is the number of subjects in cohort i. To help interpret this measure, we can consider an alternative (but equivalent) formulation of rank biserial correlation. If we make some hypothesis on the statistic being tested (e.g. the statistic will be larger for HOA than AD), then take all pairs of AD and HOA subjects, rank biserial correlation is the absolute value of the fraction of pairs that support the hypothesis (in our example, pairs where the statistic is larger for the HOA subject than the AD subject) minus the fraction that are against the hypothesis (pairs where AD is larger than HOA). If all pairs support or all pairs are against the hypothesis (large effect size), $\bar{U} = 1$, whilst if an equal number are for and against (no effect size), $\bar{U} = 0$.

4.3 Results

4.3.1 Global power spectrum and functional connectivity analysis

As a first step, we aimed to characterise changes in dynamics and functional networks in people with AD, relative to healthy older adults. To do this, EEG from HOA and people with AD was projected into source space using eLORETA and downsampled to 40 ROIs (Table 4.4, section 4.2.3). To investigate potential slowing of the EEG in people with AD (Strik et al., 1997; Adler et al., 2003; Lindau et al., 2003; Dauwels et al., 2011; Hatz et al., 2015a; Liu et al., 2016; Wang et al., 2015; Goossens et al., 2017), we calculated the power spectrum of the EEG for each subject, averaged over all ROIs. There was no significant difference in total broadband (1-45 Hz) power between AD and HOA subjects ($p = 0.3745$). To explore the contributions of different rhythms to the overall EEG, we calculated the relative power spectrum averaged over all ROIs (Figure 4.2A). It can be seen that slower frequencies, between around 3 and 10 Hz, are more prominent in the people with AD than the HOA. Furthermore, faster frequencies (above around 15 Hz) are less prominent in the people with AD, suggesting a slowing of the EEG in AD. To further quantify these observations, we calculated total relative power in each of the five classic frequency bands, given in Table 4.3, (Figure 4.2B). Delta, theta and alpha relative power was found to increase on average in people with AD, whilst beta and gamma rhythms decreased on average. However, the

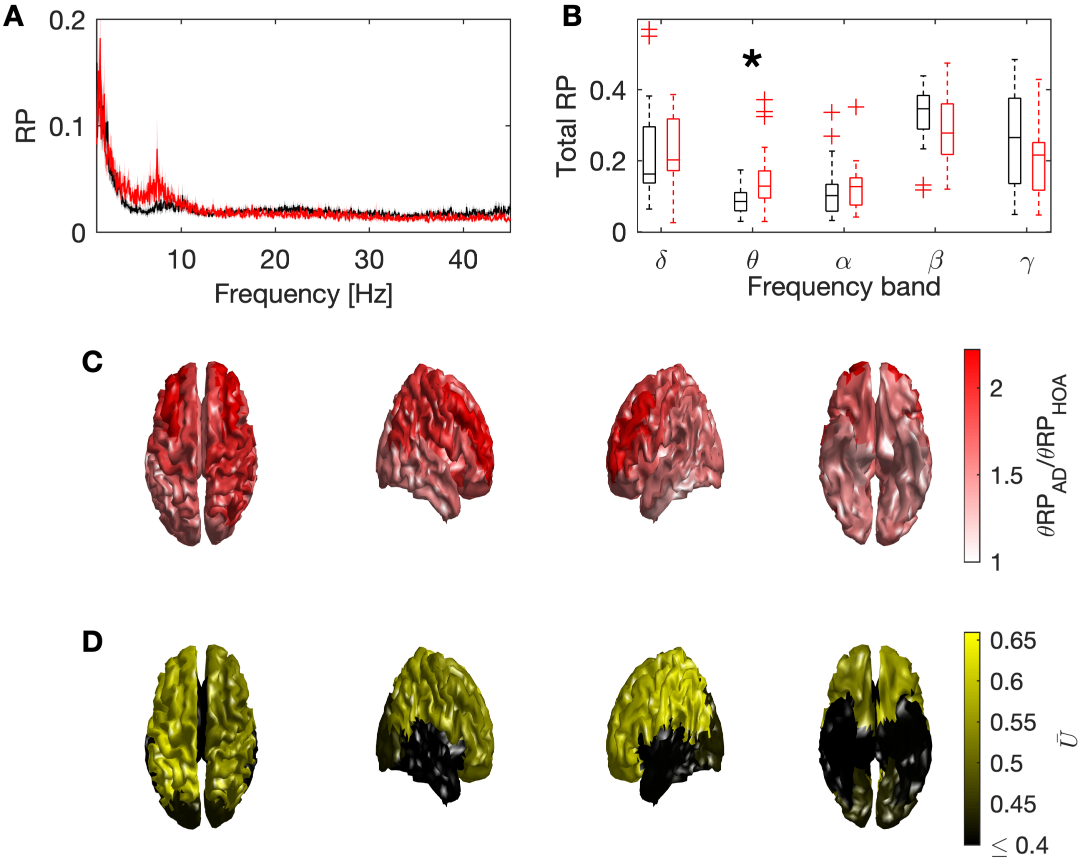

Figure 4.2: **Power spectral analysis**. (A) Average relative power over all ROIs. The black line is HOA, and the red is AD. Shaded regions are standard error on the mean. (B) Boxplots of total relative power in each frequency band. Black boxes are HOA, red is AD. The only significant change in AD is the increase in the θ (4-8 Hz) band. (C) Ratio of the within-group mean θ relative power in AD vs HOA for each ROI shows an increase over all ROIs. (D) Effect size of increase in θ relative power for each lobe (see Table 4.4). Frontal and parietal lobes in both hemispheres were significant to $p < 0.05$ after Bonferonni adjustment of p-values. In C and D, views are (from left to right) top down with subject facing towards top of page, right hemisphere, left hemisphere and from underneath looking up with subject facing towards top of page.

only significant difference was the increase in theta relative power (θRP) ($p = 0.0187$; see Table 4.3 for p-values in other bands). For this reason, we focused our remaining analysis on the theta band. Figure 4.2C-D show spatial distributions and effect sizes for changes in theta power, suggesting that the observed slowing of the EEG is predominantly driven by the frontal and parietal lobes.

We extended this analysis into the spatial domain by constructing theta band functional networks, calculating the phase locking factor (PLF; Equation 1.23) between the activity of each pair of ROIs. To quantify average synchrony in the network, mean degree (MD; Rubinov and Sporns (2010); Equation 1.25) was calculated. To complement this, we used small-worldness (SW; Humphries and Gurney (2008); Equation 1.33) as a quantification of topological organization of

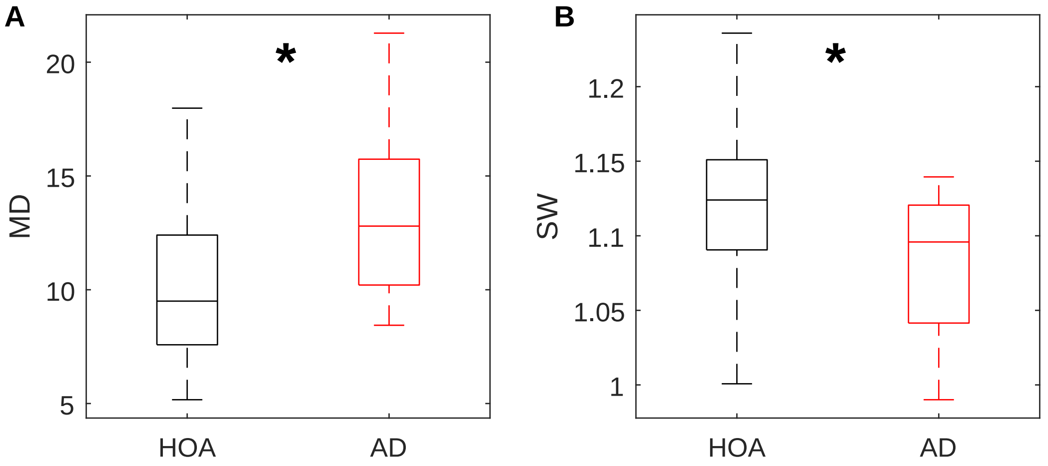

Figure 4.3: **Global graph theoretical measures for θ band networks**. In all cases, black is HOA and red is AD. (A) Mean degree increases significantly in AD. (B) Small-worldness decreases significantly in AD. A star denotes significance (Bonferroni corrected $p < 0.05$).

the networks. MD was found to increase significantly ($p = 0.0111$) in people with AD, suggesting the presence of enhanced synchrony on average in AD. However, SW was found to decrease significantly ($p = 0.0318$) in people with AD, suggesting that the topology of the network AD networks are organized less efficiently for information transfer (Latora and Marchiori, 2001). Figure 4.3 shows boxplots of each of these measures for HOA vs AD.

4.3.2 Relationships between functional network measures and cognition

The relationship between specific changes to functional networks in AD and the phenotype of the disease is not well understood. To investigate this, we calculated the correlation between spectral and functional network measures and cognitive test scores. 20 out of the 21 AD subjects we analysed undertook the mini mental state examination (MMSE), which provides a score out of 30 based on cognitive tasks (Folstein et al., 1975). Average scores for both the HOA and AD cohorts are given in Table 4.1.

The Pearson's correlation between MMSE score and each of the measures (θRP, MD, SW) was calculated. The only measure that exhibited a significant correlation with MMSE score was SW (Figure 4.4), suggesting that functional network topology is associated with cognitive decline in AD. A full list of correlations and p-values can be found in Table 4.5.

To develop a deeper understanding of the relationship between functional network topology and cognitive deficits in AD, we tested whether small-worldness correlates with particular aspects of cognition using the MMSE subscores, which

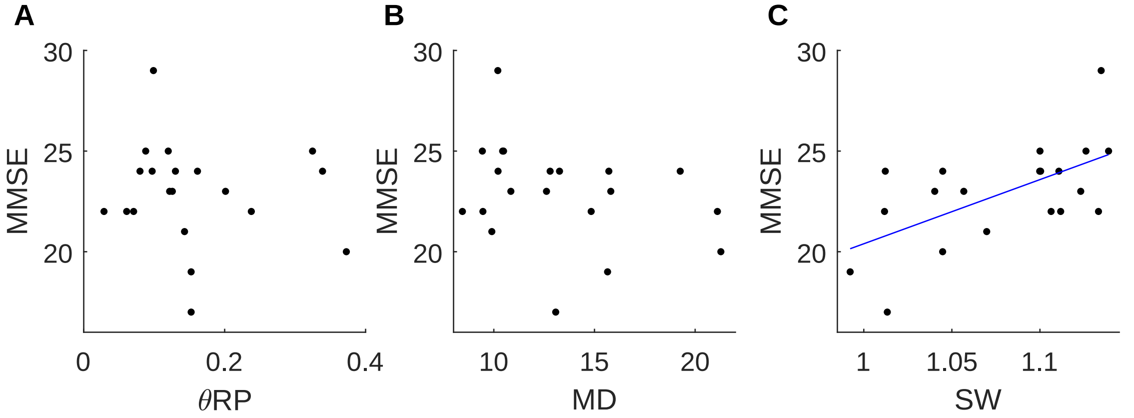

Figure 4.4: **Correlation between MMSE score and global EEG measures**. Plots of MMSE score against (A) theta band relative power, (B) mean degree, (C) small-worldness. Each black dot represents a single subject. Blue lines show linear model fit in the case of significant correlation.

	r	p
Relative Power	-0.1203	0.6133
Mean Degree	-0.3150	0.1761
Small-Worldness	0.5921	0.0060*

Table 4.5: Correlations and p-values for power spectral and graph theoretical measures vs MMSE score.

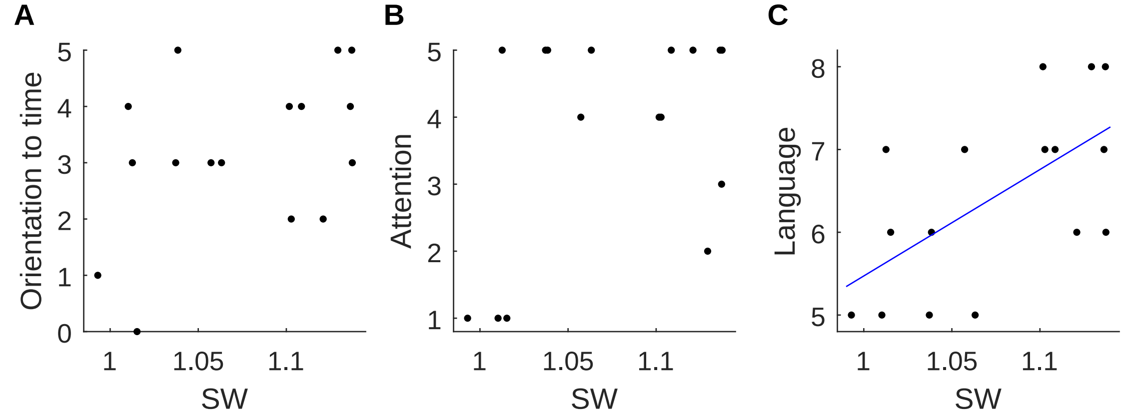

Figure 4.5: **Correlation between MMSE subscores and small-worldness**. Plots of theta band small-worldness against orientation to time (A), attention by serial 7s (B), and language (C) for the people with AD. Each black dot represents a single subject. Blue lines show linear model fit in the case of significant correlation.

	r	p
Orientation to time	0.4360	0.0905
Attention	0.3995	0.1252
Language	0.6132	0.0115*

Table 4.6: Correlations and p-values for MMSE subscores vs small-worldness.

were available for 16 of the 21 people with AD (the missing subscores were due to some recruiting clinics only provided total MMSE score). Subscores were orientation to time, orientation to place, immediate recall, attention, memory, language, and drawing overlapping pentagons. Table 4.2 shows subject scores for each of these subscores. There was almost no variance in the 16 AD subjects for orientation to place, immediate recall, memory, or pentagons; for this reason we ruled these subscores out of further analysis. We therefore calculated the correlation of orientation to time, attention (by serial 7s), and language with small-worldness. Of these three subscores, only language was significantly correlated with small-worldness, suggesting that changes to the topology of the functional networks in AD is more predominantly associated with language deficits than attention or orientation to time. Table 4.6 and Figure 4.5 show correlations and p-values of each of these subscores against small-worldness.

4.3.3 Local topology changes influence small-worldness

In order to add insight into how the pathology of AD relates to behaviour, we sought to further understand how the changes in small-worldness that are associated with language deficits arise in AD. We therefore examined the causes of the observed changes in small-worldness at the level of nodes of the functional networks.

Small-worldness is defined as the ratio of clustering coefficient to characteristic path length (Humphries and Gurney, 2008). To understand whether reduced small-worldness in AD is due to a reduction in clustering coefficient, increased characteristic path length, or both, we quantified each of these measures for the networks. Clustering coefficient demonstrated a small but non-significant decrease in AD ($p = 0.1223$), whilst characteristic path length significantly increased ($p = 0.0303$), suggesting that changes to small-worldness are primarily driven by larger path lengths in the functional network. To identify whether this is a global effect or whether it is driven by certain regions of the brain, we calculated the closeness centrality for each node, which can be interpreted as a local counterpart to (inverse) characteristic path length (section 1.8.3). That is, nodes with small closeness contribute to a larger characteristic path length.

On average, closeness centrality was found to decrease in all ROIs (Figure 4.6A). To gain understanding at the higher level of organisation of lobes of the brain, we averaged closeness centrality into eight lobes (left and right frontal, temporal, parietal, and occipital lobes), and then compared the resulting measure in AD vs HOA for each lobe, via non-parametric statistical testing (Mann-Whitney U test). Effect sizes for the Mann-Whitney U test (quantified by the rank biserial correlation (Cureton, 1956; Wendt, 1972)) for each lobe are shown in Figure 4.6B. After Bonferroni correction for multiple hypotheses, only the closeness

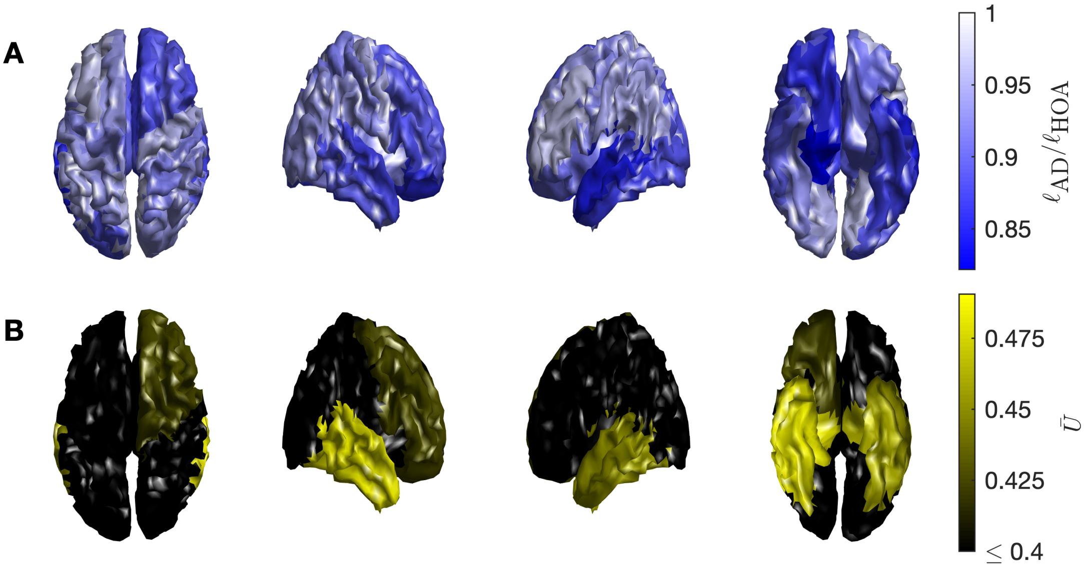

Figure 4.6: **Closeness centrality of ROIs in theta band networks** Decreases in closeness are likely to drive reduced small-worldness in AD. Here, we show (A) the ratio of within-group mean θ closeness in AD vs HOA for each ROI shows a decrease in all ROIs, and (B) effect sizes for each lobe. Effect sizes are largest in the temporal lobes, with the right temporal lobe being significant to $p < 0.05$ after Bonferroni adjustment. For the left temporal lobe, $p = 0.0579$.

	Relative Power	Degree	Closeness
Right Frontal Lobe	0.0307*	0.2521	0.1014
Left Frontal Lobe	0.0150*	0.0138*	0.4224
Right Temporal Lobe	0.7780	0.7441	0.0343*
Left Temporal Lobe	0.1926	0.1143	0.0579
Right Parietal Lobe	0.0206*	0.1076	0.5918
Left Parietal Lobe	0.0118*	0.0579	1.0000
Right Occipital Lobe	0.1539	0.0243*	1.0000
Left Occipital Lobe	0.1539	0.0418*	1.0000

Table 4.7: Bonferroni corrected p-values for local power and graph theoretical measures.

of the right temporal lobe is significantly different for AD vs HOA (Bonferroni adjusted $p = 0.0343$). However, the effect size for the left temporal lobe is also high (Bonferroni adjusted pvalue $p = 0.0579$), and we note that Bonferroni correction is highly conservative, carrying increased chance of type II errors (false negatives) (Perneger, 1998). Figure 4.6 and Table 4.7 demonstrate that the temporal lobes both have a much larger effect size than the rest of the brain. We therefore suggest that it is likely that path length increases in both temporal lobes drive the increased small-worldness in AD.

4.3.4 Modelling the mechanisms of changes to functional connectivity

In order to better understand the dynamic and network mechanisms that underpin the observed changes to functional connectivity in AD, we used a computational model to simulate brain activity across the ROIs. Figure 4.2C-D demonstrated heterogeneous slowing of the power spectrum across ROIs in HOA and AD. Since the distribution of intrinsic frequencies of coupled oscillators plays a vital role in phase locking (Gambuzza et al., 2016; Stam et al., 2007a; Lowet et al., 2017), we sought to uncover whether these distributed local power spectral changes alone could account for the observed changes in functional connectivity. To do this, a computational model of coupled stochastically driven oscillators (each representing an ROI) was simulated (see section 4.2.6). In the model, spatially heterogeneous alterations to the power spectrum were incorporated via the intrinsic natural frequencies of the oscillators, which are free parameters of the model. For each subject, the intrinsic frequency of each oscillator was inferred from the data by computing the frequency of the power spectral peak in the 6-13 Hz alpha-theta band for its respective ROI (see section 4.2.6). Coupling between oscillators was represented by an effective connectivity (EC) matrix. To focus on the consequences of changes to node frequencies, a representative HOA EC was computed using the median natural frequency distribution for HOA for local dynamics and the median HOA FC as the optimization target (see section 4.2.6). Using this EC matrix for all subjects, but individual distributions of frequencies across nodes, we then simulated the model for each subject and examined whether the model revealed differences in FC across cohorts. This method is outlined in Figure 4.7.

Figure 4.8 shows the simulated networks for all 47 subjects, and Figure 4.9A shows an analysis of mean degrees for HOA and AD. The mean degree of the simulated AD networks was significantly larger than in the HOA networks ($p = 0.0152$), suggesting that power spectral slowing may be responsible for the observed increased mean degree in the AD networks. Furthermore, the spatial distributions of the alterations in degree largely replicate those seen in the empir-

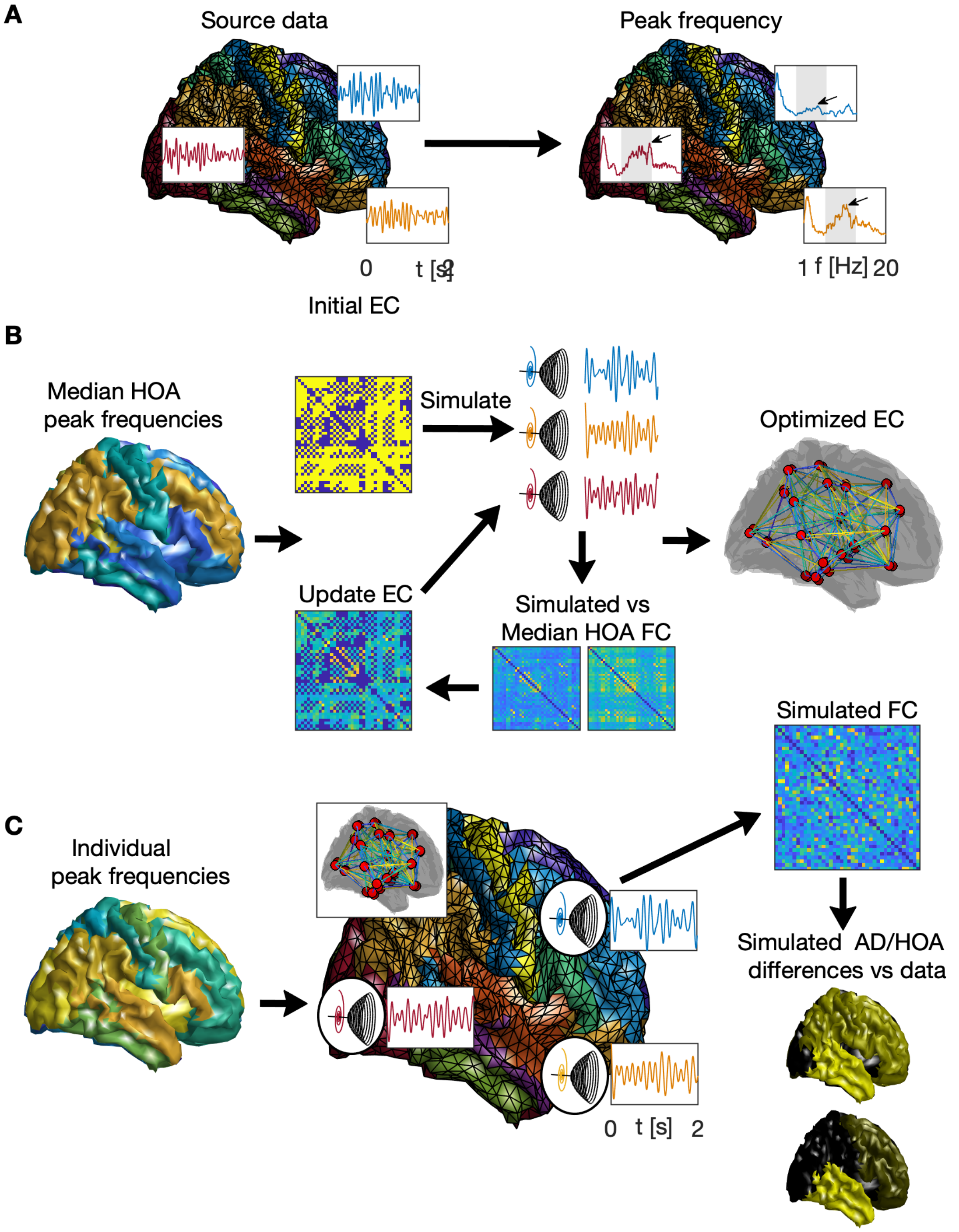

Figure 4.7: **Modelling methods to explore whether local power spectral differences can account for functional network changes in AD.** (A) The natural frequency distribution for each subject was given for each ROI by the frequency with peak power in the 6-13 Hz band in the data. (B) To generate a representitative HOA EC, the natural frequencies of each ROI were given by their median value from the HOA subjects. EC was optimized using an iterative algorithm in order to replicate the median HOA FC. (C) For each subject, time series were simulated using individual natural frequencies and the template EC. Comparisons were then made between HOA and AD simulations to test whether changes to local dynamics explain FC differences in the data.

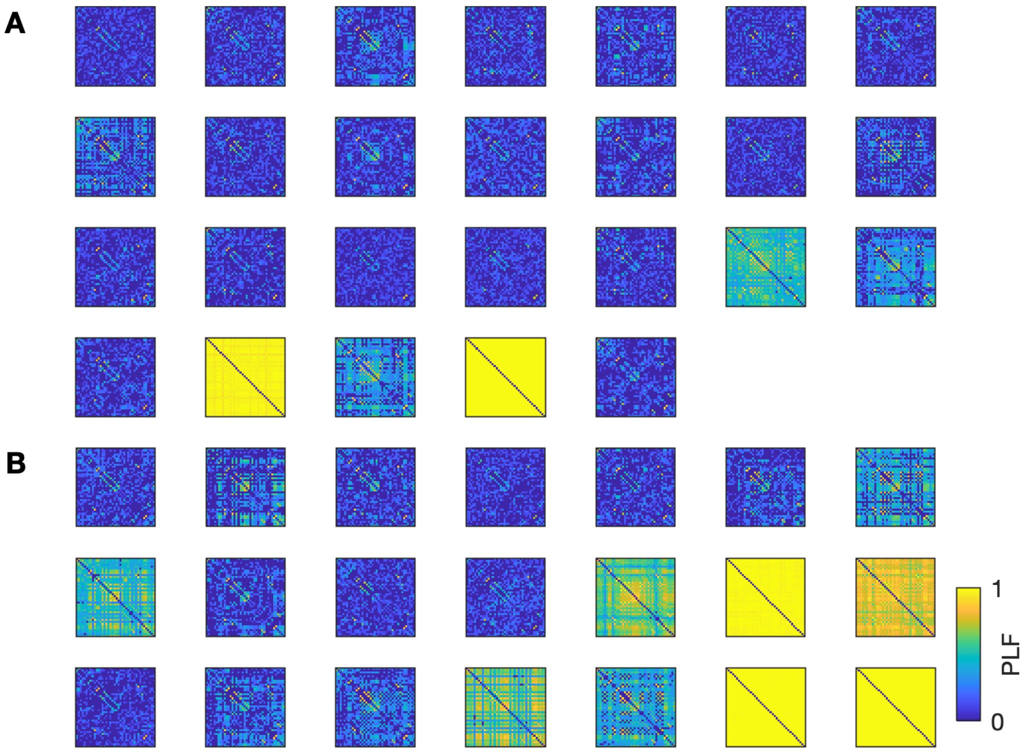

Figure 4.8: **Simulated networks with $G = 1$.** (A) Simulated HOA networks. (B) Simulated AD networks. For all networks, the underlying structural connectivity remains the same, with the only difference being the natural frequencies of the Hopf oscillators adjusted to the peak power spectral frequencies in the data for their respective ROIs. All networks are plotted on the same colour scale (bottom right).

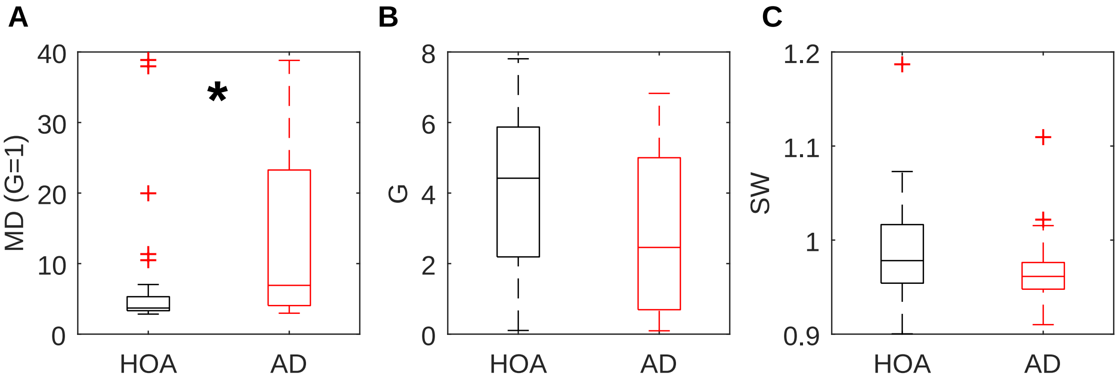

Figure 4.9: **Comparisons of HOA and AD in simulated functional networks.** (A) Initially, networks were simulated with the same effective connectivity, with the only differences between subjects in the model was the natural frequency of the Hopf oscillators, set to the subject specific power spectral peak frequency. Mean degree of these networks significantly increased. (B) Global coupling strength in the networks was then altered such that the mean degree of a given subject's simulated network equaled the mean degree of the subject's empirical network. G was found to decrease non-significantly. (C) Small worldness does not significantly decrease in the simulated networks, however, the effect size of the decrease is large ($p = 0.0507$).

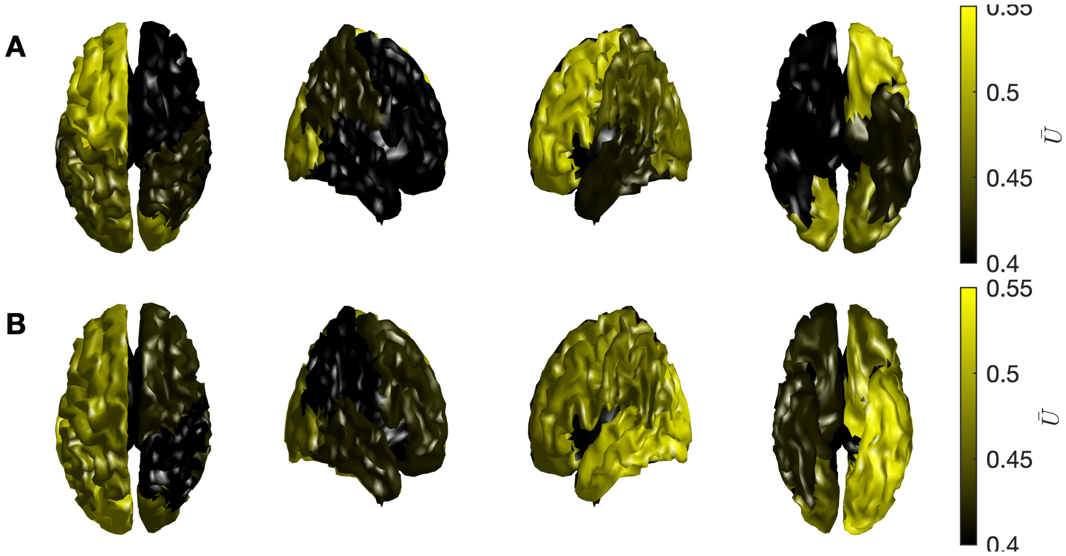

Figure 4.10: **Spatial distribution of effect sizes for changes of degree in AD in the simulated networks are reflective of those in the empirical networks.** (A) Effect sizes for increase in degree in each lobe in the data. (B) Same as A, but in the simulated networks where the only difference between AD and HOA are the frequency distributions. The distribution is largely similar, with exception of a much larger increase in degree in the left temporal lobe in the simulated AD networks than in the data.

ical data (Figure 4.10), with an exception of a large increase in degree of the left temporal lobe not observed in the data. However, the effect size for the increase in MD was notably larger in simulations than in the data. In order to correct this, the global coupling constant in the model was adjusted for each subject until the mean degree of the simulated functional networks matched the mean degree of the empirical functional networks. Figure 4.11 shows the simulated networks for all 47 subjects with global coupling adjusted. The resulting estimates of global coupling strength were smaller in the AD cohort, though not significantly different from the HOA (Figure 4.9B, HOA = 4.12 ± 0.45, AD = 2.91 ± 0.53; $p = 0.1016$). This supports the disconnection hypothesis of AD, since lower global coupling strength was required in the AD cohort to recreate the observed differences in FC mean degree.

In the simulated functional networks, small-worldness was found to decrease, but not significantly ($p = 0.0502$), in AD compared to HOA. However, we examined the spatial distribution of changes to closeness centrality in AD compared to HOA, and found this did not replicate the subject data. For example, in the subject data, the largest effect sizes were found in the temporal lobes, whilst simulated networks exhibited large effect sizes in the right frontal, temporal, and parietal lobes (Figure 4.12A, Table 4.8). Therefore, we found that changes to the intrinsic dynamics alone, via the incorporation of the distribution of intrinsic frequencies across nodes, was not sufficient to describe topological changes to the functional network; particularly increased path lengths in the temporal lobes. This

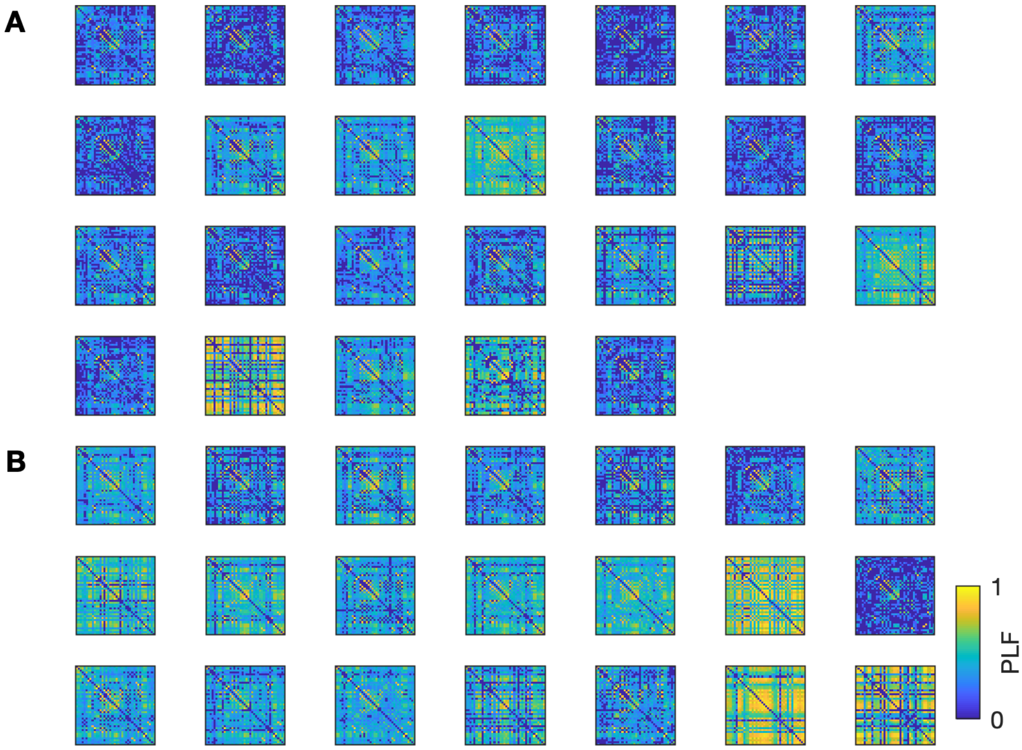

Figure 4.11: **Simulated networks with G optimized.** In these simulations, global coupling constant G was optimized using Matlab's fzero function such that the mean degree of the simulated network matched the mean degree of the empirical network. (A) Simulated HOA networks. (B) Simulated AD networks. For all networks, the underlying structural connectivity remains the same, with the only difference being the global coupling strengths and natural frequencies of the Hopf oscillators adjusted to the peak power spectral frequencies in the data for their respective ROIs.

	$\alpha = 1$	$\alpha = 0.5$
Right Frontal Lobe	0.0320*	1.0000
Left Frontal Lobe	0.1814	1.0000
Right Temporal Lobe	0.0051*	0.0003*
Left Temporal Lobe	1.0000	0.0004*
Right Parietal Lobe	0.0320*	0.4893
Left Parietal Lobe	0.2660	1.0000
Right Occipital Lobe	0.4224	0.5386
Left Occipital Lobe	0.0794	0.48932

Table 4.8: Bonferroni corrected p-values for closeness centrality in the simulated networks with no temporal lobe disconnection ($\alpha = 1$) and temporal lobe disconnection ($\alpha = 0.5$).

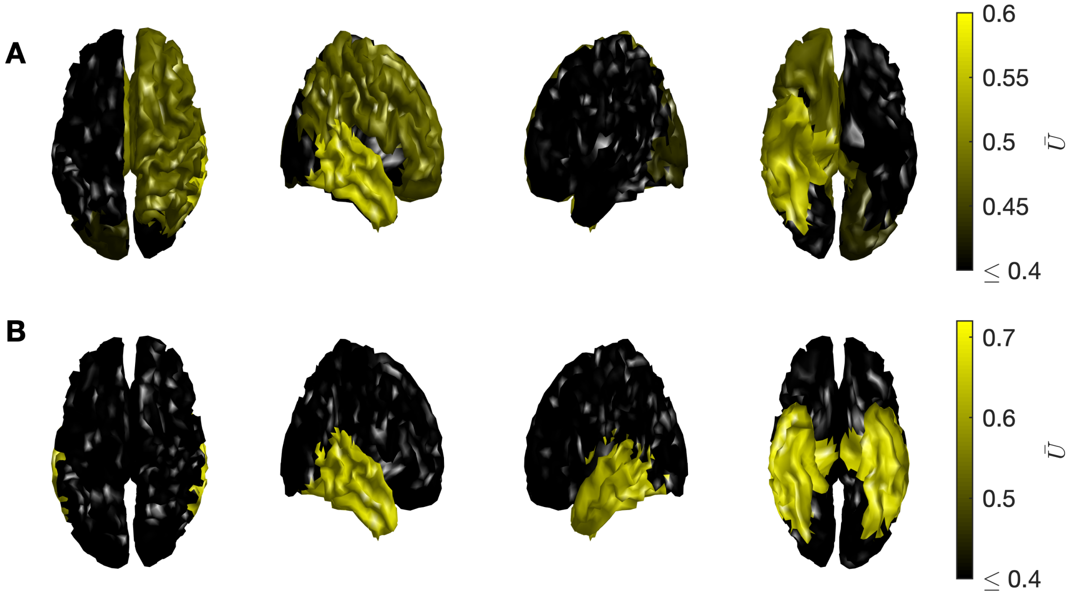

Figure 4.12: **In the simulated networks, temporal lobe disconnection is required for similar spatial distributions of changes in closeness to the data.** (A) Effect sizes of closeness centrality in simulated networks (no temporal lobe disconnection). The largest effect sizes for changes in closeness centrality were found in the frontal, parietal, and temporal lobes. (B) Effect sizes of closeness centrality in simulated networks (with temporal lobe disconnection). The largest effect sizes were found in the two temporal lobes, which more accurately represents the results seen in the data.

suggested that alterations to the effective connectivity would be required in order for the model to fully explain the data.

To test this, we simulated a reduction in temporal lobe connectivity by multiplying all effective connections to ROIs in the temporal lobes by a constant $0 \leq \alpha < 1$. We simulated the model for a range of values of α and found that the spatial distributions of changes in closeness centrality in AD networks demonstrated large effect sizes constrained to the temporal lobes, therefore closely replicating the data. Figure 4.12B and Table 4.8 demonstrate these results for $\alpha = 0.5$. Simulations over a range of values of α showed consistency in the results, particularly for $\alpha < 0.8$ (Figure 4.13). These results suggest that the observed changes in functional connectivity are due to reduced effective connectivity (likely due to loss of synaptic connectivity) between the temporal lobes and the rest of the brain, combined with alterations to the intrinsic frequencies of oscillations within nodes.

4.4 Discussion

In this chapter, EEG from people with AD and HOA controls was analysed in order to uncover disruptions to connectivity in the brain and altered local dynamics.

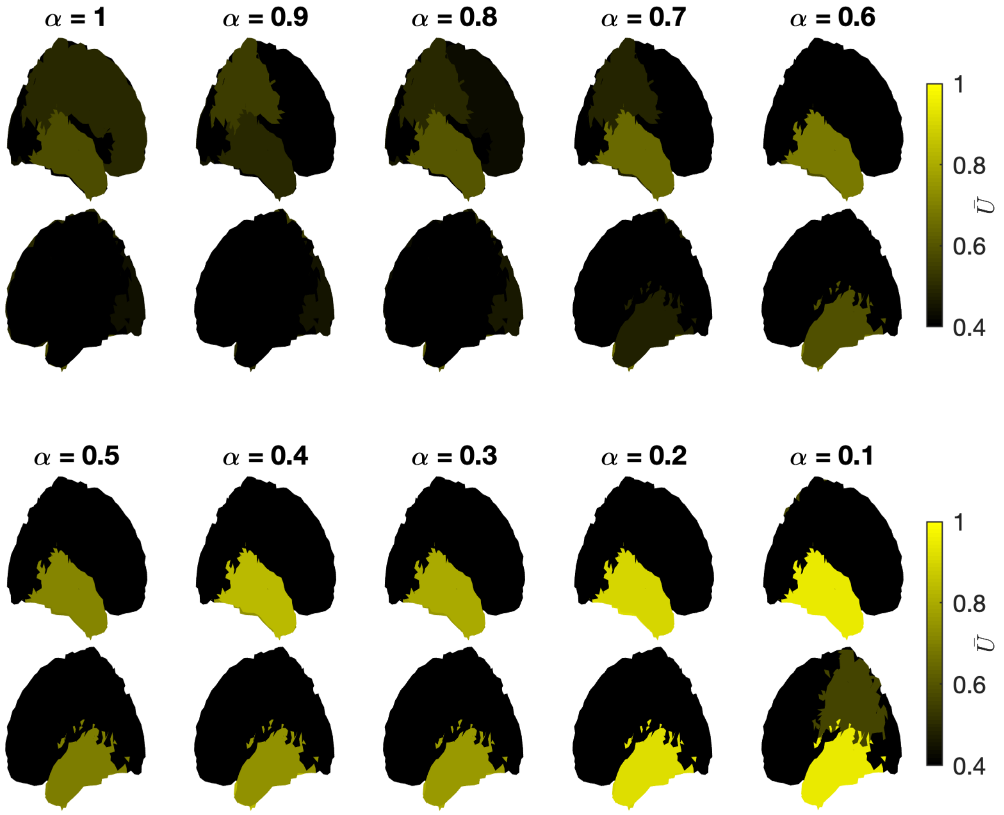

Figure 4.13: **Effect sizes for closeness centrality for a range of α.** For each simulation, subject specific intrinsic frequencies were used in the model, and for the AD group all temporal lobe connections in the effect connectivity matrix were multiplied by a constant α. Closeness centrality for the resulting functional networks was calculated and reported here are the effect sizes for differences between AD and HOA.

Through correlations with cognitive tests scores, we studied how the extent of these alterations were reflected in cognitive decline in the AD cohort. We found that whilst significant alterations to the power spectrum and average synchrony between regions of the brain were identified, these were not indicators of the level of cognitive decline in people with AD. However, topological organization of the networks, as quantified by small-worldness, was found to significantly and positively correlate with MMSE score, particularly the language sub-score. Reduced small-worldness was found to be driven predominantly by reduced closeness of the temporal lobes, which computational modelling suggests was likely driven by impaired synaptic connectivity between the temporal lobes and other regions, in combination with heterogeneous spectral slowing. These results give potential insight into the role that disruption to temporal lobe connectivity plays in language impairments in AD, and more generally advances our understanding of how the disconnection hypothesis of AD relates to the phenotype of the disease.

4.4.1 Methodology

A major methodological difference between the study presented here and the majority of previous EEG studies in AD is that the EEG presented here was recorded in an eyes open, as opposed to an eyes closed state. It has been shown that both the power spectrum and functional networks are different in eyes open and eyes closed conditions (Wu et al., 2010; Tan et al., 2013; Miraglia et al., 2016; Kan et al., 2017). Therefore our work provides insight into a different active network than the large literature on EEG in AD recorded in eyes closed resting state conditions (Strik et al., 1997; Adler et al., 2003; Lindau et al., 2003; Dauwels et al., 2011; Hatz et al., 2015a; Wang et al., 2015; Liu et al., 2016; Goossens et al., 2017; Ianof et al., 2017). Since cognitive deficits in AD predominantly relate to the awake and alert states, it is possible that studying eyes open data gives key insight into how network deficits drive cognitive decline. This could underpin our finding that network small-worldness correlated with MMSE score in the AD cohort, whereas previous studies conducted in the eyes closed paradigm found no such correlations in both EEG and fMRI (Stam et al., 2007a; Sanz-Arigita et al., 2010). An additional key strength of the data used in this study is that all subjects were free from dementia related medications, meaning the results presented here can not be an artifact of medication induced alterations to network states.

Another methodological step taken was to map the EEG into source space. Source space analyses have the advantage of being able to attribute activity to specific regions of the brain, thereby allowing for anatomical interpretation of the results (Michel et al., 2004). This is particularly useful when studying neurological disorders, as it allows for study of the spatial distribution of neuropathology. However, the method of source mapping we used relies on a number of key assumptions. Firstly, a simplifying assumption in building the forward model was to consider the head as being constructed of three homogeneously conducting layers of tissue (Fuchs et al., 2002; Oostenveld et al., 2003). Secondly, we worked with the assumption that a template head model would provide a sufficient mapping for all subjects. A range of methods for building the forward model, from a single homogeneously conducting sphere to highly detailed, realistic models containing many layers of anisotropically conducting tissue, are available (Hallez et al., 2007), but a trade-off between computational expense and accuracy of the results must be made when deciding on a method to generate a forward model. In the absence of individual MRI scans, the three (homogeneous and isotropic) layer boundary element method template head model used in this study has been shown to perform to a much higher standard than a three layer spherical head model and to a comparable level as individually derived three layer head models (Fuchs et al., 2002). Furthermore, boundary-element method models are reasonably computationally inexpensive (Hallez et al., 2007). For these reasons, there is a trend in studies such as ours where individual MRIs are unavailable, to use a template head model consisting of three homogeneously and isotropically conducting layers (Cantero et al., 2009; Canuet et al., 2011; Aoki et al., 2015; Hata et al., 2016; Ianof et al., 2017; Ikeda et al., 2017; Vecchio et al., 2017; Smith et al., 2018; Medvedeva and Yanho, 2018; Farina et al., 2018). It is, however, unclear to what extent the effect of aging and potential cortical atrophy in people with AD may have on the validity of this template head model. Nonetheless, there exists much precedent for use of a template head model in studies concerning older adults and people with AD (Canuet et al., 2012; Vecchio et al., 2014, 2017; Hata et al., 2016; Ianof et al., 2017; Medvedeva and Yanho, 2018). For people with AD, data was recorded within days of diagnosis, so whilst severe cortical atrophy is unlikely, this cannot be ruled out without validation using an MRI. Regardless, because of the use of a template head model that may not capture individual differences, changes in head shape due to aging, and the fact we can not with certainty rule out the presence of atrophy, all statistical analyses were performed on the level of lobes of the brain, meaning results are likely to be robust to small errors in localization.

Furthermore, the functional networks derived from the source space data are dependent on the combination of reconstruction method and functional connectivity method (Hassan et al., 2014, 2017; Finger et al., 2016). Here, our choice of eLORETA was motivated by desire to map 64 channel EEG to large-scale source dynamics (see e.g. Schirner et al. (2015); Finger et al. (2016)). Estimation of spatially smooth current source density by inverse modelling is dependent on the number of electrodes used (Hassan et al., 2017); due to discrete sampling of electrodes on the scalp, the information that can be used to describe source dynamics is limited by the number of electrodes. For studies with a similar number of electrodes to the one presented here (60-71 electrodes), eLORETA has been demonstrated to outperform other linear inverse methods such as minimum norm estimates and linearly constrained minimum variance beamforming at localizing sources and network estimation in studies with known source origin such as simulations (Pascual-Marqui et al., 2011; Finger et al., 2016), deep brain stimulation (Mideksa et al., 2016), and comparisons of resting state networks with fMRI (Liu et al., 2018), further motivating our use of the eLORETA algorithm to perform source reconstruction. The choice of PLF was motivated by simulations demonstrating the eLORETA/PLF combination could accurately recreate ground truth functional connectivity matrices (Finger et al., 2016). Since eLORETA incorporates spatial smoothness constraints, neighbouring source points will demonstrate strong instantaneous correlations (Pascual-Marqui et al., 2011). To mitigate these source leakage effects zero-lag PLF values were disregarded in our study (Schmidt et al., 2014).

A methodological point of note in this study is the use of 20 seconds of data. Typically, EEG studies use epoch lengths of the order seconds to minutes (Gudmundsson et al., 2007). For epoch lengths of these orders of magnitude, studies of spectral measures have found little information to be gained from using epochs longer than approximately 20 seconds (Gasser et al., 1985; Salinsky et al., 1991; Gudmundsson et al., 2007), whilst studies of small-worldness properties of functional networks derived from phase measures have demonstrated reliability at around 6 seconds epoch length (Fraschini et al., 2016). However, it is worth noting that long term EEG, intracranial, and simulation studies have demonstrated that over periods of hours and days there are fluctuations in functional network measures (Honey et al., 2007; Kunhert et al., 2010; Chu et al., 2012) such as small-worldness derived from phase locking networks (Kunhert et al., 2010).

4.4.2 Electrophysiological and network markers of Alzheimer's Disease

Power spectral slowing in the EEG of people with AD has been established for over 20 years (Strik et al., 1997), and has been consistently identified as increases in low frequency power (Strik et al., 1997; Adler et al., 2003; Lindau et al., 2003; Dauwels et al., 2011; Hatz et al., 2015a; Liu et al., 2016; Wang et al., 2015), decreases in high frequency power power (Strik et al., 1997; Lindau et al., 2003; Dauwels et al., 2011; Liu et al., 2016; Wang et al., 2015), and reduced peak frequency (Goossens et al., 2017). Our power spectral results were largely consistent with this literature, particularly identifying increases in the contributions of slow (theta) rhythms and reductions to peak power spectral frequency. However, many of these past studies were performed in sensor space, therefore very few studies have identified regions of the brain responsible for this power spectral slowing, information which may potentially be insightful for the development of treatments and understanding disease progression. In this study, increases in the relative power of slow oscillatory activity was localized to the frontal and parietal lobes, which is largely in agreement with the results of Ianof et al. (2017). Interestingly, we found no correlation between theta band relative power and cognition as measured by MMSE. Engels et al. (2016) also found cortical theta power did not correlate with MMSE score in people with AD, but source reconstructed hippocampal theta power did. This suggests that while we found no correlation between slowing and MMSE scores, this could be due to our restricting source space to the cortical surface.

Disconnection between regions of the brain is believed to play an important role in cognitive decline in AD (Delbeuck et al., 2003). An EEG marker of this is reduced synchrony between regions of the brain (Adler et al., 2003; Pijnenburg et al., 2008; Wang et al., 2014, 2015; Hata et al., 2016). However, in this study and others (Koenig et al., 2005a; Gallego-Jutgla et al., 2015; Cantero et al., 2009), increases in functional connectivity were identified in AD, here quantified by a significantly increased weighted mean degree. It is possible that these inconsistencies are due to variations in methodology; choice of functional connectivity and use of weighted or unweighted networks can result in differences in the functional network structure, topology, and sensitivity to changes in AD (Dauwels et al., 2010; Joudaki et al., 2012; Jalili, 2016). Important to note, however, is that the increased mean degree may not be in opposition to the disconnection hypothesis; using computational modelling, we found that changes in mean degree (as well as localized changes in degree) were well explained by intrinsic changes in dynamics, namely power spectral slowing (Figure 4.10). In fact, to accurately recreate mean degrees on a subject-by-subject basis, global coupling strength decreased (albeit non-significantly) in AD, suggestive of global disconnection. The slowing itself may also be evidence for disconnection in AD, since modelling studies have suggested power spectral slowing may arise from disconnection between the cortex and thalamus (Abuhassan et al., 2014) identified in fMRI studies (Wang et al., 2012). Changes in mean degree did not correlate with cognitive test scores, which may also be supportive of the hypothesis that power spectral changes are driving the differences in MD since power spectral differences showed no correlation to MMSE.

Small-worldness was used as a measure of network topology (Humphries and Gurney, 2008), since a small-world network is structured for efficient information transfer on both a local and global scale (Watts and Strogatz, 1998; Latora and Marchiori, 2001), and small-worldness of the functional network has consistently been reported to reduce in AD (Stam et al., 2007a; de Hann et al., 2009; Wang et al., 2014; Vecchio et al., 2017). Our results were in line with this past literature, finding that small-worldness was reduced in the AD cohort. Furthermore, we found that the reduction in small-worldness was driven by an increased characteristic path length, which is also in line with previous literature (Stam et al., 2007a; Vecchio et al., 2014). To understand better how these changes arose, closeness centrality of each node (which is a local counterpart to the inverse of characteristic path length) was calculated, and found to decrease in the temporal lobes, suggesting that increased path lengths in the temporal lobes are likely highly important for the changes in global network topology seen in AD. Furthermore, small-worldness was found to significantly correlate with MMSE score in the AD cohort, which suggests that network topology, as opposed to the amount of synchrony in the network, is highly important for cognition and is likely a key driver of cognitive deficits in AD.

A small-world network has both high local and global efficiency (Latora and

	Efficiency
Right Frontal Lobe	0.0740
Left Frontal Lobe	0.1116
Right Temporal Lobe	0.0538
Left Temporal Lobe	0.0435*
Right Parietal Lobe	0.0740
Left Parietal Lobe	0.1263
Right Occipital Lobe	0.3410
Left Occipital Lobe	0.0574
Global	0.0297*

Table 4.9: Bonferroni corrected p-values for local and global effeciency.

	$\alpha = 1$	$\alpha = 0.5$
Right Frontal Lobe	0.0243*	0.3115
Left Frontal Lobe	0.2028	0.6201
Right Temporal Lobe	0.0299*	0.0029*
Left Temporal Lobe	0.1014	0.0110*
Right Parietal Lobe	0.0197*	0.1443
Left Parietal Lobe	0.2389	0.4893
Right Occipital Lobe	0.3453	0.9665
Left Occipital Lobe	0.0954	0.1814

Table 4.10: Bonferroni corrected p-values for local efficiency in the simulated networks with no temporal lobe disconnection ($\alpha = 1$) and temporal lobe disconnection ($\alpha = 0.5$).

Marchiori, 2001). Many more recent studies have used efficiency based measures to study AD (Berlot et al., 2016; Afshari and Jalili, 2017; Sami et al., 2018), since global efficiency is a measure of how efficiently information can be transferred through the network (Latora and Marchiori, 2001) and local efficiency is suited to study local effects of neurodegeneration as a measure of tolerance of the network to dysfunction at a given node (Latora and Marchiori, 2001; Rubinov and Sporns, 2010; Sami et al., 2018). For these reasons, we also ran the topological analysis with global and local efficiency replacing small-world and closeness (see Table 4.9). Global and local patterns of efficiency reflected those of small-worldness and path length; notably global efficiency was found to reduce significantly and the largest effect sizes for reductions in local efficiency were in the temporal lobes. Much like for small-worldness, there was a positive correlation between global efficiency and MMSE score, but this was smaller than the correlation for small-worldness vs MMSE and non-significant. In the modelling study, spatial distributions of alterations to local efficiency closely matched those of closeness centrality (Table 4.10), also requiring temporal lobe disconnection to drive similar spatial patterns as in the data. Importantly, this allows us to interpret our results in terms of information transfer in the network, suggesting that in AD the temporal lobes play less of a role in aiding the efficient flow of information through the brain than in HOA. This, combined with the highly related increased closeness, suggest that the temporal lobes are becoming functionally less integrated with the rest of the brain in AD.

A computational model based on that of Dermitas et al. (2017) was used to explore the mechanisms underpinning functional network differences in the AD cohorts. Dermitas et al. (2017) used individual structural MRIs to derive initial EC matrices for the iterative optimization algorithm. It was therefore reasonable to assume the optimized EC is representative of synaptic EC, and to use these to make inferences on changes of the structure of the brain in AD. In this study, a template, unweighted structural MRI was used for initial EC, and hence the simple iterative algorithm used for optimization is unlikely to give a global optimum. Hence, we do not aim to interpret the EC matrices derived here as representative of structural differences between regions of the brain. Instead, the only interpretation we make is that the effective connectivity matrices are sufficient to generate realistic functional connectivity. For this reason, all analyses of the model output are related to the simulated functional connectivity, and we do not analyse individual effective connectivity in a similar manner to Dermitas et al. (2017). That said, the effective connectivity presented here can still give important insight into how effective connectivity changes in AD. Our modelling results suggest that given a generative model of HOA functional connectivity, alterations to long range effective connections in the temporal lobe are required to cause functional connectivity representative of the AD cohort.

A key assumption of the modelling procedure is that power spectral differences are intrinsic to regions of interest and not a result of altered connectivity. Whilst the accuracy of this assumption is unclear, provided we view the model as a way to generate realistic functional connectivity patterns and not a biophysically realistic representation of neuronal activity, this assumption does not alter the results. However, it is important that we interpret results such as those shown in Figure 4.9 and Figure 4.10 as showing that intrinsic power spectral differences are a potential and sufficient mechanism to drive certain changes to functional connectivity in AD, but without further experimental evidence we can not know whether this is the true mechanism. Regardless, this does not change the key result presented here, which demonstrates that even intrinsic power spectral changes would not be sufficient to drive the changes in small-worldness and closeness observed in the data, and that further synaptic mechanisms (such as temporal lobe disconnection) are required.

Whilst other neurodegenerative disorders or dementia aetiologies were not examined in this study, the methods used here are likely to be applicable. Spectral slowing and functional network alterations have been reported in vascual dementia (Neto et al., 2015; van Straaten et al., 2015), dementia with Lewy bodies (Kai et al., 2005; Andersson et al., 2008; Bonnani et al., 2008; Roks et al., 2008; Dauwan et al., 2016), and frontotemporal lobar degeneration (Lindau et al., 2003; de Hann et al., 2009; Yu et al., 2016; Sami et al., 2018). Many of these studies have found differences in the sensor space topography of spectral and network alterations that can discriminate between AD and other types of dementia (Bonnani et al., 2008; Nishida et al., 2011; Neto et al., 2015; Dauwan et al., 2016; Yu et al., 2016; Sami et al., 2018), but very few have applied source reconstruction (Nishida et al. (2011) being a notable exception) to study the spatial differences in terms of cortical generators. Therefore it would be of interest for future work to apply the source space and computational modelling approaches used here to study other dementias.

4.4.3 Temporal lobe disconnection, phenotype, and the potential role of tau pathology

In this chapter, we augmented our functional network study with computational modelling and correlation with cognitive test scores. This allowed us to relate functional network changes with pathological mechanisms, and increase our understanding of how specific network disruptions can drive exact cognitive deficits characteristic of AD.

Small-worldness of the functional network was found to significantly correlate with both total MMSE score and the language subscore, suggesting topology of the functional network plays a key role in driving language deficits in early stage AD. Local graph theoretical analysis and computational modelling suggested that changes in small-worldness were a result of long range structural and functional disconnection in the temporal lobes. Language impairment in AD has previously found to be linked to temporal lobe atrophy in structural MRI, functional MRI, SPECT, PET, CT and post-mortem studies (Harasty et al., 1999; Galton et al., 2000; Domoto-Reilly et al., 2012), and language impairments have been linked to neuronal death and functional connectivity in the temporal lobe in other neurological disorders such as temporal lobe epilepsy (Bartha et al., 2005; Trimmel et al., 2018). Whilst past studies in AD have identified temporal lobe network deficiencies in both functional (Medvedeva and Yanho, 2018; Canuet et al., 2012) and effective networks (Dermitas et al., 2017), this is the first study the authors are aware of that have complemented this with cognitive test scores and found a direct link with language deficiencies in AD.

The pathological mechanisms driving the effective connectivity, functional connectivity, and cognitive changes reported here are still unclear, but we hypothesise tau pathology plays a critical role. AD has two primary pathologies, namely amyloid plaques and neurofibrillary tangles due to hyperphosphorlyated tau protein (Querfurth and LaFerla, 2010). In AD, tau pathology originates in and around the temporal cortex (Braak and Braak, 1991), and temporal lobe tau pathology has consistently been reported in people with AD in both post-mortem and neuroimaging studies (Saint-Aubert et al., 2017; Galton et al., 2000). From the EEG, it is not possible to directly measure tau burden in our cohort of subjects. However, functional network measures such as closeness and local efficiency have been identified to negatively correlate with tau burden (Cope et al., 2018), meaning interpreting these as a potential proxy for tau burden would suggest temporal lobe tauopathy in our subjects. PET imaging has correlated the severity of temporal lobe tau burden with language impairments in AD (Bejanin et al., 2017), whilst post-mortem studies have demonstrated particularly strong tau burden in the temporal cortex of aphasic people with AD (Galton et al., 2000). Therefore, there is much evidence alluding to tauopathy as a pathological driver for the network and cognitive changes reported here. Whilst amyloidopathy is also likely important for cognitive changes in AD, this link appears to be less direct, with many studies finding tau burden correlates more strongly with cognitive test scores than amyloid (Nelson et al., 2012) - more specifically, a PET study found that temporal lobe tau burden correlates with language deficiencies in AD, but temporal lobe amyloid burden does not (Bejanin et al., 2017).

4.4.4 Summary and conclusions

In this chapter, we propose long range synaptic disconnection in the temporal lobes as a potential mechanism directly underpinning cognitive and language deficits in AD. The results presented here suggest that this synaptic disconnection manifests itself in the form of reduced effective connectivity between the temporal lobes and other anatomical regions of the brain. This reduced effective connectivity results in reduced functional integration of the temporal lobes and less efficient global network organization (reduced 'small-worldness'), in turn leading to cognitive deficits in the form of language dysfunction. Increased mean degree is also observed in the networks, but computational modelling suggests that this change, unlike the topological network measures, can be well described by heterogeneous power spectral slowing; in fact, global disconnection was required to accurately replicate the mean degree of each network. The results presented here give key insight into a specific link between disconnection, namely functional and effective disconnection of the temporal lobes, and language deficiencies in the early stages of AD. The anatomically localized nature of the findings and links with a specific cognitive domain mean that these results have the potential to inform treatments and therapies for people diagnosed with Alzheimer's disease.

Chapter 5

Reduced EEG microstate sequence complexity and altered cortical generators in Alzheimer's disease

The work presented in this chapter was performed in collaboration with Dr George Stothart (data acquisition), Dr Nina Kazanina (data acquisition), Dr Jon T Brown (supervision), and Dr Marc Goodfellow (supervision). The author's contribution to this chapter includes preprocessing and analysis of the data, formulation of hypotheses and methodological design (analysis), interpretation of results, visualization of the data, and writing of the chapter.

5.1 Introduction

Spectral slowing and functional disconnection between EEG time series are widely reported in AD (Babiloni et al. (2016); section 1.3; chapter 4), and the focus of the previous chapter. These data are typically measured on a time scale of the order of seconds to minutes in order to obtain reliable estimates (Gudmundsson et al., 2007; Fraschini et al., 2016). However, it is believed that information processing in the brain happens on a millisecond scale (Koenig et al., 2002; Khanna et al., 2015; Michel and Koenig, 2018), and thus the brain's resting state is composed of rapid transitioning between a number of distinct resting state networks corresponding to different cognitive domains (Lehmann et al., 1998; Britz et al., 2010; Michel and Koenig, 2018). EEG microstate analysis is a method proposed to study this switching behaviour of the resting state (Khanna et al. (2015); Michel and Koenig (2018); section 1.8.4).

Microstate analysis involves studying the instantaneous topographic maps of the EEG (Lehmann et al., 1987; Koenig et al., 1999). Past studies of EEG microstates have remarkably found the EEG to be comprised of only a small number of topographic classes, such that the EEG remain stable in a given class for periods of the order tens or hundreds of milliseconds before rapidly switching to another class (Koenig et al., 1999; Khanna et al., 2015; Michel and Koenig, 2018). These rapidly switching periods of quasi-stability are hypothesised to be the electrophysiological correlates of the brain's resting state networks relating to different functions underpinning information processing (Lehmann et al., 1987; Michel et al., 2001; Koenig et al., 2005b; Britz et al., 2010; Musso et al., 2010; Khanna et al., 2015; Milz et al., 2016), earning microstates the nickname "atoms of thought" (Lehmann et al., 1998). Alterations to microstates have been observed in healthy development and aging (Koenig et al., 2002) and a range of neurological disorders including dementia (Ihl et al., 1993; Dierks et al., 1997; Strik et al., 1997; Stevens and Kircher, 1998; Nishida et al., 2013), schizophrenia (Koenig et al., 1999; Lehmann et al., 2005; Nishida et al., 2013), and depression (Strik et al., 1995; Atluri et al., 2018) - see Khanna et al. (2015) for a comprehensive review.

In Alzheimer's disease research, EEG microstates have received relatively little attention. Early in the history of microstates, a number of studies identified alterations to EEG microstate statistics in people with Alzheimer's disease (Ihl et al., 1993; Dierks et al., 1997; Strik et al., 1997; Stevens and Kircher, 1998), but these studies used adaptive windows as opposed to the more modern clustering methods to define microstates (see subsection 1.8.4 for a discussion on adaptive windowing vs clustering tools), meaning that alterations to the well studied 'canonical maps' (Khanna et al. (2015); Michel and Koenig (2018); section 1.8.4) have not been characterised in AD. Since the functional significance of these maps in cognition have been uncovered in recent years (Britz et al., 2010; Brodbeck et al., 2012; Milz et al., 2016; Seitzman et al., 2017), characterization of EEG microstates using clustering methods can potentially give crucial insight into the mechanisms underpinning impaired cognition in AD.

Much interest has been given to how properties such as duration of a microstate, percentage of time within a class (coverage of the class), and topography of microstate maps are altered in neurological disorders (Strik et al., 1995, 1997; Dierks et al., 1997; Stevens and Kircher, 1998; Koenig et al., 1999, 2002; Lehmann et al., 2005; Irisawa et al., 2006; Kikuchi et al., 2007; Kindler et al., 2011; Nishida et al., 2013; Andreou et al., 2014; Tomescu et al., 2015; Gao et al., 2017; Zappasodi et al., 2017). Patterns of transitions between classes have also been shown to alter in neurological disorders (Lehmann et al., 2005; Nishida et al., 2013; Tomescu et al., 2015), suggesting that studying transitioning behaviour of microstates may give further mechanistic insights into cognition and neurological disorders as well as increase sensitivity of electrophysiological biomarkers. However, the 'syntax analysis' (Lehmann et al., 2005; Nishida et al., 2013) used to analyse transitioning behaviour in these studies assumes stationary and Markovian transitioning, whilst recent work has brought into question the validity of these assumptions (Van De Ville et al., 2010; von Wegner et al., 2017). Therefore novel methodologies for studying the transitioning behaviour of EEG microstates that do not rely on these assumptions could give new insights into alterations to information processing and switching between active networks in AD on the millisecond scale, and potentially act as a more sensitive neurophysiological signature of AD in the EEG.

In this chapter, we analyse EEG microstates in unmedicated people with early stage AD with the objectives to characterize alterations to microstates such as altered topographies, coverage, and duration. Furthermore, we present a novel measure of the transitioning behaviour of EEG microstates which does not assume this to be Markovian or stationary, by applying the Lempel-Ziv complexity (LZC) algorithm (Lempel, 1976) to the microstate sequences. We hypothesise that there will be alterations to the transitioning dynamics and topographies of the canonical maps in AD. Since these maps are related to information processing in different cognitive domains, this can give crucial insight into mechanisms underpinning cognitive impairment in AD.

5.2 Materials and methods

5.2.1 EEG acquisition and preprocessing

EEG acquisition was performed externally by collaborators and is described in section 4.2.1. Preprocessing is described in section 4.2.2. EEGs were bandpass filtered at 1-30 Hz in line with past microstate studies (Koenig et al., 1999; Khanna et al., 2014).

5.2.2 Microstate extraction

Microstates were extracted using a k-means clustering method based on that of Koenig et al. (1999). The method is briefly outlined here. The global field potential (GFP) of the EEG at each time point is given by the standard deviation over all electrodes at that time point (Koenig et al., 1999). Topographic maps at the peaks of the GFP were extracted as these have the highest signal-to-noise ratio (Lehmann et al., 1987). GFP peak maps were then clustered using the k-means clustering algorithm described in Koenig et al. (1999), with a k-means++ algorithm used to select the initial k maps (Arthur and Vassilvitskii, 2007). For a given value of k, the clustering algorithm was repeated 20 times and the resulting cluster maps that explained most variance were chosen to be the optimum (Koenig et al., 1999). Microstates were defined to switch at the midpoints between GFP peaks, and all time points within a microstate were assigned to the class of the GFP peak.

The choice of k is non-trivial. For each subject, we used the Krzanowski-Lai criterion (Krzanowski and Lai, 1988) to assess the optimum number of microstates (Hatz et al., 2015a). In this data, there were no significant differences between the optimum number of microstates in AD and HOA as identified by a non-parametric Mann-Whitney U test. The median optimum over all subjects was four, so $k = 4$ maps were used for all subjects.

Since k-means clustering is performed on a subject-wise basis, it is important for statistical purposes that the four classes are comparable both within and between cohorts. Firstly, for each cohort (HOA or AD), a global clustering algorithm was performed (Khanna et al., 2014) to relabel classes such that classes were comparable between subjects within a cohort. Secondly, visual inspection and calculation of correlation coefficients of the four globally clustered centroid maps per cohort were used to align classes such that class labels were comparable between cohorts.

5.2.3 Microstate analysis

Basic microstate statistics

Mean microstate duration for each class and percent time spent within a class (coverage) were calculated (Strik et al., 1995, 1997; Dierks et al., 1997; Stevens and Kircher, 1998; Koenig et al., 1999, 2002). For each measure, a two-way ANOVA was performed to asses statistical differences, including terms for disease group, microstate class, and an interaction term. Since ANOVA tests are parametric and rely on assumptions of normality, significant results were post-hoc validated using a non-parametric Mann-Whitney U test; namely significant interaction terms were tested with Mann-Whitney U tests for each class, whilst significant disease group terms were assessed by averaging over classes and performing a Mann-Whitney U test between groups.

Analysis of microstate syntax, i.e. Markovian transitioning, was performed by extracting the transition matrix from the data by counting the number of transitions from class i to class j and normalizing by the total number of transitions (Lehmann et al., 2005; Kikuchi et al., 2011; Nishida et al., 2013). Edges of the matrix were tested (Kikuchi et al., 2011) using a two-way ANOVA including terms for edge and the interaction between edge and disease group.

Topographic differences between groups were assessed with class-wise one way topographic analyses of variance (TANOVA) (Strik et al., 1998; Milz et al., 2016), comparing the topographic dissimilarity (Strik et al., 1998) against 999 non-parametric surrogates computed by permutation of group labels. TANOVA

p-values are then computed vs this null distribution by rank ordering the dissimilarities of the surrogates and original data in descending order, then computing the position of the original data set in this distribution. Finally, this is divided by 1000 (999 surrogates + 1 original data set). Therefore a minimum possible p-value of 0.001 is available, deemed sufficient to identify significant differences in topographies.

Microstate complexity

Here we present a novel measure of EEG microstate transitioning that, unlike the Markovian syntax analysis, does not rely on assumptions of stationarity or Markovianity (von Wegner et al., 2017). The measure involves calculating the Lempel-Ziv complexity (LZC) (Lempel, 1976) of the microstate sequence. The LZC of a string is defined as the number of different substrings within the string when read from left to right. A string is said to have low complexity if there are a small number of frequently repeating sequences. The algorithm for computing LZC, which is outlined in Figure 5.1, is the basis of a number of lossless compression algorithms (Ziv and Lempel, 1977, 1978; Welch, 1984) that identify distinct substrings in the data that are repeated frequently, allowing for these strings to be replaced by a marker (Lempel, 1976) reducing the size of the data.

LZC has in the past been used to calculate the complexity of a univariate EEG signal (see subsection 5.2.5), but we believe use of this measure to explore the complexity of the microstate sequences is novel. We refer to this measure of microstate LZC as C. For calculation of C, the EEG was converted to a discrete text sequence by computing the microstate sequence for the data, thereby mapping each time point from $\mathbb{R}^{64}$ to a single, discrete value in the set of microstate classes $\{A, B, C, D\}$, creating a single string of length equal to that of the original EEG time series. LZC was then computed on the transitioning sequence (e.g. a sequence AAABBCCCDAADD would be reduced to ABCDAD, and LZC calculated on the reduced sequence). The choice of computing LZC on the transitioning sequence instead of the raw microstate sequence was motivated by the fact the latter is likely to be strongly influenced by the increase in microstate duration. Since LZC tends to increase with sequence length, only the only first N entries of the switching-sequence were used to calculate C . Here, we chose $N = 250$ as this number is small enough that all subjects had a switching sequence of length greater than or equal to this number.

All statistical comparisons of microstate LZC between groups was performed using a non-parametric Mann-Whitney U test.

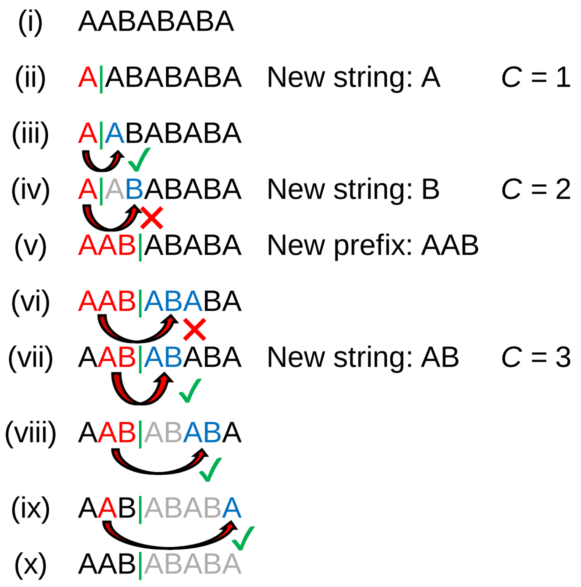

Figure 5.1: **Calculation of LZC from a string**. (i) We aim to calculate the LZC from a string S consisting of A's and B's. The k'th entry of S is denoted $S[k]$. (ii) We begin with a prefix of length one, demonstrated by the vertical green line separating the prefix from the rest of the string. The aim is to describe S in terms of a small number of substrings of the prefix (pointers). LZC (C) is the number of distinct substrings in the data. The initial prefix (A) is a new substring, so we initialize $C = 1$. (iii) Working from left to right, the pointer matches $S[2]$ (both are the letter A), so complexity does not increase. (iv) However, $S[3]$ is the letter B and hence does not match the pointer. Therefore a new substring has been identified (B), and C increases to 2. (v) Since the current prefix is not sufficient to describe the whole data, we then move it right to the point at which there is no match, making a new prefix AAB. (vi) Pointer AAB does not match $S[4,5,6]$, so we next explore substrings of the prefix as the pointer. (vii) Pointer AB matches with $S[4,5]$, so a new string is defined and complexity increases ($C = 3$). (viii) Furthermore the pointer AB also matches with $S[6,7]$. (ix) The pointer A matches with $S[8]$. (x) S is fully described by these 3 substrings, meaning the LZC of S is 3.

5.2.4 Cortical source localization

Cortical source localization was performed using the eLORETA algorithm (Pascual-Marqui, 2007, 2009) implemented in the sLORETA/eLORETA software package (`http://www.uzh.ch/keyinst/loreta.htm`). This package uses a 3 layer BEM head model (Fuchs et al., 2002) based on the Montreal Neurological Institute average MRI brain map (MNI152) (Mazziotta et al., 2001) and a 6239 voxel source space limited to a cortical grey matter surface. This model has been validated and demonstrated to perform to a similar standard as individual MRI derived head models (Fuchs et al., 2002). Visualization of results was performed using custom written Matlab routines and used the 'Colin27_2016' template MRI and cortical surface implemented in Brainstorm (Tadel et al., 2011), which is documented and freely available for download online under the GNU general public license (`http://neuroimage.usc.edu/brainstorm`).

To compare two topographic maps, for example the cluster average for a class between groups, the difference between maps was computed and then source localized using eLORETA. The source space representation of the topographic difference map shows the difference between cortical generators underpinning the two maps, since the forward model assumes linear mixing, i.e. $Y = \Phi X$ therefore $Y_2 - Y_1 = \Phi(X_2 - X_1)$, where Y is the topographic map in sensor space, Φ is the leadfield, and X is the set of cortical sources generating the map. To gain a measure of statistical effect size between groups, the subject-wise maps are source localized and then a t-statistic computed on a voxel-wise basis (Milz et al., 2016).

5.2.5 Additional EEG complexity measures

To compare how our novel measure of EEG complexity based on the LZC of microstate sequences performs compared to classical measures of EEG complexity, we additionally computed two such measures often used in the literature. Firstly, past literature has used an alternate method for calculation of the LZC of the EEG (Abásolo et al., 2006; Hornero et al., 2009; Sabeti et al., 2009; Dauwels et al., 2011; Fernández et al., 2011; Liu et al., 2016), which we label time-series LZC. For a given EEG time series (i.e. a single channel), each time point is mapped from $\mathbb{R}$ to a value from a discrete set, by binarizing the data based on the median. LZC of this binary sequence is then computed as outlined above. Here, this was computed for each channel and averaged to give a single value of time series LZC for each subject.

An advantage of microstate LZC over time series LZC is that microstate LZC accounts for multivariate patterns in the data. Therefore we also compare against Ω-complexity, which is a widely used multivariate measure of EEG complexity (Saito et al., 1998; Molnár et al., 2006; Irisawa et al., 2006; Czigler et al., 2008; Dauwels et al., 2010, 2011) based on information theory, and uses information contained in the covariance matrix to estimate the complexity of the path of the EEG through N dimensional space, where N is the number of channels. Given EEG with a covariance matrix Γ which has eigenvalues λ_i (where $i = 1, \ldots, N$ and N is the number of EEG electrodes), Ω-complexity is given by

$$\Omega = \exp\left(- \sum_{i=1}^{N} \left(\frac{\lambda_i}{\Lambda} \cdot \log\left(\frac{\lambda_i}{\Lambda} \right) \right) \right), \tag{5.1}$$

where, $\Lambda = \sum_{i=1}^{N} \lambda_i$. Ω-complexity is close to zero if all channels follow a highly similar time course, whilst it is close to one if the channels follow very different

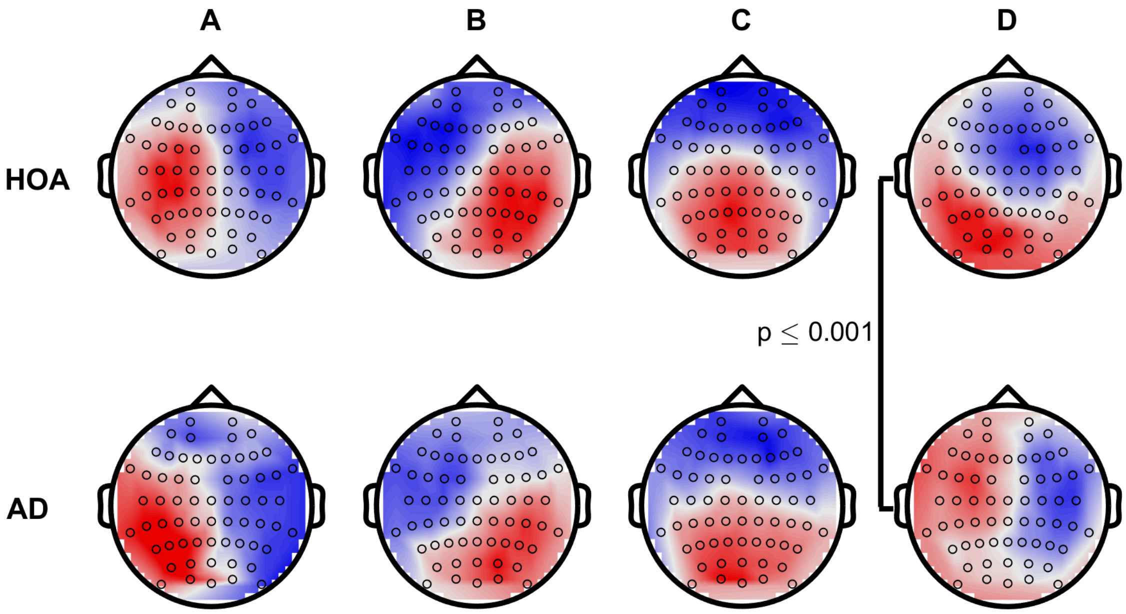

Figure 5.2: **Microstate topographies for the four classes**. (Top) Globally clustered maps for HOA cohort, for classes A-D from left to right. (Bottom) As above, but for the AD cohort. Black circles mark the electrode locations.

time courses.

5.3 Results

5.3.1 Parietal inactivation alters the topography of class D in AD

Microstate topographies for each of the four classes in HOA and AD are shown in Figure 5.2, and for the HOA subjects largely align with the four canonical classes (Khanna et al., 2015; Michel and Koenig, 2018), which are electrophysiological correlates of the auditory (A), visual (B), saliency (C), and frontoparietal working memory/attention (D) resting state networks (Britz et al., 2010; Michel and Koenig, 2018). To test for alterations to the topographies in AD, a topographic analysis of variance (TANOVA) (Strik et al., 1998; Milz et al., 2016) was performed for each microstate class. Class D was found to be significantly different in AD (class A, $p = 0.0690$; B, $p = 0.1980$; C, $p = 0.8980$; D, $p \leq 0.001$; Figure 5.2). Source reconstruction was used to explore cortical source generators underpinning this alteration (Pascual-Marqui et al., 2014; Milz et al., 2016; Atluri et al., 2018). Figure 5.3A shows the eLORETA solution of the instantaneous map given by the difference of the global class D maps for HOA and AD (i.e. the difference

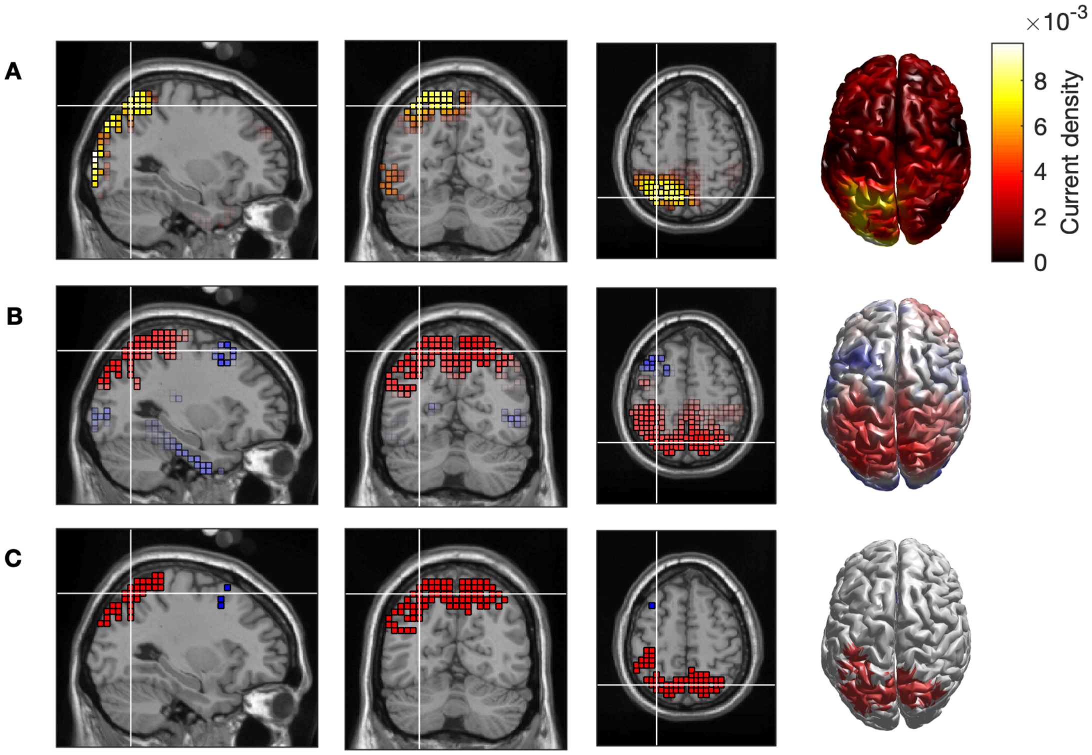

Figure 5.3: **Cortical source generators underpinning alterations to microstate class D in AD**. (A) eLORETA solution to the instantaneous topography given by taking the difference between the global class D maps for HOA and AD. (B) t-statistic for voxel-wise comparisons of the subject-wise class D maps for HOA vs AD. Red indicates HOA $>$ AD, whilst blue is AD $>$ HOA. (C) Voxels with t-values such that $p < 0.05$. Red voxels indicate HOA $>$ AD, and blue voxels are AD $>$ HOA.

between the top and bottom rows of column D of Figure 5.2). We subsequently calculated the eLORETA solution on a subject wise basis and calculated voxel-wise t-statistics to quantify spatially distributed alterations in AD to find that parietal sources were less active in the people with AD, particularly weighted more towards the left hemisphere (Figure 5.3B-C).

5.3.2 Increased microstate duration in AD

Having found changes to the topography and underlying cortical generators to class D in AD, we next explored whether the transitioning behaviour of the microstate sequences were altered. For each subject and microstate class, mean duration, coverage, and the Markovian syntax transition matrix were extracted. Tables 5.1-5.3 show the two-way ANOVA tables for testing for differences in groups and class. For mean duration, there was a significant disease group term ($p = 0.0019$) but a non-significant interaction term, suggesting that mean duration of microstates changes in AD, and this is a global trend over all microstate classes. For this reason, we do not perform pairwise comparisons of classes. Since

Source	Sum Sq.	DF	Mean Sq.	F	P
Class	237.2	3	79.1	0.67	0.5674
Group	1162.7	1	1162.7	9.95	0.0019
Class*Group	430.7	3	143.6	1.23	0.3007
Error	21029	180	116.8		
Total	22809	187			

Table 5.1: **Two-way ANOVA table for mean duration of microstates**. The class term refers to the four microstate classes, whilst the group term refers to clinical diagnosis, i.e. AD vs HOA.

Source	Sum Sq.	DF	Mean Sq.	F	P
Class	0.0256	2	0.0128	1.72	0.1803
Class*Group	0.0040	2	0.0020	0.27	0.7657
Error	1.3478	182	0.0074		
Total	1.3791	187			

Table 5.2: **Two-way ANOVA table for coverage of microstate classes**. The class term refers to the four microstate classes, whilst the group term refers to clinical diagnosis, i.e. AD vs HOA.

Source	Sum Sq.	DF	Mean Sq.	F	P
Edge	0.0037	6	6.1e-4	0.5891	0.7391
Edge*Group	0.0067	6	0.0011	1.0725	0.3777
Error	0.5688	546	0.0010		
Total	0.5835	563			

Table 5.3: **Two-way ANOVA table for Markovian switching between microstate classes**. The edge term refers to the edges of the Markovian transition matrix, whilst the group term refers to clinical diagnosis, i.e. AD vs HOA.

ANOVA is a parametric test and relies on assumptions of normality, we verified this change in mean microstate duration with a non-parametric Mann-Whitney U test ($p = 0.0214$). Hence mean microstate duration (T) significantly increased in AD (HOA 41.42 ± 0.90 ms; AD 46.42 ± 1.89 ms), shown in Figure 5.4A. No significant results were found for coverage of microstates.

All analyses were additionally conducted on a pairwise basis for class D to further verify that changes to the topography of this class in AD did not alter switching statistics. No differences were found for any test.

5.3.3 Microstate sequence complexity reduces in AD

Whilst there were no differences in Markovian transitioning, it is likely that microstate transitioning is non-Markovian (Van De Ville et al., 2010; von Wegner et al., 2017). We therefore next calculated the Lempel-Ziv complexity (LZC) of

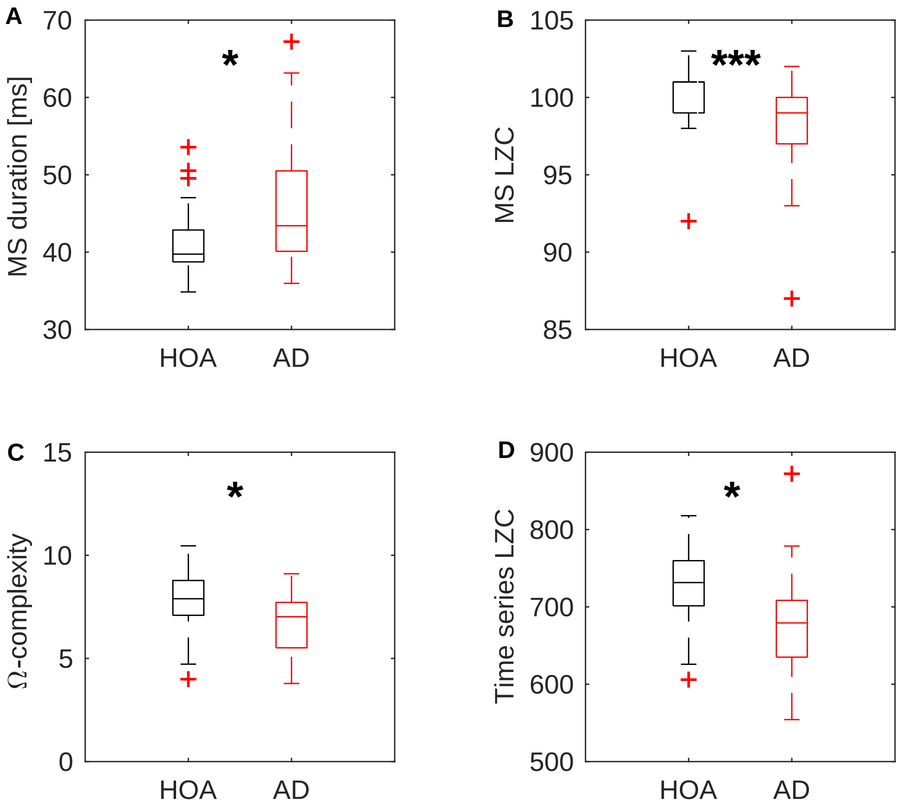

Figure 5.4: **Microstate and complexity statistics are significantly altered in AD**. (A) Mean duration of microstates. (B) Microstate LZC. (C) Ω-complexity. (D) Time series LZC. Stars denote significance of Mann-Whitney U test: *$p < 0.05$, **$p < 0.01$, ***$p < 0.001$.

the microstate transitioning sequence (C), a measure which does not assume Markovianity.

We found a significant reduction in C in AD (HOA 101 ± 2; AD 99 ± 3; $p = 0.0023$. Since C takes on integer values, statistics reported here are median ± interquartile range.) (Figure 5.4B), suggesting that higher order or non-Markovian alterations to microstate transitioning are present in the EEG of people with AD, to which a Markovian transitioning analysis is not sensitive.

5.3.4 Comparisons with classical measures of EEG complexity

We next compared how C performed against classical EEG complexity measures which have been previously reported to reduce in AD; namely Ω-complexity (Saito et al., 1998; Molnár et al., 2006; Irisawa et al., 2006; Czigler et al., 2008; Dauwels et al., 2010, 2011) and time-series LZC (Abásolo et al., 2006; Hornero et al., 2009; Sabeti et al., 2009; Dauwels et al., 2011; Fernández et al., 2011; Liu et al., 2016). The former measure predominantly captures spatial complexity, being founded in covariance of the time series, whilst the latter predominantly captures temporal complexity and is a univariate measure. Whilst both of these measures were found to significantly decrease in our data set (Ω-complexity $p = 0.0191$; time series LZC $p = 0.0127$; Figure 5.4C-D), the effect size of these differences were notably lower than for C, suggesting that additional information can be gained by capturing both spatial and temporal patterns. Whilst no significant correlation existed between C and time series LZC ($r = 0.1363$, $p = 0.3611$), there was a small but significant correlation between Ω-complexity and C ($r = 0.3002$, $p = 0.0403$).

5.4 Discussion

In this chapter, a microstate analysis was performed on the EEG of HOA controls and people with AD. We will now discuss aspects of the methodology and implications of the results presented here.

5.4.1 Methodology

A key methodological factor that may affect results and therefore must be addressed is the use of eyes-open EEG. The majority of past EEG microstate studies have been performed on eyes-closed resting state data. A detailed study of differences in EEG microstates between eyes-open and eyes-closed conditions was performed by Seitzman et al. (2017). This article did not study optimum number of microstates, but percentage of variance was studied for 2-22 microstate classes. Whilst for a given number of microstates eyes-open data typically had less variance explained than the eyes-closed state, the curves of variance explained vs number of classes had almost identical forms. This suggests that optimization criteria such as Krzanowski-Lai (Krzanowski and Lai, 1988) (used here to choose the optimum number of microstates), which typically search for the ‘elbow’ in such a curve, would identify optima at the same point in both states. Furthermore, Seitzman et al. (2017) found that, given four classes, the eyes-open classes largely matched those of the four classical eyes-closed classes. Therefore the results of Seitzman et al. (2017) support our results that in eyes open data, four microstate classes are optimum and the topographies of these classes should largely match those reported in eyes closed data.

A further potential effect of using eyes-open data is reduced microstate duration. The microstates presented here are shorter than those typically seen in the literature, which are usually more than 80 ms (Lehmann et al., 1987). von Wegner et al. (2017) found that microstate duration is closely related to frequency of neuronal oscillations in the EEG, and Khanna et al. (2014) predicted that factors such as eyes-open data and aging would result in reduced microstate durations due to different dominant frequencies. Comparisons of eyes-open and eyes-closed microstates further supports this, demonstrating reduced microstate durations in the eyes-open data (Stevens and Kircher, 1998; Seitzman et al., 2017). Therefore it is possible that an identical study in eyes-closed data may result in different durations to this study.

There are a number of strengths to the data presented here. Firstly, all patients were unmedicated. Past studies have shown that drugs can alter EEG microstate statistics such as duration and topography (Lehmann et al., 1993; Yoshimura et al., 2007), so by recording data from unmedicated people with AD it is ensured that any differences between cohorts are not artifacts of medication. Secondly, the data presented here was recorded on 64 channel EEG. Whilst reliable EEG microstate estimates can be obtained from as few as eight electrodes (Khanna et al., 2014), use of high density EEG allows for more reliable source space reconstructions (Song et al., 2015), allowing for estimation of cortical sources underpinning microstate topographies. This gives the opportunity to gain more mechanistic insights into the disruption of spatiotemporal brain dynamics in AD.

5.4.2 Microstate complexity measure

In this work we present a novel application of Lempel-Ziv complexity (LZC) (Lempel, 1976) to microstate sequences. LZC was chosen to study microstate transitions over classical syntax analysis approaches due to underlying assumptions of each of the methods. Syntax analysis assumed transitioning behaviour is first order Markovian (Lehmann et al., 2005). Stationarity of the data is also assumed to enable the use of transitions over the whole data set to generate the transition matrix (Lehmann et al., 2005; Nishida et al., 2013). Mechanistically, this method is unlikely to give full information of the switching dynamics of microstates since EEG microstate switching is neither Markovian nor stationary (Van De Ville et al., 2010; von Wegner et al., 2017). Therefore methods of analysing microstate transitioning that account for higher order properties may give greater insight into alterations in information processing in neurological disorders.

LZC bypasses these issues by making no underlying assumptions in terms of whether the data is Markovian or stationary. LZC aims to calculate the number of sub-sequences within a sequence (Lempel, 1976), and hence highly structured first order Markovian data or repetitive stationary data will lead to low LZC due to repeating sub-sequences, whilst higher order transitions or non-stationarity will lead to a wider range of sub-sequences and hence increased LZC. In this study, we demonstrated that the LZC of microstate transition sequences had a notably larger effect size in separating people with AD from controls than Markovian syntax analysis, suggesting higher order alterations to transitioning between microstates in AD.

LZC has in the past been used to identify reduced complexity of the EEG in people with AD (Abásolo et al., 2006; Gómez et al., 2006; Hornero et al., 2009; Dauwels et al., 2011; Liu et al., 2016). For these studies, the methodology involved binarizing a univariate EEG time series based on a threshold such as the median of the data, and then calculating the LZC of this binary sequence. Application of LZC to the microstate sequences is an improvement over this method for a number of reasons. Firstly, the choice of binning is less arbitrary. By using microstates, binning of the EEG is chosen based on repeating spatiotemporal patterns and quasi-stable states which have some neurophysiological basis related to active networks (Michel et al., 2001; Milz et al., 2016). This further means that microstate LZC accounts for the multivariate nature of the EEG, not accounted for in classical time series LZC. In essence, microstate LZC is a spatially extended version of the LZC method classically used in EEG literature.

Time series LZC is strongly dependent on a dominant frequency, such that a relationship between slowing of EEG and loss of LZC in AD has been shown (Dauwels et al., 2011). This is unsurprising since the binarized time series will be largely driven by the dominant frequency of the original time series, and slowing of this frequency will lead to less frequent switching between states, resulting in more repetitive sequences and hence reduced LZC. Assuming a relationship between oscillatory frequency and microstate duration (von Wegner et al., 2017), the same can be said of microstate LZC when performed on raw microstate sequences. However, if the microstate sequence is reduced to a transition sequence, the measure is independent of microstate duration and slowing. A similar reduction cannot be made for time series LZC, since a binary sequence reduced to a switching sequence results in simple switching between two states. Since slowing is consistently reported in the EEG of people with AD (Babiloni et al., 2016), an orthogonal EEG biomarker could have great application for aiding diagnosis of the disease, which is the focus of the next chapter.

5.4.3 Alterations to class D and the frontoparietal network

Our results suggest that microstate class D has an altered topography in AD. It is difficult to compare this result with previous studies, since many studies of microstates in AD were published prior to development of k-means methods of microstate extraction and used adaptive segmentation (Ihl et al., 1993; Dierks et al., 1997; Strik et al., 1997; Stevens and Kircher, 1998), so therefore do not study class D specifically. One study of AD microstates in the literature uses k-means clustering, in which no alterations to any of the four microstate classes were observed in AD (Nishida et al., 2013). It is unclear why this discrepency between the results presented here and past literature occurs, although there are a number of potential explanations. Whilst a key difference between studies is the number of channels - our study used 64 channel EEG vs the 19 channel EEG used by Nishida et al. (2013) - and hence increased spatial resolution, this seems an unlikely explanation for differences in results as microstates are reliable with as few as eight channels (Khanna et al., 2014). The fact that this data was recorded in the eyes-open state is a potential factor, but Seitzman et al. (2017) found no differences in the topography of class D in eyes-open and eyes-closed in healthy adults and during attentional tasks, so it is unclear to what extent the topography of class D in eyes-open data would be altered in AD compared to eyes-closed. Methodology may play a role; it is unclear in Nishida et al. (2013) how classes are aligned between subjects and whether global clustering algorithms (Khanna et al., 2014) were used, but it appears that all subjects across all groups were used for defining the topographies of the four classes, whereas in this study classes are defined independently for each group.

It has been suggested that class D is related to the frontoparietal network and the attention/working memory cognitive domains (Britz et al., 2010; Nishida et al., 2013; Khanna et al., 2015; Seitzman et al., 2017). Source space reconstruction of class D maps demonstrated that the change in topography in AD was due to reduced parietal activation, supporting the hypothesis of alterations to the frontoparietal network in AD. It is worth noting at this point that the differences shown in Figure 5.3C were not corrected for multiple hypotheses, instead using a cutoff value of $p < 0.05$ following the steps of Milz et al. (2016). Under Benjamini-Hochberg post correction for 6239 hypotheses, no voxels remained significant. However, since the topographic analysis demonstrated significant differences in AD, it is still of interest to see which voxels displayed the largest effect sizes and hence were most likely candidates for altered cortical generators in AD. A possible mechanism by which altered spatial topography of the frontoparietal network may arise is disruptions to long range synaptic connectivity, since alterations to functional and effective connectivity in the frontoparietal network have been reported in recent fMRI studies of people with AD (Neufang et al., 2011; Zhao et al., 2018).

5.4.4 Alterations to microstate duration and switching statistics

After studying microstate topographies in AD, we next studied how microstate duration was altered in AD. Mean microstate duration was found to increase in AD. Reports of microstate duration are inconsistent in the past literature, which has found increased mean duration in AD (Ihl et al., 1993), reduced duration of the longest microstate (Dierks et al., 1997; Strik et al., 1997), a reduced mean duration in dementia (non-specific) (Stevens and Kircher, 1998), or no changes in duration in AD (Nishida et al., 2013). Methodology may account for differences between this study and those of Dierks et al. (1997), Strik et al. (1997), and Stevens and Kircher (1998) which used adaptive windowing as opposed to k-means clustering, however this would not explain why the results of Nishida et al. (2013) differ from the results presented here. Furthermore Ihl et al. (1993) used adaptive window segmentation and found results that match those presented in this study. An additional potential factor that could account for these differences is the use of eyes-open data, as this has been shown to effect microstate duration (Seitzman et al., 2017), however Stevens and Kircher (1998) found a decrease in duration in both eyes-open and eyes-closed states in non-specific dementia. Interestingly, we might expect microstate duration to increase in AD due to slowing of the EEG (von Wegner et al., 2017) which is well established in AD (Strik et al., 1997; Adler et al., 2003; Lindau et al., 2003; Dauwels et al., 2011; Hatz et al., 2015a; Liu et al., 2016; Wang et al., 2015; Goossens et al., 2017; Tait et al., in press) - this was the original hypothesis made by Dierks et al. (1997), who expressed their surprise that a decreased microstate duration was found instead.

We found no changes in the Markovian transition matrices between HOA and AD, but did find a significant reduction in microstate transitioning complexity in AD. These results suggest that microstate LZC is sensitive to higher-order or non-Markovian alterations to transitioning in AD. Reduced transitioning LZC is suggestive of more repetitive switching between active networks in AD, possibly indicating less complex information processing. This gives key insight into the mechanisms underpinning cognitive deficits in AD.

5.4.5 Conclusions

In this chapter, a number of key results that give crucial insight into the mechanisms underpinning cognitive impairment in AD have been identified. Parietal inactivation was shown to relate to a changing topography in microstate class D. This microstate class is related to the frontoparietal network and attention/working memory (Britz et al., 2010; Nishida et al., 2013; Seitzman et al., 2017), which are impaired early in the AD staging (Perry and Hodges, 1999). Microstate duration was found to increase in AD, whilst a novel application of Lempel-Ziv complexity to the EEG microstate switching was found to decrease in AD. These results are suggestive of slower, more repetitive, and less complex microstate transitions, which likely reflects similar attributes to the switching between active brain networks associated with a range of cognitive domains (Lehmann et al., 1987; Michel et al., 2001; Koenig et al., 2005b; Khanna et al., 2015; Milz et al., 2016). A key advantage to the measure presented here is that it is independent to slowing of neuronal oscillations in the EEG, and therefore has the potential as a biomarker to greatly increase the ability of the EEG to diagnose AD when combined with measures of EEG slowing, which is discussed further in the following chapter. Medication has in the past been shown to alter microstate statistics (Lehmann et al., 1993; Yoshimura et al., 2007), so the mechanistic insights presented in the manuscript may potential aid future drug development for AD.

Chapter 6

Combining temporal scales of the EEG for a robust predictor of AD

The work presented in this chapter was performed in collaboration with Dr George Stothart (data acquisition), Dr Nina Kazanina (data acquisition), Dr Edoardo Barvas and the San Marino Neurological Unit (data acquisition), Dr Francesco Tamagnini (conceptualization), Dr Jon T Brown (supervision), and Dr Marc Goodfellow (supervision, conceptualization, methodological design). The author's contribution to this chapter includes preprocessing and analysis of the data, methodological design, interpretation of results, visualization of the data, and writing of the chapter.

6.1 Introduction

Early diagnosis of AD has a wide range of clinical, social, and economic benefits (Leifer, 2003; Dubois et al., 2016; Alzheimer's Association, 2018), but at present, diagnosis of AD is made at the clinical stage based on already prevalent cognitive deterioration (Agronin, 2014). Therefore development of tools to aid in the early or prodromal diagnosis of AD is a crucial task in dementia research.

The focus of chapters 4 and 5 was the use of EEG as a tool to understand mechanistically the alterations to the brain's electrical activity in AD. However, since EEG is non-invasive, relatively inexpensive compared to functional imaging methods such as fMRI or MEG, and is currently implemented in healthcare systems for diagnosis of epilepsy, EEG is a suitable candidate as a tool for aiding AD diagnosis. Previous EEG studies have demonstrated potential for aiding early diagnosis of AD (Dauwels et al., 2010; Poil et al., 2013; Nakamura et al., 2018). However, at present no single measure is able to accurately classify early stage AD, and hence a combination of measures containing complementary information must be used to achieve greater classification accuracy (Poil et al., 2013; Simpraga et al., 2017).

The majority of studies using M/EEG to aid with diagnosis focus on spectral and functional network measures (Dauwels et al., 2010; Maestú et al., 2019), which are typically assessed on a time scale of the order of seconds to minutes in order to obtain reliable estimates (Gudmundsson et al., 2007; Fraschini et al., 2016). Such measures were studied in chapter 4. We hypothesise that by combining these measures with analyses at a much finer temporal scale, namely an EEG microstate analysis (chapter 5), novel information can be gained to improve the ability of the EEG to classify AD. To test this hypothesis, in this chapter we combine the spectral measure described in chapter 4, namely theta band relative power, with the measure of microstate sequence complexity described in chapter 5 to develop a classifier for AD.

An important but rarely taken step is to validate the model on an independent data set to ensure generalizability and robustness. Whilst cross validation of the classifier on the training set theoretically tests these properties, supervised feature selection is often based on the full cohort resulting in overestimates of generalizibility and robustness (Smialowski et al., 2010). Therefore it is crucial to assess the performance of a classifier against independent data not used in feature selection (Smialowski et al., 2010). Here, the classification model is therefore validated against a set of clinical EEG recorded by independent neurologists from an independent and geographically distant cohort of patients.

All subjects in the development and validation of the classifier were either healthy older adults (HOA) or had a clinical diagnosis of (early stage) AD. A key clinical challenge in AD research is early diagnosis at the prodromal stages (Nakamura et al., 2018), in which patients display mild cognitive impairment (MCI) due to AD pathology but do not have dementia (Dubois et al., 2014). The ability to differentiate between prodromal AD and MCI due to non-AD aetiologies is crucial for correctly administering pharmacological intervention at the early stages to prevent the pathological progress of the disease (Sperling et al., 2014). In this chapter, we therefore additionally test the ability of the model to predict future conversion to AD (within four years of EEG acquisition) on a cohort of cognitively heterogeneous people with MCI.

6.2 Materials and methods

6.2.1 EEG acquisition

Training data

Acquisition of the training EEG was performed externally by collaborators and is described in section 4.2.1.

	HOA	AD
Age (± SEM; years)	69 (± 2)	72 (± 2)
n	7	9
Male	4	3
Female	3	6

Table 6.1: Age and gender of HOA and AD cohorts in the San Marino data

Test data

All data acquisition and work described in section 6.2.1: Test data was performed externally by collaborators[1]. All appropriate approvals for the procedures were obtained from the Republic of San Marino Ethical Committee for Research and Experimentation (Ref. 0015 SM) and the University of Exeter Medical School Research Ethics Committee. Participants provided written informed consent before participating and were free to withdraw at any time. People with AD were recruited on a consecutive incident patient basis. Diagnosis of AD was given by neuropsychologists and neurologists at the Republic of San Marino State Hospital using neurological, neuroimaging, physical and biochemical examination and a battery of neuropsychological tests according to the IWG-2 criteria (Dubois et al., 2014). Age matched healthy controls were recruited from caregivers of patients and were in normal general health and neurological and neuropsychological assessment showed no evidence of dementing or other neuropsychological disorders. Exclusion criteria were those described in the IWG-2 criteria (Dubois et al., 2014). Data on subjects is given in Table 6.1. Resting-state EEG (19 channel, sampled at 512 Hz) was recorded from all subjects including eyes-open and eyes-closed epochs, which were consistent accoss the two groups.

MCI data

All data acquisition and work described in section 6.2.1: MCI data was performed externally by collaborators[2]. Recruitment and other procedures, including participant consent, guidelines for inclusion, and ethical approvals, were as described in section 4.2.1. The diagnosis of MCI was given to individuals who had made a formal, corroborated complaint of memory impairment and exhibited objective memory decline greater than at least one standard deviation from age and education-appropriate norms, but who were not demented and had preserved functions of daily living and general intellect on clinical examination. Four years following data acquisition, dementia status was reassessed by clinical assessment. Subjects who did not receive a dementia diagnosis during this four year period were clas-

---

[1] Data was acquired by Dr Edoardo Barvas and the Neurological Unit at the San Marino State Hospital

[2] Data was acquired by Dr George Stothart (University of Bath Department of Psychology) and Dr Nina Kazanina (University of Bristol School of Psychological Science)

	MCIs	MCIc
Age (± SEM; years)	80 (± 2)	76 (± 6)
MMSE (± SEM)	25 (± 1)	26 (± 1)
n	7	4
Male	5	4
Female	2	0

Table 6.2: Age, gender, and cognitive data for the MCI cohort

sified as MCI-stable (MCIs). Subjects who had a diagnosis of AD during the four year period were classified as prodromal AD or MCI-converters (MCIc). The remaining subjects ($n = 14$) were either unavailable for clinical follow-up, deceased, or had a diagnosis of non-AD or mixed dementia within four years of data acquisition and were excluded from the analysis. Data on MCI subjects is given in Table 6.2. EEG acquisition is as described in section 4.2.1.

6.2.2 EEG preprocessing

Training and MCI data

Preprocessing for the training and MCI data sets is as described in section 4.2.2. When the classifier was validated on the test data, the training data was first spatially downsampled to the same 19 channels as the test data and temporally downsampled to 512 Hz using linear interpolation and the classifier was retrained on this downsampled training data.

Test data

For 14 of the 16 test subjects, EEG data was sampled at 512 Hz. Data for the remaining two subjects was sampled at 128 Hz and resampled to 512 Hz using linear interpolation. For all subjects, data was recorded with 19 electrodes in the standard 10-20 format. Epochs of eyes open data at least 20 seconds in length were manually extracted from the full EEG recordings. These epochs were then processed with TAPEEG to identify a single optimal 20 second epoch of resting state data per subject (Hatz et al., 2015b). These epochs were then preprocessed as described in section 4.2.2.

6.2.3 EEG analysis

Two features were extracted from the data for each subject; namely the theta relative power (θRP) and microstate complexity (C). θRP and C were calculated as described in sections 4.2.4 and 5.2.3 respectively. These two features were chosen as biomarkers for AD based on the results of chapters 4 and 5. Note

	HOA(train)	AD(train)	HOA(test)	AD(test)	MCIs	MCIc
HOA(train)		0.1695 (0.3339)	0.0338 (0.1015)	0.1720 (0.3339)	0.1781 (0.3339)	0.6238 (0.6743)
AD(train)			0.0155 (0.1015)	0.0233 (0.1015)	0.9364 (0.9364)	0.2346 (0.3911)
HOA(test)				0.4191 (0.5714)	0.0338 (0.1015)	0.4909 (0.6136)
AD(test)					0.0194 (0.1015)	0.6294 (0.6743)
MCIs						0.2909 (0.4364)
MCIc						

Table 6.3: **p-values for pairwise comparisons of the six cohorts for age**. Uncorrected p-values are reported, with false discovery rate corrected p-values in brackets accounting for multiple hypotheses.

that for calculation of C, data was first bandpass filtered into the 1-30 Hz band as described in chapter 5. All analyses were performed in sensor space, so no cortical source localization was performed prior to calculation of θRP.

6.2.4 Classification

Classification models were built using a binary support vector machine (Christianini and Shawe-Taylor, 2000), implemented in Matlab's function 'fitcsvm' (`https://uk.mathworks.com/help/stats/fitcsvm.html`). The box constraint and kernel scale were optimized, whilst all other parameters were set to default. All classification rates, sensitivities, and specificities reported for the training set were calculated using 10-fold cross validation, whilst the full training set was used to build the classification model which was tested on the test and MCI data sets.

6.3 Results

6.3.1 Participant demographics

Participant demographics are given in Tables 4.1, 6.1, and 6.2. Across the six cohorts (HOA training / AD training / HOA test / AD test / MCIs / MCIc), there was a significant effect of age ($\chi^2 = 12.63$, $p = 0.0271$, Kruskal-Wallis test). Pairwise Mann-Whitney U-tests demonstrated that the HOA test cohort was different to the HOA training, AD training, and MCIs cohorts at a level of $p < 0.05$. Additionally, the AD test cohort was different to the AD training and MCIs cohorts at a level of $p < 0.05$. However, following correction for multiple hypotheses, no differences were significant. The p-values for all pairwise comparisons of age are given in Table 6.3.

	HOA(train)	AD(train)	MCIs	MCIc
HOA(train)		1×10^{-7} (7×10^{-7})	3×10^{-4} (0.001)	0.0138 (0.0207)
AD(train)			0.0032 (0.0065)	0.0253 (0.0304)
MCIs				0.7939 (0.7939)
MCIc				

Table 6.4: **p-values for pairwise comparisons of the South West of England cohorts for MMSE score**. Uncorrected p-values are reported, with false discovery rate corrected p-values in brackets accounting for multiple hypotheses.

	C	θRP	C+θRP
CR	68.1	72.3	85.1
Sens.	61.9	66.7	81.0
Spec.	73.1	76.9	88.5

Table 6.5: **Classification statistics from EEG measures in the training set**. Classification rate (CR), sensitivity (Sens.), and specificity (Spec.) for SVM classification models using EEG measures as predictors. Measures are given as percentages. Statistics were derived using 10-fold cross validation and a binary SVM classifier.

Mini-mental state examination scores were available for the data collected in the South West of England, namely the HOA training / AD training / MCIs / MCIc data. Across thse four cohorts, there was a significant effect of MMSE score ($\chi^2 = 37.35, p = 3.89 \times 10^{-8}$). Pairwise testing found that, with the exception of MCI stable vs converters, there were differences in MMSE scores between all pairs of cohorts to $p < 0.05$. These results remained significant following correction for multiple hypotheses. The p-values for all pairwise comparisons of MMSE are given in Table 6.4.

6.3.2 Microstate complexity and theta relative power are robust and generalizable biomarkers of AD

We first applied the neurophysiological biomarkers of AD identified in the previous chapters for aiding diagnosis of AD. A support vector machine (SVM) classifier was built combining θRP and C, and 10-fold cross validated on the training data set (Figure 6.1A). Table 6.5 shows statistics for this classifier. Classification rate, sensitivity, and specificity were all greater than 80%, with a classification rate of 85.1%.

For comparison purposes, we also studied SVMs using each measure independently as a feature, also shown in Table 6.5. θRP had higher classification rate, sensitivity, and specificity than C, but all statistics were notably lower in either one-feature model than the combined model, supporting the hypothesis

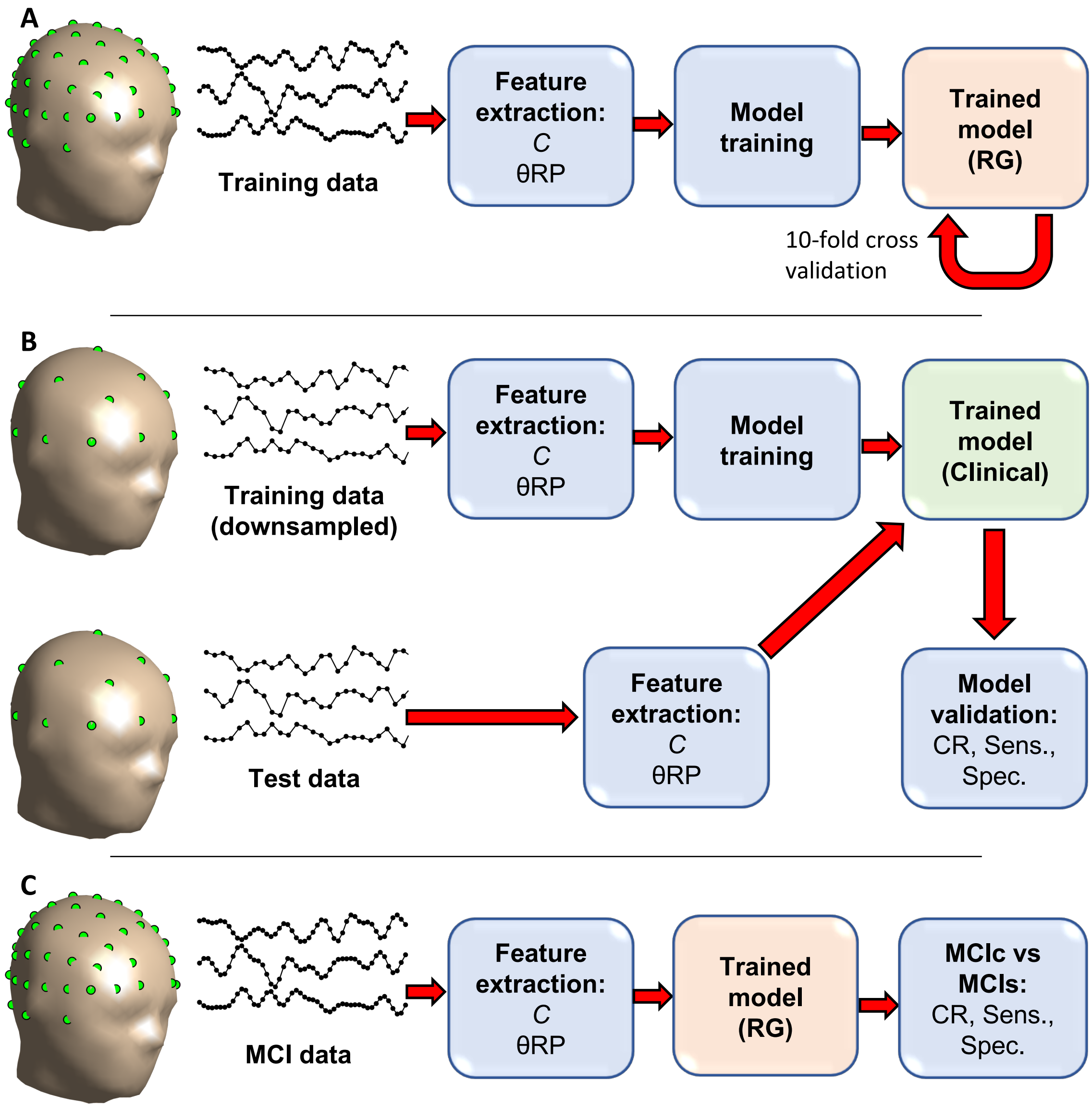

Figure 6.1: **Methodology for building and testing the classifier**. (A) Training data (RG: 64 channel, 1 kHz sampling rate) was used to build and optimize a classification model based on C and θRP. The model was 10-fold cross validated to assess performance. (B) Independent test data (clinical grade: 19 channels, 512 Hz sampling rate) was used to assess generalizability and robustness of the model. First, the training data was spatially and temporally downsampled to clinical grade and the model retrained for clinical grade data. Then the test data was assessed by the trained model and the prediction of the model compared to clinical diagnosis. (C) MCI data (RG) was additionally assessed by the trained RG classification model. Prediction of the models were compared against the patients' dementia status four years following EEG acquisition. **Abbreviations**: RG, research grade; C, microstate LZC; θRP, theta band relative power; MCI, mild cognitive impairment; CR, classification rate; Sens., sensitivity; Spec., specificity; MCIc, MCI converters to AD; MCIs, MCI stable non-demented.

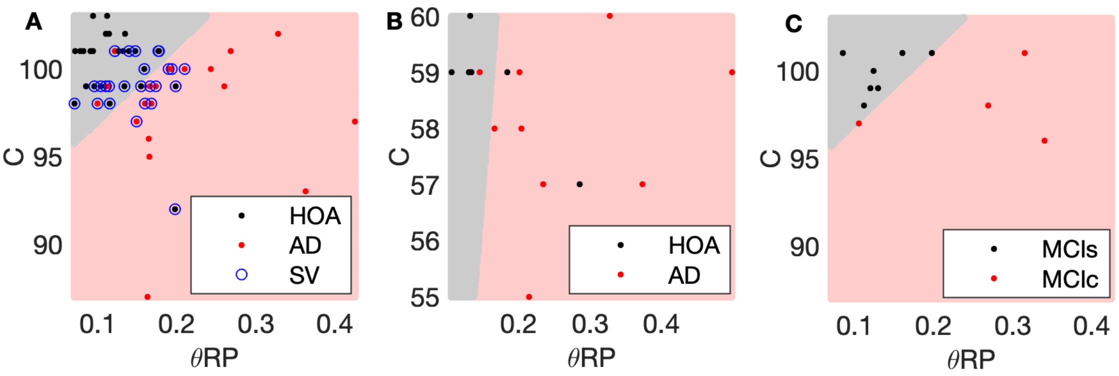

Figure 6.2: **SVM regions for the θRP+C classifier**. The SVM predictor classifier points within the pale red region as AD and points within the gray region as HOA. (A) Training data set overlaid on 64 channel model. (B) Test data set overlaid on 19 channel classifier model (trained to the training set downsampled spatially and temporally). (C) MCI data set overlaid on 64 channel model. All models were trained on the data set shown in A. Blue circles in A show the support vectors for training in the 64 channel model.

	Test data	MCI data
CR	81.3	90.9
Sens.	88.9	100
Spec.	71.4	85.7

Table 6.6: **Classification statistics from EEG measures in the test and MCI data sets**. Classification rate (CR), sensitivity (Sens.), and specificity (Spec.) for SVM classification models using EEG measures as predictors. Measures are given as percentages. Statistics were derived using a binary SVM classifier trained to the training data set.

that use of two measures on separate time scales can increase the accuracy of classification. Figure 6.2A shows each subject in the (θRP,C) plane, overlaid on predictions of the classifier for all of this space.

Whilst the use of 10-fold cross validation and a small number of features ensures the model is not overfit to the data, feature selection was based on group level statistics of the full training set. This means a true independent data set must be used to ensure that the model is generalizable and robust (Smialowski et al., 2010). We therefore tested the C+θRP model on an independent and geographically distinct cohort of data (Figure 6.1B). Table 6.6 shows the classification statistics for this model, whilst Figure 6.2B shows the locations of subjects in the (θRP,C) plane. 13/16 of the test subjects were correctly classified, with high sensitivity (8/9 AD patients correctly classified) and high specificity (5/7 HOA subjects correctly classified). These results suggest the C+θRP classifier is robust and generalizable to clinical data sets with lower spatial and temporal resolution than research grade EEG, as well as geographically generalizable.

6.3.3 Using the classifier to predict future progression to AD

We next tested the prognostic value of the classifier. EEG from a cohort of people with MCI was tested on the trained model, and classified as HOA or AD by the classifier. This classification was compared to the dementia status of the patients four years following data acquisition (Figure 6.1C). The location of each subject in the (θRP,C) plane is shown in Figure 6.2C. Four of the four subjects who converted to AD (MCIc) were classified as AD by the model, whilst six of the seven subjects who did not receive a dementia diagnosis in the four years following EEG acquisition (MCIs) were classified as HOA. One subject from the MCIs cohort was incorrectly predicted to have an AD diagnosis. Therefore the model correctly predicted the four year diagnosis of 10/11 people with MCI in this preliminary cohort (90.9% classification rate). These results are summarised in Table 6.6. A crucial point of note is that there was almost no differences in MMSE score between the MCIs and MCIc cohorts (Tables 6.1 and 6.4), suggesting that these patients were cognitively heterogeneous at the time of data acquisition.

6.4 Discussion

One of the key motivations for use of EEG microstates to study AD was due to a much finer temporal resolution (Koenig et al., 1999) than spectral and functional network analyses (Gudmundsson et al., 2007) often performed on EEG. We hypothesised that by combining temporal scales in a classifier, additional information could be gained for improved classification. Indeed, we found that by combining results from chapter 4 (theta band relative power; θRP) with results from chapter 5 (microstate LZC; C), classification rate, sensitivity, and specificity in the training set were greatly increased compared to using these measures alone.

A crucial methodological step was choice of the features θRP and C. Altered spectral features have been consistently reported in the EEG of people with AD (Babiloni et al., 2016) and has been identified as a powerful tool for classification of AD from the EEG (Adler et al., 2003; Lindau et al., 2003; Poil et al., 2013; Hatz et al., 2015a; Wang et al., 2015; Simpraga et al., 2017). In chapter 4, θRP was identified as a spectral measure which is able to separate AD patients from HOA patients with large effect size. In chapter 5, both C and mean microstate duration were identified as biomarkers of AD. C was chosen over mean microstate duration as a complementary biomarker for two reasons. Firstly, in chapter 5, C was able to separate AD and HOA with a much larger effect size than microstate duration. Secondly, microstate duration is potentially dependent on the frequency of neuronal oscillations (von Wegner et al., 2017), suggesting that mean microstate duration may not be orthogonal to θRP. Whilst theta-band functional networks were also identified as a biomarker of AD in chapter 4, functional network measures are dependent on the size of the network (Joudaki et al., 2012), suggesting that clinical EEG montages may give different results to the higher density research grade montage presented in chapter 4.

A key advantage to this study was testing the classifier on an independent test cohort to ensure generalizability and robustness. Whilst cross validation of the classifier on the training set theoretically tests these qualities, supervised feature selection was based on group statistics of the full training cohort, meaning cross validation is likely to overestimate the generalizability and robustness of the model (Smialowski et al., 2010). Therefore it is crucial to assess the performance of the classifier against independent data not used in feature selection (Smialowski et al., 2010). In this data set, the model was validated against a set of clinical EEG recorded by independent neurologists from an independent and geographically distant cohort of patients. Not only did this serve as validation of the model against an independent test set, it demonstrated that whilst features were chosen based on research grade EEG with high spatial and temporal resultion (64 channels, 1 kHz sampling rate), the model was generalizable to lower resolution clinical EEG (19 channels, 512 Hz sampling rate). This suggests that the model is potentially useful in a clinical setting.

A key clinical challenge in AD is early diagnosis at the prodromal stages (Nakamura et al., 2018). All subjects in the training data set were free from dementia related medications and EEG was recorded within days of diagnosis, suggesting this data is useful for diagnosis of early stage AD. To test whether this data could be used to aid with prodromal diagnosis (i.e. whether patients with mild cognitive impairment due to an AD aetiology had EEG similar to those with early stage AD), EEG from a test set of four MCI patients who converted to AD within four years of data collection was run through the classification model. All four subjects were classified as AD patients by the classifier, giving 100% specificity. Additionally, we found that patients with MCI who did not receive an AD (or other dementia) diagnosis within four years of data acquisition were mostly (for six out of seven patients) classified as healthy in the model. It is important to note that there were no differences in cognitive test scores between these patients, and all patients within this group were classified as MCI following a battery of cognitive, neuroimaging, and biochemical tests, suggesting that EEG could be a powerful tool for identification of AD aetiology in MCI. However, it should be stated that this cohort was small, so whilst these results are promising, future work is required to validate these results on a larger cohort.

Chapter 7

General discussion

7.1 Summary of key findings

In this thesis, we have studied how the dynamics of the brain are altered in clinical Alzheimer's disease and experimental models of related pathologies to understand mechanisms underpinning AD and develop electrophysiological biomarkers for aiding early diagnosis. The key findings of this thesis are summarised below.

In chapter 2, a biophysical model of layer II medial entorhinal cortex stellate cells (mEC-SCs) was used to uncover the ionic mechanisms underpinning clustered AP firing patterns observed electrophysiological data. mEC-SCs are crucial for spatial navigation and memory (Tennant et al., 2018), which are known to be impaired in clinical AD (Lithfous et al., 2013; Allison et al., 2016) and animal models featuring AD pathologies (Ramsden et al., 2005; Yue et al., 2011; Blackmore et al., 2017; Fu et al., 2017). Booth et al. (2016a) identified alterations to the clustering dynamics of mEC-SCs in the rTg4510 animal model of tauopathy, motivating our use of a biophysical neuron model to understand the underpinning ionic mechanisms.

By performing a bifurcation analysis on the deterministic formulation of the model, we found that the clustering dynamics in the stochastic model were due to noisy perturbations on a deterministic burster. Bursting was of the fast-slow subHopf/homoclinic type (Izhikevich, 2000) with the persistent sodium and slow A-type potassium currents driving the slow dynamics. Alterations to the AHP and h-currents were sufficient to alter the clustering dynamics by changing the number of spikes per cluster via flip bifurcations, or into tonic firing or resting regimes. Experimental data suggested that there were no changes to the h-current but an increase in AHP amplitude in the rTg4510 animals (Booth et al., 2016a), so we concluded it was likely (based on inspection of realistic dynamic regimes) that reductions in the proportion of clustered APs in rTg4510 mEC-SCs (Booth et al., 2016a) arose due to increased conductance of the AHP current driving the underlying dynamics through a flip (spike-subtracting) bifurcation. An independent model validation was the finding that the model additionally displayed theta (4-12 Hz) range subthreshold resonance in realistic AP firing regimes, which is in line with experimental data (Alonso and Klink, 1993).

In chapter 3, functional connectivity was analysed from multi-scaled electrophysiological data recorded in the *CHMP2B*$^{\text{intron5}}$ model of frontotemporal dementia which exhibits neurodegeneration, synaptic loss, and behavioural impairments. Within a region of the brain (whisker barrel cortex), local functional networks had a significantly increased average synchrony and synchronizable topology. Conversely, macro-scale functional networks derived from skull-screw EEG electrodes placed at six locations on the cortex demonstrated a reduction in synchrony, particularly in the frontal electrodes. A computational model of the mouse brain was used to study potential interplay between macro-scale and local synchrony. Whilst regimes did exist in which an increase in local coupling alone could explain reductions in macro-scale synchrony, the simulated EEG signals in these regimes exhibited unrealistic signal-to-noise ratios suggestive of locally hypersynchronous delta band activity that did not reflect the data. In regimes with more realistic dynamics, increases in local coupling resulted in increases in macro-scale synchrony. We therefore suggested that white matter impairments in these transgenic animals (Ghazi-Noori et al., 2012) reduced the long range coupling in the network and observed increases in local functional connectivity are potentially a compensatory mechanism by which long range functional connectivity may be restored (Abuhassan et al., 2014).

Chapter 4 studied EEG recorded from human AD patients. Compared to controls, the AD patients exhibited increases in slow spectral power and decreases in fast power, with largest effect size in the theta frequency range. This spectral slowing was spatially heterogeneous, most predominantly affecting the frontal and parietal cortices. Functional networks had reduced small-worldness, suggesting less efficient topology for information transfer through the network. In the AD patients, small-worldness correlated with general MMSE scores and the language subscore. Interestingly, an analysis of local properties of the functional networks attributed the reduced small-worldness to decreased closeness centrality of the temporal lobes, one of the regions of the brain responsible for language processing. To ensure that heterogeneous spectral slowing, a potentially local mechanism, was not solely responsible for these spatially distributed alterations to the functional network, a computational model of the whole brain was used. We found that slowing alone could not replicate alterations to the functional network structure, but reduced effective connectivity between the temporal lobes and rest of the brain was sufficient to accurately describe the empirical data. When combined, these results suggest that loss of synaptic connectivity between the temporal lobes and the rest of the brain is a potential mechanism by which cognitive impairment, specifically language deficiencies, arise in AD.

Alterations to EEG microstates in AD were next studied in chapter 5. The topography of canonical class D, which is related to the frontoparietal working memory/attention network (Britz et al., 2010), was found to be altered in AD. Cortical source localization suggested these alterations were due to reduced activation of the parietal lobe in class D. The duration of microstates significantly increased in AD, which may be related to the slowing of neuronal oscillations identified in chapter 4 (von Wegner et al., 2017). Finally, whilst no alterations were found to the Markovian transitioning matrix between AD and HOA, a novel application of the LZC algorithm identified less complex transitioning (i.e. more repetitive, with fewer distinct sequences of transitions).

Finally, chapter 6 combined the electrophysiological biomarkers of AD identified in chapters 4 and 5 to build a predictive classifier for AD. The data set studied in chapters 4-5 was used to train a model using theta band relative power (θRP) and microstate LZC (C) as features, which had a classification rate of 85% when 10-fold cross validated on the training set. An independent and geographically distinct set of clinical EEG was used as a test set to validate the classifier and test generalizability and robustness. The accuracy of the classifier on the test set remained high, with classification rate of 81%. In a small preliminary cohort of 11 MCI patients, the classifier was additionally able to predict whether a patient would convert to AD within four years of EEG acquisition accurately for 10/11 patients (91% accuracy), suggesting the EEG is potentially a powerful prognostic tool.

7.2 Limitations and future work

7.2.1 Bridging the gap between experimental model and clinical disease

This thesis was structured in two parts; chapters 2-3 studied rodent models of dementia pathologies, whilst chapters 4-6 studied clinical AD in humans. Translational research is crucial for fully uncovering the mechanisms of Alzheimer's disease and development of treatments and therapies. An example relevant to this thesis is impaired orientation to space in human AD (Lithfous et al., 2013; Allison et al., 2016), which can lead patients into unsafe situations due to the tendancy to get lost and wander (Jones, 2017). Due to the deep localization of the spatial navigation networks in the brain, recording of spatially modulated grid cell or place cell activity requires invasive depth electrodes (Ekstrom et al., 2003; Jacobs et al., 2010, 2013), presenting a challenge for understanding the neuronal mechanisms underpinning impaired orientation to space in human AD and electrophysiological effects of pharmacological interventions. However, animal models provide the opportunity to study the effect that pathologies related to AD have on spatial navigation systems (Booth et al., 2016a; Fu et al., 2017; Tait et al., 2018), potentially leading to future development of targeted pharmacological interventions to counteract these alterations to neuronal dynamics and eventually treat impairments to spatial orientation in human AD.

Chapters 4-5 identified a number of electrophysiological biomarkers of AD in humans, which are likely apparent even in the prodromal stages of the disease (chapter 6). A focus of this work was to correlate electrophysiological changes with cognitive dysfunction. Future work should involve the use of animal models to futher understand the biophysical mechanisms underpinning these biomarkers, with aims towards development and testing of interventions at the early or prodromal stages of AD to treat or slow the progression of cognitive impairment. Many of these biomarkers are constructed from whole brain dynamics (e.g. functional networks, microstates), so a first step may be the use of high-density extracranial microarray EEG combined with source reconstruction (Lee et al., 2013), as opposed to low resolution invasive EEG such as the data presented in chapter 3. Such data could allow for whole brain functional connectivity studies in rodents which replicate those performed in humans in this thesis. Furthermore, it is currently unclear whether rodents exhibit EEG microstates, so this could be an avenue for future work. Invasive recordings could supplement this work, acting as validation of source reconstruction and to study local mechanisms.

7.2.2 Extensions to multi-modal research

A primary focus of this thesis was the use of EEG to characterize alterations to neuronal dynamics in clinical AD. Future work should involve integrating the EEG with a range of other data sets including neuropsychological test scores, fluid biomarkers, structural/diffusion neuroimaging, and other functional neuroimaging modalities to obtain more accurate results and more mechanistic insight into the disease (as discussed below).

The absence of individual structural MRIs was a key limitation of chapter 4 (and was discussed in detail in section 4.4.1), since it is unclear what the effects of aging and cortical atrophy in AD have on the accuracy of the source reconstruction. Combining the EEG with structural MRI is a method to avoid this issue. Furthermore, volumetric or surface based analyses of the structural MRI can be used to quantify the degree of atrophy in the brain in AD patients (Frisoni et al., 2009). An analysis which may be of interest to AD research combining these results with the EEG would be to study the effects of localized atrophy on whole brain neuronal dynamics, for example either through correlation analysis of regional EEG statistics and regional atrophy, or through the use of computational models to simulate dynamics with atrophy (e.g. reductions in coupling parameters (de Haan et al., 2017)) at nodes proportional to the regional atrophy of those nodes. Additionally, by simulating brain dynamics on individual (potentially atrophied) brains and forward mapping to the EEG, then source reconstructing to a template, errors in the source reconstruction due to atrophy can be studied. Diffusion and functional MRI can additionally be used to generate more accurate source reconstructions and computational models, for example as prior estimates for source localization algorithms (Ou et al., 2010) or model parameterization (Schirner et al., 2015; Dermitas et al., 2017). These are all potential avenues for future work.

Many of the results of this thesis relied on computational models of neuronal dynamics. Wherever possible, results of computational models should be validated against experimental data, highlighting the importance of multiple imaging modalities. Modelling results may be used to inform future experiments for model validation; examples motivated by this thesis include the use of dynamic clamp to validate our model predictions that alteration to the AHP in entorhinal cortex stellate cells affect clustering dynamics, and the collection of diffusion weighted imaging to test model predictions that the temporal lobes are effectively/structurally becoming disconnected in people with AD.

Multi-modal research can give greater mechanistic insight than uni-modal approaches. In chapter 4, EEG was combined with neuropsychological cognitive test scores to gain insight into possible relationships between functional disconnection and cognitive impairment in AD. As discussed above, correlations between graph theoretical/spectral/microstate statistics and regional atrophy assessed by structural MRI analyses could give insight into the extent to which atrophy can explain these alterations to dynamics. Furthermore, correlation analysis with PET or CSF biomarkers for tau and amyloid beta can give insight into how the different pathologies related to AD mediate the alterations to neuronal dynamics seen in the EEG of AD patients. This extension of the analysis to multiple modalities is an avenue for future work, and at present we are working with collaborators at the San Marino State Hospital Neurological Unit to collect and analyse EEG, MRI, CSF biomarker, and broad neuropsychological assessments of healthy controls, people with AD, and people with MCI.

Combining multiple experimental conditions in a single imaging modality can additionally give greater insight into the mechanisms underpinning AD. For example, the focus of this thesis (chapters 3-6) has been resting state EEG. Stothart et al. (2016) demonstrated that visual evoked potentials (VEPs) are altered in AD. Using the dynamical systems and source space reconstruction approaches applied in this thesis, combined with more biophysically realistic neural mass models (section 1.6), future work will study how meso-scale network dysfunction (Figure 1.1) underpin these alterations to VEPs. There is additionally potential to apply parameters of such models as a biomarker for AD to gain additional diagnostic accuracy, and to correlate these meso-scale network parameters with features of the resting state data such as spectral slowing to gain deeper insight into the local mechanisms underpinning spectral slowing which were not biophysically modelled in chapter 4.

Multi-modal analysis in experimental rodent models can additionally be used to gain insight into the relationship between single cell dynamics and network dynamics, which are often not accounted for in detail in neural mass models. An example motivated by this thesis is uncovering the role of action potential clustering in mEC-SCs in generating theta nested gamma rhythms and grid cell firing. This will involve development of a low dimensional model which qualitatively captures the clustered AP dynamics of mEC-SCs such as the Izhikevich neuron (Izhikevich, 2007; Hasslemo and Shay, 2014) and simulation of large scale networks of neurons to observe the LFP. In rodent models of tauopathy, theta nested gamma and grid cell firing are disrupted (Booth et al., 2016a; Fu et al., 2017), so a key question is whether the alterations to single cell dynamics in tauopathy studied in chapter 2 or synaptic deficits are reposible for these alterations. An alternative approach to simulating a large network of neurons is to use a neural mass model for tractable bifurcation analysis; for example, use of a mean-field model of networks of Izhikevich neurons (Visser and Van Gils, 2014) which can capture mEC-SCs dynamics (Izhikevich, 2007; Hasslemo and Shay, 2014). This work can give crucial insight into the mechanisms underpinning impaired orientation to space in people with AD.

7.2.3 Brain dynamics as a clinical biomarker of AD

In chapter 6, we focused on using the dynamics of the EEG as a tool for aiding diagnosis of AD and as a prognostic tool for people with MCI. Whilst the results were promising, the analyses were performed in reasonably small preliminary cohorts of data. A crucial extension for future work is therefore demonstrating success in larger clinical cohorts. The prognostic analysis in people with MCI compared the results of the model to clinical follow-up at a single time point, so an additional extension for this work should be to perform longitudinal data acquisition with regular clinical assessment such that the limitations of the prognostic value of brain dynamics as a clinical biomarker of AD can be explored.

A consideration for any potential clinical biomarkers is cost. Whilst EEG is relatively inexpensive compared to fMRI, PET, or MEG (Crosson et al., 2010) and is currently implemented in healthcare systems for the diagnosis of epilepsy (Smith, 2005), it is costly in comparison to neuropsychological and cognitive tests such as the MMSE. Therefore an EEG based biomarker must have value over cognitive test scores that justify the additional cost. Indeed, in chapter 6 we showed that our biomarker had prognostic value for cognitively homogeneous (as quanitified by MMSE score) people with MCI. Furthermore, relatively inexpensive commercial EEG headsets can potentially be used to lower the cost of EEG recordings (Stamps and Hamam, 2010). However, it is important that accuracy of the biomarkers be maintained when using these commercial headsets. Future work will involve quantifying the extent to which commerical Emotiv EEG headsets (`www.emotiv.com`) replicate the results of research and clinical grade EEG to assess viability of these headsets as a biomarker for AD. Alternatively, task related EEG may require fewer electrodes to record localized evoked potentials, so future work will additionally involve the study of visual evoked potentials which are known to change in AD (Stothart et al., 2016).

As discussed above, at present we are working with collaborators who are collecting EEG, MRI, tau and amyloid CSF biomarkers, and neuropsychological assessments. Future work should involve combining these various modalities to increase diagnostic accuracy and explore which modalities have the greatest diagnostic/prognostic value. Additionally, future work will include longitudinal collection and analysis of data to study the progression of AD.

7.3 Conclusions

Computational modelling and analysis of electrophysiological data on multiple spatial scales is a powerful tool for understanding the mechanisms underpinning cognitive impairment in AD. In this thesis, we have uncovered ionic mechanisms underpinning alterations to single cell dynamics in the spatial navigations systems of the brain in a rodent model of dementia pathology, and future work should involve exploring the relationship between these single cell dynamics and network dynamics. Furthermore, we studied the relationship between local and whole brain functional networks in a rodent model of neurodegeneration to demonstrate how synaptic degenerations on multiple spatial scales manifest in terms of integration between the brain's processing systems. We uncovered alterations to whole brain dynamics recorded by EEG. These alterations include spectral slowing, reduced small-worldness of the brain's functional networks, and changes to the EEG microstates in people with AD, and that EEG is a useful tool for aiding with early and prodromal diagnosis of AD. The primary focus of future work should be integrating this resting state EEG with task related EEG (e.g. VEPs), imaging modalities, CSF biomarkers, and neuropsychological assessment to gain further insight into AD, increase diagnostic and predictive accuracy of models, and serve as validation of computational modelling results.

Bibliography

D. Abásolo, R. Hornero, C. Gómez, M. García, and M. López. Analysis of EEG background activity in Alzheimer's disease patients with Lempel-Ziv complexity and central tendancy measure. *Med Eng Phys*, 28(4):315–22, 2006. doi: 10.1016/j.medengphy.2005.07.004.

K. Abuhassan, D. Coyle, and L. Maguire. Compensating for thalamocortical synaptic loss in Alzheimer's Disease. *Front Comput Neurosci*, 8:65, 2014. doi: 10.3389/fncom.2014.00065.

G. Adler, S. Brassen, and A Jajcevic. EEG coherence in Alzheimer's dementia. *J. Neural Transm*, 110:1051–1058, 2003. doi: 10.1007/s00702-003-0024-8.

S. Afshari and M. Jalili. Directed functional networks in alzheimer's disease: Disruption of global and local connectivity measures. *IEEE J Biomed Health Inform*, 21(4):949–955, 2017. doi: 10.1109/JBHI.2016.2578954.

M. Agronin. *Alzheimer's Disease and Other Dementias: A Practical Guide*. Routledge, 3rd edition, 2014.

M. Akin and M. Kemal Kiymik. Application of Periodogram and AR Spectral Analysis to EEG Signals. *J Med Syst*, 24(4):247–256, 2000. doi: 10.1023/A:1005553931564.

S.L. Allison, A.M. Fagan, J.C. Morris, and D. Head. Spatial Navigation in Preclinical Alzheimer's Disease. *J Alzheimers Dis*, 52(1):77–90, 2016. doi: 10.3233/JAD-150855.

A. Alonso and R. Klink. Differential electroresponsiveness of stellate and pyramidal-like cells of medial entorhinal cortex layer II. *J. Neurophysiol*, 70(1):128–143, 1993. doi: 10.1152/jn.1993.70.1.128.

Alzheimer's Association. 2018 Alzheimer's Disease Facts and Figures. *Alzheimer's and Dementia*, 14(3):367–429, 2018.

Alzheimer's Disease International. World alzheimer report 2018: The state of the art of dementia research, new frontiers, 2018.

American Psychiatric Association. *Diagnostic and statistical manual of mental disorders (IV-TR)*. Washington, D.C., 2000.

M. Andersson, O. Hansson, L. Minthon, I. Rosén, and E. Londos. Electroencephalogram variability in dementia with Lewy bodies, Alzheimer's disease, and controls. *Dement Geriatr Cogn Disord*, 26:284–290, 2008. doi: 10.1159/000160962.

C. Andreou, P.L. Faber, G. Leicht, D. Schoettle, N. Polomac, I.L. Hanganu-Opatz, D. Lehmann, and C. Mulert. Resting-state connectivity in the prodropmal phase of schizophrenia: insights from EEG microstates. *Schizophr. Res.*, 152:513–520, 2014. doi: 10.1016/j.schres.2013.12.008.

Y. Aoki, R. Ishii, R.D. Pascual-Marqui, L. Canuet, S. Ikeda, M. Hata, K. Imajo, H. Matsuzaki, T. Musha, T. Asada, M. Iwase, and M. Takeda. Detection of EEG-resting state independent networks by eLORETA-ICA method. *Front. Hum. Neurosci.*, 9:31, 2015. doi: 10.3389/fnhum.2015.00031.

D. Arthur and S. Vassilvitskii. K-means++: The Advantages of Careful Seeding. *SODA '07: Proceedings of the Eighteenth Annual ACM-SIAM Symposium on Discrete Algorithms*, pages 1027–1035, 2007.

S. Atluri, W. Wong, S. Moreno, D.M. Blumberger, Z.J. Daskalakis, and F. Farzan. Selective modulation of brain network dynamics by seizure therapy in treatment-resistant depression. *NeuroImage: Clinical*, 20:1176–1190, 2018. doi: 10.1016/j.nicl.2018.10.015.

F.A Azevedo, L.R. Carvalho, L.T. Grinberg, J.M. Farfel, R.E. Ferretti, R.E. Leite, W. Jacob Filho, R. Lent, and S. Herculano-Houzel. Equal numbers of neuronal and nonneuronal cells make the human brain an isometrically scaled-up primate brain. *J Comp Neurol*, 513(5):532–541, 2009. doi: 10.1002/cne.21974.

C. Babiloni, R. Lizio, N. Marzano, P. Capotosto, A. Soricelli, A.I. Triggiani, S. Cordone, L. Gesualdo, and C. Del Percio. Brain neural synchronization and functional coupling in Alzheimer's disease as revealed by resting state EEG rhythms. *Int J Psychophysiol*, 103:88–102, 2016. doi: 10.1016/j.ijpsycho.2015.02.008.

A. Badhwar, A. Tam, C. Dansereau, P. Orban, F. Haffstardter, and P. Bellec. Resting-state network dysfunction in Alzheimer's disease: A systematic review and meta-analysis. *Alzheimers Dement (Amst)*, 8:73–85, 2017. doi: 10.1016/j.dadm.2017.03.007.

M. Barahona and L.M. Pecora. Synchronization in small-world systems. *Phys Rev Lett*, 89(5):054101, 2002. doi: 10.1103/PhysRevLett.89.054101.

B. Barak, N. Feldman, and E. Okun. Cardiovascular Fitness and Cognitive Spatial Learning in Rodents and in Humans. *J Gerontol A Biol Sci Medi Sci*, 70(9):1059–1066, 3015. doi: 10.1093/gerona/glu162.

R. Barrio and A. Shilnikov. Parameter-sweeping techniques for temporal dynamics of neuronal systems: case study of Hindmarsh-Rose model. *J Math Neurosci.*, 1(1):6, 2011. doi: 10.1186/2190-8567-1-6.

L. Bartha, T. Benke, G. Bauer, and E. Trinka. Interictal language functions in temporal lobe epilepsy. *J Neurol Neurosurg Psychiatry*, 76(6):808–814, 2005. doi: 10.1136/jnnp.2004.045385.

D. S. Bassett and E. T. Bullmore. Small-World Brain Networks Revisited. *The Neuroscientist*, 23(5):499?516, 2017. doi: 10.1177/1073858416667720.

R. Becker, J. Silvi, D.M. Fat, A. L'Hours, and R. Laurenti. A method for deriving leading causes of death. *Bull. World Health Organ.*, 84:297–304, 2006. doi: 10665/269620.

P. Beed, A. Gundlfinger, S. Scheiderbauer, J. Song, C. Böhm, A. Burgalossi, M. Brecht, I. Vida, and D. Schmitz. Inhibitory Gradient along the Dorsoventral Axis in the Medial Entorhinal Cortex. *Neuron*, 79:1197–1207, 2013. doi: 10.1016/j.neuron.2013.06.038.

A. Bejanin, D.R. Schonhaut, R. La Joie, J.H. Kramer, S.L. Baker, N. Sosa, N. Ayakta, A. Cantwell, M. Janabi, M. Lauriola, J.P. O'Neil, M.L. Gorno-Tempini, Z.A. Miller, H.J. Rosen, B.L. Miller, W.J. Jagust, and G.D. Rabinovici. Tau pathology and neurodegeneration contribute to cognitive impairment in alzheimer's disease. *Brain*, 140(12): 3286–3300, 2017. doi: 10.1093/brain/awx243.

R. Berlot, C. Metzler-Baddeley, M.A. Ikram, Jones D.K., and M.J. O'Sullivan. Global Efficiency of Structural Networks Mediates Cognitive Control in Mild Cognitive Impairment. *Front Aging Neurosci*, 8:292, 2016. doi: 10.3389/fnagi.2016.00292.

R.F. Betzel and D.S. Bassett. Multi-scale brain networks. *NeuroImage*, 160:73–83, 2017. doi: 10.1016/j.neuroimage.2016.11.006.

T. Blackmore, S. Meftah, T.K. Murray, P.J. Craig, A. Blockeel, K. Phillips, B. Eastwood, M.J. O'Neill, H. Marston, Z. Ahmed, G. Gilmour, and F. Gastambide. Tracking progressive pathological and functional decline in the rTg4510 mouse model of tauopathy. *Alzheimers Res Ther*, 9(1):77, 2017. doi: 10.1186/s13195-017-0306-2.

A. Boehlen, U. Heinemann, and I. Erchova. The range of intrinsic frequencies represented by medial entorhinal cortex stellate cells extends with age. *J Neurosci*, 30(13): 4585–4589, 2010. doi: 10.1523/JNEUROSCI.4939-09.2010.

M. Boly, O. Gosseries, M. Massimini, and M. Rosanova. Functional Neuroimaging Techniques. In S. Laureys, G. Tononi, and O. Gosseries, editors, *The Neurology of Consciousness: Cognitive Neuroscience and Neuropathology*, chapter 2. Elsevier Science & Technology, 2015.

M. Bonilla-Quintana, K.C.A. Wedgwood, R.D. O'Dea, and S. Coombes. An Analysis of Waves Underlying Grid Cell Firing in the Medial Entorhinal Cortex. *J Math Neurosci*, 7:9, 2017. doi: 10.1186/s13408-017-0051-7.

L. Bonnani, A. Thomas, P. Tiraboschi, B. Perfetti, S. Varanese, and M. Onofrj. EEG comparisons in early Alzheimer's disease, dementia with Lewy bodies, and Parkinson's disease with dementia patients with a 2-year follow-up. *Brain*, 131(3):690–705, 2008. doi: 10.1093/brain/awm322.

M. Bonnin and F. Corinto. Phase Noise and Noise Induced Frequency Shift in Stochastic Nonlinear Oscillators. *IEEE. Trans. Circuits Syst. I, Reg. Papers*, 60(8), 2013. doi: 10.1109/TCSI.2013.2239131.

C.A. Booth, T. Ridler, T.K. Murray, M.A. Ward, E. de Groot, M. Goodfellow, K.G. Phillips, A.D. Randall, and J.T. Brown. Electrical and Network Neuronal Properties Are Preferentially Disrupted in Dorsal, But Not Ventral, Medial Entorhinal Cortex in a Mouse Model of Tauopathy. *J. Neurosci.*, 36(2):312–324, 2016a. doi: 10.1523/JNEUROSCI.2845-14.2016.

C.A. Booth, J. Witton, J. Nowacki, K. Tsaneva-Atanasova, M.W. Jones, A.D. Randall, and J.T. Brown. Altered Intrinsic Pyramidal Neuron Properties and Pathway Specific Synaptic Dysfunction Underlie Aberrant Hippocampal Network Function in a Mouse Model of Tauopathy. *J. Neurosci.*, 36(2):350–363, 2016b. doi: 10.1523/JNEUROSCI.2151-15.2016.

C. Börgers and N. Kopell. Effects of Noisy Drive on Rhythms in Networks of Excitatory and Inhibitory Neurons. *Neural Comput*, 17(3):557–608, 2005. doi: 10.1162/0899766053019908.

H. Braak and E. Braak. Neuropathological stageing of Alzheimer-related changes. *Acta Neuropathol*, 82:239–259, 1991. doi: 10.1007/BF00308809.

H. Braak and E. Braak. Staging of Alzheimer's disease-related neurofibrillary changes. *Neurobiol Aging*, 16(3):271–278, 1995. doi: 10.1016/0197-4580(95)00021-6.

M. Breakspear, S. Heitmann, and A. Daffertshofer. Generative models of cortical oscillations: neurobiological implications of the Kuramoto model. *Front Hum Neurosci*, 4:190, 2010. doi: 10.3389/fnhum.2010.00190.

K. Britz, D. Van De Ville, and C.M. Michel. BOLD correlates of EEG topography reveal rapid resting-state network dynamics. *NeuroImage*, 52:1162–1170, 2010. doi: 10.1016/j.neuroimage.2010.02.052.

V. Brodbeck, A. Kuhn, F. von Wegner, A. Morzelewski, E. Tagliazucchi, S. Borisov, C.M. Michel, and H. Laufs. EEG microstates of wakefulness and NREM sleep. *NeuroImage*, 62:2129–2139, 2012. doi: 10.1016/j.neuroimage.2012.05.060.

J.T. Brown, J. Chin, S.C. Leise, M.N. Pangalos, and A.D. Randall. Altered intrinsic neuronal excitability and reduced Na+ currents in a mouse model of Alzheimer's disease. *Neurobiol Aging*, 32:2109.e1–e14, 2011. doi: 10.1016/j.neurobiolaging.2011.05.025.

K. Brueggen, C. Fiala, C. Berger, S. Ochmann, C. Bablioni, and S.J. Teipel. Early Changes in Alpha Band Power and DMN BOLD Activity in Alzheimer's Disease: A Simultaneous Resting State EEG-fMRI Study. *Front Aging Neurosci*, 9:319, 2017. doi: 10.3389/fnagi.2017.00319.

E. Bullmore and O. Sporns. Complex brain networks: graph theoretical analysis of structural and functional systems. *Nat Rev Neurosci*, 10:186–198, 2009. doi: 10.1038/nrn2575.

R.L. Burden and J.D. Faires. *Numerical Analysis*. Brooks/Cole, Cengage Learning, ninth edition, 2010.

A. Burns and S. Iliffe. Dementia. *BMJ*, 338:b75, 2009. doi: 10.1136/bmj.b75.

M.A. Busche and A. Konnerth. Impairments of neural circuit function in Alzheiemr's disease. *Phil Trans R Soc B*, 371:20150429, 2016. doi: 10.1098/rstb.2015.0429.

M.A. Busche, C. Grienberger, A.D. Keskin, B. Song, U. Neumann, M. Staufenbiel, H. Forstl, and A. Konnerth. Decreased amyloid-β and increased neuronal hyperactivity by immunotherapy in Alzheimer's models. *Nat Neurosci*, 18(12):1725–1728, 2015a. doi: 10.1038/nn.4163.

M.A. Busche, M. Kekus, H. Adelsberger, T. Noda, H. Forstl, I. Nelken, and A. Konnerth. Rescue of long-range circuit dysfunction in Alzheimer's disease models. *Nat Neurosci*, 18(11):1623–1630, 2015b. doi: 10.1038/nn.4137.

M.A. Busche, S. Wegmann, S. Dujardin, C. Commins, J. Schiantarelli, N. Klickstein, T.V. Kamath, G.A. Carlson, I. Nelken, and B.T. Hyman. Tau impairs neural circuits, dominating amyloid-βeffects, in Alzheimer models in vivo. *Nat Neurosci*, 22:57–64, 2019. doi: 10.1038/s41593-018-0289-8.

G. Buzsáki. Large-scale recording of neuronal ensembles. *Nat Neurosci*, 7:446–451, 2004. doi: 10.1038/nn1233.

G. Buzsáki. *Rhythms of the Brain*. Oxford University Press, 2006.

J.L. Cantero, M. Atienza, A. Cruz-Vadell, A. Suarez-Gonzalez, and E. Gil-Neciga. Increased synchronization and decreased neural complexity underlie thalamocortical oscillatory dynamics in mild cognitive impairment. *NeuroImage*, 46:938–948, 2009. doi: 10.1016/j.neuroimage.2009.03.018.

C.B. Canto, F.G. Wouterlood, and M.P. Witter. What Does the Anatomical Organization of the Entorhinal Cortex Tell Us? *Neural Plast*, 2008:381243, 2008. doi: 10.1155/2008/381243.

L. Canuet, R. Ishii, R.D. Pascual-Marqui, M. Iwase, R. Kurimoto, Y. Aoki, S. Ikeda, H. Takahashi, T. Nakahachi, and M. Takeda. Resting-State EEG Source Localization and Functional Connectivity in Schizophrenia-Like Psychosis of Epilepsy. *PLoS One*, 6(11):e27863, 2011. doi: 10.1371/journal.pone.0027863.

L. Canuet, I. Tellado, V. Courceiro, C. Fraile, L. Fernandez-Novoa, R. Ishii, M. Takeda, and R. Cacabelos. Resting-State Network Disruption and APOE Genotype in Alzheimer's Disease: A lagged Functional Connectivity Study. *PLoS ONE*, 7(9):e46289, 2012. doi: 10.1371/journal.pone.0046289.

P. Channell, G. Cymbalyuk, and A. Shilnikov. Origin of Bursting through Homoclinic Spike Adding in a Neuron Model. *PRL*, 98:134101, 2007. doi: 10.1103/PhysRevLett.98.134101.

R. Chassefeyre, J. Martínez-Hernández, F. Bertaso, N. Bouquier, B. Blot, M. Laporte, S. Fraboulet, Y. Couté, A. Devoy, A.M. Isaacs, K. Pernet-Gallay, R. Sadoul, L. Fagni, and Y. Goldberg. Regulation of Postsynaptic Function by the Dementia-Related ESCRT-III Subunit CHMP2B. *J. Neurosci.*, 35(7):3155–3173, 2015. doi: 10.1523/JNEUROSCI.0586-14.2015.

T.W. Chen, T.J. Wardill, Y. Sun, S.R. Pulver, S.L. Renninger, A. Baohan, E.R. Schreiter, R.A. Kerr, M.B. Orger, V. Jayaraman, L.L. Looger, K. Svoboda, and D.S. Kim. Ultrasensitive flourescent proteins for imaging neuronal activity. *Nature*, 499(7458):295–300, 2013. doi: 10.1038/nature12354.

S.A. Chong, I. Benilova, H. Shaban, B. de Strooper, H. Devijver, D. Moechars, W. Eberle, C. Bartic, F. Van Leuven, and G. Callewaert. Synaptic dysfunction in hippocampus of transgenic mouse models of Alzheimer's disease: a multi-electrode array study. *Neurobiol Dis*, 44:284–291, 2011. doi: 10.1016/j.nbd.2011.07.006.

N. Christianini and J.C. Shawe-Taylor. *An Introduction to Support Vector Machines and Other Kernel-Based Learning Methods*. Cambridge University Press, 2000.

C. Chu, M. Kramer, J. Pathmanathan, M. Bianchi, M. Westover, L. Wizon, and S. Cash. Emergence of stable functional networks in long-term human electroencephalography. *J Neurosci*, 32(8):2703–2713, 2012. doi: 10.1523/JNEUROSCI.5669-11.2012.

S.M. Ciupek, J. Cheng, Y.O. Ali, H.C. Lu, and D. Ji. Progressive Functional Impairmants of Hippocampal Neurons in a Tauopathy Mouse Model. *J Neurosci*, 35(21):8118–8131, 2015. doi: 10.1523/JNEUROSCI.3130-14.2015.

E.L. Clayton, R. Mancuso, T.T. Nielsen, S. Mizielinska, H. Holmes, N. Powell, F. Norona, J.O. Larsen, C. Milioto, K.M. Wilson, M.F. Lythgoe, S. Ourselin, J.E. Nielsen, P. Johannsen, I. Holm, J. Collinge, FReJA, P.L. Oliver, D. Gomez-Nicola, and A.M. Isaacs. Early microgliosis precedes neuronal loss and behavioural impairment in mice with a frontotemporal dementia-causing CHMP2B mutation. *Human Molecular Genetics*, 26 (5):873–887, 2017. doi: 10.1093/hmg/ddx003.

J.D. Clements and J.M. Bekkers. Detection of spontaneous synaptic events with an optimally scaled template. *Biophys J*, 73(1):220–229, 1997. doi: 10.1016/S0006-3495(97)78062-7.

S. Coombes. Waves, bumps, and patterns in neural field theories. *Biol Cybern*, 93(2): 91–108, 2005. doi: 10.1007/s00422-005-0574-y.

S. Coombes and Á. Byrne. Next Generation Neural Mass Models. In F. Corinto and A. Torcini, editors, *Nonlinear Dynamics in Computational Neuroscience*. Springer, Cham, 2019.

T.E. Cope, T. Rittman, R.J. Borchert, P.S. Jones, D. Vatansever, K. Allinson, L. Passamonti, P. Vazquez Rodriguez, W.R. Bevan-Jones, J.T. O'Brien, and J.B. Rowe. Tau burden and the functional connectome in Alzheimer?s disease and progressive supranuclear palsy. *Brain*, 141(2):550–567, 2018. doi: 10.1093/brain/awx347.

L.E. Cox, L. Ferraiuolo, E.F. Goodall, P.R. Heath, A. Higginbottom, H. Mortiboys, H.C. Hollinger, J.A. Hartley, A. Brockington, C.E. Burness, K.E. Morrison, S.B. Wharton, A.J. Grierson, P.G. Ince, J. Kirby, and P.J. Shaw. Mutations in CHMP2B in Lower Motor Neuron Predominant Amyotrophic Lateral Sclerosis (ALS). *PLOS One*, 5(3): 1–16, 2010. doi: 10.1371/journal.pone.0009872.

J.L. Crimins, A.B. Rocher, and J.I. Luebke. Electrophysiological changes precede morphological changes to frontal cortical pyramidal neurons in the rTg4510 mouse model of progressive tauopathy. *Acto Neuropathol*, 124(6):777–795, 2012. doi: 10.1007/s00401-012-1038-9.

B. Crosson, A. Ford, K.M. McGregor, M. Meinzer, S. Cheshkov, X. Li, D. Walker-Batson, and R.W. Briggs. Functional Imaging and Related Techniques: An Introduction for Rehabilitation Researchers. *J Rehabil Res Dev*, 47(2):vii–xxxiv, 2010. doi: 10.1682/JRRD.2010.02.0017.

M. Cruts, J. Theuns, and C. van Broeckhoven. Locus-Specific Mutation Databases for Neurodegenerative Brain Diseases. *Human Mutation*, 33(9):1340–1344, 2012. doi: 10.1002/humu.22117.

J.L. Cummings, T. Mortstorf, and K. Zhong. Alzheimer's disease drug-development pipeline: few candidates, frequent failures. *Alzheimers Res Ther*, 6(4):37, 2014. doi: 10.1186/alzrt269.

E.E. Cureton. Rank-biserial correlation. *Psychometrika*, 21(3):287–290, 1956. doi: 10.1007/BF02289138.

B. Czigler, D. Csikós, Z. Hidasi, Z. Anna Gaál, E. Csibri, E. Kiss, P. Salaz, and M. Molnár. Quantitative EEG in early Alzheimer's disease patients - power spectrum and complexity features. *Int J Psychophysiol*, 68(1):75–80, 2008. doi: 10.1016/j.ijpsycho.2007.11.002.

M. Dauwan, E. van Dellen, L. van Boxtel, E. van Straaten, H. de Waal, A. Lemstra, A. Gouw, W. van der Flier, P. Scheltens, I. Sommer, and C. Stam. EEG directed connectivity from posterior brain regions is decreased in dementia with Lewy bodies: a comparison with Alzheimer's disease and controls. *Neurobiol Aging*, 41:122–129, 2016. doi: 10.1016/j.neurobiolaging.2016.02.017.

J. Dauwels, F. Vialatte, T. Musha, and A Cichocki. A comparative study of synchrony measures for the early diagnosis of Alzheimer's Disease based on EEG. *NeuroImage*, 49:668–693, 2010. doi: 10.1016/j.neuroimage.2009.06.056.

J. Dauwels, J. Srinivasan, M.R. Reddy, T. Musha, F.B. Vialatte, C. Latchoumane, J. Jeong, and A. Cichocki. Slowing and Loss of Complexity in Alzheimer's EEG: Two Sides of the same Coin? *International Journal of Alzheimer's Disease*, 2011:539621, 2011. doi: 10.4061/2011/539621.

O. David and K.J. Friston. A neural mass model for MEG/EEG: coupling and neuronal dynamics. *NeuroImage*, 20(3):1743–1755, 2003. doi: 10.1016/j.neuroimage.2003.07.015.

O. David, D. Cosmelli, and K.J. Friston. Evaluation of different measures of functional connectivity using a neural mass model. *NeuroImage*, 21:659–673, 2004. doi: 10.1016/j.neuroimage.2003.10.006.

C.A. Davies, D.M.A. Mann, P.Q. Sumpter, and P.O. Yates. A quantitative morphometric analysis of the neuronal and synaptic content of the frontal and temporal cortex in patients with Alzheimer's disease. *J Neurol Sci*, 78(151-164), 1987. doi: 10.1016/0022-510X(87)90057-8.

W. de Haan, K. Mott, E.C.W. van Straaten, P. Scheltens, and C.J. Stam. Activity Dependent Degeneration Explains Hub Vulnerability in Alzheimer's Disease. *PLoS Comput Biol*, 8(8):e1002582, 2012a. doi: 10.1371/journal.pcbi.1002582.

W. de Haan, W.M. van der Flier, H. Wang, P.F.A. Van Mieghem, P. Scheltens, and C.J. Stam. Disruption of functional brain networks in Alzheimer's disease: what can we learn from graph spectral analysis of resting state magnetoencephalography? *Brain Connectivity*, 2(2), 2012b. doi: 10.1089/brain.2011.0043.

W. de Haan, E.C.W. van Straaten, A.A. Gouw, and C.J. Stam. Altering neuronal excitability to preserve network connectivity in a computational model of Alzheimer's disease. *PLoS Comput Biol*, 13(9):e1005707, 2017. doi: 10.1371/journal.pcbi.1005707.

W. de Hann, Y. Pijnenburg, R. Strijers, Y. Made, P. van der Flier, W. Scheltens, and C. Stam. Functional neural network analysis in frontotemporal dementia and Alzheimer's disease using EEG and graph theory. *BMC Neuroscience*, 10:101, 2009. doi: 10.1186/1471-2202-10-101.

G. Deco, V.K. Jirsa, P.A. Robinson, M. Breakspear, and K. Friston. The Dynamic Brain: From Spiking Neurons to Neural Masses and Cortical Fields. *PLoS Comput Biol*, 4(8): e1000092, 2008. doi: 10.1371/journal.pcbi.1000092.

G. Deco, A. Ponce-Alvarez, D. Mantini, G.L. Romani, P. Hagmann, and M. Corbetta. Resting-State Functional Connectivity Emerges from Structurally and Dynamically Shaped Slow Linear Fluctuations. *J Neurosci*, 33(27):11329–11252, 2013. doi: 10.1523/JNEUROSCI.1091-13.2013.

G. Deco, A. Ponce-Alvarez, P. Hagmann, G.L. Romani, D. Mantini, and M. Corbetta. How Local Excitation-Inhibition Ratio Impacts the Whole Brain Dynamics. *J Neurosci*, 32 (23):7886–7898, 2014. doi: 10.1523/JNEUROSCI.5068-13.2014.

G. Deco, M.L. Kringelbach, V.K. Jirsa, and P. Ritter. The dynamics of resting fluctuations in the brain: metastability and its dynamical cortical core. *Sci Rep*, 7:3095, 2017a. doi: 10.1038/s41598-017-03073-5.

G. Deco, E. Tagliazucchi, H. Laufs, A. Sanjuán, and M.L. Kringelbach. Novel Intrinsic Ignition Method Measure Local-Global Integration Characterizes Wakefulness and Deep Sleep. *eNeuro*, 4(5):ENEURO.0106–17.2017, 2017b. doi: 10.1523/ENEURO.0106-17.2017.

X. Delbeuck, M. Van der Linden, and F. Collette. Alzheimer's disease as a disconnection syndrome? *Neuropsychol Rev.*, 13(2):79–92, 2003. doi: 10.1023/A:1023832305702.

W. Deng, J.B. Aimone, and F.H. Gage. New neurons and new memories: how does adult hippocampal neurogenesis affect learning and memory? *Nat Rev Neurosci*, 11: 339–350, 2010. doi: 10.1038/nrn2822.

M. Dermitas, C. Falcon, A. Tucholka, J.D. Gispert, J.L. Molinuevo, and G. Deco. A whole-brain computational modeling approach to explain the alterations in resting-state functional connectivity during progression of Alzheimer's disease. *NeuroImage: Clinical*, 16:343–354, 2017. doi: 10.1016/j.nicl.2017.08.006.

R.S. Desikan, F. Ségonne, B. Fischl, B.T. Quinn, B.C. Dickerson, D. Blacker, R.L. Buckner, A.M. Dale, R.P. Maguire, B.T. Hyman, M.S. Albert, and R.J. Killiany. An automated labeling system for subdividing the human cerebral cortex on MRI scans into gyral based regions of interest. *NeuroImage*, 31:968–980, 2006. doi: 10.1016/j.neuroimage.2006.01.021.

F. Devalle, A. Roxin, and Montbrió. Firing rate equations require a spike synchrony mechanism to correctly describe fast oscillations in inhibitory networks. *PLoS Comput Biol*, 13(21):e1005881, 2017. doi: 10.1371/journal.pcbi.1005881.

C.T. Dickson, J. Magistretti, M.H. Shalinsky, E. Fransén, M.E. Hasselmo, and A. Alonso. Properties and role of I_h in the pacing of subthreshold oscillations in entorhinal cortex layer II neurons. *J. Neurophysiol.*, 83:2562–2579, 2000. doi: 10.1152/jn.2000.83.5.2562.

T. Dierks, V. Jelic, P. Julin, K. Maurer, L.O. Wahlund, O. Almkvist, W.K. Strik, and B. Winblad. EEG-microstates in mild memory impairment and Alzheimer's disease: possible association with disturbed information processing. *J Neural Transm*, 104:483–495, 1997. doi: 10.1007/BF01277666.

T. Dierks, V. Jelic, R.D. Pascual-Marqui, L.O. Wahlund, Julin. P., D.E.J. Linden, K. Maurer, B. Winblad, and A. Nordberg. Spatial pattern of cerebral glucose metabolism (PET) correlates with localization of intracerebral EEG-generators in Alzheimer's disease. *Clin Neurophys*, 111:1817–1824, 2000. doi: 10.1016/S1388-2457(00)00427-2.

E.W. Dijkstra. A note on two problems in connexion with graphs. *Numerische Mathematik*, 1:269–271, 1959. doi: 10.1007/BF01386390.

P.D. Dodson, H. Pastoll, and M.F. Nolan. Dorsal-ventral organization of theta-like activity intrinsic to entorhinal stellate neurons is mediated by differences in stochastic current fluctuations. *J Physiol*, 589(12):2993–3008, 2011. doi: 10.1113/jphysiol.2011.205021.

D.A. Dombeck, M.S. Graziano, and D.W. Tank. Functional clustering of neurons in motor cortex determined by cellular resolution imaging in awake behaving mice. *J Neurosci*, 29(44):13751–13760, 2009. doi: 10.1523/JNEUROSCI.2985-09.2009.

K. Domoto-Reilly, D. Sapolsky, M. Brickhouse, and B.C. Dickerson. Naming impairment in Alzheimer's disease is associated with left anterior temporal lobe atrophy. *NeuroImage*, 63(1):348–355, 2012. doi: 10.1016/j.neuroimage.2012.06.018.

A.D. Jr Dorval and J.A. White. Channel noise is essential for perithreshold oscillations in entorhinal stellate neurons. *J Neurosci*, 25(43):10025–10028, 2005. doi: 10.1523/JNEUROSCI.3557-05.2005.

E. Drummond and T. Wisniewski. Alzheimer's disease: experimental models and reality. *Acta Neuropathol.*, 133(2):155–175, 2017. doi: 10.1007/s00401-016-1662-x.

B. Dubois, H.H. Feldmann, C. Jacova, H. Hampel, J.L. Molinuevo, K. Blennow, S.T. DeKosky, S. Gauthier, D. Selkoe, R. Bateman, S. Cappa, S. Crutch, S. Engelborghs, G.B. Frisoni, N.C. Fox, D. Galasko, M.O. Habert, G.A. Jicha, A. Nordberg, F. Pasquier, G. Rabinovici, P. Robert, C. Rowe, S. Salloway, M. Sarazin, S. Epelbaum, L.C. de Souza, B. Vellas, P.J. Visser, L. Schneider, Y. Stern, P. Scheltens, and J.L. Cummings. Advancing research diagnostic criteria for Alzheimer's Disease: The IWG-2 criteria. *Lancet Neurol*, 13(6):614–629, 2014. doi: 10.1016/S1474-4422(14)70090-0.

B. Dubois, A. Padovani, P. Scheltens, A. Rossi, and G. Dell?Agnello. Timely diagnosis for Alzheimer's disease: A literature review on benefits and challenges. *J Alzheimers Dis*, 49(3):617–631, 2016. doi: 10.3233/JAD-150692.

J.T. Dudman and M.F. Nolan. Stochastically gating ion channels enable patterned spike firing through activity-dependent modulation of spike probability. *PLoS Comput Biol*, 5 (2):e1000290, 2009. doi: 10.1371/journal.pcbi.1000290.

F.H. Duffy, M.S. Albert, and G. McAnulty. Brain electrical activity in patients with presenile and senile dementia of the Alzheimer type. *Ann Neurol*, 16(4):439–448, 1984. doi: 10.1002/ana.410160404.

J.C. Eccles. Interpretation of action potentials evoked in the cerebral cortex. *Electroencephalogr. Clin. Neurophysiol.*, 3:449–464, 1951. doi: 10.1016/0013-4694(51)90033-8.

G.T. Einevoll, C. Kayser, N.K. Logothetis, and S. Panzeri. Modelling and analysis of local field potentials for studying the function of cortical circuits. *Nat Rev Neurosci*, 14:770–785, 2013. doi: 10.1038/nrn3599.

A.D. Ekstrom, M.J. Kahana, J.B. Caplan, T.A. Fields, E.A. Isham, E.L. Newman, and I. Fried. Cellular networks undelying human spatial navigation. *Nature*, 425:184–188, 2003. doi: 10.1038/nature01964.

M.M.A. Engels, A. Hillebrand, W.M. van der Flier, C.J. Stam, P. Scheltens, and E.C.W. van Straaten. Slowing of Hippocampal Activity Correlates with Cognitive Decline in Early Onset Alzheimer's Disease. An MEG Study with Virtual Electrodes. *Front Hum Neurosci*, 10:238, 2016. doi: 10.3389/fnhum.2016.00238.

B. Ermentrout. *Simulating, Analyzing, and Animating Dynamical Systems*. Society for Industrial and Applied Mathematics, 2002.

G.B. Ermentrout and N. Kopell. Parabolic Bursting in an Excitable System Coupled with Slow Oscillations. *SIAM J. Appl. Math.*, 46(2):233–253, 1986. doi: 10.1137/0146017.

C. Erö, M.-O. Gewaltig, D. Keller, and H. Markram. A Cell Atlas for the Mouse Brain. *Front. Neuroinform.*, 12:84, 2018. doi: 10.3389/fninf.2018.00084.

L. Fan, H. Li, J. Zhuo, Y. Zhang, J. Wang, L. Chen, Z. Yang, C. Chu, S. Xie, A.R. Laird, P.T. Fox, S.B. Eickhoff, C. Yu, and T. Jiang. The Human Brainnetome Atlas: A New Brain Atlas Based on Connectional Architecture. *Cerebral Cortex*, 26(8):3508–3526, 2016. doi: 10.1093/cercor/bhw157.

B. Farina, G. Della Marca, G. Maestoso, N. Amoroso, E.M. Valenti, G.A. Carbone, C. Massullo, A. Contardi, and C. Imperatori. The Association among Default Mode Network Functional Connectivity, Mentalization, and Psycopathology in a Nonclinical Sample: An eLORETA Study. *Psychopathology*, 51:16–23, 2018. doi: 10.1159/000485517.

A. Fernández, M.I. López-Ibor, A. Turrero, J.M. Santos, M.D. Morón, R. Hornero, C. Gómez, M.A. Méndez, T. Ortiz, and J.J. López-Ibor. Lempel-Ziv complexity in schizophrenia: a MEG study. *Clin Neurophysiol*, 122(11):2227–2235, 2011. doi: 10.1016/j.clinph.2011.04.011.

F.R. Fernandez and J.A. White. Artificial Synaptic Conductances Reduce Subthreshold Oscillations and Periodic Firing in Stellate Cells of the Entorhinal Cortex. *J Neurosci*, 28(14):3790–3803, 2008. doi: 10.1523/JNEUROSCI.5658-07.2008.

L.A. Ferrat, M. Goodfellow, and R.J. Terry. Classifying dynamic transitions in high dimensional neural mass models: A random forest approach. *PLoS Comput Biol*, 14(3): e1006009, 2018. doi: 10.1371/journal.pcbi.1006009.

H. Finger, M. Bönstrup, B. Cheng, A. Messé, C. Hilgetag, G. Thomalla, C. Gerloff, and P. König. Modeling of Large-Scale Functional Brain Networks Based on Structural Connectivity from DTI: Comparison of EEG Derived Phase Coupling Networks and Evaluation of Alternative Methods along the Modeling Path. *PLoS Comput Biol*, 12(8): e1005025, 2016. doi: 10.1371/journal.pcbi.1005025.

R. FitzHugh. Impulses and Physiological States in Theoretical Models of Nerve Membrane. *Biophys. J.*, 1(6):445–466, 1961. doi: 10.1016/S0006-3495(61)86902-6.

M.F. Folstein, S.E. Folstein, and P.R. McHugh. “Mini-Mental State”: A Practical Method for Grading the Cognitive State of Patients for the Clinician. *J. Psychiat. Res.*, 12: 189–198, 1975. doi: 10.1016/0022-3956(75)90026-6.

E. Fransén, A.A. Alonso, C.T. Dickson, J. Magistretti, and M.E. Hasselmo. Ionic Mechanisms in the Generation of Subthreshold Oscillations and Action Potential Clustering in Entorhinal Layer II Stellate Neurons. *Hippocampus*, 14:368–384, 2004. doi: 10.1002/hipo.10198.

M. Fraschini, M. Demuru, A. Crobe, F. Marrosu, C.J. Stam, and A. Hillebrand. The effect of epoch length on estimated EEG functional connectivity and brain network organization. *J Neural Eng*, 13(3):036015, 2016. doi: 10.1088/1741-2560/13/3/036015.

D.R. Freestone, P.J. Karoly, D. Nesić, P. Aram, M.J. Cook, and D.B. Grayden. Estimation of effective connectivity via data-driven neural modelling. *Front Neurosci*, 8:383, 2014. doi: 10.3389/fnins.2014.00383.

M. Frigo and S.G. Johnson. FFTW: An Adaptive Software Architecture for the FFT. *Proc Int Conf Acoust Speech Signal Process*, 3:1381–1384, 1998. doi: 10.1109/ICASSP.1998.681704.

G.B. Frisoni, A. Prestia, P.E. Rasser, M. Bonetti, and P.M. Thompson. In vivo mapping of incremental cortical atrophy from incipient to overt Alzheimer’s disease. *J Neurol*, 256: 916, 2009. doi: 10.1007/s00415-009-5040-7.

K.J. Friston, L. Harrison, and W. Penny. Dynamic causal modelling. *NeuroImage*, 19(4): 1273–1302, 2003. doi: 10.1016/S1053-8119(03)00202-7.

H. Fu, G.A. Rodriguez, M. Herman, S. Emrani, E. Nahmani, G. Barrett, H.Y. Figueroa, E. Goldberg, S.A. Hussaini, and K.E. Duff. Tau pathology induced excitatory neuron loss, grid cell dysfunction, and spatial memory deficits reminiscent of early Alzheimer’s disease. *Neuron*, 93:533–541, 2017. doi: 10.1016/j.neuron.2016.12.023.

M. Fuchs, J. Kastner, M. Wagner, S. Hawes, and J.S. Ebersole. A standardized boundary element method volume conductor model. *Clin Neurophysiol.*, 113(5):702–712, 2002. doi: 10.1016/S1388-2457(02)00030-5.

E. Gallego-Jutgla, J. Sole-Casals, F.B. Vialatte, J. Dauwels, and A. Cichocki. A Theta-Band EEG Based Index for Early Diagnosis of Alzheimer's Disease. *J Alzheimers Dis*, 43:1175–1184, 2015. doi: 10.3233/JAD-140468.

C.J. Galton, K. Petterson, J.H. Xuereb, and J.R. Hodges. Atypical and typical presentations of Alzheimer's disease: a clinical, neuropsychological, neuroimaging and pathological study of 13 cases. *Brain*, 123(3):484–498, 2000. doi: 10.1093/brain/123.3.484.

L.V. Gambuzza, J. Gomez-Gardenes, and M. Frasca. Amplitude dynamics favors synchronization in complex networks. *Sci Rep*, 6:24915, 2016. doi: 10.1038/srep24915.

G. Gao, H. Jia, X. Wu, D. Yu, and Y. Feng. Altered resting-state EEG microstate parameters and enhanced spatial complexity in male adolescent patients with mild spastic diplegia. *Brain Topogr*, 30:233–244, 2017. doi: 10.1007/s10548-016-0520-4.

D.L. Garden, P.D. Dodson, C. O'Donnell, M.D. White, and M.F. Nolan. Tuning of synaptic integration in the medial entorhinal cortex to the organization of grid cell firing fields. *Neuron*, 60(5):875–889, 2008. doi: 10.1016/j.neuron.2008.10.044.

E. Gascon, K. Lynch, H. Ruan, S. Almeida, J.M. Verheyden, W.W. Seeley, D.W. Dickson, L. Petrucelli, D. Sun, J. Jiao, H. Zhou, M. Jakovcevski, S. Akbarian, W.-D. Yao, and F.-B. Gao. Alterations in microRNA-124 and AMPA receptors contribute to social behavioral deficits in frontotemporal dementia. *Nat Med*, 20:1444–1451, 2014. doi: 10.1038/nm.3717.

T. Gasser, P. Bächer, and H. Steinberg. Test-retest reliability of spectral parameters of the EEG. *Electroencephalogr Clin Neurophysiol*, 60(4):312–319, 1985. doi: 10.1016/0013-4694(85)90005-7.

W. Gerstner, W.M. Kistler, R. Naud, and L. Paninski. *Neuronal Dynamics*. Cambridge University Press, 2014.

S. Ghazi-Noori, K.E. Froud, S. Mizielinska, C. Powell, M. Smidak, M. Fernandez de Marco, C. O'Malley, M. Farmer, N. Parkinson, E.M.C Fisher, E.A. Asante, S. Brandner, J. Collinge, and A. Isaacs. Progressive neuronal inclusion formation and axonal degeneration in CHMP2B mutant transgenic mice. *Brain*, 135:819–832, 2012. doi: 10.1093/brain/aws006.

L.M. Giocomo and M.E. Hasselmo. Time constants of h current in Layer II stellate cells differ along the dorsal to ventral axis of medial entorhinal cortex. *J. Neurosci*, 28(38): 9414–9425, 2008. doi: 10.1523/JNEUROSCI.3196-08.2008.

L.M. Giocomo and M.E. Hasselmo. Knockout of HCN1 subunit flattens dorsal-ventral frequency gradient of medial entorhinal neurons in adult mice. *J. Neurosci*, 29(23): 7625–7630, 2009. doi: 10.1523/JNEUROSCI.0609-09.2009.

L.M. Giocomo, E.A. Zilli, E. Fransen, and M.E. Hasselmo. Temporal frequency of subthreshold oscillations scales with entorhinal grid cell field spacing. *Science*, 315(5819): 1719–1722, 2007. doi: 10.1126/science.1139207.

L.M. Giocomo, T. Stensola, T. Bonnevie, T. Van Cauter, M.B. Moser, and E.I. Moser. Topography of head direction cells in medial entorhinal cortex. *Curr Biol*, 24:252–262, 2014. doi: 10.1016/j.cub.2013.12.002.

P. Glendinning. *Stability, instability and chaos: an introduction to the theory of nonlinear differential equations*. Cambridge University Press, 1994.

J.H. Goldwyn and E. Shea-Brown. The What and Where of Adding Channel Noise to the Hodgkin-Huxley Equations. *PLoS Comput Biol*, 7(11):e1002247, 2011. doi: 10.1371/journal.pcbi.1002247.

J.H. Goldwyn, N.S. Imennov, M. Famulare, and E. Shea-Brown. Stochastic differential equation models for ion channel noise in Hodgkin-Huxley neurons. *Phys Rev E*, 83: 041908, 2011. doi: 10.1103/PhysRevE.83.041908.

C. Gómez, R. Hornero, D. Abásolo, A. Fernández, and M. López. Complexity analysis of the magnetoencephalogram background activity in Alzheimer's disease patients. *Med Eng Phys*, 28(9):851–859, 2006. doi: 10.1016/j.medengphy.2006.01.003.

J.T. Goncalves, J.E. Anstey, P. Golshani, and C. Portera-Cailliau. Circuit level defects in the developing neocortex of Fragile X mice. *Nat Neurosci*, 16(7):903–909, 2013. doi: 10.1038/nn.3415.

M. Goodfellow, C. Rummel, E. Abela, M.P. Richardson, K. Schindler, and J.R. Terry. Estimation of brain network ictogenicity predicts outcome from epilepsy surgery. *Sci Rep*, 6:29215, 2016. doi: 10.1038/srep29215.

J. Goossens, J. Laton, J. Van Schependom, J. Gielen, H. Strufs, S. Can Mossevelde, T. Van den Bossche, J. Goeman, P.P. De Deyn, A. Sieben, J.J. Martin, Van Broeckhoven C., J. van der Zee, S. Engelborghs, and G. Nagels. EEG Dominant Frequency Peak Differentiates Between Alzheimer's Disease and Frontotemporal Lobal Degeneration. *J Alzheimers Dis*, 55:53–58, 2017. doi: 10.3233/JAD-160188.

J. Götz and L.M. Ittner. Animal models of Alzheimer's disease and frontotemporal dementia. *Nat Rev Neurosci*, 9(7):532–544, 2008. doi: 10.1038/nrn2420.

R. Goutagny, N. Gu, C. Cavanagh, J. Jackson, J.G. Chabot, R. Quirion, S. Krantic, and S. Wililams. Alterations in hippocampal network oscillations and theta-gamma coupling arise before Aβoverproduction in a mouse model of Alzheimer's disease. *Eur J Neurosci*, 37(12):1896–1902, 2013. doi: 10.1111/ejn.12233.

S. Gudmundsson, T.P. Runarsson, S. Sigurdsson, G. Eiriksdottir, and K. Johnsen. Reliability of quantitative EEG features. *Clin. Neurophys.*, 118(10):2162–2171, 2007. doi: 10.1016/j.clinph.2007.06.018.

T. Guo, W. Noble, and D.P. Hanger. Roles of tau protein in health and disease. *Acta Neuropathol*, 133(5):665–704, 2017. doi: 10.1007/s00401-017-1707-9.

T. Hafting, M. Fyhn, S. Molden, M.B. Moser, and E.I. Moser. Microstructure of a spatial map in the entorhinal cortex. *Nature*, 436:801–806, 2005. doi: 10.1038/nature03721.

H. Hallez, B. Vanrumste, R. Grech, J. Muscat, W. De Clercq, A. Vergult, Y. D'Asseler, K.P. Camilleri, S.G. Fabri, S. Van Huffel, and I. Lemahieu. Review on solving the forward problem in EEG source analysis. *Journal of NeuroEngineering and Rehabilitation*, 4: 46, 2007. doi: 10.1186/1743-0003-4-46.

J.A. Harasty, G.M. Halliday, J.J. Kril, and C. Code. Specific temporoparietal gyral atrophy reflects the pattern of language dissolution in Alzheimer's disease. *Brain*, 122(4):675–686, 1999. doi: 10.1093/brain/122.4.675.

M. Hassan and F. Wendling. Electroencephalography source connectivity: toward high time/space resolution brain networks. In *arXiv:1801.02549*, 2018.

M. Hassan, O. Dufor, I. Merlet, C. Berrou, and F. Wendling. EEG Source Connectivity Analysis: From Denser Array Recordings to Brain Networks. *PLoS ONE*, 9(8):e105041, 2014. doi: 10.1371/journal.pone.0105041.

M. Hassan, I. Merlet, A. Mheich, A. Kabbara, A. Biraben, A. Nica, and F. Wendling. Identification of Interictal Epileptic Networks from Dense-EEG. *Brain Topogr*, 30:60–76, 2017. doi: 10.1007/s10548-016-0517-z.

M.E. Hasslemo and C.F. Shay. Grid cell firing patterns may arise from feedback interaction between intrinsic rebound spiking and transverse travelling waves with multiple heading angles. *Front Syst Neurosci*, 8:201, 2014. doi: 10.3389/fnsys.2014.00201.

M. Hata, T. Kazui, H.and Tanaka, R. Ishii, L. Canuet, R.D. Pascual-Marqui, Y. Aoki, S. Ikeda, H. Kanemoto, K. Yoshiyama, M. Iwase, and M. Takeda. Functional connectivity assessed by resting state EEG correlates with cognitive decline of Alzheimer's disease - An eLORETA study. *Clin Neurophysiol*, 127:1269–1278, 2016. doi: 10.1016/j.clinph.2015.10.030.

F. Hatz, M. Hardmeier, N. Benz, M. Ehrensperger, U. Gschwandtner, S. Ruegg, C. Schindler, A.U. Monsch, and P. Fuhr. Microstate connectivity alterations in patients with early Alzheimer's disease. *Alzheimers Res Ther*, 7:78, 2015a. doi: 10.1186/s13195-015-0163-9.

F. Hatz, M. Hardmeier, H. Bousleiman, S. Rüegg, C. Schindler, and P. Fuhr. Reliability of fully automated versus visually controlled pre- and post-processing of resting-state EEG. *Clin Neurophysiol*, 126(2):268–274, 2015b. doi: 10.1016/j.clinph.2014.05.014.

I. Heggland, P. Kvello, and M.P. Witter. Electrophysiological Characterization of Networks and Single Cells in the Hippocampal Region of a Transgenic Rat Model of Alzheimer's Disease. *eNeuro*, 6(1):ENEURO.0448–17.2019, 2019. doi: 10.1523/ENEURO.0448-17.2019.

M. Hiltunen, T. van Groen, and J. Jolkkonen. Functional Roles of Amyloid-βPeptides: Evidence from Experimental Studies. *J Alzheimers Dis*, 18(2):401–412, 2009. doi: 10.3233/JAD-2009-1154.

M.W. Hirsch, S. Smale, and R.L. Devaney. *Differential Equations, Dynamical Systems, and an Introduction to Chaos*. Academic Press, 3rd edition, 2003.

J. Hlinka and S. Coombes. Using computational models to relate structural and functional brain connectivity. *Eur J Neurosci*, 36(2):2137–2145, 2012. doi: 10.1111/j.1460-9568.2012.08081.x.

A.L. Hodgkin. The local electric changes associated with repetitive action in a non-medullated axon. *J Physiol*, 107(2):165–181, 1948. doi: 10.1113/jphysiol.1948.sp004260.

A.L. Hodgkin and A.F. Huxley. A quantitative description of membrane current and its application to conduction and excitation in nerve. *J. Physiol.*, 117:500–544, 1952. doi: 10.1113/jphysiol.1952.sp004764.

A. Holtmaat, T. Bonhoeffer, D.K. Chow, J. Chuckowree, V. De Paola, S.B. Hofer, M. Hubener, T. Keck, G. Knott, W.C. Lee, R. Mostany, T.D. Mrsic-Flogel, E. Nedivi, C. Portera-Cailliau, K. Svoboda, J.T. Trachtenberg, and L. Wilbrecht. Long term, high resolution imaging in the mouse neocortex through a chronic cranial window. *Nat Protoc.*, 4(8):1128–1144, 2009. doi: 10.1038/nprot.2009.89.

C. Honey, R. Kötter, Breakspear M., and O. Sporns. Network structure of the cerebral cortex shapes functional connectivity on multiple time scales. *Proc Natl Acad Sci USA*, 104(24):10240–10245, 2007. doi: 10.1073/pnas.0701519104.

C.J. Honey, O. Sporns, L. Cammoun, X. Gigandet, J.P. Thiran, R. Meuli, and P. Hagmann. Predicting human resting-state functional connectivity. *PNAS*, 106(6), 2009. doi: 10.1073/pnas.0811168106.

B.V. Hooli, Z.M. Kovacs-Vajna, K. Mullin, M.A. Blumenthal, M. Mattheisen, C. Zhang, C. Lange, G. Mohapatra, L. Bertram, and R.E. Tanzi. Rare autosomal copy number variations in early-onset familiar Alzheimer's disease. *Mol Psychiatry*, 19(6):676–681, 2014. doi: 10.1038/mp.2013.77.

R. Hornero, D. Abásolo, J. Escudero, and C. Gómez. Nonlinear analysis of electroencephalogram and magnetoencephalogram recordings in patients with Alzheimer's disease. *Phil. Trans. R. Soc. A*, 367:317–366, 2009. doi: 10.1098/rsta.2008.0197.

M.D. Humphries and K. Gurney. Network Small World-Ness: A Quantitative Method for Determining Canonical Network Equivalence. *PLoS One*, 3(4):e0002051, 2008. doi: 10.1371/journal.pone.0002051.

J.N. Ianof, F.J. Fraga, L.A. Ferreira, R.T. Ramos, J.L.C. Demario, R. Baratho, L.F.H. Basile, R. Nitrini, and R. Anghinah. Comparative analysis of the electroencephalogram in patients with Alzheimer's disease, diffuse axonal injury patients and healthy controls using LORETA analysis. *Dement Neuropsychol*, 11(2):176–185, 2017. doi: 10.1590/1980-57642016dn11-020010.

R. Ihl, T. Dierks, L. Froelich, E. Martin, and K. Maurer. Segmentation of the Spontaneous EEG in Dementia of the Alzheimer Type. *Neuropsychobiology*, 27:231–246, 1993. doi: 10.1159/000118986.

S. Ikeda, R. Ishii, L. Canuet, and R.D. Pascual-Marqui. Source estimation of epileptic activity using eLORETA kurtosis analysis. *BMJ Case Rep*, 2017:bcr–2017–222123, 2017. doi: 10.1136/bcr-2017-222123.

S. Irisawa, T. Isotani, T. Yagyu, S. Morita, K. Nishida, K. Yamada, M. Yoshimura, G. Okugawa, K. Nobuhara, and T. Kinoshita. Increased omega complexity and decreased microstate duration in nonmedicated schizophrenic patients. *Neuropsychobiology*, 54 (2):134–139, 2006. doi: 10.1159/000098264.

A.M. Isaacs, P. Johannsen, I. Holm, J.E. Nielsen, and FReJA. Frontotemporal dementia caused by CHMP2B mutations. *Curr Alzheimer Res*, 8(3):246–251, 2011. doi: 10.2174/156720511795563764.

E.M. Izhikevich. Neural Excitability, Spiking and Bursting. *Int. J. Bifurc. Chaos*, 10(6): 1171–1266, 2000. doi: 10.1142/S0218127400000840.

E.M. Izhikevich. Resonate-and-fire neurons. *Neur Net*, 14:883–894, 2001. doi: 10.1016/S0893-6080(01)00078-8.

E.M. Izhikevich. Simple Model of Spiking Neurons. *IEEE Trans Neural Net*, 14(6):1569–1572, 2003. doi: 10.1109/TNN.2003.820440.

E.M. Izhikevich. *Dynamical Systems in Neuroscience: The Geometry of Excitability and Bursting*. MIT Press, 2007.

J. Jacobs, M.J. Mahana, A.D. Ekstrom, M.V. Mollison, and I. Fried. A sense of direction in human entorhinal cortex. *Proc Nat Acad Sci USA*, 107(14):6487–6492, 2010. doi: 10.1073/pnas.0911213107.

J. Jacobs, C.T. Weidemann, J.F. Miller, A. Solway, J.F. Burke, X.-X. Wei, N. Suthana, M.R. Sperling, A.D. Sahran, I. Fried, and M. Kahana. Direct recordings of grid-like neuronal activity in human spatial navigation. *Nat Neurosci*, 16:1188–1190, 2013. doi: 10.1038/nn.3466.

M. Jalili. Functional Brain Networks: Does the Choice of Dependency Estimator and Binarization Method Matter? *Sci. Rep.*, 6:29780, 2016. doi: 10.1038/srep29780.

J.L. Jankowsky and H. Zheng. Practical considerations for choosing a mouse model of Alzheimer's disease. *Mol Neurodegener*, 12:89, 2017. doi: 10.1186/s13024-017-0231-7.

B.H. Jansen and V.G. Rit. Electroencephalogram and visual evoked potential generation in a mathematical model of coupled cortical columns. *Biol. Cybern.*, 73:357–366, 1995. doi: 10.1007/BF00199471.

B.H. Jansen, G. Zouridakis, and M.E. Brandt. A neurophysiologically-based mathematical model of flash visual evoked potentials. *Biol. Cybern.*, 68:275–283, 1993. doi: 10.1007/BF00224863.

R.W. Jones. Safety, legal issues, and driving. In *Alzheimer's Disease*. Oxford University Press, 2017.

A. Joudaki, N. Salehi, M. Jalili, and M.G. Knyazeva. EEG-Based Functional Brain Networks: Does the Network Size Matter? *PLoS One*, 7(4):e35673, 2012. doi: 10.1371/journal.pone.0035673.

T. Kai, Y. Asai, K. Sakuma, T. Koeda, and K. Nakashima. Quantitative electroencephalogram analysis in dementia with Lewy bodies and Alzheimer's disease. *J Neurol Sci*, 237(1-2):89–95, 2005. doi: 10.1016/j.jns.2005.05.017.

M. Kaku. *The Future of the Mind: The Scientific Quest to Understand, Enhance, and Empower the Mind*. Allen Lane, 2014.

D.P.X. Kan, P.E. Croarkin, C.K. Phang, and P.F. Lee. EEG Differences Between Eyes-Closed and Eyes-Open Conditions at the Resting Stage for Euthymic Participants. *Neurophysiology*, 49(6):432–440, 2017. doi: 10.1007/s11062-018-9706-6.

H. Kantz and T. Schreiber. *Nonlinear Time Series Analysis*. Cambridge University Press, 2nd edition, 2004.

S. Keeley, A. Byrne, A.A. Fenton, and J. Rinzel. Firing Rate Models for Gamma Oscillations. *J Neurophysiol*, page Article in Press, 2019. doi: 10.1152/jn.00741.2018.

A. Khanna, A. Pascual-Leone, and F Farzan. Reliability of Resting-State Microstate Features in Electroencephalography. *PLoS ONE*, 9(12):e114163, 2014. doi: 10.1371/journal.pone.0114163.

A. Khanna, A. Pascual-Leone, C.M. Michel, and F Farzan. Microstates in resting-state EEG: Current status and future directions. *Neuroscience and Biobehavioural Reviews*, 49:105–113, 2015. doi: 10.1016/j.neubiorev.2014.12.010.

M. Kikuchi, T. Koenig, Y. Wada, M. Higashima, Y. Koshino, W. Strik, and T. Dierks. Native EEG and treatment effects in neuroleptic-naive schizophrenic patients: time and frequency domain approaches. *Schizophrenia Res*, 97:163–172, 2007. doi: 10.1016/j.schres.2007.07.012.

M. Kikuchi, T. Koenig, T. Munesue, A. Hanaoka, W. Strik, T. Dierks, Y. Koshino, and Y. Minabe. EEG microstate analysis in drug-naive patients with panic disorder. *PLoS One*, 6(7):e22912, 2011. doi: 10.1371/journal.pone.0022912.

J. Kindler, D. Hubl, W. Strik, T. Dierks, and T. Koenig. Resting-state EEG in schizophrenia: auditory verbal hallucinations are related to shortening of specific microstates. *Clin Neurophysiol*, 122:1179–1182, 2011. doi: 10.1016/j.clinph.2010.10.042.

A. King. The search for better animal models of Alzheimer's disease. *Nature*, 559:S13–S15, 2018. doi: 10.1038/d41586-018-05722-9.

W. Klimesch. EEG alpha and theta oscillations reflect cognitive and memory performance: a review and analysis. *Brain Research Reviews*, 29:169–195, 1999. doi: 10.1016/S0165-0173(98)00056-3.

T. Koenig, D. Lehmann, M.C.G. Merlo, K. Kochi, D. Hell, and M. Koukkou. A deviant EEG brain microstate in acture, neuroleptic-naive schizophrenics at rest. *Eur Arch Psychiatry Clin Neurosci*, 249:205–211, 1999. doi: 10.1007/s004060050.

T. Koenig, L. Prichep, D. Lehmann, P. Valdes Sosa, E. Braeker, H. Kleinlogel, R. Isenhart, and E.R. John. Millisecond by Millisecond, Year by Year: Normative EEG Microstates and Developmental Stages. *NeuroImage*, 16:41–48, 2002. doi: 10.1006/nimg.2002.1070.

T. Koenig, L. Prichep, T. Dierks, D. Hubl, L.O. Wahlund, E.R. John, and V. Jelic. Decreased EEG synchronization in Alzheimer's disease and mild cognitive impairment. *Neurobiol Aging*, 26(2):165–171, 2005a. doi: 10.1016/j.neurobiolaging.2004.03.008.

T. Koenig, D. Studer, D. Hubl, L. Melie, and W.K. Strik. Brain connectivity and different time scales measured with EEG. *Phil. Trans. R. Soc. B*, 360:1015–1024, 2005b. doi: 10.1098/rstb.2005.1649.

T. Kreuz, J.S. Haas, A. Morelli, H.D.I Abarbanel, and A. Politi. Measuring spike train synchrony. *J. Neurosci. Methods*, 165(1):151–161, 2007. doi: 10.1016/j.jneumeth.2007.05.031.

E. Kropff, J.E. Carmichael, M.B. Moser, and E.I. Moser. Speed cells in the medial entorhinal cortex. *Nature*, 523:419–424, 2015. doi: 10.1038/nature14622.

W.J. Krzanowski and Y.T. Lai. A Criterion for Determining the Number of Groups in a Data Set Using Sum-of-Squares Clustering. *Biometrics*, 44(1):23–34, 1988. doi: 10.2307/2531893.

M. Krzywinski and N. Altman. Points of significance: Comparing samples - part II. *Nat Methods*, 11:355–356, 2014. doi: 10.1038/nmeth.2900.

M. Kunhert, C. Elger, and K. Legnertz. Long-term variability of global statistical properties of epileptic brain networks. *Chaos*, 20:043126, 2010. doi: 10.1063/1.3504998.

Y.A. Kuznetsov. *Elements of Applied Bifurcation Theory*. Springer-Verlag New York, 1998.

J.P. Lachaux, E. Rodriguez, J. Martinerie, and F.J. Varela. Measuring phase synchrony in brain signals. *Hum Brain Mapp*, 8(4):194–208, 1999. doi: 10.1002/(SICI)1097-0193(1999)8:4¡194::AID-HBM4¿3.0.CO;2-C.

G. Lancaster, D. Iatsenko, A. Piddle, V. Ticcinelli, and A. Stefanovska. Surrogate data for hypothesis testing of physical systems. *Phys Rep*, 748:1–60, 2018. doi: 10.1016/j.physrep.2018.06.001.

V. Latora and M. Marchiori. Efficient Behaviour of Small-World Networks. *Phys Rev Lett*, 87(19):198701, 2001. doi: 10.1103/PhysRevLett.87.198701.

C. Lee, R. Oostenveld, S.H. Lee, L.H. Kim, H. Sung, and J.H. Choi. Dipole Source Localization of Mouse Electroencephalogram Using the Fieldtrip Toolbox. *PLoS One*, 8(11):e79442, 2013. doi: 10.1371/journal.pone.0079442.

J. Lee, D. Kim, and H.-S. Shin. Lack of delta waves and sleep disturbances during non-rapid eye movement sleep in mice lacking $\alpha 1_{\mathrm{G}}$-subunit of T-type calcium channels. *Proc Natl Acad Sci USA*, 101(52):18195–18199, 2004. doi: 10.1073/pnas.0408089101.

D. Lehmann, H. Ozaki, and I. Pal. EEG alpha map series: brain micro-states by space-oriented adaptive segmentation. *Electroencephalogr Clin Neurophysiol.*, 67(3):271–288, 1987. doi: 10.1016/0013-4694(87)90025-3.

D. Lehmann, J. Wackermann, C.M. Michel, and T. Koenig. Space-oriented EEG segmentation reveals changes in brain electric field maps under the influence of a nootropic drug. *Psychiatry Res: Neuroimaging*, 50(4), 1993. doi: 10.1016/0925-4927(93)90005-3.

D. Lehmann, W.K. Strik, B. Henggeler, T. Koenig, and M. Koukkou. Brain electric microstates and momentary conscious mind states as building blocks of spontaneous thinking: I. Visual imagery and abstract thoughts. *International Journal of Psychophysiology*, 29(1):1–11, 1998. doi: 10.1016/S0167-8760(97)00098-6.

D. Lehmann, P.L. Faber, S. Galderisi, W.M. Herrmann, T. Kinoshita, M. Koukkou, A. Mucci, R.D. Pascual-Marqui, N. Saito, J. Wackermann, G. Winterer, and T. Koenig. EEG microstate duration and syntax in acute, medicatio-naive, first episode schizophrenia: a multi-center study. *Psychiatry Res: Neuroimaging*, 138:141–156, 2005. doi: 10.1016/j.pscychresns.2004.05.007.

B.P. Leifer. Early diagnosis of Alzheimer's disease: Clinical and economic benefits. *J Am Geriatr Soc*, 51:S281–288, 2003. doi: 10.1046/j.1532-5415.5153.x.

E.S. Lein, M.J. Hawrylycz, N. Ao, M. Ayres, A. Bensinger, A. Bernard, et al. Genome-wide atlas of gene expression in the adult mouse brain. *Nature*, 445(7124):168–76, 2007. doi: 10.1038/nature05453.

J. Lempel, A. ad Ziv. On the Complexity of Finite Sequences. *IEEE Trans Inform Theory*, 22(1):75–81, 1976. doi: 10.1109/TIT.1976.1055501.

L. Levedev and I. Vorovich. *Functional Analysis in Mechanics*. Springer, 2002.

M. Lindau, V. Jelic, S. Johansson, C. Andersen, L. Wahlund, and O. Almkvist. Quantitative EEG abnormalities and cognitive dysfunctional in frontotemporal dementia and Alzheimer's disease. *Dement Geriatr Cogn Disord*, 15:106–114, 2003. doi: 10.1159/000067973.

S.G. Lindquist, H. Braedgaard, K. Svenstrup, A.M. Isaacs, and J.E. Nielsen. Frontotemporal dementia linked to chromosome 3 (FTD-3) - current concepts and the detection of a previously unknown branch of the Danish FTD-3 family. *Eur. J. Neurol.*, 15:667–670, 2008. doi: 10.1111/j.1468-1331.2008.02144.x.

S. Lithfous, A. Dufour, and O. Després. Spatial navigation in normal aging and the prodromal stage of Alzheimer's disease: Insights from imaging and behavioural studies. *Ageing Res Rev*, 12(1):201–213, 2013. doi: 10.1016/j.arr.2012.04.007.

Q. Liu, M. Ganzetti, N. Wenderoth, and D. Mantini. Detecting Large-Scale Brain Networks Using EEG: Imapct of Electrode Density, Head Modeling and Source Localization. *Front Neuroinform*, 12:4, 2018. doi: 10.3389/fninf.2018.00004.

X. Liu, C. Zhang, Z. Ji, Y. Ma, X. Shang, Q. Zhang, W. Zheng, X. Li, J. Gao, R. Wang, J. Wang, and H. Yu. Multiple characteristics analysis of Alzheimer's electroencephalogram by power spectral density and Lempel-Ziv complexity. *Cogn Neurodyn*, 10:121–133, 2016. doi: 10.1007/s11571-015-9367-8.

C.-Y. Lo, P.-N. Wang, K.-H. Chou, J. Wang, Y. He, and C.-P. Lin. Diffusion Tensor Tractography Reveals Abnormal Topological Organization in Strucutral Cortical Networks in Alzheimer's Disease. *J Neurosci*, 30(50):16876–16885, 2010. doi: 10.1523/JNEUROSCI.4136-10.2010.

M.A. Lopes and A.V. Goltsev. Distinct dynamical behaviour in Erdos-Renyi networks, regular random networks, ring lattices, and all-to-all neuronal networks. *Phys. Rev. E*, 99:022303, 2019. doi: 10.1103/PhysRevE.99.022303.

E. Lowet, M.J. Roberts, A. Peter, B. Gips, and P. De Weerd. A quantitative theory of gamma synchronization in macaque V1. *eLife*, 6:e26642, 2017. doi: 10.7554/eLife.26642.

T.B. Luke, E. Barreto, and P. So. Complete Classification of the Macroscopic Behaviour of a Heterogeneous Network of Theta Neurons. *Neural Comput*, 25:3207–3234, 2013.

H. Lütcke, F. Gerhard, F. Zenke, W. Gerstner, and F. Helmchen. Inference of neuronal network spike dynamics and topolgy from calcium imaging data. *Front Neural Circuits*, 7:Article 201, 2013. doi: 10.3389/fncir.2013.00201.

F. Maestú, P. Cuesta, O. Hasan, A. Fernandéz, M. Funke, and P.E. Schulz. The Importance of the Validation of M/EEG With Current Biomarkers in Alzheimer's Disease. *Front Hum Neurosci*, 13:17, 2019. doi: 10.3389/fnhum.2019.00017.

H. Markram. The blue brain project. *Nat Rev Neurosci*, 7(2):153–160, 2006. doi: 10.1038/nrn1848.

H. Markram, E. Muller, S. Ramaswamy, M.W. Reimann, M. Abdellah, C.A. Sanchez, A. Ailamaki, L. Alonso-Nanclares, N. Antille, S. Arsever, G.A.A. Kahou, T.K. Berger, A. Bilhili, N. Buncic, A. Chialimourda, G. Chindemi, J.-D. Courcol, F. Delalondre, and F. Schürmann. Reconstruction and Simulation of Neocortical Microcircuitry. *Cell*, 163 (2):456–492, 2015. doi: 10.1016/j.cell.2015.09.029.

J. Mazziotta, A. Toga, A. Evans, P. Fox, J. Lancaster, K. Zilles, R. Woods, T. Paus, G. Simpson, B. Pike, C. Holmes, L. Collins, P. Thompson, D. MacDonald, M. Iacoboni, T. Schormann, K. Amunts, N. Palomero-Gallagher, S. Geyer, L. Parsons, K. Narr, N. Kabani, G. Le Goualher, D. Boomsma, T. Cannon, R. Kawashima, and B. Mazoyer. A probabilistic atlas and reference system for the human brain: International Consortium for Brain Mapping (ICBM). *Philos Trans R Soc Lond B Biol Sci*, 356:1293–1322, 2001. doi: 10.1098/rstb.2001.0915.

A. Mazzoni, H. Lindén, H. Cuntz, A. Lansner, S. Panzeri, and G.T. Einevoll. Computing the Local Field Potential (LFP) from Integrate-and-Fire Network Models. *PLoS Comput Biol*, 11(12):e1004584, 2015. doi: 10.1371/journal.pcbi.1004584.

E. McGowan, J. Erikson, and M. Hutton. A decade of modeling Alzheimer's disease in transgenic mice. *Trends Genet*, 22(5):281–289, 2006. doi: 10.1016/j.tig.2006.03.007.

G. McKhann, D. Drachman, M. Folstein, R. Katzman, D. Price, and E. Stadlan. Clinical diagnosis of Alzheimer's disease: Report of the NINCDS-ADRDA work group under the auspices of Department of Health and Human Services Task Force on Alzheimer's Disease. *Neurology*, 34:939, 1984. doi: 10.1212/wnl.34.7.939.

B.L. McNaughton, F.P. Battaglia, O. Jensen, E.I. Moser, and M.B. Moser. Path integration and the neural basis of the 'cognitive map'. *Nat Rev Neurosci*, 7(8):663–678, 2006. doi: 10.1038/nrn1932.

A.V. Medvedeva and N.N. Yanho. Functional Connectivity as a Neurophysiological Biomarker of Alzheimer's Disease. *Journal of Alzheimer's Parkinsonism and Dementia*, 3(1):023, 2018.

N. Menkes-Caspi, H.G. Yamin, V. Kellner, T.L. Spires-Jones, D. Cohen, and E.A. Stern. Pathological Tau Disrupts Ongoing Network Activity. *Neuron*, 85(5):959–966, 2015. doi: 10.1016/j.neuron.2015.01.025.

C.M. Michel and T. Koenig. EEG microstates as a tool for studying the temporal dynamics of whole-brain neuronal networks: A review. *NeuroImage*, 180:577–593, 2018. doi: 10.1016/j.neuroimage.2017.11.062.

C.M. Michel, G. Thur, S. Morand, A. Khateb, A.J. Pegna, R. Grave de Peralta, S. Gonzalez, M. Seeck, and T. Landis. Electric source imaging of human brain functions. *Brain Res Rev*, 36:108–118, 2001. doi: 10.1016/S0165-0173(01)00086-8.

C.M. Michel, M.M. Murray, G. Lantz, S. Gonzalez, L. Spinelli, and R.G. de Peralta. EEG source imaging. *Clin Neurophysiol*, 115:2195–2222, 2004. doi: 10.1016/j.clinph.2004.06.001.

K.G. Mideksa, A. Singh, N. Hoogenboom, H. Hellreigel, H. Krause, A. Schnitzler, G. Deuschl, J. Raethjen, G. Schmidt, and M. Murhuraman. Comparison of imaging modalities and source-localization algorithms in locating the induced activity during deep brain stimulation of STN. In *2016 28th Annual International Conference of the IEEE Engineering in Medicine and Biology Society (EMBC)*, pages 105–108, 2016.

P. Milz, P.L. Faber, D. Lehmann, T. Koenig, K. Kochi, and R.D. Pascual-Marqui. The functional significance of EEG microstates - Associations with modalities of thinking. *NeuroImage*, 125:643–656, 2016. doi: 10.1016/j.neuroimage.2015.08.023.

F. Miraglia, F. Vecchio, P. Bramanti, and P.M. Rossini. EEG characteristics in eyes open versus eyes closed conditions: Small world network architecture in healthy aging and age related brain degeneration. *Clinical Neurophysiology*, 127:1261–1268, 2016. doi: 10.1016/j.clinph.2015.07.040.

R. Mito, D. Raffelt, T. Dhollander, D.N. Vaughan, J.D. Tournier, O. Salvado, A. Brodtmann, C.C. Rowe, V.L. Villemagne, and A. Connelly. Fibre-specific white matter reductions in Alzheimer's disease and mild cognitive impairment. *Brain*, 141:888–902, 2018. doi: 10.1093/brain/awx355.

P. Mitra and H. Bokil. *Observed Brain Dynamics*. Oxford University Press, New York, 2008.

M. Molnár, R. Csuhaj, S. Horvátth, I. Vastagh, Z.A. Gaál, B. Czigler, A. Bálint, D. Csikós, and Z. Nagy. Spectral and complexity features of the EEG changed by visual input in a case of subcortical stroke compared to healthy controls. *Clin Neurophysiol*, 117(4): 771–780, 2006. doi: 10.1016/j.clinph.2005.12.022.

E. Montbrió, D. Pazó, and A. Roxin. Macroscopic Description for Networks of Spiking Neurons. *Phys Rev X*, 5:021028, 2015. doi: 10.1103/PhysRevX.5.021028.

R.J. Moran, S.J. Kiebel, K.E. Stephan, R.B. Reilly, J. Daunizeau, and K.J. Friston. A neural mass model of spectral responses in electrophysiology. *NeuroImage*, 37(3): 706–720, 2007. doi: 10.1016/j.neuroimage.2007.05.032.

J.H. Morrison and M.G. Baxter. The ageing cortical synapse: hallmarks and implications for cognitive decline. *Nat Rev Neurosci*, 13:240–250, 2012. doi: 10.1038/nrn3200.

E.I. Moser, E. Kropff, and M.B. Moser. Place cells, grid cells, and the brain's spatial representation system. *Annu Rev Neurosci*, 31:69–89, 2008. doi: 10.1146/annurev.neuro.31.061307.090723.

V.B. Mountcastle. The columnar organization of the neocortex. *Brain*, 120:701–722, 1997. doi: 10.1093/brain/120.4.701.

C. Mulert, L. Jäger, R. Schmitt, P. Bussfeld, O. Pogarell, H.J. Möller, G. Juckel, and U. Hegerl. Integration of fMRI and simultaneous EEG: towards a comprehensive understanding of localization and time-course of brain activity in target detection. *NeuroImage*, 22:83–94, 2004. doi: 10.1016/j.neuroimage.2003.10.051.

M.P. Murphy and H. LeVine III. Alzheimer's Disease and the β-Amyloid Peptide. *J Alzheimers Dis*, 19(1):311–323, 2010. doi: 10.3233/JAD-2010-1221.

F. Musso, J. Brinkmeyer, A. Mobascher, T. Warbrick, and G. Winterer. Spontaneous brain activity and EEG microstates. A novel EEG/fMRI analysis approach to explore resting-state networks. *NeuroImage*, 52:1149–1161, 2010. doi: 10.1016/j.neuroimage.2010.01.093.

J. Nagumo, S. Arimoto, and S. Yoshizawa. An active pulse transmission line simulating nerve axon. *Proc. IRE*, 50:2061–2070, 1962. doi: JRPROC.1962.288235.

A. Nakamura, P. Cuesta, A. Fernandéz, Y. Aragata, K. Iwata, I. Kuratsubo, et al. Electromagnetic signatures of the preclinical and prodromal stages of Alzheimer's disease. *Brain*, 141(5):1470–1485, 2018. doi: 10.1093/brain/awy044.

T. Nakazono, H. Jun, M. Blurton-Jones, K.N. Green, and K.M. Igarashi. Gamma oscillations in the entohrinal hippocampal circuit underlying memory and dementia. *Neurosci Res*, 129:40–46, 2018. doi: 10.1016/j.neures.2018.02.002.

S.E. Nasrabady, B. Rizvi, J.E. GOldman, and A.M. Brickman. White matter changes in Alzheimer's disease: a focus on myelin and oligodendrocytes. *Acta Neuropathol Commun*, 6:22, 2018. doi: 10.1186/s40478-018-0515-3.

P.T. Nelson, I. Alafuzoff, E.H. Bigio, C. Bouras, H. Braak, N.J. Cairns, et al. Correlation of Alzheimer Disease Neuropathologic Changes with Cognitive Status: A Review of the Literature. *J Neuropathol Exp Neurol*, 71(5):362–381, 2012. doi: 10.1097/NEN.0b013e31825018f7.

G.T Neske. The Slow Oscillation in Cortical and Thalamic Networks: Mechanisms and Functions. *Front Neural Circuits*, 9:88, 2016. doi: 10.3389/fncir.2015.00088.

T.V. Ness, M.W.H. Remme, and G.T. Einevoll. h-Type Membrane Current Shapes the Local Field Potential from Populations of Pyramidal Neurons. *J. Neurosci*, 38(26): 6011–6024, 2018. doi: 10.1523/JNEUROSCI.3278-17.2018.

E. Neto, E. Allen, H. Aurlien, H. Nordby, and T. Eichele. EEG spectral features discriminate between Alzheimer's and vascual dementia. *Front Neurol*, 6:25, 2015. doi: 10.3389/fneur.2015.00025.

S. Neufang, A. Akhrif, V. Riedl, H. Förstl, A. Kurz, C. Zimmer, et al. Disconnection of frontal and parietal areas contributes to impaired attention in very early Alzheimer's disease. *J Alzheimers Dis*, 25(2):309–321, 2011. doi: 10.3233/JAD-2011-102154.

K. Nishida, M. Yoshimura, T. Isotani, T. Yoshida, Y. Kitaura, A. Saito, H. Mii, M. Kato, Y. Takekita, A. Suwa, S. Morita, and T. Kinoshita. Differences in quantitative EEG between frontotemporal dementia and Alzheimer's disease as revealed by LORETA. *Clin Neurophysiol*, 122(9):1718–1725, 2011. doi: 10.1016/j.clinph.2011.02.011.

K. Nishida, Y. Morishima, M. Yoshimura, T. Isotani, S. Irisawa, K. Jann, et al. EEG microstates associated with salience and frontoparietal networks in frontotemporal dementia, schizophrenia, and Alzheimer's disease. *Clin Neurophysiol*, 124:1106–1114, 2013. doi: 10.1016/j.clinph.2013.01.005.

M.F. Nolan, J.T. Dudman, P.D. Dodson, and B. Santoro. HCN1 Channels Control Resting and Active Integrative Properties of Stellate Cells from Layer II of the Entorhinal Cortex. *J. Neurosci*, 27(46):12440–12451, 2007. doi: 10.1523/JNEUROSCI.2358-07.2007.

G. Nolte, O. Bai, L. Wheaton, Z. Mari, S. Vorbach, and M. Hallett. Identifying true brain interaction from EEG data using the imaginary part of coherency. *Clinical Neurophysiology*, 115:2292–2307, 2004. doi: 10.1016/j.clinph.2004.04.029.

P.L. Nunez and R. Srinivasan. *Electric Fields of the Brain: The neurophysics of EEG*. Oxford University Press, 2006.

Office for National Statistics. Deaths registered in England and Wales (series DR): 2017, 2018.

J. O'Keefe, N. Burgess, J.G. Donnett, K.J. Jeffery, and E.A. Maguire. Place cells, navigational accuracy, and the human hippocampus. *Phil. Trans. R. Soc. Lond. B*, 353: 1333–1340, 1998. doi: 10.1098/rstb.1998.0287.

S. Olbrich, C. Mulert, S. Karch, M. Trenner, G. Leicht, O. Pogarell, and U. Hegerl. EEG-vigilance and BOLD effect during simultaneous EEG/fMRI measurement. *NeuroImage*, 45(2):319–332, 2009. doi: 10.1016/j.neuroimage.2008.11.014.

P. Olejniczak. Neurophysiologic Basis of EEG. *J Clin Neurophysiol*, 23:186–189, 2006. doi: 10.1097/01.wnp.0000220079.61973.6c.

R. Oostenveld, D.F. Stegeman, P. Praamstra, and A. van Oosterom. Brain symmetry and topographic analysis of lateralized event-related potentials. *Clin Neurophysiol*, 114(7): 1194–1202, 2003. doi: 10.1016/S1388-2457(03)00059-2.

R. Oostenveld, P. Fries, E. Maris, and J.M. Schoffelen. FieldTrip: Open Source Software for Advanced Analysis of MEG, EEG, and Invasive Electrophysiological Data. *Comput Intell Neurosci*, 2011:156869, 2011. doi: 10.1155/2011/156869.

W. Ou, A. Nummenmaa, J. Ahveninen, J.W. Belliveau, M.S. Hämäläinen, and P. Golland. Multimodal functional imaging using fMRI-informed regional EEG/MEG source estimation. *NeuroImage*, 51(1):97–108, 2010. doi: 10.1109/IEMBS.2009.5333926.

J.J. Palop, J. Chin, and L. Mucke. A network dysfunction perspective on neurodegenerative disease. *Nature*, 443:768–773, 2006. doi: 10.1038/nature05289.

S. Panzeri, J.H. Macke, J. Gross, and C. Kayser. Neural population coding: combining insights from microscopic and mass signals. *Trends Cogn Sci*, 19(3):162–172, 2015. doi: 10.1016/j.tics.2015.01.002.

R.B. Pascual-Marqui, D. Lehmann, M. Koukkou, K. Kochi, P. Anderer, B. Saletu, H. Tanaka, K. Hirata, E.R. John, L. Prichep, R. Biscay-Lirio, and T. Kinoshita. Assessing interactions in the brain with exact low-resolution electromagnetic tomography. *Phil Trans R Soc A*, 369:3768–3784, 2011. doi: 10.1098/rsta.2011.0081.

R.D. Pascual-Marqui. Discrete, 3D distributed, linear imaging methods of electric neuronal activity. Part 1: exact, zero error localization. In *arXiv:0710.3341v2*, 2007.

R.D. Pascual-Marqui. Theory of the EEG inverse problem. In S. Tong and N. Thakor, editors, *Quantitative EEG analysis: methods and clinical applications*, pages 121–140. Boston: Artech House, 2009.

R.D. Pascual-Marqui, D. Lehmann, P. Faber, P. Milz, K. Kochi, M. Yoshimura, K. Nishida, T. Isotani, and T. Kinoshita. The resting microstate networks (RMN): cortical distributions, dynamics, and frequency specific information flow. In *arXiv:1411.1949v2*, 2014.

H. Pastoll, H.L. Ramsden, and M.F. Nolan. Intrinsic electrophysiological properties of entorhinal cortex stellate cells and their contribution to grid cell firing fields. *Front Neural Circuits*, 6:Article 17, 2012. doi: 10.3389/fncir.2012.00017.

H. Pastoll, L. Solanka, M.C.W. Van Rossum, and M. Nolan. Feedback Inhibition Enables Theta-Nested Gamma Oscillations and Grid Firing Fields. *Neuron*, 77:141–154, 2013. doi: 10.1016/j.neuron.2012.11.032.

L.M. Pecora and T.L. Carroll. Master stability functions for synchronized coupled systems. *Phys Rev Lett*, 80:2109, 1998. doi: 10.1103/PhysRevLett.80.2109.

D.B. Percival and A.T. Walden. *Spectral Analysis for Physical Applications: Multitaper and Conventional Univariate Techniques*. Cambridge University Press, 1993. doi: 10.1017/CBO9780511622762.

T.V. Perneger. What's wrong with Bonferroni adjustments. *BMJ*, 316(7139):1236–1238, 1998. doi: 10.1136/bmj.316.7139.1236.

R.J. Perry and J.R. Hodges. Attention and executive deficits in Alzheimer's disease: A critical review. *Brain*, 122(3):383–404, 1999. doi: 10.1093/brain/122.3.383.

G. Petkov, M. Goodfellow, M.P. Richardson, and J.R. Terry. A critical role for network structure in seizure onset: a computational modeling approach. *Front Neurol*, 5:261, 2014. doi: 10.3389/fneur.2014.00261.

Y. Pijnenburg, R. Strijers, Y. Made, W. van der Flier, P. Scheltens, and C. Stam. Investigation of resting-state EEG functional connectivity in frontotemporal lobar degenerations. *Clin Neurophysiol*, 119:1732–1738, 2008. doi: 10.1016/j.clinph.2008.02.024.

L. Pini, M. Pievani, M. Bocchetta, D. Altomare, P. Bosco, E. Cavedo, S. Galluzzi, M. Marizzoni, and G.B. Frisoni. Brain atrophy in Alzheimer's Disease and aging. *Ageing Res Rev*, 30:25–48, 2016. doi: 10.1016/j.arr.2016.01.002.

D.A. Pizzagalli, T.R. Oakes, A.S. Fox, M.K. Chung, C.L. Larson, H.C. Abercrombie, S.M. Schaefer, R.M. Benca, and R.J. Davidson. Functional but not strucutral subgenual prefrontal cortex abnormalities in melancholia. *Mol Psychiatry*, 9:393–405, 2004. doi: 10.1038/sj.mp.4001469.

S.S. Poil, W. de Haan, W.M. van der Flier, H.D. Mansvelder, P. Scheltens, and K. Linkenkaer-Hansen. Integrative EEG biomarkers predict progression to Alzheimer's disease at the MCI stage. *Front Aging Neurosci*, 5:58, 2013. doi: 10.3389/fnagi.2013.00058.

H.W. Querfurth and F.M. LaFerla. Alzheimer's disease. *N Engl J Med*, 32(4):329–344, 2010. doi: 10.1056/NEJMra0909142.

M. Ramsden, L. Kotilinek, C. Forster, J. Paulson, E. McGowan, K. SantaCruz, A. Guimaraes, M. Yue, J. Lewis, G. Carlson, M. Hutton, and K.H. Ashe. Age-dependent neurofibrillary tangle formation, neuron loss, and memory impairment in a mouse model of human tauopathy (p301L). *J. Neurosci.*, 25(46):10637–10647, 2005. doi: 10.1523/JNEUROSCI.3279-05.2005.

A.E. Reineberg, D.E. Gustavson, C. Benca, M.T. Banich, and N.P. Friedman. The Relationship Between Resting State Network Connectivity and Individual Differences in Executive Functions. *Front Psychol*, 9:1600, 2018. doi: 10.3389/fpsyg.2018.01600.

P. Ritter, M. Schirner, A.R. McIntosh, and V.K. Jirsa. The virtual brain integrates computational modelling and multimodal neuroimaging. *Brain Connect*, 3(2):121–145, 2013. doi: 10.1089/brain.2012.0120.

E.D Roberson. Mouse models of frontotemporal dementia. *Ann Neurol*, 72(6):837–849, 2012. doi: 10.1002/ana.23722.

C. Robinson. *Dynamical Systems: Stability, Symbolic Dynamics, and Chaos*. Chapman and Hall/CRC, 1998.

A.B. Rocher, J.L. Crimins, J.M. Amatrudo, M.S. Kinson, M.A. Todd-Brown, J. Lewis, and J.I. Luebke. Structural and functional changes in tau mutant mice neurons are not linked to the presence of NFTs. *Exp Neurol*, 223(2):385–393, 2010. doi: 10.1016/j.expneurol.2009.07.029.

G. Roks, E. Korf, W. van der Flier, P. Scheltens, and C. Stam. The use of EEG in the diagnosis of dementia with Lewy bodies. *J Neurol Neurosurg Psychiatry*, 79:377–380, 2008. doi: 10.1136/jnnp.2007.125385.

S.E. Rose, F. Chen, J.B. Chalk, F.O. Zelaya, W.E. Strugnell, M. Benson, J. Semple, and D.M. Doddrell. Loss of connectivity in Alzheimer's disease: an evaluation of white matter tract integrity with colour coded MR diffusion tensor imaging. *J Neurol Neurosurg Psychiatry*, 69(4):528–530, 2000. doi: 10.1136/jnnp.69.4.528.

H.G. Rotstein, T. Oppermann, J.A. White, and N. Kopell. The dynamic structure underlying subthreshold oscillatory activity and the onser of spikes in a model of medial entorhinal cortex stellate cells. *J Comput Neurosci*, 21:271–292, 2006. doi: 10.1007/s10827-006-8096-8.

M. Rubinov and O. Sporns. Complex network measures of brain connectivity: Uses and interpretations. *NeuroImage*, 52:1059–1069, 2010. doi: 10.1016/j.neuroimage.2009.10.003.

C. Rummel, E. Abela, M. Müller, M. Hauf, O. Scheidegger, R. Wiest, and K. Schindler. Uniform approach to linear and nonlinear interraltion patterns in multivariate time series. *Phys Rev E Stat Nonlin Soft Matter Phys*, 83(6):066215, 2011. doi: 10.1103/PhysRevE.83.066215.

T.E. Rusten and H. Stenmark. How do ESCRT proteins control autophagy? *J. Cell Sci.*, 122:2179–2183, 2009. doi: 10.1242/jcs.050021.

M. Sabeti, S. Katebi, and R. Boostani. Entropy and complexity measures for EEG signal classiciation of schizophrenic and control participants. *Artif Intell Med*, 47(3):263–274, 2009. doi: 10.1016/j.artmed.2009.03.003.

L. Saint-Aubert, L Lemoine, K. Chiotis, A. Leuzy, E. Rodriguez-Vieitez, and A. Nordberg. Tau PET imaging: present and future directions. *Mol Neurodegener*, 12:19, 2017. doi: 10.1186/s13024-017-0162-3.

N. Saito, T. Kuginuki, T. Yagyu, T. Kinoshita, T. Koenig, R.D. Pascual-Marqui, K. Kochi, J. Wackermann, and D. Lehmann. Global, regional, and local measures of complexity of multichannel electroencephalography in acute, neuroleptic-naive, first-break schizophrenics. *Biol Psychiatry*, 43(11):794–802, 1998. doi: 10.1016/S0006-3223(97)00547-7.

M. Salinsky, B. Oken, and L. Morehead. Test-retest reliability in EEG frequency analysis. *Electroencephalogr Clin Neurophysiol*, 79(5):382–392, 1991. doi: 10.1016/0013-4694(91)90203-G.

S. Sami, N. Williams, L.E. Hughes, T.E. Cope, T. Rittman, I.T.S. Coyle-Gilchrist, R.N. Henson, and J.B. Rowe. Neurophysiological signatures of Alzheimer's disease and frontotemporal lobar degeneration: Pathology vs phenotype. *Brain*, 141:2500–2510, 2018. doi: 10.1093/brain/awy180.

E.J. Sanz-Arigita, M. Schoonheim, J.S. Damoiseaux, S.A.R.B. Rombouts, E. Maris, F. Barkhof, P. Scheltens, and C.J. Stam. Loss of 'Small-World' Networks in Alzheimer's Disease: Graph Analysis of fMRI Resting-State Functional Connectivity. *PLoS ONE*, 5 (11):e13788, 2010. doi: 10.1371/journal.pone.0013788.

P. Sanz-Leon, S.A. Knock, A. Spiegler, and V.K. Jirsa. Mathematical framework for large-scale brain network modelling in The Virtual Brain. *NeuroImage*, 111:385–430, 2015. doi: 10.1016/j.neuroimage.2015.01.002.

M. Schirner, S. Rothmeier, V. K. Jirsa, McIntosh A. R., and P Ritter. An automated pipeline for constructing personalized virtual brains from multimodal neuroimaging data. *NeuroImage*, 117:343?357, 2015. doi: 10.1016/j.neuroimage.2015.03.055.

H. Schmidt, G. Petkov, M.P. Richardson, and J.R. Terry. Dynamics on Networks: The Role of Local Dynamics and Global Networks on the Emergence of Hypersynchronous Neural Activity. *PLoS Comput Biol*, 10(11):e1003947, 2014. doi: 10.1371/journal.pcbi.1003947.

T. Schreiber and A. Schmitz. Improved Surrogate Data for Nonlinearity Tests. *Phys Rev E*, 77(4):635–638, 1996. doi: 10.1103/PhysRevLett.77.635.

B.A. Seitzman, M. Abell, S.C. Bartley, M.A. Erickson, A.R. Bolbecker, and W.P. Hetrick. Cognitive manipulation of brain electric microstates. *NeuroImage*, 146:533–543, 2017. doi: 10.1016/j.neuroimage.2016.10.002.

D.J. Selkoe. Alzheimer's Disease Is a Synaptic Failure. *Science*, 298(5594):789–791, 2002. doi: 10.1126/science.1074069.

L.F. Shampine and J. Kierzenka. A BVP Solver based on residual control and the MATLAB PSE. *ACM Trans. Math. Softw.*, 27(3):299–316, 2001. doi: 10.1145/502800.502801.

B. Shan, J. Wang, B. Deng, Z. Zhang, and X. Wei. Estimate the effective connectivity in multi-coupled neural mass model using particle swarm optimization. *Physica A*, 469: 89–101, 2017. doi: 10.1016/j.physa.2016.11.038.

G.M. Shankar, S. Li, T.H. Mehta, A. Garcia-Munoz, N.E. Shepardson, I. Smith, F. Brett, M.A. Farrell, M.J. Rowan, C.A. Lemere, C.M. Regan, D.M. Walsh, B.L. Sabatini, and D.J. Selkoe. Amyloid-βprotein dimers isolated directly from Alzheimer's brains impair synaptic plasticity and memory. *Nat Med*, 14:837–842, 2008. doi: 10.1038/nm1782.

C.F. Shay, M. Ferrante, G.W. IV Chapman, and M. E. Hasselmo. Rebound spiking in layer II medial entorhinal cortex stellate cells: possible mechanism of grid cell function. *Neurobiol Learn Mem*, 129:83–98, 2016. doi: 10.1016/j.nlm.2015.09.004.

A.-M. Shiarli, R. Jennings, J. Shi, K. Bailey, Y. Davidson, J. Tian, et al. Comparison of extent of tau pathology in patients with frontotemporal dementia with Parkinsonism linked to chromosome 17 (FTDP-17), frontotemporal lobar degeneration with Pick bodies and early onset Alzheimer's disease. *Neuropathol Appl Neurobiol*, 32(4):374–387, 2006. doi: 10.1111/j.1365-2990.2006.00736.x.

S. Simpraga, R. Alvarez-Jimenez, H.D. Mansvelder, J.M.A. van Gerven, G.J. Groeneveld, S.S. Poil, and K. Linkenkaer-Hansen. EEG machine learning for accurate detection of cholinergic intervention and Alzheimer's disease. *Sci. Rep.*, 7:5775, 2017. doi: 10.1038/s41598-017-06165-4.

G. Skibinski, N.J. Parkinson, J.M. Brown, L. Chakrabarti, S.L. Lloyd, H. Hummerich, et al. Mutations in the endosomal ESCRTIII-complex subunit CHMP2B in frontotemporal dementia. *Nat Genet*, 37(8):806–808, 2005. doi: 10.1038/ng1609.

P. Smialowski, D. Frishman, and S. Kramer. Pitfalls of supervised feature selection. *Bioinformatics*, 26(3):440–443, 2010. doi: 10.1093/bioinformatics/btp621.

E.E. Smith, J.F. Cavanagh, and J.J.B. Allen. Intracranial source activity (eLORETA) related to scalp-level asymmetry scores and depression status. *Psychophysiology*, 55 (1), 2018. doi: 10.1111/psyp.13019.

S. Smith. EEG in the diagnosis, classification, and management of patients with epilepsy. *J Neurol Neurosurg Psychiatry*, 76(Suppl 20):ii2–ii7, 2005. doi: 10.1136/jnnp.2005.069245.

S.L. Smith and M. Hausser. Parallel processing of visual space by neighboring neurons in mouse visual cortex. *Nat Neurosci*, 13(9):1144–1149, 2010. doi: 10.1038/nn.2620.

S.M. Smith, P.T. Fox, K.L. Miller, D.C. Glahn, P.M. Fox, C.E. Mackay, et al. Correspondence of the brain's functional architecture during activation and rest. *Proc Natl Acad Sci USA*, 106(31):13040–13045, 2009. doi: 10.1073/pnas.0905267106.

L. Solanka, M.C.W. van Rossum, and M.F. Nolan. Noise promotes independent control of gamma oscillations and grid firing within recurrent attractor networks. *eLife*, 4:e06444, 2015. doi: 10.7554/eLife.06444.

T. Solstad, C.N. Boccara, E. Kropff, M.B. Moser, and E.I. Moser. Representation of geometric borders in the entorhinal cortex. *Science*, 322(5909):1865–1868, 2008. doi: 10.1126/science.1166466.

J. Song, C. Davey, C. Poulsen, P. Luu, S. Turovets, E. Anderson, K. Li, and D. Tucker. EEG source localization: Sensor density and head surface coverage. *Journal of Neuroscience Methods*, 256:9–21, 2015. doi: 10.1016/j.jneumeth.2015.08.015.

R.C. Sotero. Topology, Cross-Frequency, and Same-Frequency Band Interactions Shape the Generation of Phase-Amplitude Coupling in a Neural Mass Model of a Cortical Column. *PLoS Comput Biol*, 12(11):e1005180, 2016. doi: 10.1371/journal.pcbi.1005180.

R.A. Sperling, D.M. Rentz, K.A. Johnson, J. Karlawish, M. Donohue, and D.P. Salmon. The A4 study: stopping AD before symptoms begin? *Sci Transl Med*, 6:228fs13, 2014. doi: 10.1126/scitranslmed.3007941.

A. Spiegler and V. Jirsa. Systematic approximations of neural fields through networks of neural masses in the virtual brain. *NeuroImage*, 83:704–725, 2013. doi: j.neuroimage.2013.06.018.

M.G. Spillantini and M. Goedert. Tau pathology and neurodegeneration. *Lancet Neurol*, 12(6):609–622, 2013. doi: 10.1016/S1474-4422(13)70090-5.

O. Sporns, G. Tononi, and R. Kötter. The Human Connectome: A Structural Description of the Human Brain. *PLoS Comput Biol*, 1(4):e42, 2005. doi: 10.1371/journal.pcbi.0010042.

J.C. Sprott. *Chaos and Time Series Analysis*. Oxford University Press, 2003.

C.J. Stam. Modern network science of neurological disorders. *Nat Rev Neurosci*, 15: 683–695, 2014. doi: 10.1038/nrn3801.

C.J. Stam, B. Jones, G. Nolte, M. Breakspear, and P. Scheltens. Small-world networks and functional connectivity in Alzheimer's disease. *Cereb Cortex*, 17(1):92–99, 2007a. doi: 10.1093/cercor/bhj127.

C.J. Stam, G. Nolte, and A. Daffertshofer. Phase Lag Index: Assessment of Functional Connectivity from Multi Channel EEG and MEG with Diminished Bias from Common Sources. *Human Brain Mapping*, 28:1178–1193, 2007b. doi: 10.1002/hbm.20346.

C.J. Stam, W. de Haan, A. Daffertshofer, B.F. Jones, I. Manshanden, A.M. van Cappellen van Walsum, et al. Graph theoretical anlaysis of magnetoencephalographic functional connectivity in Alzheimer's disease. *Brain*, 132(1):213–224, 2009. doi: 10.1093/brain/awn262.

K. Stamps and Y. Hamam. Towards inexpensive BCI control for wheelchair navigation in the enabled environment - a hardware survey. In *Proceedings of the 2010 International Conference on Brain Informatics*, pages 336–345. Heidelberg: Springer-Verlag, 2010.

A. Stevens and T. Kircher. Cognitive decline unlike normal aging is associated with alterations of EEG temporo-spatial characteristics. *Eur Arch Psychiatry Clin Neurosci*, 248: 259–266, 1998. doi: 10.1007/s004060050047.

C. Stosiek, O. Garaschuk, K. Holthoff, and A. Konnerth. *In vivo* two-photon calcium imaging of neuronal networks. *Proc Natl Acad Sci USA*, 100(12):7319–7324, 2003. doi: 10.1073/pnas.1232232100.

G. Stothart, G. Petkov, N. Kazanina, M. Goodfellow, L. Tait, and J. Brown. Graph-theoretical measures provide translational markers of large-scale brain network disruption in human dementia patients and animal models of dementia. *Int J Psychophysiol*, 108:71, 2016. doi: 10.1016/j.ijpsycho.2016.07.232.

W.J. Strik, R. Chiaramonti, G.C. Muscas, M. Paganini, T.J. Mueller, A.J. Fallgatter, A. Versari, and R. Zappoli. Decreased EEG microstate duration and anteriorisation of the brain electrical fields in mild and moderate dementia of the Alzheimer type. *Psychiatry Res*, 75:183–191, 1997. doi: 10.1016/S0925-4927(97)00054-1.

W.K. Strik, T. Dierks, T. Becker, and D. Lehmann. Larger topographical variance and decreased duration of brain electric microstates in depression. *J Neural Transm*, 99: 213–222, 1995. doi: 10.1007/BF01271480.

W.K. Strik, A.J. Fallgatter, D. Brandeis, and R.D. Pascual-Marqui. Three-dimensional tomography of event-related potentials during response inhibition: evidence for phasic frontal lobe activation. *Electroencephalogr Clin Neurophysiol*, 108:406–413, 1998. doi: 10.1016/S0168-5597(98)00021-5.

S.H. Strogatz. *Nonlinear Dynamics and Chaos: With Applications to Physics, Biology, Chemistry, and Engineering*. CRC Press, 2nd edition, 2014.

J. Sun, X. Hong, and S. Tong. Phase Synchronization Analysis of EEG Signals: An Evaluation Based on Surrogate Tests. *IEEE Trans Biomed Eng*, 59(8):2254–2263, 2012. doi: 10.1109/TBME.2012.2199490.

K.J. Suter, B.N. Smith, and F.E. Dudek. Electrophysiological Recording from Brain Slices. *Methods*, 18(2):86–90, 1999. doi: 10.1006/meth.1999.0761.

F. Tadel, S. Baillet, J.C. Mosher, D. Pantazis, and R.M. Leahy. Brainstorm: A User-Friendly Application for MEG/EEG Analysis. *Comput Intell Neurosci*, 2011:879716, 2011. doi: 10.1155/2011/879716.

M.S. Tahaei, M. Jalili, and M.G. Knyazeva. Synchronizability of EEG-based functional networks in Early Alzheimer's disease. *IEEE Trans Neural Syst Rehabil Eng*, 20(5): 636–641, 2012. doi: 10.1109/TNSRE.2012.2202127.

L. Tait, K. Wedgwood, K. Tsaneva-Atanasova, J.T. Brown, and M. Goodfellow. Control of clustered action potential firing in a mathematical model of entorhinal cortex stellate cells. *J. Theor. Biol.*, 449:23–34, 2018. doi: 10.1016/j.jtbi.2018.04.013.

L. Tait, G. Stothart, E. Coulthard, J.T. Brown, N. Kazanina, and M. Goodfellow. Network Substrates of Cognitive Impairment in Alzheimer's Disease. *Clin Neurophysiol*, in press.

F. Tamagnini, J. Novelia, T.L. Kerriga, J.T. Brown, K. Tsaneva-Atanasova, and A.D. Randall. Altered intrinsic excitability of hippocampal Ca1 pyramidal neurons in aged PDAPP mice. *Front Cell Neurosci*, 9:372, 2015. doi: 10.3389/fncel.2015.00372.

B. Tan, X. Kong, P. Yang, Z. Jin, and L. Li. The Difference of Brain Functional Connectivity between Eyes-Closed and Eyes-Open Using Graph Theoretical Analysis. *Comput Math Methods Med*, 2013:976365, 2013. doi: 10.1155/2013/976365.

S.A. Tennant, L. Fischer, D.L.F. Garden, K.Z. Gerlei, C. Martinez-Gonzalez, C. McClure, E.R. Wood, and M.F. Nolan. Stellate Cells in the Medial Entorhinal Cortex are Required for Spatial Learning. *Cell Rep*, 22(5):1313–1324, 2018. doi: 10.1016/j.celrep.2018.01.005.

M. Tomescu, T. Rihs, M. Roinishvili, F. Karahanoglu, M. Schneider, S. Menghetti, et al. Schizophrenia patients and 22q11.2 deletion syndrome adolescents at risk express the same deviant patterns of resting state EEG microstates: a candidate endophenotype of schizophrenia. *Schizophr Res Cogn*, 2:159–165, 2015. doi: 10.1016/j.scog.2015.04.005.

K. Trimmel, A.L. van Graan, L. Caciagli, A. Haag, M.J. Koepp, P.J. Thompson, and J.S. Duncan. Left temporal lobe language network connectivity in temporal lobe epilepsy. *Brain*, 141(8):2406–2418, 2018. doi: 10.1093/brain/awy164.

S.J. Tripathy, J. Savitskaya, S.D. Burton, N.N. Urban, and R.C. Gerkin. NeuroElectro: a window to the world's neuron electrophysiological data. *Front. NeuroInform.*, 8:40, 2014. doi: 10.3389/fninf.2014.00040.

K. Tsaneva-Atanasova, H.M. Osinga, T. Reiß, and A. Sherman. Full system bifurcation analysis of endocrine bursting models. *J Theor Biol*, 264(4):1133–1146, 2010. doi: 10.1016/j.jtbi.2010.03.030.

A. Tsang, C.A. Lebel, S.L. Bray, B.G. Goodyear, M. Hafeez, R.C. Sotero, C.R. McCreary, and R. Frayne. White Matter Structural Connectivity Is Not Correlated to Cortical Resting-State Functional Connectivity over the Healthy Adult Lifespan. *Front Aging Neurosci*, 9:144, 2017. doi: 10.3389/fnagi.2017.00144.

P.J. Uhlhaas and W. Singer. Neural Synchrony in Brain Disorders: Relevance for Cognitive Dysfunctions and Pathophysiology. *Neuron*, 52(1):155–168, 2006. doi: 10.1016/j.neuron.2006.09.020.

M. Ursino, F. Cona, and M. Zavaglia. The generation of rhythms within a cortical region: Analysis of a neural mass model. *NeuroImage*, 52(3):1080–1094, 2010. doi: 10.1016/j.neuroimage.2009.12.084.

D. Van De Ville, J. Britz, and C.M. Michel. EEG microstate sequences in healthy humans at rest reveal scale-free dynamics. *Proc Natl Acad Sci USA*, 107(42):18179–18184, 2010. doi: 10.1073/pnas.1007841107.

E. van Straaten, J. den Haan, H. de Waal, W. van der Flier, F. Barkhof, N. Prins, and C. Stam. Disturbed phase relations in white matter hyperintensity based vascular dementia: An EEG directed connectivity study. *Clin Neurophysiol*, 126(3):497–504, 2015. doi: 10.1016/j.clinph.2014.05.018.

F. Vecchio, F. Miraglia, C. Marra, D. Quaranta, M.D. Vita, P. Bramanti, and P.M. Rossini. Human brain networks in cognitive decline: A graph theoretical analysis of cortical connectivity from EEG data. *J Alzheimers Dis*, 41:113–127, 2014. doi: 10.3233/JAD-132087.

F. Vecchio, F. Miraglia, D. Piludu, G. Granata, R. Romanello, M. Caulo, et al. “Small world” artchitecture in brain connectivity and hippocampal volume in Alzheimer's Disease: a study via graph theory from EEG data. *Brain Imaging and Behav*, 11:473–485, 2017. doi: 10.1007/s11682-016-9528-3.

A. Vernay, L. Therreau, B. Blot, V. Risson, S. Dirrig-Grosch, R. Waegaert, et al. A transgenic mouse expressing CHMP2Bintron5 mutant in neurons develops histological and behavioural features of amyotrophic lateral sclerosis and frontotemporal dementia. *Hum Mol Genet*, 25(15):3341–3360, 2016. doi: 10.1093/hmg/ddw182.

M. Vinck, R. Oostenveld, M. van Wingerden, F. Battaglia, and C.M.A. Pennartz. An improved index of phase-synchronization for electrophysiological data in the presence of volume-conduction, noise and sample-size bias. *NeuroImage*, 55(4):1548–1565, 2011. doi: 10.1016/j.neuroimage.2011.01.055.

S. Visser and S.A. Van Gils. Lumping Izhikevich neurons. *EPJ Nonlinear Biomedical Physics*, 2(6), 2014. doi: 10.1140/epjnbp19.

D. Vitacco, D. Brandeis, R.D. Pascual-Marqui, and E. Martin. Correspondence of Event-Related Potential Tomography and Functional Magnetic Resonance Imaging During Language Processing. *Hum Brain Mapp*, 17:4–12, 2002. doi: 10.1002/hbm.10038.

F. von Wegner, E. Tagliazucchi, and H. Laufs. Information-theoretical analysis of resting state EEG microstate sequences - non-Markvianity, non-stationarity and periodicities. *NeuroImage*, 158:99–111, 2017. doi: 10.1016/j.neuroimage.2017.06.062.

J. Wackermann, D. Lehmann, C.M. Michel, and W.K. Strik. Adaptive segmentation of spontaneous EEG map series into spatially defined microstates. *Int J Psychophysiol*, 14:269–283, 1993. doi: 10.1016/0167-8760(93)90041-M.

E. Wallace, M. Benayoun, W. van Drongelen, and J.D. Cowan. Emergent Oscillations in Networks of Stochastic Spiking Neurons. *PLoS One*, 6(5):e14804, 2011. doi: 10.1371/journal.pone.0014804.

R. Wang, J. Wang, H. Yu, X. Wei, C. Yang, and B. Deng. Decreased coherence and functional connectivity of electroencephalograph in Alzheimer's disease. *Chaos*, 24: 033136, 2014. doi: 10.1063/1.4896095.

R. Wang, J. Wang, H. Yu, X. Wei, C. Yang, and B. Deng. Power spectral density and coherence analysis of Alzheimer's EEG. *Cogn Neurodyn*, 9:291–304, 2015. doi: 10.1007/s11571-014-9325-x.

Z. Wang, X. Jia, P. Liang, Z. Qi, Y. Yang, W. Zhou, and K. Li. Changes in thalamus connectivity in mild cognitive impairment: Evidence from resting state MRI. *Eur J Radiol*, 81:277–285, 2012. doi: 10.1016/j.ejrad.2010.12.044.

D.J. Watts and S.H. Strogatz. Collective dynamics of 'small-world' networks. *Nature*, 393: 440–442, 1998. doi: 10.1038/30918.

S.J. Webster, A.D. Bachstetter, P.T. Nelson, F.A. Schmitt, and L.J. Van Eldik. Using mice to model Alzheimer's dementia: an overview of the clinical disease and preclinical behavioural changes in 10 mouse models. *Front. Genet.*, 5:88, 2014. doi: 10.3389/fgene.2014.00088.

P.D. Welch. The use of Fast Fourier Transform for the estimation of power spectra: A method based on time average over short, modified periodograms. *IEEE Trans Audio Electrocoust*, 15(2):70–73, 1967. doi: 10.1109/TAU.1967.1161901.

T. Welch. A Technique for High-Performance Data Compression. *Computer*, 17(6):8–19, 1984. doi: 10.1109/MC.1984.1659158.

F. Wendling, F. Bartolomei, J.J. Bellanger, and P. Chauvel. Epileptic fast activity can be explained by a model of GABAergic dendritic inhibition. *Eur J Neurosci*, 15:1499–1508, 2002. doi: 10.1046/j.1460-9568.2002.01985.x.

H.W. Wendt. Dealing with a common problem in social science: A simplified rank-biserial coefficient of correlation based on the U statistic. *Eur J Soc Psychol*, 2(4):463–465, 1972. doi: 10.1002/ejsp.2420020412.

J.A. White, T. Budde, and A.R. Kay. A Bifurcation Analysis of Neuronal Subthreshold Oscillations. *Biophys J*, 69:1203–1217, 1995. doi: 10.1016/S0006-3495(95)79995-7.

J.A. White, R. Klink, A. Alonso, and A.R. Kay. Noise From Voltage-Gated Ion Channels May Influence Neuronal Dynamics in the Entorhinal Cortex. *J. Neurophysiol.*, 80:262–269, 1998. doi: 10.1152/jn.1998.80.1.262.

J.A. White, J.T. Rubinstein, and A.R. Kay. Channel noise in neurons. *Trends Neurosci.*, 23:131–137, 2000. doi: 10.1016/S0166-2236(99)01521-0.

M.A. Whittington, R.D. Traub, N. Kopell, B. Ermentrout, and E.H. Buhl. Inhibition-based rhythms: experimental and mathematical observations on network dynamics. *Int J Psychophysiol*, 38(3):315–336, 2000. doi: 10.1016/S0167-8760(00)00173-2.

A.D. Wickenden. Overview of Electrophysiological Techniques. *Curr Protoc Pharmacol*, 64:11.1.1–17, 2014. doi: 10.1002/0471141755.ph1101s64.

H.R. Wilson and J.D. Cowan. Excitatory and Inhibitory interactions in localized populations of model neurons. *Biophys J.*, 12(1):1–24, 1972. doi: 10.1016/S0006-3495(72)86068-5.

J. Witton, L.E. Staniaszek, U. Bartsch, A.D. Randall, M.W. Jones, and J.T. Brown. Disrupted hippocampal sharp-wave ripple-associated spike dynamics in a transgenic mouse model of dementia. *J Physiol*, 594(16):4615–4630, 2016. doi: 10.1113/jphysiol.2014.282889.

K.-F. Wong and X.-J. Wang. A Recurrent Network Mechanism of Time Integration in Perceptual Decisions. *J Neurosci*, 26(4):1314–1328, 2006. doi: 10.1523/JNEUROSCI.3733-05.2006.

S. Wook Oh, J.A. Harris, L. Ng, B. Winslow, N. Cain, S. Mihalas, et al. A mesoscale connectome of the mouse brain. *Nature*, 508:207–214, 2014. doi: 10.1038/nature13186.

World Health Organization. Dementia fact sheet, 2017.

L. Wu, T. Eichele, and V.D. Calhoun. Reactivity of hemodynamic responses and functional connectivity to different states of alpha synchrony: a concurrent EEG-fMRI study. *NeuroImage*, 52(4):1252–1260, 2010. doi: 10.1016/j.neuroimage.2010.05.053.

X. Wu, R. Li, A.S. Fleisher, E.M. Reiman, K. Chen, and L. Yao. Altered Default Mode Network Connectivity in Alzheimer's Disease - A Resting Functional MRI and Bayesian Network Study. *Hum Brain Mapp*, 32(11):1868–1881, 2011. doi: 10.1002/hbm.21153.

P. Wulff, A.A. Ponomarenko, M. Bartos, T.M. Morotkova, E.C. Fuchs, F. Bähner, et al. Hippocampal theta rhythm and its coupling with gamma oscillations require fast inhibition onto parvalbumin-positive interneurons. *Proc Natl Acad Sci USA*, 106(9):3562–3566, 2009. doi: 10.1073/pnas.0813176106.

M. Yoshida, A. Jochems, and M.E. Hasselmo. Comparison of Properties of Medial Entorhinal Cortex Layer II Neurons in Two Anatomical Dimensions with and without Cholinergic Activation. *PLoS One*, 8(9):e73904, 2013. doi: 10.1371/journal.pone.0073904.

M. Yoshimura, T. Koenig, S. Irisawa, T. Isotani, K. Yamada, M. Kikuchi, et al. A pharmaco-EEG study on antipsychotic drugs in healthy volunteers. *Psychopharmacology (Berl)*, 191(4):995–1004, 2007. doi: 10.1007/s00213-007-0737-8.

P.A. Young, P.H. Young, and D.L. Tolbert. *Basic Clinical Neuroscience*. Wolters Kluwer, 3rd edition, 2015.

M. Yu, A. Gouw, A. Hillebrand, B. Tijms, C. Stam, E. van Straaten, and Y. Pijnenburg. Different functional connectivity and networks topology in behavioural variant of frontotemporal dementia and Alzheimer's disease: an EEG study. *Neurobiol Aging*, 42: 150–162, 2016. doi: 10.1016/j.neurobiolaging.2016.03.018.

M. Yue, A. Hanna, J. Wilson, H. Roder, and C. Janus. Sex difference in pathology and memory decline in rTg4510 mouse model of tauopathy. *Neurobiol Aging*, 32(4):590–603, 2011. doi: 10.1016/j.neurobiolaging.2009.04.006.

F. Zappasodi, P. Croce, A. Giordani, G. Assenza, M.N. Giannatoni, P. Profice, G. Granata, P.M. Rossini, and F. Tecchio. Prognostic value of EEG microstates in acute stroke. *Brain topogr*, 30(5):698–710, 2017. doi: 10.1007/s10548-017-0572-0.

M. Zavaglia, F. Cona, and F. Ursino. A Neural Mass Model to Simulate Different Rhythms in a Cortical Region. *Comput Intel Neurosci*, 2010:456140, 2010. doi: 10.1155/2010/456140.

X. Zhang, W. Zhong, J. Brankack, S.W. Weyer, U.C. Müller, A.B.L. Tort, and A. Draguhn. Impaired theta-gamma coupling in APP-deficient mice. *Sci Rep*, 6:21948, 2016. doi: 10.1038/srep21948.

Z. Zhang, M. Descoteaux, J. Zhang, G. Girard, M. Chamberland, D. Dunson, A. Srivastava, and H. Zhu. Mapping population based structural connectomes. *NeuroImage*, 172:130–145, 2018. doi: 10.1016/j.neuroimage.2017.12.064.

Q. Zhao, H. Lu, H. Metmer, W.X.Y. Li, and J. Lu. Evaluation functional connectivity of executive control network and frontoparietal network in Alzheimer's disease. *Brain Res*, 1678:262–272, 2018. doi: 10.1016/j.brainres.2017.10.025.

J. Zimmerman, A. Perry, M. Breakspear, M. Schirner, P. Sachdev, W. Wen, et al. Differentiation of Alzheimer's disease based on local and global parameters in personalized Virtual Brain models. *NeuroImage Clin*, 19:240–251, 2018. doi: 10.1016/j.nicl.2018.04.017.

J. Ziv and A. Lempel. A universal algorithm for sequential data compression. *IEEE Trans Inform Theor*, 23(3), 1977. doi: 10.1109/TIT.1977.1055714.

J. Ziv and A. Lempel. Compression of individual sequences via variable-rate coding. *IEEE Trans Inform Theor*, 24(5), 1978. doi: 10.1109/TIT.1978.1055934.

D. Zumsteg, R. A. Wennberg, V. Treyer, A. Buck, and H. G. Wieser. H215O or 13NH3 PET and electromagnetic tomography (LORETA) during partial status epilepticus. *Neurology*, 65(10):1657–1660, 2005. doi: 10.1212/01.wnl.0000184516.32369.1a.

D. Zumsteg, A. Friedman, H.G. Wieser, and R.A. Wennberg. Propogation of interictal discharges in temporal lobe epilepsy: Correlation of spatiotemporal mapping with intracranial foramen ovale electrode recordings. *Clin Neurophysiol*, 117:2615–2626, 2006. doi: 10.1016/j.clinph.2006.07.319.